

# The NumWEC project

Numerical estimation of energy delivery from a  
selection of wave energy converters

Final report

Aurélien Babarit<sup>1</sup>, Jørgen Hals<sup>2</sup>, Adi Kurniawan<sup>2</sup>,  
Made Muliawan<sup>2</sup>, Torgeir Moan<sup>2</sup> and Jørgen Krokstad<sup>3</sup>

<sup>1</sup>Laboratoire de Mécanique des Fluides - CNRS UMR6598  
Ecole Centrale de Nantes, 1 rue de la Noe, 44300 Nantes, France

<sup>2</sup>Centre for Ships and Ocean Structures  
Norges teknisk-naturvitenskapelige universitet, Otto Nielsens V. 10  
7491 Trondheim, Norway

<sup>3</sup>Statoil  
PO box 200, Lilleaker, 0216 Oslo, Norway

15 December 2011



**Statkraft**



*Centrale  
Nantes*



**NTNU – Trondheim**  
Norwegian University of  
Science and Technology

# Contents

<b>I The NumWEC project</b>	<b>ii</b>
<b>Introduction</b>	<b>iii</b>
<b>Assumptions and limitations</b>	<b>iv</b>
<b>Results</b>	<b>v</b>
<b>Further research</b>	<b>v</b>
<b>Acknowledgement</b>	<b>vi</b>
<b>II Reports from device studies</b>	<b>vii</b>
<b>1 Bref-HB inspired by Seabased</b>	<b>viii</b>
<b>2 F-2HB inspired by Wavebob</b>	<b>ix</b>
<b>3 F-3OF inspired by Langlee</b>	<b>x</b>
<b>4 F-OWC inspired by OEBuoy</b>	<b>xi</b>
<b>5 F-HBA inspired by Pontoon</b>	<b>xii</b>
<b>6 B-OF inspired by Oyster2</b>	<b>xiii</b>
<b>7 B-HBA inspired by Wavestar</b>	<b>xiv</b>
<b>8 Bref-SHB inspired by Ceto</b>	<b>xv</b>

# **Part I**

## **The NumWEC project**

## Introduction

The converted useful energy represents the income side of a wave energy project. It may be estimated once the external dimensions, working principle, machinery function and local wave resource are known. On the cost side the picture becomes more complex, with contributions from design, fabrication, installation, operation, maintenance and eventually decommissioning. As long as the technical solutions are uncertain or unknown on a detailed level, cost estimates are inevitably hampered by large uncertainties.

In order to provide a benchmark for the income potential of wave energy converters, the project described in this document was carried out in order to estimate and analyse the energy conversion for a representative selection of converter designs. Such a benchmark may later serve as a premise, setting the upper limits to the cost for a design to be viable.

On this background the main objective of this work has been to use numerical modelling tools to estimate the energy delivery which can be expected from a selection of wave energy converters currently in development. The project may be summarised as

- Using a “state of the art” numerical approach.
- Studying design from all of the following categories: heaving buoys, surging flaps and oscillating water columns; floating systems, bottom-referenced devices and bottom-fixed systems.
- Studying eight different designs and their operation in five different locations in European waters.
- Estimating the yearly energy delivery from each WEC design, including its distribution with time, and identifying and quantifying its uncertainties.
- Defining a set of performance measures that later can be related to cost (financial cost and energy cost), and estimating the values of these for each converter design.
- Identifying and suggesting further research tasks to be conducted in order to decrease the uncertainties and improve the performance.

It is our hope that the results we have arrived at will serve as a valuable benchmark for the development of wave energy technology in that they provide a target for the cost reduction of converter concepts.

In Part I of this document, we present the background and framework of the studies that we have carried out, while Part II contains a technical report for each of the eight converter designs that have been studied.

**In referring to this work, please refer primarily to the published papers (see the Results section below), and in particular to our summary paper, *Numerical benchmarking study of a selection of Wave Energy Converters in Renewable Energy*.**

## Assumptions and limitations

No cost estimates have been made in this study. It has not been our intention to judge between good and bad designs. As the results show, all of the wave energy converters have scores in the same order of magnitude for the performance measures that was defined. The potential for success rather depends on how cheap and how robust it is possible to make each device, and on how efficient its fabrication, installation and maintenance can be made.

The choice of designs to include in the study was based on availability of data, on level of maturity, on diversity and on our interests. Plausible assumptions have been made where information was scarce or missing.

No advanced motion control strategies have been applied. In all cases (except for the F-HBA device) linear machinery forces were considered, where the power take-off parameters were optimised as a constant for each sea state. In cases where it was relevant, simplified representations of hydraulic systems and direct-coupled electric generators were investigated.

For each wave energy converter a wave to wire model was developed. They were based on the following assumptions

- The waves and fluid-structure interactions was modelled using linear potential theory
- The waves were assumed to be mono-directional.
- The power take-off systems were modelled by an input-output relation for the machinery force.
- Mooring systems was represented by linear springs and dampers adjusted to keep the device in place with minimum influence on the power absorption.
- An approximate representation of viscous losses was included where this was expected to have strong influence. The drag coefficients was then be based on best available information, which might have been inaccurate.
- Amplitude constraints were included by repulsive energy potentials.

The numerical wave-to-wire models were used to estimate the mean annual absorbed energy for each converter at each site. The performance has further been computed in terms of the following measures:

- Yearly energy output per characteristic mass
- Yearly energy output per characteristic wetted surface area
- Yearly energy output per unit characteristic machinery force
- Yearly energy output per unit characteristic excitation force.
- Duration curves (distribution of output power in function of fractions of the year).

## Results

As mentioned a separate technical report was written for each of the eight wave energy converters that was studied. These are found in Part II of this document. These contain detailed information about the configuration of each system and how we chose to model them.

A detailed account for the wave statistics and other parameters of each deployment site that has been considered is given in the report on the Bref-HB device, see Chapter 1.

**A comparative analysis based on the results of the eight studies was published as an article in the Elsevier journal *Renewable Energy*:**

- Numerical benchmarking study of a selection of Wave Energy Converters.

**Please refer to this paper as the main reference for the work that has been carried out within the NumWEC project.**

Additionally, the following papers were published as a direct result of the project:

- Made Jaya Muliawan, Zhen Gao, A. Babarit, Torgeir Moan: Analysis of a Two-Body Floating Wave Energy Converter with Particular Focus on the Effect of Mooring System on Energy Capture, OMAE2011-49135
- A. Babarit, Jørgen Hals, Adi Kurniawan, Jørgen Krokstad, Torgeir Moan: Power absorption Measures and Comparisons of Selected Wave Energy Converters, OMAE2011-49360
- Adi Kurniawan, Jørgen Hals, Torgeir Moan Norwegian: Modelling and Simulation of a Floating Oscillating Water Column, OMAE2011-49263.
- An extension of the F-2HB paper (OMAE2011-49135) has been submitted to the Journal of OMAE.

## Further research

Based on the studies that have been carried out, we present here a general list of topics that would need further investigation, and that are relevant to some or all of the designs included here:

- Solutions for safe and robust end-stop mechanisms
- Elimination or mitigation of snap load events on wires
- Cost-efficient mooring and foundations systems
- Smoothing of energy output through the use of energy storage or averaging between individual units
- Component design for durability and robustness
- Motion control strategies for exploiting installed equipment at maximum

## Acknowledgement

This research was carried out as part of the Statkraft Ocean Energy Research Program, sponsored by Statkraft ([www.statkraft.no](http://www.statkraft.no)). This support is gratefully acknowledged. The project was carried out in collaboration between Ecole Centrale de Nantes (ECN), the Centre for Ships and Ocean Structures (CeSOS) at NTNU, and Statkraft.

Thanks also go to all the developers and associates who have shared information and discussed the results with us: namely Halvar Gravråkmo from Uppsala University, Thomas Soulard and Jochem Weber from Wavebob, Julius Espedal from Langlee and Øyvind Rogne from NTNU, Morten Kramer from DTU and Enrique Vidal Sanchez from Wavestar, Marco Alves from the Wave Energy Centre, Giovanni Mattarolo and Marc Andreeowsky from EDF, Arnaud Vazeille from EDF EN, and Nils Myklebust from Pontoon Power Converter . Finally, Aurélien Babarit would also like to thank CeSOS for hosting him during the realisation of this study.



## **Part II**

# **Reports from device studies**

# **Chapter 1**

**A bottom-referenced  
heaving buoy (Bref-HB)  
inspired by the Seabased  
WEC**

# Numerical estimation of energy delivery from a selection of Wave Energy Converters – small bottom-referenced heaving buoy

Aurélien Babarit<sup>1</sup>, Jørgen Hals<sup>2</sup>

<sup>1</sup>Laboratoire de Mécanique des Fluides - CNRS UMR6598  
Ecole Centrale de Nantes, 1 rue de la Noe, 44300 Nantes, France  
<sup>2</sup>CeSOS, NTNU

August 2010

## Summary

This document reports the pilot study of the project “Numerical estimation of energy production from a selection of Wave Energy Converters”. It contains a mathematical model and simulation results for the study of a small bottom-referenced heaving buoy wave energy converter (Bref-HB). The design was inspired by the Seabased WEC which is currently under development in Sweden, but is not identical to it.

Results of the study are the following criteria:

- The annual mean power.
- The yearly energy output / displacement.
- The yearly energy output / wetted surface.
- The power per unit of significant PTO force.
- The power per unit of excitation force
- The duration curves.

These criteria were estimated using the mathematical model described in this report. Results are given in the following table and in figure (1).

From these results and the study, main conclusions are :

- The mean annual power level that one can expect from this device is about 3 kW on a site whose wave resource is between 20-40 kW/m.

Site	SEM -REV	EMEC	Yeu	Lisboa	Belmullet	Danish site
$\gamma$	1.	1	3.3	3.3	3.3	1
Mean power [kW]	1.6	2.8	3.3	3.5	5.0	2.7
Energy / Mass [MWh/m <sup>3</sup> ]	0.46	0.78	0.92	1.00	1.40	0.76
Energy / Wetted surface [MWh/m <sup>2</sup> ]	0.34	0.57	0.68	0.73	1.04	0.56
Energy / PTO force [kWh/N]	1.5	2.1	2.3	2.2	2.6	2.22
Energy / Wave force [kWh/N]	0.89	1.19	1.27	1.21	1.18	1.34

Table 1: Evaluation criteria for the small bottom-referenced heaving buoy. The uncertainty is estimated to  $\pm 30\%$ .

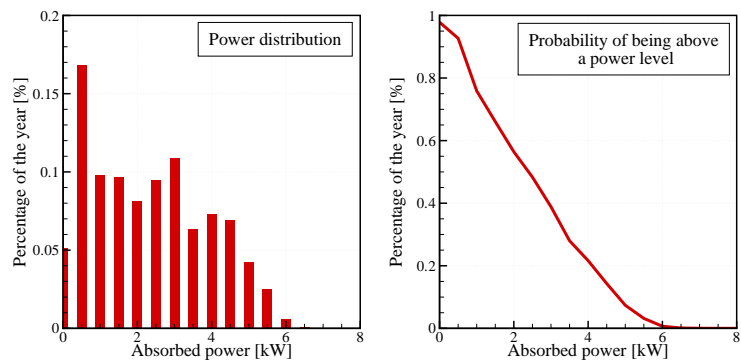


Figure 1: Distribution of the power production on a typical 30 kW/m wave site.

- The uncertainty on these figures is about 30%. It comes from the modelling of the viscous losses and a dependence on the length of the wire.
- High tide leads to a reduction of the absorbed power up to 30%. Low tide might lead to an increase of the absorbed power up to 8%.
- A scaling up by a factor 2 of the system (displacement times 8) leads to an increase of the power by a factor 5.3. It also lead to a decrease of the criteria energy per PTO force and energy per wave force. Depending on how scale the costs, it could be beneficial to scale up the system in order to decrease the cost of energy.
- The instantaneous output power could be limited to 10 times the mean annual power without losing a significant amount of energy production.
- The viscous effects are significant. It is observed that they have a positive influence on the energy production.
- Both heave and surge motions contribute to the wave energy absorption
- The performance in term of absorbed energy is slightly inferior for the linear generator machinery as compared to an idealised linear damper.

# Contents

<b>1 System description - The Bref-HB wave energy converter</b>	<b>6</b>
1.1 Mechanical parameters . . . . .	6
1.1.1 Buoy . . . . .	7
1.1.2 Connecting line . . . . .	7
1.1.3 Generator unit . . . . .	7
1.2 Cost criteria . . . . .	8
1.2.1 Displacement, mass and wetted surface . . . . .	8
1.2.2 Significant forces . . . . .	10
<b>2 Mathematical model</b>	<b>10</b>
2.1 System kinematics . . . . .	10
2.2 Equation of motion . . . . .	11
2.3 Hydrodynamic forces . . . . .	12
2.3.1 Wave radiation force . . . . .	12
2.3.2 Wave excitation force . . . . .	14
2.3.3 Viscous damping forces . . . . .	15
2.4 Machinery model . . . . .	16
2.4.1 PTO taken as a linear damper . . . . .	16
2.4.2 PTO modelled as a simplified electric generator . . . . .	16
2.5 Treatment of the end stops . . . . .	18
2.6 Assembled model . . . . .	18
2.7 Implementation . . . . .	19
<b>3 Sites locations and wave data</b>	<b>20</b>
3.1 France/SEM-REV test site . . . . .	20
3.2 Scotland/EMEC test site . . . . .	21
3.3 France/Yeu island . . . . .	21
3.4 Portugal/Lisboa . . . . .	21
3.5 Ireland/Belmullet . . . . .	22
3.6 Danemark/Danish site . . . . .	22
<b>4 Simulation results and energy assessment</b>	<b>22</b>
4.1 Verification tests . . . . .	22
4.2 RAOs . . . . .	26
4.2.1 Optimisation of the PTO damping coefficient . . . . .	28
4.2.2 Assessment of non linearities effects on the response . . . . .	28
4.2.3 Assessment of viscous damping effects . . . . .	28
4.2.4 Assessment of the effect of the length of the wire . . . . .	32
4.2.5 Conclusions . . . . .	34
4.3 Power matrix and criteria . . . . .	34
4.3.1 Power matrix of the small Bref-HB . . . . .	34
4.3.2 Assessment of the uncertainties . . . . .	39

4.3.3	Conclusion	42
4.4	Parametric studies	42
4.4.1	Effect of the tide	42
4.4.2	Effect of the scale	43
4.4.3	Effect of limitation of the maximal output power	43
4.5	Power flow	44
4.6	Linear damper PTO vs. generator with DC-level control	46
<b>5</b>	<b>Conclusions and recommendations</b>	<b>49</b>

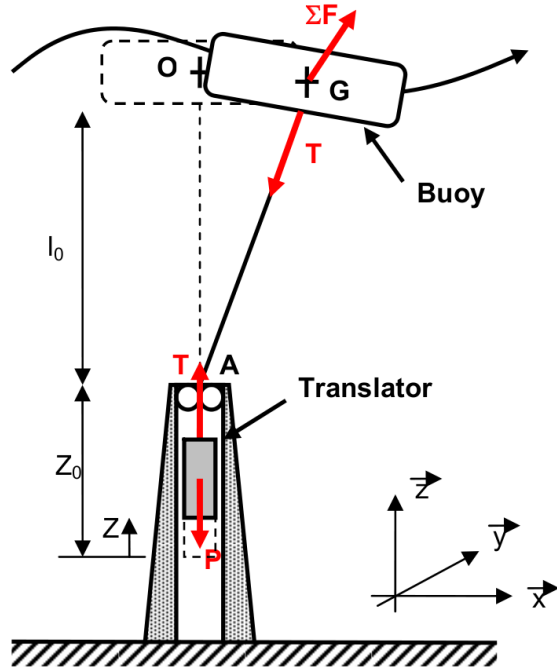


Figure 2: Sketch of the system.

## 1 System description - The Bref-HB wave energy converter

The small bottom-referenced heaving buoy wave energy converter consists of a circular buoy floating on the ocean surface. Through a wire it is connected to a machinery unit standing at the sea bottom. The machinery consists of a linear generator placed inside a steel hull mounted on a concrete ballast structure. A simplified sketch of the system is shown in Figure 2, and a picture including the different components is found in Figure 3.

### 1.1 Mechanical parameters

This wave energy device was inspired by the Seabased WEC and its predecessors that have been extensively studied at Uppsala universitet. The system being commercialised by the Seabased company seems to be derived directly from the work done by and published by researchers at Uppsala University, although there may of course be differences that are not publicly known. The system parameters used in the present study has thus been obtained mainly from publication by the Uppsala University research group, and includes the PhD theses of Mikael Eriksson [6] and Rafael Waters [10], as well as a series of articles, [11, 7, 12]. Some material has also been gathered from web pages on the internet. Tables 2 and 3 summarise



Figure 3: Components of the small Bref-HB wave energy converter.

the parameters.

### 1.1.1 Buoy

The buoy was originally made with a rectangular cross-section. In the more recent version of the buoy the shape has been rounded, as can be seen from Figure 3. There are two alternative shapes found: one circular closed shape, and one “hexagonal donut” shape. In the present study it has been decided to assume a circular buoy with ellipsoidal cross-section. Its parameters are given in Table 2.

### 1.1.2 Connecting line

For the connection between the buoy and the machinery unit Vectran material with Dynema or polyester coating has been tried, but the latest versions have used steel wire with plastic coating. According to our information, the diameter of the wire has been around 30 mm, and the wire stiffness has been reported to 450 kN/m. In the present study we model the line as massless.

### 1.1.3 Generator unit

The generator unit consists of a steel pressure vessel, which is pressurised such that the internal pressure equals the surrounding pressure. The entry of the wire from the buoy is done through a membrane system to keep water from entering the vessel. The main characteristics of the generator unit are given by the parameters collected in Table 3.

The generator has permanent magnets mounted on the translator feeding a magnetic flux through the coils mounted on the stator. This gives rise to an electric voltage induced at the generator terminals when the translator moves. Both the magnitude of the electric voltage and the frequency will be proportional to the speed of the translator.

Table 2: System parameters

Property	Value	Unit
long axis of the buoy	1.5	m
short axis of the buoy	0.63	m
draft	0.63	m
height	1.26	m
displacement	2.83	$\text{m}^3$
mass of the buoy	1000	kg
centre of mass	-0.3	m below the free surface
Moment of inertia $I_{xx}$	2910	$\text{kg}\cdot\text{m}^2$
Moment of inertia $I_{yy}$	2910	$\text{kg}\cdot\text{m}^2$
Moment of inertia $I_{zz}$	5407	$\text{kg}\cdot\text{m}^2$
Wire stiffness	450000	kg/m
Stroke length	1.8	m
Stiffness upper end stop spring	243000	kg/m
Stiffness lower end stop spring	215000	kg/m
Stiffness of translator spring	6200	kg/m
Mass of the translator	1898	kg
crossectional shape <sup>1</sup>	ellipsoidal	
long axis	1.5	m
short axis	0.63	m

According to published information, the unit has in sea trials been tested by applying constant electric resistance directly on the generator terminals ( $\Delta$  coupled). In more recent tests it has been tried to connect the generator to a passive rectifier unit with a large capacitor and a resistor in parallel on the other side. The intention is to finally connect the rectifier to a DC-link before inverting to three-phase current adaptable to a power grid.

The total stroke length of the translator before the end stop springs are engaged is 1.8 m, i.e. the maximum amplitude from the mid-position is 0.9 m.

For verification and comparison the power take off force will alternatively be modelled as a linear damper (Section 2.4). It will serve as a convenient tool for reference and comparison to other wave energy converter (WEC) designs as it is the most commonly used assumption in the modelling of machinery systems for WECs.

## 1.2 Cost criteria

### 1.2.1 Displacement, mass and wetted surface

The wetted surface and mass are two of the relevant costs related criteria which could be derived for any wave energy converter.

Table 3: Generator unit parameters.

Property	Value	Unit
height	m	8.0
diameter	m	1.28
stroke length (between end stops)	m	1.8
height at wire exit	m	8.0
stator length	mm	1264
translator length	mm	1867
stator width	m	0.40
translator mass <sup>2</sup>	kg	1140
stiffness translator springs	N/m	6200
stiffness upper endstop spring	kN/m	243
stiffness lower endstop spring	kN/m	216
initial stretch of the translator springs <sup>3</sup>	m	1.2
initial tension of the translator springs	N	7.44
generator gyrator modulus <sup>4</sup>	Vs/m	200
winding inductance (per phase)	mH	5.5
winding resistance (per phase)	ohm	0.45
capacitor size for DC link	F	24.5
air gap	mm	3
pole width	mm	50
nominal speed	m/s	0.7
nominal power	kW	10
nominal current (from power/voltage)	A	75
nominal force (from power/velocity)	kN	15
DC voltage setpoint (typical)	V	$\in [50, 150]$
electrical load resistance	ohm	$\in [2.2, 27]$
mechanical load resistance <sup>5</sup>	kNs/m	$\in [???$

Criteria	unit
Significant wetted surface	42 m <sup>2</sup>
Significant mass	31 tons

Table 4: Significant wetted surface and mass of the small bottom-referenced heaving buoy.

In the case of a small bottom-referenced heaving buoy, the two parts of the system - the buoy and the generator - should be considered because both of them would contribute significantly to the cost of the system. Actually, it has been decided to even include the weight of the anchors because the system reacts against the sea bottom via these anchors.

The mass of the buoy is equal to 1000 kg, the mass of the generator is about 10 tons and the mass of the anchors is between 10 and 30 tons. We considered here 20 tons. Hence, the overall significant mass is 31 tons.

The wetted surface of the buoy is about 9 m<sup>2</sup>. The generator height is 8 meters, and its diameter 1.28 meters. Then, its surface is about 33 m<sup>2</sup>. Hence the total significant wetted surface is 42 m<sup>2</sup>.

### 1.2.2 Significant forces

The two other cost criteria considered are the significant PTO force and the significant wave force. They both have zero mean values. So, they are defined as their RMS over the whole year.

## 2 Mathematical model

The mathematical model was developed referring to the sketch and nomenclature given in Figure 2.

### 2.1 System kinematics

It is assumed that the attachment point of the wire and the gravity centre of the buoy are close. It allows neglecting coupling effects between rotations of the buoy and the wire. The buoy being axisymmetric, the motion remains in the plane defined by the wave direction vector and the vertical axis.

Let  $(x_G, y_G, z_G)$  be the motion of the gravity center  $G$  of the buoy from its equilibrium position  $O$  and  $\vec{\Omega} = (\phi, \theta, \psi)$  be its rotational motion. Let  $X = (x_G, y_G, z_G, \phi, \theta, \psi)$  the position vector of the buoy. Let  $Z$  be the motion of the translator. Let  $M$  be its mass and  $[I]$  be its inertia matrix.

Let  $L$  be the length of the line connecting the buoy to the translator. At rest, the system is at equilibrium, i.e:

$$L_0 = l_0 + Z_0$$

Let  $l$  be the length between the gravity center of the buoy and point  $A$  where the wire enters the generator.

$$l = |AG| \quad (1)$$

At time  $t$ , the length of the line is:

$$L = l + Z_0 - Z \quad (2)$$

The height of the generator is 8 m. Hence,  $Z_0$  was set equal to 4 m. Regarding  $l_0$ , it depends on the water depth  $h$  via the relation  $l_0 + 2Z_0 = h$ .

## 2.2 Equation of motion

In this study, fluid structure interactions are modelled within the frame of the usual linear potential theory, which is the state of the art in wave energy conversion [1]. Viscous effects are taken into account via additional quadratic damping coefficients as in [2]. Hence, the hydrodynamic forces acting on the buoy can be written:

- $\vec{F}_{ex}$  the wave excitation force, due to the incident and diffracted wave field.
- $\vec{F}_{rad}$  the radiation force, composed of two parts. One is proportional to the acceleration of the buoy. Its coefficient is the added mass matrix  $[\mu_\infty]$ . The other involves the history of the velocity of the buoy, via a convolution product with the radiation memory function. Let  $\vec{F}_{mem}$  be this part of the radiation force.
- $\vec{F}_{viscous}$  is the damping force associated with viscous effects.
- $\vec{F}_A$  is the force resulting from the action of the Archimedes buoyancy force. By linearising around the mean equilibrium position of the whole system {Buoy+Translator}, one can show that  $\vec{F}_A = \begin{pmatrix} M\vec{g} \\ \vec{0} \end{pmatrix} - K_H X$  in which  $K_H$  is the hydrostatic stiffness matrix.

Let  $\vec{T}$  be the tension in the wire. Let  $\vec{T} = T\vec{t}$ , in which  $\vec{t}$  is defined as:  $\vec{t} = \frac{\vec{G}\vec{A}}{\|\vec{G}\vec{A}\|}$ . Let  $[m]$  be the mass matrix of the buoy. By application of Newton's law, one can write:

$$([m] + [\mu_\infty])\vec{\gamma}_G = \vec{F}_{ex} + \vec{F}_{mem} + \vec{F}_{viscous} + \vec{F}_A + \begin{pmatrix} \vec{T} \\ \vec{0} \end{pmatrix} \quad (3)$$

Let consider the system {Translator}. One can show:

$$M\ddot{Z} = T - Mg + F_m - K_Z Z + F_{es} \quad (4)$$

in which:

- $-Mg$  is the weight of the translator.
- $F_m$  is the electromagnetic force due to the energy conversion system. The model used for this force is detailed in section 2.4.
- $-K_Z Z$  is the restoring force due to the spring connecting the translator with the seabed.
- $F_{es}$  is the force associated with the end stops. It is detailed in section 2.5

## 2.3 Hydrodynamic forces

### 2.3.1 Wave radiation force

The radiation force  $\overrightarrow{F}_{rad}$  is given by  $\overrightarrow{F}_{rad} = -[\mu_\infty] \overrightarrow{\gamma}_G - \overrightarrow{F}_{mem}$  with :

$$\overrightarrow{F}_{mem}(t) = \int_0^t [K_{rad}(t - \tau)] \overrightarrow{V}_G(\tau) d\tau \quad (5)$$

$[K_{rad}(t)]$  is the impulse response matrix of the radiation force.

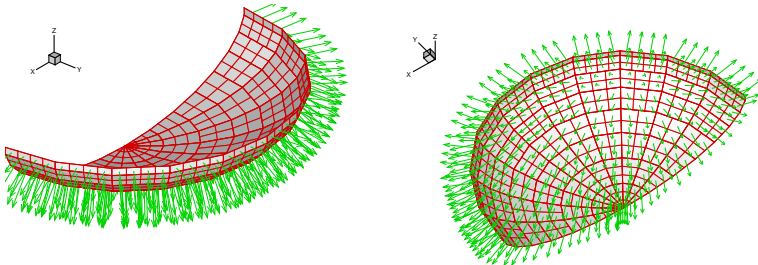


Figure 4: Mesh used for the hydrodynamic calculations. It is composed of 380 flat panels.

The BEM code Achil3D [5] was used for the calculation of all hydrodynamic datas. Figure (4) shows the used mesh. The impulse response function of the radiation force have been plotted in figure (5). The computed added mass matrix is:

$$[\mu_\infty] = \begin{pmatrix} 0.39 \cdot 10^3 & 0 & 0 & 0 & 0.64 \cdot 10^3 & 0 \\ 0 & 0.39 \cdot 10^3 & 0 & -0.64 \cdot 10^3 & 0 & 0 \\ 0 & 0 & 0.39 \cdot 10^3 & 0 & 0 & 0 \\ 0 & -0.64 \cdot 10^3 & 0 & 0.11 \cdot 10^4 & 0 & 0 \\ 0.64 \cdot 10^3 & 0 & 0 & 0 & 0.11 \cdot 10^4 & 0 \\ 0 & 0 & 0 & 0 & 0 & 0 \end{pmatrix} \quad (6)$$

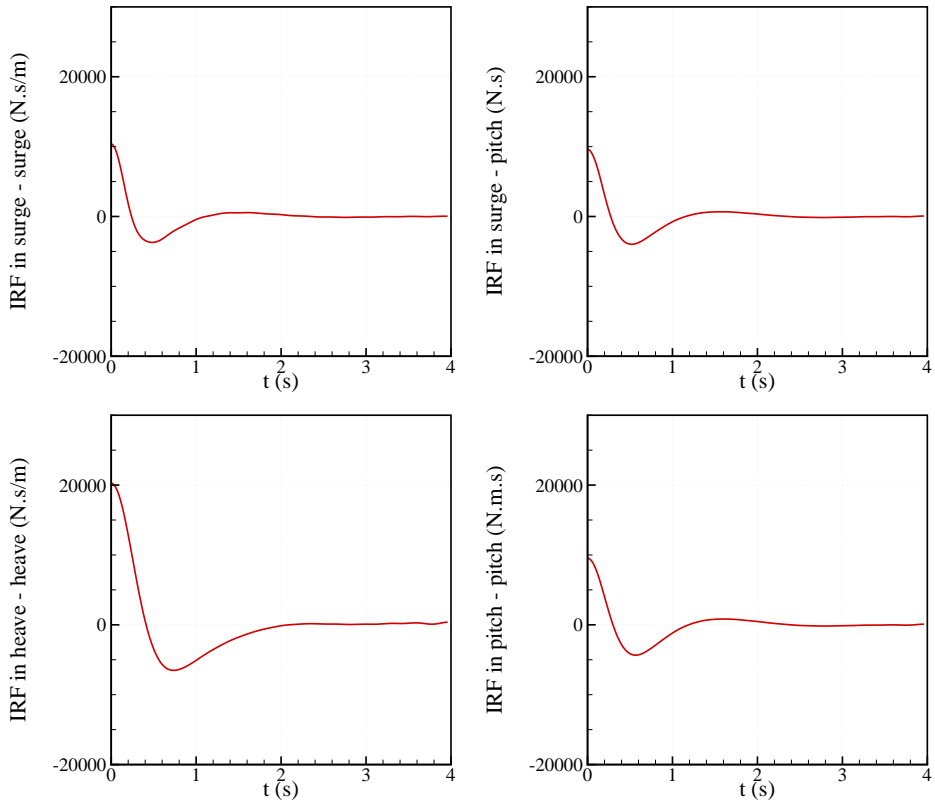


Figure 5: Impulse response functions of the radiation force of the small bottom-referenced heaving buoy in surge, heave and pitch.

The minimum water depth in all the sites considered in this study being 40 m (SEM-REV test site, see section 3), all these hydrodynamic calculations were performed in deep water. However, one could ask about the influence on the water depth on these coefficients, and so on the calculation of energy production.

Then, to assess these uncertainties, the added mass and wave radiation damping coefficients in frequency domain have been calculated for three different water depths  $h$  :  $h = 20$  m,  $h = 40$  m,  $h = \text{deep water}$ . The surge

- surge and heave - heave coefficients have been plotted in figure (6). As it was expected, differences between these coefficients can be seen only in the longest waves. However, because the small Bref-HB is small, one can see that these differences are very small. Hence, one can say that, provided that the water depth is greater than 40 m, using the hydrodynamic coefficients and function calculated in deep water will not cause large uncertainties.

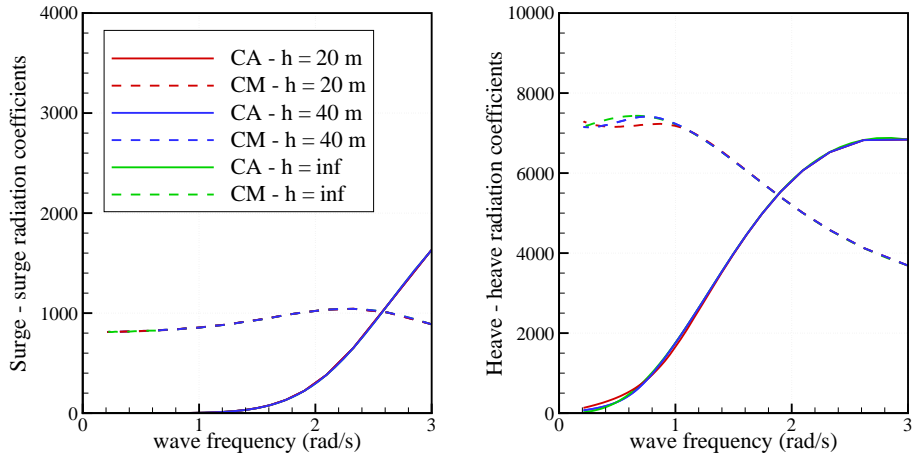


Figure 6: Radiation coefficients in surge and heave of the small bottom-referenced heaving buoy for three water depths.

### 2.3.2 Wave excitation force

Using King's approach [3], let  $[K_{ex}(t, \beta)]$  be the force response associated to an impulsive elevation on the free surface at location  $(0, 0)$  propagating along a direction such as the angle between this direction and the x axis is  $\beta$ .

Using the superposition principle, the wave excitation force is then given by :

$$\mathbf{F}_{ex}(t) = \int_0^t [K_{ex}(t - \tau, \beta)]\eta(\tau, \beta) d\tau \quad (7)$$

with  $\eta(t, \beta)$  being the component of the free surface elevation at a given reference location propagating in the direction  $\beta$ .

In case of a regular wave,  $\eta(t, \beta)$  is a simple sine function  $a \sin(\omega t + \varphi)$  with  $a$  the amplitude of the wave,  $\omega$  its circular frequency and  $\varphi$  an initial phase. In case of random waves,  $\eta(t, \beta)$  will be considered here as a sum of  $N_c$  elementary sine functions whose amplitudes  $(a_j)_{j=1, N_c}$  are derived from the standard Jonswap energy spectrum [4] and whose phases  $(\varphi_j)_{j=1, N_c}$  are set randomly.

The impulse response functions of the wave excitation force have been plotted in figure (7) for a wave measurement at the location  $(0, 0)$  on the free surface.

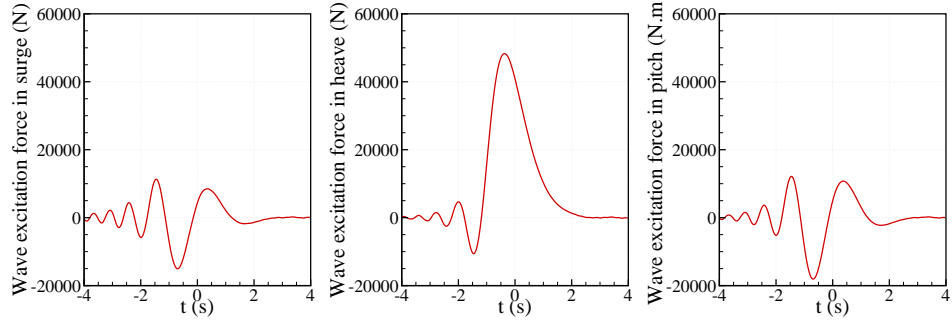


Figure 7: Impulse response functions of the wave excitation force of the small bottom-referenced heaving buoy in deep water. It is assumed that the incident wave field is measured at location  $(0, 0)$  on the free surface.

### 2.3.3 Viscous damping forces

The viscous damping forces have been modelled under the form of the Morrison equation by:

$$\vec{F}_{viscous} = -\frac{1}{2}\rho[C_D] (\vec{V}_G - \vec{V}_0) \left\| \vec{V}_G - \vec{V}_0 \right\| \quad (8)$$

with:

- $\vec{V}_0$  is the undisturbed flow velocity taken at the instantaneous position of the gravity center.
- $[C_D]$  is the viscous damping coefficient matrix. Here, it is considered as a diagonal matrix  $diag(C_x A_x, C_y A_y, C_z A_z)$  with  $A_x = A_y = 1.48$  and  $A_z = 7.07$ .

In surge and sway, the Keulegan-Carpenter number  $K_{Cx,y} = \frac{2\pi A}{D}$  in surge is expected to be in the range  $[0, 3]$ . In heave, it will be larger, possibly up to 10, because the draft is only 0.63 m. Hence, from the experimental results of Bearman given in [4], chapter 4, page 140, these parameters should be something between 0.5 and 1. In this study, they were chosen equal to  $C_x = C_y = 0.5$ ,  $C_z = 1.0$ . They are thought to be minimal values for these viscous losses. So they should not be exaggeratedly penalising for assessing the energy production of the device.

## 2.4 Machinery model

### 2.4.1 PTO taken as a linear damper

In the simplest case we assume that the machinery act as a linear damper, i.e. the machinery force  $F_m$  may be represented by:

$$F_m = -R_m \dot{Z} \quad (9)$$

In this case, the absorbed instantaneous power is:

$$P_m = -R_m \dot{Z}^2 \quad (10)$$

In Eriksson [6], it is stated that the power from the generator is 10 kW at a translator speed of 0.7 m. To achieve the same level of power at this velocity, the  $R_m$  coefficient was chosen equal to 20400 N.s/m.

### 2.4.2 PTO modelled as a simplified electric generator

If we want to model the machinery more in accordance with the real setup, we can introduce a simple model for the generator as shown in Hals [14]. Results can be compared to those given by Eriksson [6]. The operation of the the electric power take-off may be briefly explained as follows: The velocity of the translator, which is covered by permanent magnets, induces an electric voltage in the stator coils of the generator. A passive rectifier unit is connected to the generator terminals, and it conducts current only when the generator voltage exceeds the level on the opposite side (i.e. the DC side) of the rectifier. This means that if the voltage on the DC side is larger than zero, the translator velocity (and hence the generator voltage) must exceed a certain level before the rectifier starts conducting. Only then the generator will start giving a force back to the translator.

The DC side of the converter has a large capacitor that stores energy converted by the generator. In the trials reported in published papers, power is tapped from the condenser through an electric resistor of chosen resistance. This gives a varying DC voltage level. As far as it is understood, the idea for a grid-connected device is to set up the system to work against a controlled constant DC level (see e.g.[11]). This is what we will assume in the modelling of the generator and grid connection.

In a simplified but appropriate model for the generator and rectifier it can conveniently be assumed that the translator motion transforms directly to a DC voltage in series with a diode element. It gives a single-phase diode bridge analogy [13]. This way the dynamics of the rectifier component (three-phase signals and diode elements) are disregarded, which makes the problem easier to treat numerically. The transition from translator velocity to DC voltage may be modelled by a gyrator bond graph element, giving the bond graph shown in Figure 8. The passive rectifier is represented by the

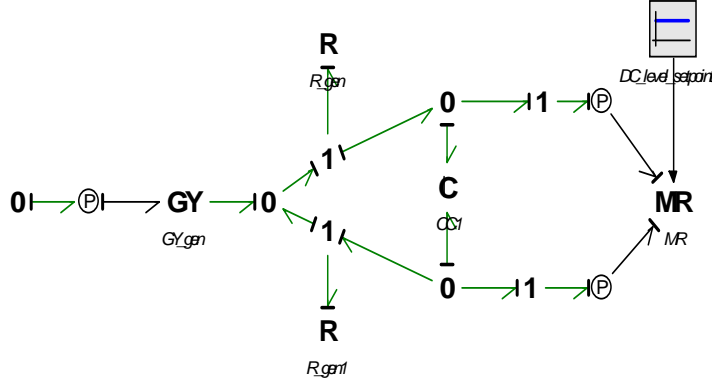


Figure 8: A bond graph model for the generator.

R elements. A controlled MR element represents the downstream system. It is controlled by a feedback P-controller to keep the DC level constant. The model is now governed by the following equations (using bond graph variables):

$$\dot{q}_6 = \frac{m_{GY} f_1 - \frac{q_6}{C_6}}{R_4} u(m_{GY} f_1 - \frac{q_6}{C_6}) - k_P \frac{q_6}{C_6} + k_P e_{DC} \quad (11)$$

$$\dot{q}_9 = \frac{m_{GY} f_1 - \frac{q_9}{C_9}}{R_{11}} u(\frac{q_9}{C_9} - m_{GY} f_1) - k_P \frac{q_9}{C_9} - k_P e_{DC} \quad (12)$$

Here,  $u(\cdot)$  is the Heaviside step function.

Regarding the parameters for the machinery model, values for the damping coefficient have been reported by among others Waters [10]. Using electric loads of values 2.2, 4.9 and  $10\Omega$  coupled with a  $\Delta$  coupling directly on the generator terminals he estimated that the corresponding damping coefficients were 12.7, 8.53 and  $5.23\text{kNs/m}$ .

A value for the gyrator modulus can be found from the nominal values given for the machine: A nominal voltage of 133 V is given for a velocity of about 0.67 m/s. This gives a gyrator modulus of about  $m_{GY} = u/v \approx 200\text{ Vs/m}$  when the full area of the translator is found between the stator surfaces.

With the given stator and translator lengths, the translator will start loosing contact area with the stator at an amplitude of  $|Z_c| > 0.305\text{ m}$ . (At an amplitude of 1.56 m the translator would be fully free from the stator.) At the extreme position ( $Z = \pm 0.9\text{ m}$ ) the contact area between the stator and translator is reduced by a factor  $r_{A,lim} = r_A(Z = Z_{lim}) = 0.4735$ . The expression for  $r_A$  as function of the translator excursion  $Z$  is thus found to be:

$$r_A(Z) = \begin{cases} 1, & |Z| > Z_c \\ 1 - \frac{|Z| - Z_c}{Z_l - Z_c}(1 - r_{A,l}) & \text{otherwise} \end{cases} \quad (13)$$

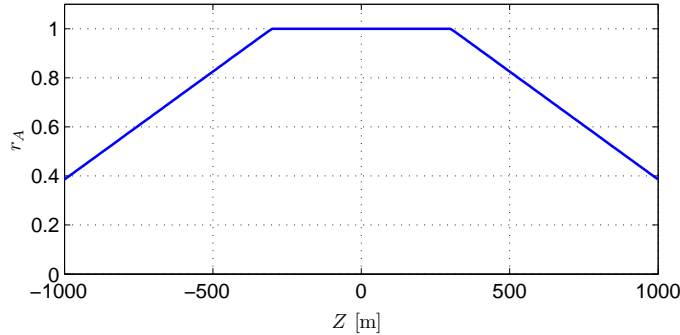


Figure 9: Reduction of the gyrator modulus due to reduced contact area between stator and translator.

A plot of this function is given in Figure 9. The complete value of the gyrator modulus now depends on  $Z$  and is given by  $m_{GY}(Z) = 200Vs/m \cdot r_A(Z)$

From the generator model we find that the machinery force  $F_m$  is given by

$$F_m = \frac{m_{GY}\dot{Z} - \frac{q_6}{C_6}}{R_4} u(m_{GY}\dot{Z}) + \frac{m_{GY}\dot{Z} - \frac{q_9}{C_9}}{R_{11}} u\left(\frac{q_9}{C_9} - m_{GY}\dot{Z}\right). \quad (14)$$

and the instantaneous power is given by:

$$P_m = F_m \dot{Z} \quad (15)$$

## 2.5 Treatment of the end stops

The endstops are modelled by a repulsive energy potential, which results in the following force equation:

$$F_{es} = -K_{min}(Z - Z_{min}) u(Z_{min} - Z) - K_{max}(Z - Z_{max}) u(Z - Z_{max}) \quad (16)$$

in which  $K_{min}$  and  $K_{max}$  are the spring coefficients of, respectively, the low end stop and the high end stop; and  $Z_{min}$  and  $Z_{max}$  are the low and high position of the end stops. If the endstop incorporates damping, this can be added accordingly, but it was not included here.

To take into account the limited stroke of 1.8 m, the low and high position of the end stop were taken equal to  $-0.9$  and  $0.9$  m.

## 2.6 Assembled model

At each time  $t$ , the unknowns of the problem are the accelerations of the {Buoy}, the acceleration of the {Translator}, the tension  $T$  in the wire and the variables  $q_6$  and  $q_9$  if the machinery model is considered. It means 8 or

10 unknowns. Equations (3) and (4) gives 7 independent relations between these unknowns. Equations (11) and (11) gives two other relations when the machinery is considered. Hence, it always lack one equation to close the problem. This last equation corresponds with the behaviour of the tension in the wire.

In this study, wire compliance is considered. Hence, the line tension is governed by a linear stiffness force relation:

$$T = k_l \Delta L u(\Delta L). \quad (17)$$

The variation of the length wire is defined as  $\Delta L = L - L_0 + \Delta L_0$  where  $\Delta L_0$  is the initial stretch of the wire (corresponding to the initial tension).

This last equation closes the mathematical problem.

## 2.7 Implementation

The mathematical problem being closed, one can solve it numerically.

In this study, two models have been implemented one in Fortran and the other using the 20sim software. A very good agreement was found between the two models, as one can see in figure (10).

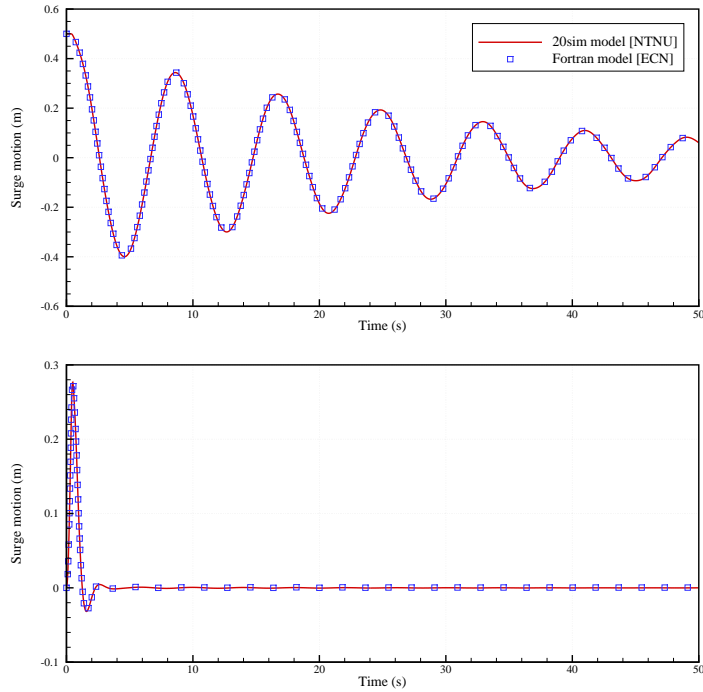


Figure 10: Comparison of the response of the small Bref-HB to a decay test computed with the 20sim and the Fortran model.

### 3 Sites locations and wave data

Five sites on the west coast of Europe are considered in this study. Figure (11) shows their approximative locations.

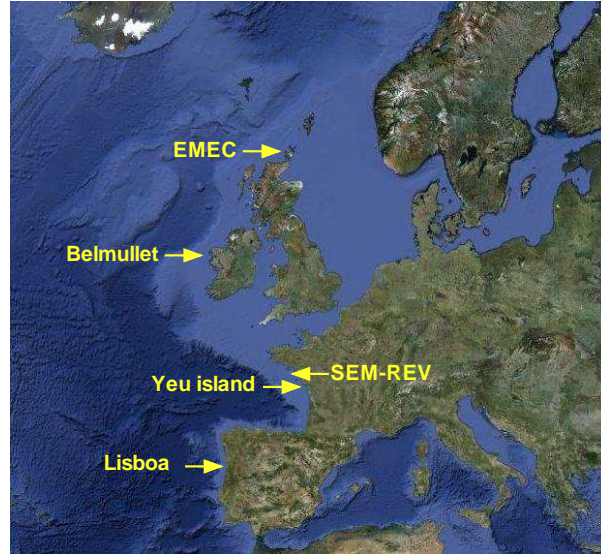
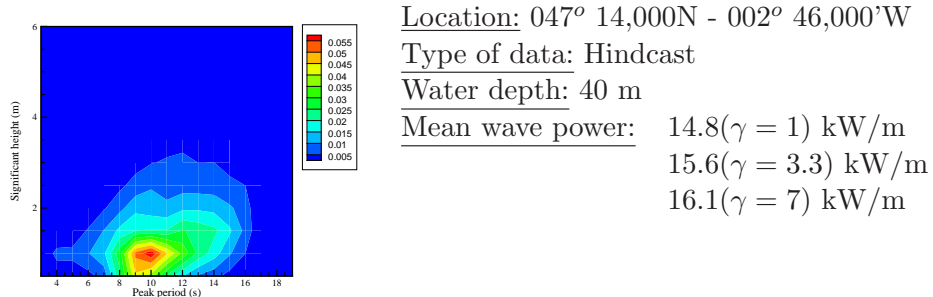


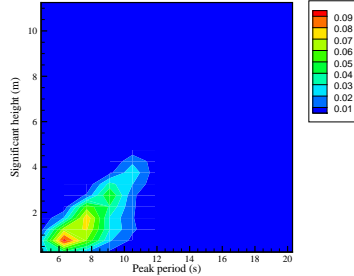
Figure 11: Location of the considered sites.

#### 3.1 France/SEM-REV test site



Source: ANEMOC wave data base.

### 3.2 Scotland/EMEC test site



Location:  $059^{\circ} 00,000'N - 003^{\circ} 66,000'W$

Type of data: Real sea measurement

Water depth: 50 m

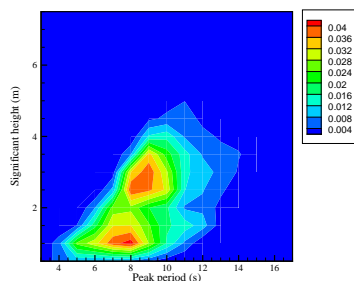
Mean wave power:  $21.8(\gamma = 1)$  kW/m

$23.0(\gamma = 3.3)$  kW/m

$23.7(\gamma = 7)$  kW/m

Source: K. Nielsen, T. Pontes (2010). Generic and site related wave data Final Technical Report, OES-IA Document No: T02-1.1.

### 3.3 France/Yeu island



Location:  $046^{\circ} 40,000'N - 002^{\circ} 25,000'W$

Type of data: Real sea measurement

Water depth: 47 m

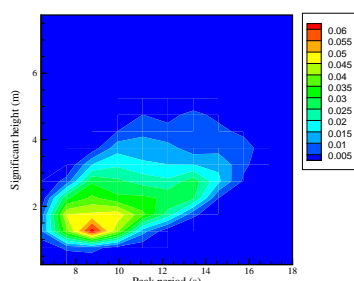
Mean wave power:  $25.5(\gamma = 1)$  kW/m

$26.8(\gamma = 3.3)$  kW/m

$26.8(\gamma = 7)$  kW/m

Source: CANDHIS wave data base [candhis.cetmef.developpement-durable.gouv.fr](http://candhis.cetmef.developpement-durable.gouv.fr).

### 3.4 Portugal/Lisboa



Location:  $039^{\circ} 00,000'N - 012^{\circ} 00,000'W$

Type of data: Real sea measurement

Water depth: 100 m

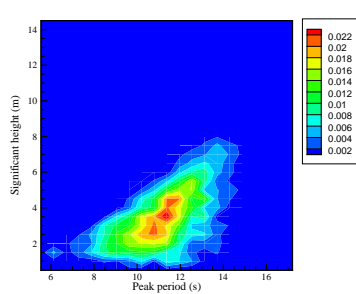
Mean wave power:  $35.6(\gamma = 1)$  kW/m

$37.5(\gamma = 3.3)$  kW/m

$38.6(\gamma = 7)$  kW/m

Source: K. Nielsen, T. Pontes (2010). Generic and site related wave data Final Technical Report, OES-IA Document No: T02-1.1.

### 3.5 Ireland/Belmullet



Location:  $054^{\circ} 00,000'N - 012^{\circ} 00,000'W$

Type of data: Real sea measurement

Water depth: 100 m

Mean wave power:  $76.5(\gamma = 1)$  kW/m  
 $80.6(\gamma = 3.3)$  kW/m  
 $83.1(\gamma = 7)$  kW/m

Source: Marine Institute. [www.marine.ie](http://www.marine.ie).

### 3.6 Danemark/Danish site

For sake of comparison with the results of the Danish Bølgekraftprogram [15] , a site characterised by the wave statistics given in table (5 ) is also considered.

Sea state	1	2	3	4	5
Hs (m)	5.6	7.0	8.4	9.8	11.2
Tp (s)	1.	1.	2.	3	4
Hours per year	4103	1982	944	445	211

Table 5: Wave statistics used in the Danish site.

## 4 Simulation results and energy assessment

### 4.1 Verification tests

In figure (12) and (13), we plotted comparisons of decay tests of the small bottom-referenced heaving buoy with an without viscous damping. The first figure is a decay test in heave and the second one in surge. In the first figure, one can see that the viscous damping does not affect the response of the system in heave, because the damping along this degree of freedom is dominated by the PTO. The second figure shows that it is not the case with the surge motion. The viscous damping is the main damping effect along this degree of freedom.

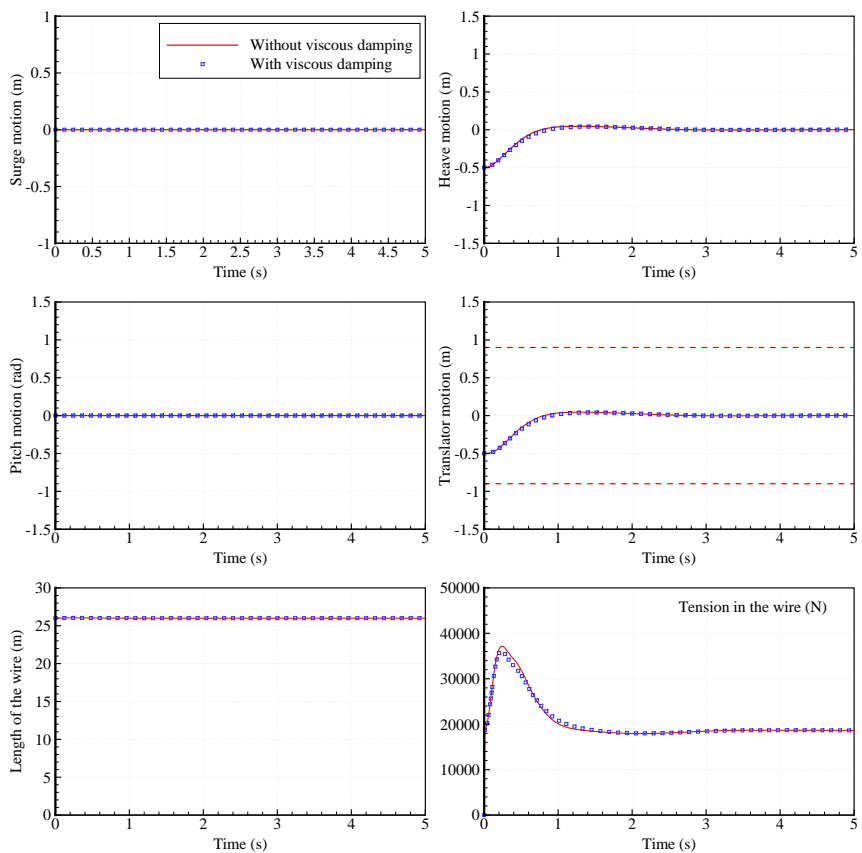


Figure 12: Decay test in heave of the small bottom-referenced heaving buoy. Initial position of the buoy in heave and the translator are shifted of -0.5 m from the equilibrium position.

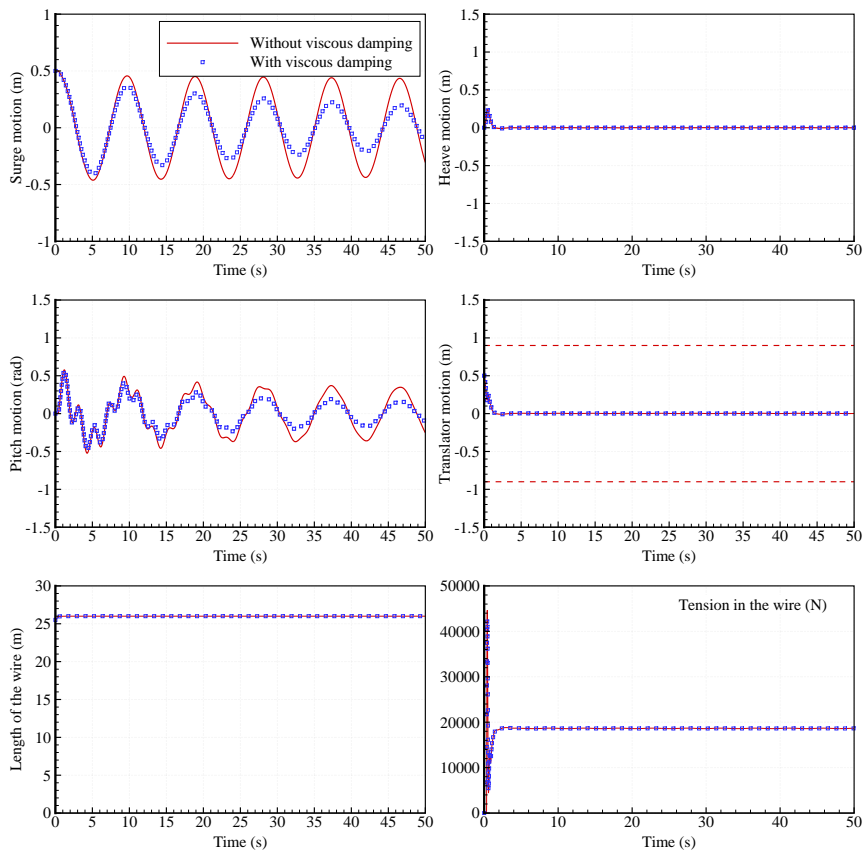


Figure 13: Decay test in surge of the small bottom-referenced heaving buoy. Initial position of the buoy in surge and the translator are shifted of 0.5 m from the equilibrium position.

From figure (13), one can see that the natural period in surge is about 9.2 s. Let's verify that it is consistent with the natural period  $T_0$  that one can calculate from the equation of motion.

The mass of the buoy is 1000 kg. For a wave period of 9.2 s, the added mass in surge is about 830 kg. The stiffness in surge is given by the ratio of the static tension in the line (18.6 kN) divided by the length  $l_0$  (22 m). With these parameters,  $T_0 = 2\pi \sqrt{\frac{1000+830}{18600}} = 9.2$  s. CQFD.

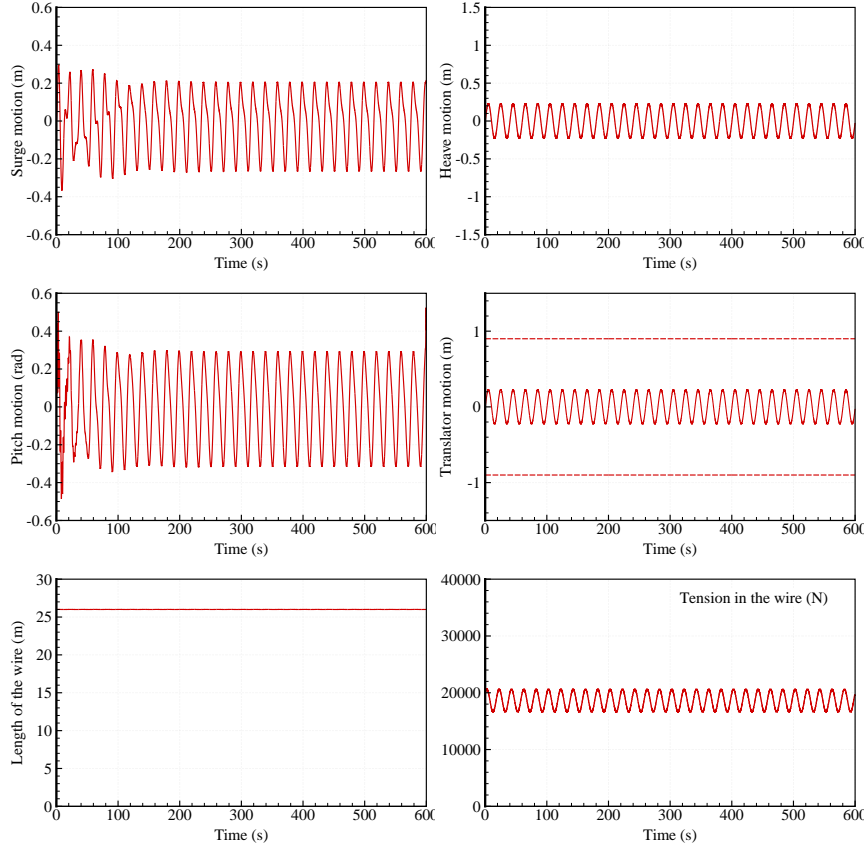


Figure 14: Response of the small bottom-referenced heaving buoy in a long regular wave. The wave height is 0.5 m and the wave period is 20 s.

The response of the small bottom-referenced heaving buoy in a regular wave with wave period equal to 20 seconds and wave height 0.5 m is plotted in figure (14). As it is expected in long waves, the amplitude of the motion in heave is equal to the wave amplitude, i.e 0.25 m.

## 4.2 RAOs

In this section, all time domain simulations were performed in regular waves with the PTO modelled as a linear damper. All quantities (mean, min, max, rms) are derived from 600s duration simulation, with a time step of 0.01s. The length of the part  $l$  of the wire at equilibrium was set equal to 22 m. To remove the transient effects, the  $15 \times T_p$  seconds of the simulations are not taken into account.

In figure (15), mean and maxima of surge, heave and pitch motion have been plotted together with the absorbed power in function of the wave period. The wave height is 2 meters and the PTO parameter is  $R_m = 20400$  N.s/m. On the surge plot, one can see that the mean value is not equal to zero. It means that in regular waves, the steady position of the buoy is shifted from the zero position, because of the non linearities. Being about 3 times the wave amplitude, one can observe that the amplitude of the motion is large despite the viscous damping.

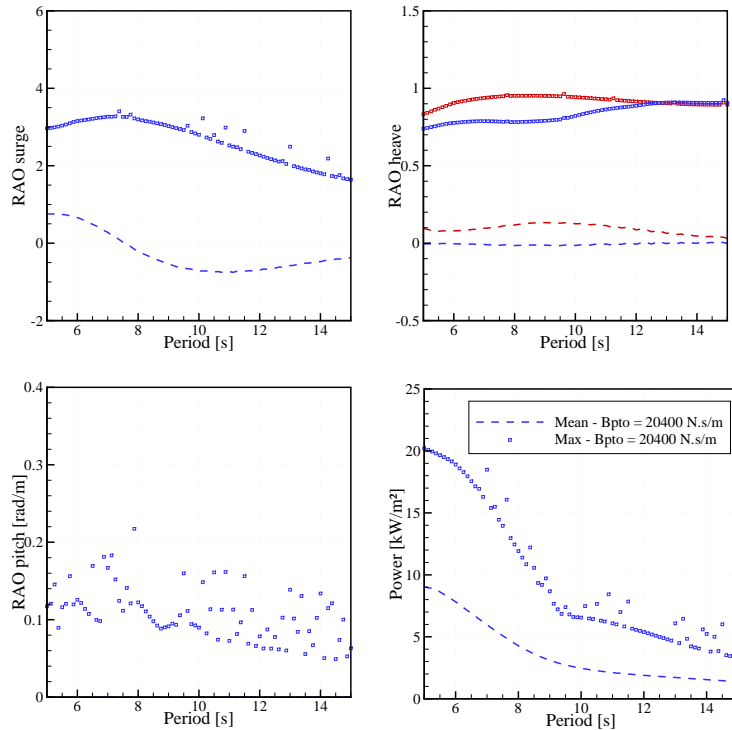


Figure 15: RAOs and power function of the small Bref-HB. The wave height is 2m and the PTO parameter is set equal to 20400 N.s/m.

On the heave plot, the blue figures correspond with the motion of the buoy and the red figures correspond with the motion of the translator. For both bodies, the amplitude of the motion is about the wave amplitude. For

the translator, it is limited by the high end stop. One could notice that it exists a shift of the mean position of the translator in heave. This is due to the shifting of the position of the buoy in surge.

The pitch motion appears to be rather scattered. But one could say that is it in the range of  $[5 - 10]^\circ$ .

Finally, one can see that the order of magnitude of the mean absorbed power is a few kilowatts per square meters of wave amplitude, which is in range with what is reported by Eriksson in his thesis [6]. Best performances are obtained with the shortest waveperiods, with a power absorption of  $9 \text{ kW/m}^2$ . Then, the mean power decreases with the increase of the wave period. It is not higher than  $2 \text{ kW/m}^2$  for wave periods greater than 10 seconds. Whatever the wave period, the maximum power appears to be about two times the mean power. It is not unexpected since a factor two is the ratio between maximum and mean power with linear systems.

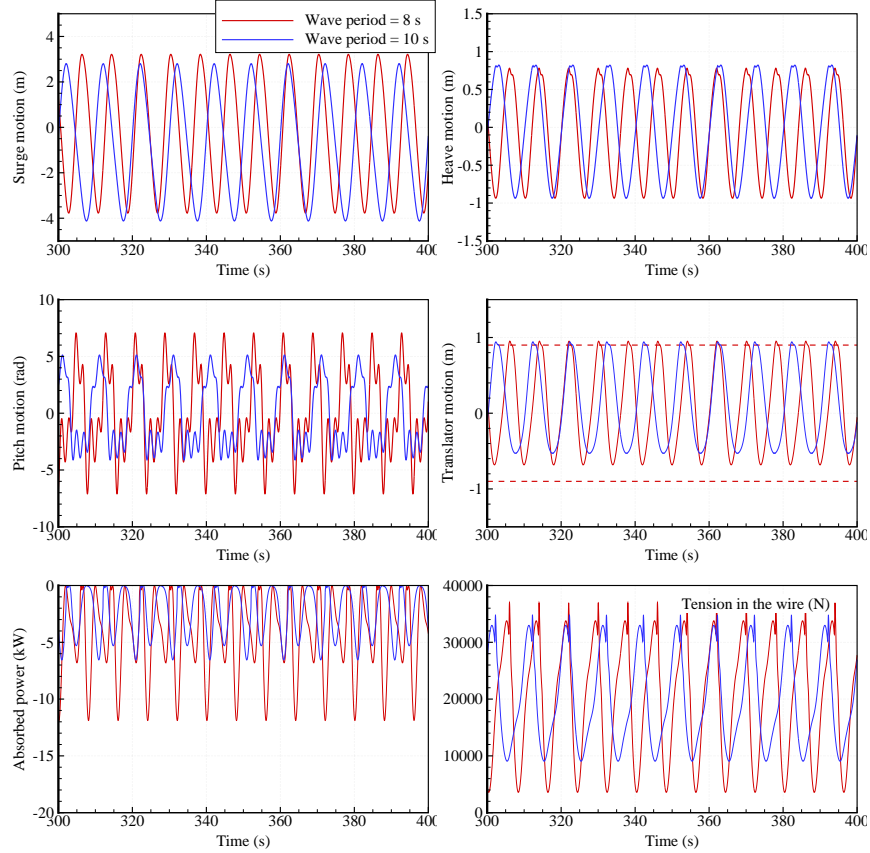


Figure 16: Comparisons of the responses of the small bottom-referenced heaving buoy in regular wave with 8 and 10 seconds wave period.

In figure (16), a comparison of the response in regular wave is plotted

for wave period 8 and 10 seconds. One can see that the change in the steepness of the maximum power in figure (15) comes from the development of asymmetries in the velocity of the translator motion.

#### 4.2.1 Optimisation of the PTO damping coefficient

Figure (17) shows a comparison of the RAOs in regular waves with and without optimisation of the PTO parameter. Without optimisation, the PTO parameter - the linear damping coefficient  $R_m$  - is set equal to its nominal value, i.e 20400 N.s/m. With optimisation,  $R_m$  is optimised in the range [10000, 40000] N.s/m.

Optimisation of the PTO damping coefficient allows to increase the power production by a factor about 2 for long wave periods. In short wavelengths, it does not bring much improvement in the energy absorption.

One can see that the amplitude of the motion is only slightly affected by the optimisation of the damping coefficient. Actually, it seems that the increase in the energy absorption comes only from the increase of the PTO damping coefficient. It shows that, with long waves, the amplitude of the motion is constrained by the end stops. Then, increasing the PTO damping coefficient is favourable, because the amplitude of the motion is already limited by the end stops. The effect of increasing the damping coefficient is then to improve the phase relation between the incident wave and the motion of the buoy.

#### 4.2.2 Assessment of non linearities effects on the response

Figure (18) shows a comparison of the RAOs calculated with three different wave heights : 1 m, 2 m, 4 m.

It appears that the strongest linearities in the system comes from the end stops. As soon as the wave height exceeds the stroke of the translator, all translational motion of the translator and the buoy are reduced in the same ratio. However, it is worth noticing than the power absorption seems to be reduced with the same ratio, and not the ratio to the square.

When the wave height is smaller than the stroke, one can observe that the main effect of non linearities is on the surge motion of the buoy. It indicates again a strong coupling between the surge motion of the buoy and the response of the translator.

#### 4.2.3 Assessment of viscous damping effects

To assess the influence of viscous damping, we plotted in figure (19) a comparison of the RAOs of the small bottom-referenced heaving buoy in regular waves without viscous damping and with two settings of viscous damping coefficients. Table (6) summarises the settings which were used.

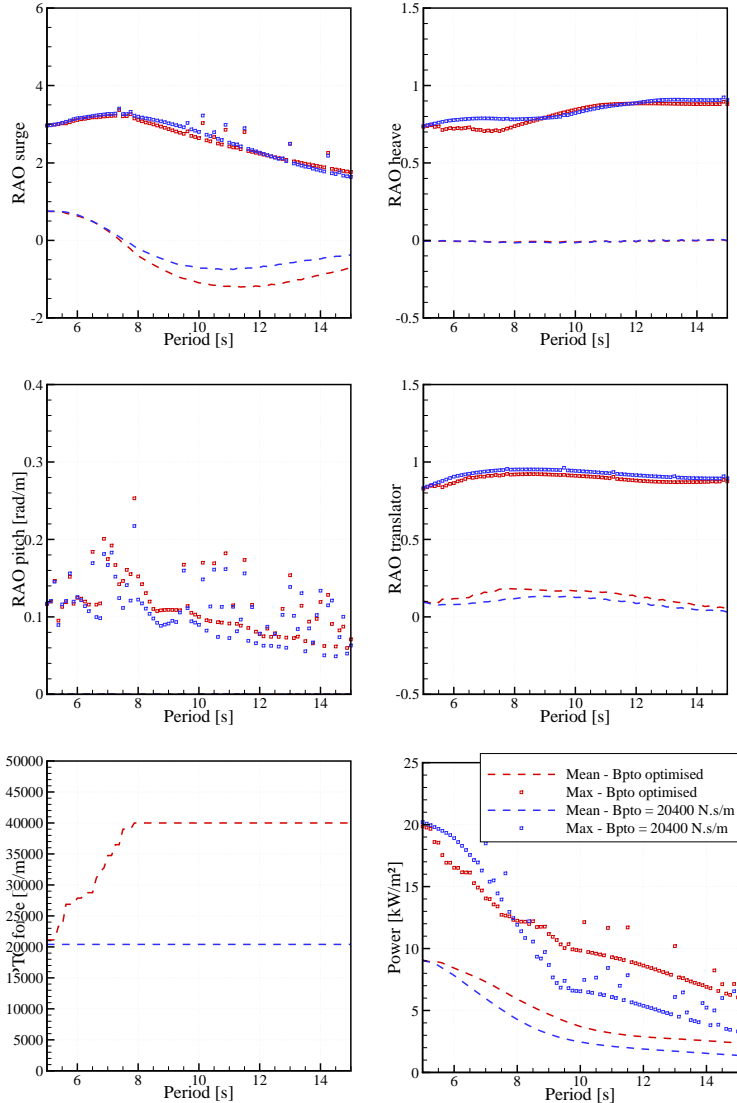


Figure 17: RAOs without and with optimisation of PTO parameter. Without optimisation, the PTO parameter is set equal to 20400. N.s/m. The wave height is 2m.

Case	$C_x$	$A_x$	$C_z$	$A_z$
Without damping	0	1.48	0	7.07
Viscous damping 1	0.5	1.48	1.0	7.07
Viscous damping 2	0.25	1.48	0.5	7.07

Table 6: Settings of viscous damping parameters.

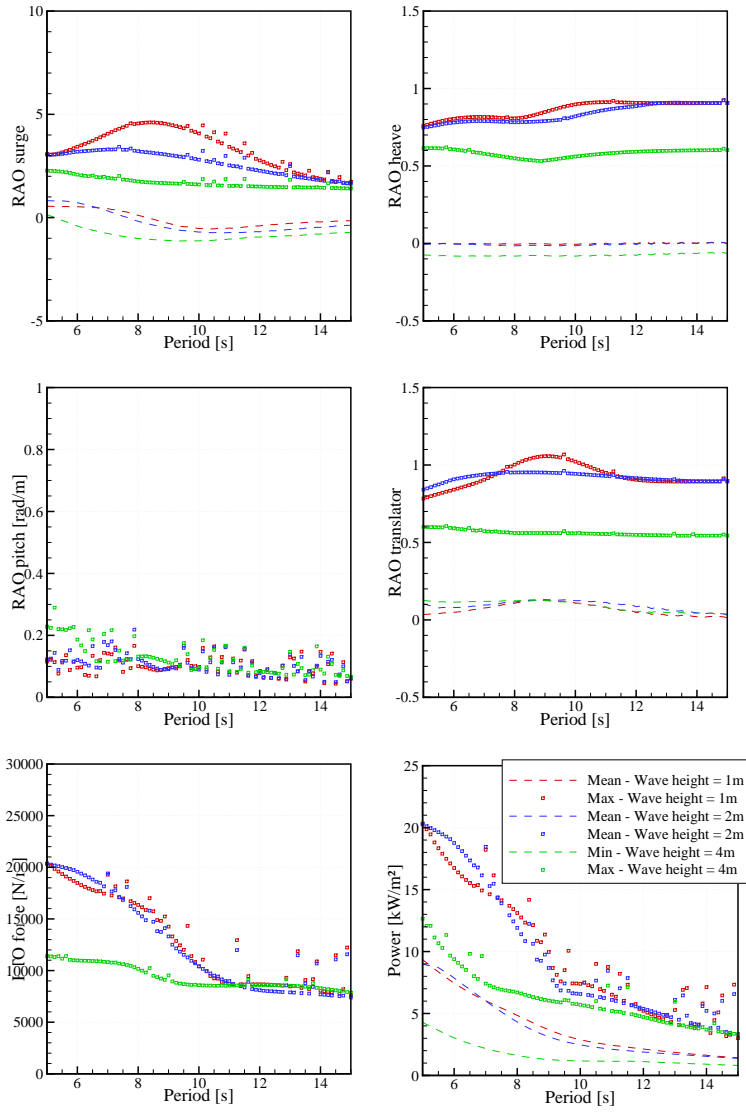


Figure 18: Comparison of the RAOs with three different wave heights.

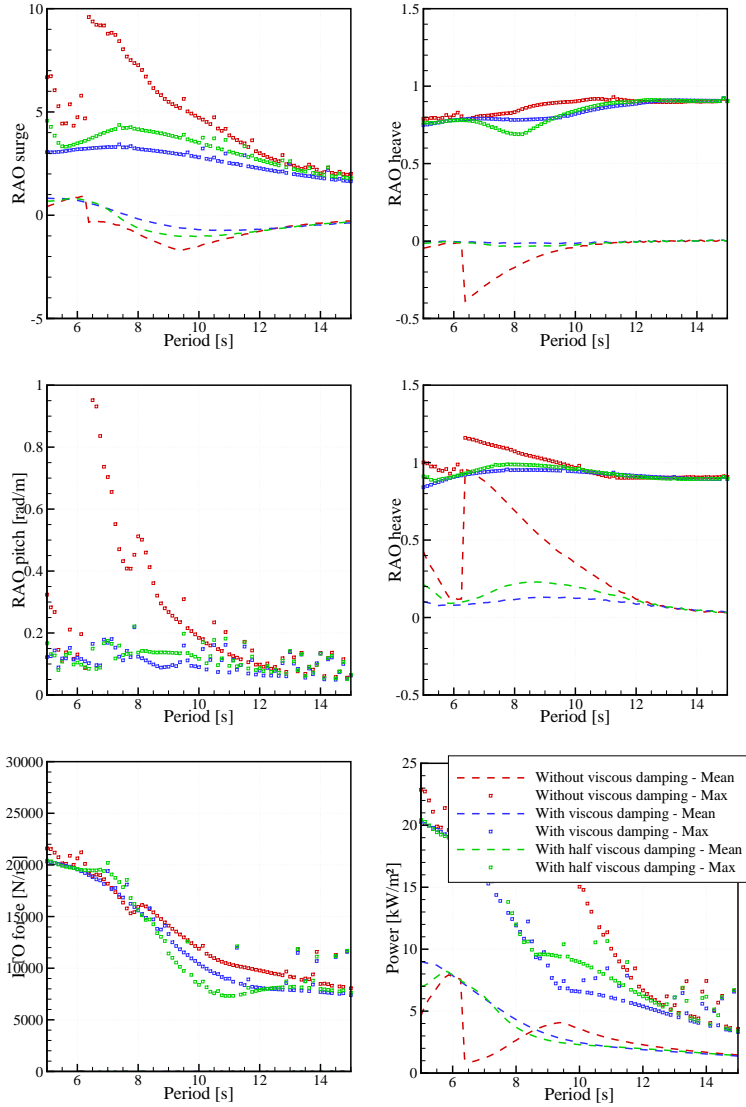


Figure 19: RAOs of the small Bref-HB without viscous effects, with viscous damping coefficients, and with half the viscous damping (meaning that the normalised damping coefficients have been divided by 2). The wave height is 2m.

In this figure, it is clear that viscous effects have an influence on the power absorption. Without viscous damping, it appears that the amplitude of the surge and pitch motion of the buoy is very large in short waves, up to 10 times the wave amplitude for the surge motion for wave period equal to 6.2 seconds. For this wave period, it leads to a large steady shift of position which drives the translator into the high end stop. Consequently, the power production drops. From the heave motion and translator motion point of view, one can see that the amplitude is not as affected as the horizontal motions. The main effect appears to be on the steady state position for the range of period [6.2 – 11] seconds.

When adding viscous damping, the amplitude of the surge motion is reduced by a factor about between 2 and 3, depending on the wave periods, and the pitch motion is reduced by a factor up to 10.

From the power absorption point of view, it is particularly interesting to notice that the addition of viscous damping does not decrease the prediction of energy production. Actually, it fills the gap in the power function curves and it gives a smoother power production with the wave period. The order of magnitude remains the same, in the range of 2 to 9  $kW/m^2$ .

Finally, one could notice that with half the viscous damping, the results are much closer to the ones with full viscous damping than the ones without viscous damping. RAOs and power function of the small bottom-referenced heaving buoy seem to be robust with an error on the estimation of the viscous damping coefficient.

#### 4.2.4 Assessment of the effect of the length of the wire

In all the previous calculations, the length  $l$  was supposed equal to 22 m, i.e a length of the wire equal to  $22 + Z_0 = 26$  m. To assess the effect of the length  $l$  connecting the buoy to the generator, we plotted in figure (20) a comparison of the RAOs with the length  $l$  equal to 22 m, 42 m and 92 m. It corresponds with water depths of, respectively, 30 m, 50 m and 100.

One can see that changing the length of the wire has an impact on the response of the small Bref-HB. The strongest one is on the surge motion. It was expected, since the stiffness in surge of the buoy is inversely related with the length of the wire ( $K_x = \frac{T_0}{l_0}$ ).

On the heave and translator motion, there is an impact of the length of the wire, but it appears to be quite limited, being maximum 10%. It appears also that the offset on the mean position of the translator is reduced with the increase of the length of the wire.

On the mean wave power absorption, overall, one can see that the impact is small, except for wave periods around 8 s. For these periods, the mean power is increased by up to 20%. One could also notice that, for the mean power, the results are the same for  $l = 42$  and  $l = 92$  m. This could indicate that when the length of the wire is sufficiently long, it does not

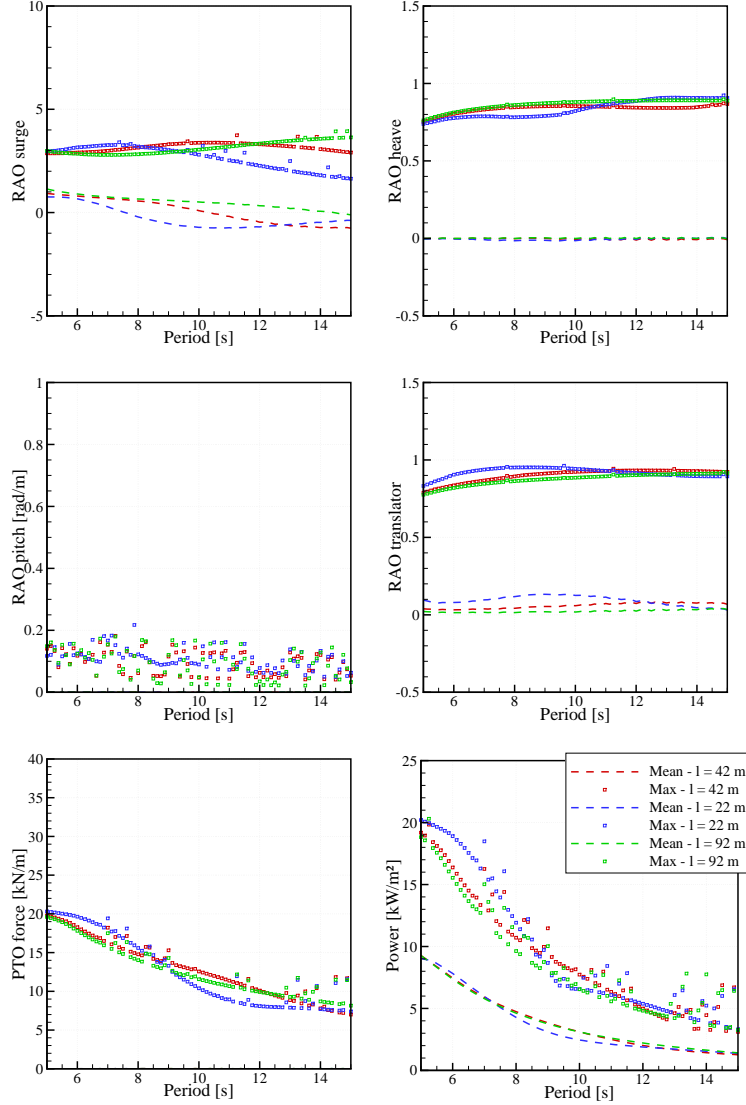


Figure 20: RAOs of the small bottom-referenced heaving buoy with three different lengths of the wire. The wave height is 2m.

affect anymore the power absorption.

#### 4.2.5 Conclusions

From these results in regular waves, it appears that:

- The order of magnitude of absorbed power from the small bottom-referenced heaving buoy is about several  $kW$  per square meters of wave amplitude in regular waves.
- Optimisation of the PTO parameter improves the energy production in long wave periods by a factor about 2. In shorter wave, no significant gain has been observed.
- The coupling between the surge motion and the translator motion contributes to the energy absorption.
- The strongest non linear effect comes from the end stops.
- Viscous damping effects have a strong influence on the motion response, but not so much on the level of energy absorption. Moreover, the response of the system seems to be robust with the viscous damping coefficients.
- The strongest effect of the length of wire is on the surge motion. On the power production, it seems that the longer is the better.

Hence, to assess the error on the estimation of the power production, models with and without viscous damping, with and without optimisation of the PTO parameter and with different lengths of the wire will be considered.

### 4.3 Power matrix and criteria

In this section, all time domain simulations were performed in irregular waves using the JONSWAP spectrum. All quantities are derived from 1200s duration simulations, with a time step of 0.01s. To remove the transient effects, the  $15 \times T_p$  seconds of the simulations are not taken into account.

#### 4.3.1 Power matrix of the small Bref-HB

Figure (21) shows the power matrix of the small bottom-referenced heaving buoy, calculated on the Yeu site ( $l_0 = 39$  m). In these calculations, the PTO was modelled as a linear damper, whose damping coefficient  $R_m$  has been optimised for each state. Left figure is the mean absorbed power and right figure is the maximum recorded over the duration of the simulation for each sea state.

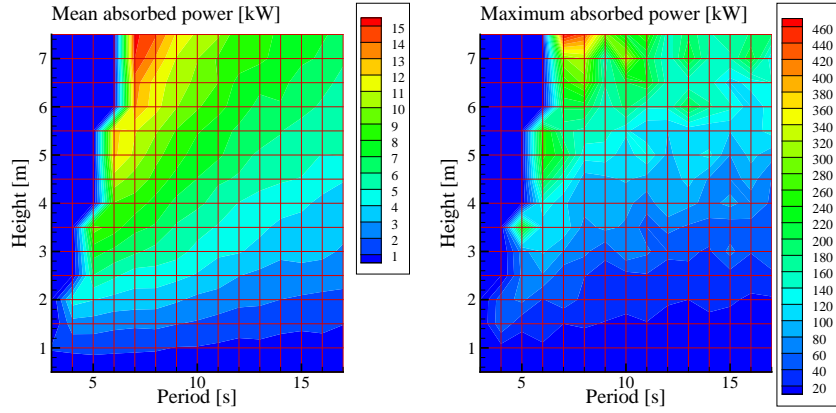


Figure 21: Power matrix of the small bottom-referenced heaving buoy with optimised PTO. Left figure is the mean absorbed power and right figure is the maximum power.

The mean absorbed power is typically about a few kilowatts, up to 15 kilowatts in the best cases. As it was expected from the results in regular waves, the system exhibits the best efficiency in the shortest sea states.

The maximum absorbed power is typically about 20 times the mean power. It is very large. This might be a drawback of the system from the power electronics point of view.

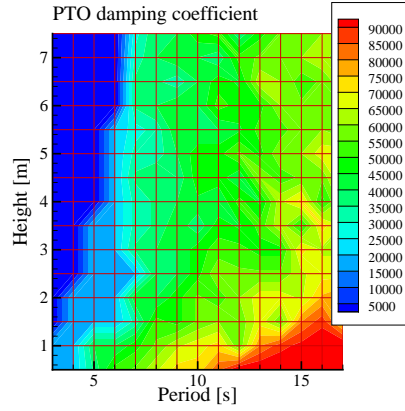


Figure 22: Optimised value of the PTO damping coefficient.

Figure (22) shows the matrix of the optimised values of the PTO damping coefficient. Surprisingly, the optimal value decreases with the wave height, particularly in long waves.

Figure (23) shows matrices of the RMS of the motion in surge, heave, pitch and translator motion.

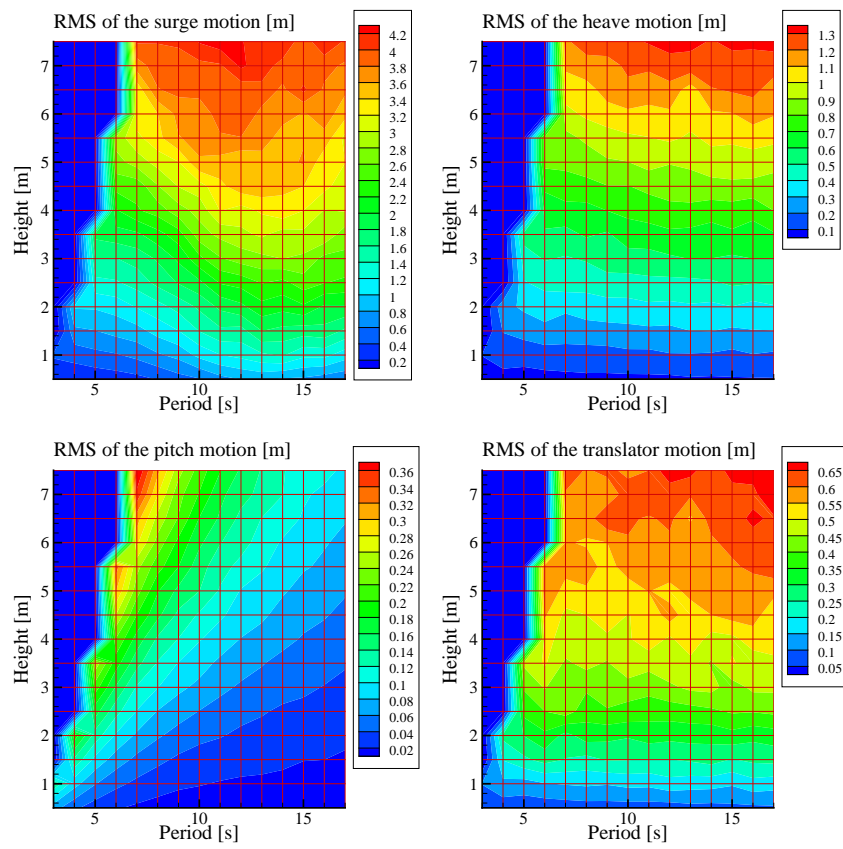


Figure 23: Matrices of the RMS of the motion of the small bottom-referenced heaving buoy.

For the surge motion, one can see that it is typically about half the significant wave height. The heave motion seems to be almost independent of the wave period. One could say that it is about 1/4 of the significant wave height. In other words, the significant heave motion is the same order of the significant wave height. For waves of significant amplitude smaller than 3 meters, one can see that the RMS of the translator motion is the same as the heave motion. When the wave height is higher, it is reduced because of the limited stroke of the translator. One can see that it does not exceed 0.8 m, which is coherent with the 0.9 m stroke of the translator. Isovalues of the pitch motion appear to be linear with the wave period and to be rather small, except in short and steep waves.

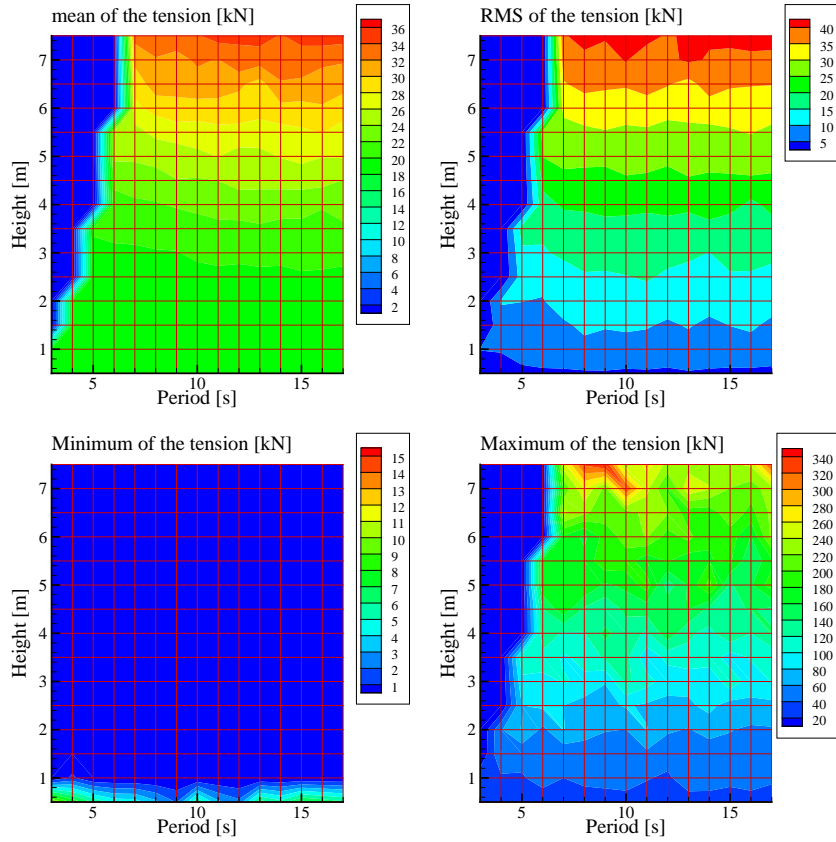


Figure 24: Statistics of the tension in the wire.

Figure (24) shows the statistics of the tension in the wire. While the translator does not reach the end stops (in moderate wave heights), the mean tension in the wire is about 20 kN. In the strongest sea states, one can see that the mean level of tension in the wire is increased up to the double, 36 kN. From the graphs of the minima of the tension, one can see

that the wire gets slack as soon as the significant height is greater than 1.5 to 2 meters. This will bring high snapping loads, as one can see in the graph of the maxima of the tension.

One shall notice that these maxima are the maxima recorded during the time simulations. They do not presume of the maxima that one can get in real conditions, which could statistically be higher.

For significant height of 3 meters, the recorded maximum tension is about 10 tons. For a sea state of 12 seconds and 7.5 meters - which statistically happens during 2.5 hours each year on the Yeu site -, the recorded maximum tension is greater than 30 tons. It means that the translator could be lifted in this case if the foundation is lighter than this value!

Table (7) summarises the criteria derived on each wave site.

Site		SEM-REV	EMEC	Yeu	Lisboa	Belmullet	Danish site
$\gamma$		1	1	3.3	3.3	3.3	1
Mean power	[kW]	1.6	2.8	3.3	3.5	5.0	2.7
Wave pow. resource	[kW/m]	14.8	21.8	26.8	37.5	80.6	14.8
Capture width	m	0.108	0.126	0.123	0.093	0.062	0.18
$l_0$	m	32	42	39	92	92	39
Energy / Mass	[MWh/m <sup>3</sup> ]	0.46	0.78	0.92	1.00	1.40	0.76
Energy / Wetted surface	[MWh/m <sup>2</sup> ]	0.34	0.57	0.68	0.73	1.04	0.57
Energy / PTO force	[kWh/N]	1.5	2.1	2.3	2.2	2.6	2.2
Energy / Wave force	[kWh/N]	0.89	1.19	1.27	1.21	1.18	1.34

Table 7: small bottom-referenced heaving buoy's criteria.

One can see that the mean annual power resource that one can expect from the small bottom-referenced heaving buoy is about a few kilowatts. It goes from 1.6 kW for the SEM-REV site up to 5.0 kW for the highly energetic Belmullet site. For a typical wave resource about 30 kW/m, the typical absorbed wave power is about 3kW/m.

Clearly, it appears that the capture width is not independent on the site. The more energetic the site, the shorter the capture width, probably because of the limited strokes and non linearities.

At the Danish site, the hydrodynamic efficiency <sup>6</sup> is about 6%. This is in range with the results of the Bølgekraftprogram [15], in which hydrodynamic efficiencies of such heaving devices were found to be between 1% and 27%.

The other criteria are the energy per PTO force and energy per wave force. These forces have been calculated as the significant forces over the whole year. On these two last criteria, it is difficult to say anything relevant. They will make sense by comparison with other wave energy devices.

Figure (25) shows the distribution of the absorbed power in function of the power level. Right figure shows the probability for the power production

---

<sup>6</sup>Defined as the ratio of the capture width divided by the diameter

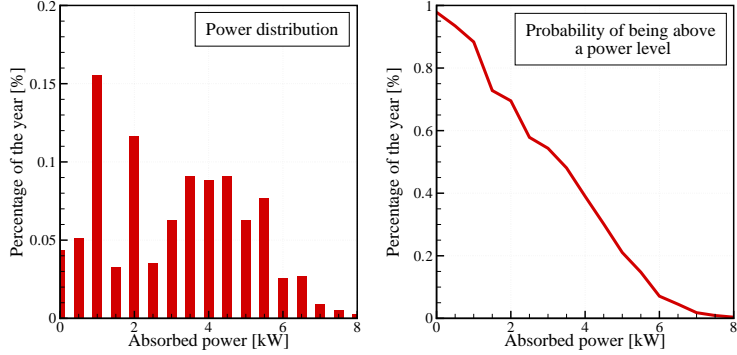


Figure 25: Distribution of the power production.

to be between two levels and right figure shows the probability for the power to be greater than a given power level. It has been calculated with the wave statistics of the Yeu site. One can see that half of the year, the absorbed wave power is greater than the mean power.

#### 4.3.2 Assessment of the uncertainties

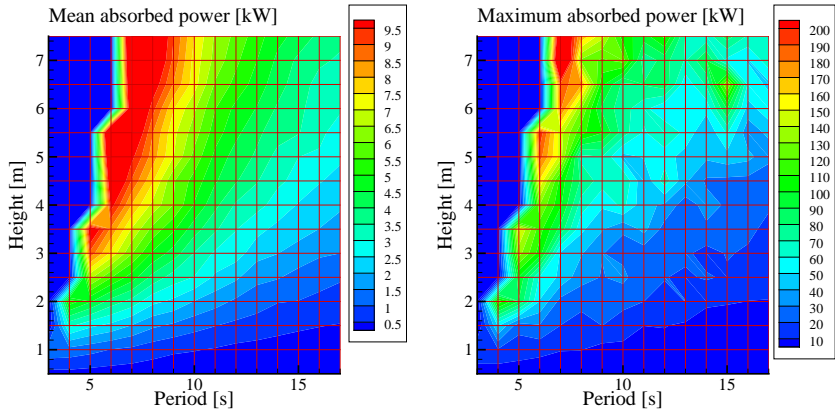


Figure 26: Power matrix of the small bottom-referenced heaving buoy device with fixed value for the PTO damping coefficient. Left figure is the mean absorbed power and right figure is the maximum power.

Figure (26) shows the power matrix of the small bottom-referenced heaving buoy calculated without optimisation of the PTO damping coefficient. Figure (27) shows the power matrix calculated without the viscous damping, and without optimisation of the PTO damping coefficient. By comparing them, one can see that the main difference is not much on the mean power

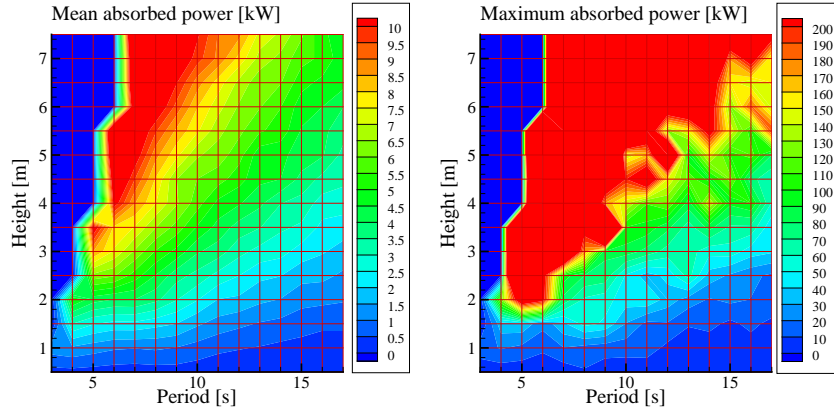


Figure 27: Power matrix of the small bottom-referenced heaving buoy device calculated with the model without viscous damping. Left figure is the mean absorbed power and right figure is the maximum power.

Site	Mean power with viscous damping and $l_0 = 22$ [kW]	Mean power without viscous damping and $l_0 = 22$ [kW]	Mean power with viscous damping and $l_0 + 4 = h$ [kW]
SEM-REV	1.1	1.4	1.1
EMEC	2.0	2.6	2.2
Yeu	2.2	3.0	2.5
Lisboa	2.1	2.9	2.4
Belmullet	3.0	4.0	3.4

Table 8: Mean power without viscous damping with fixed length of the wire, with viscous damping with fixed length of the wire and with viscous damping with length of the wire adapted to the water depth. In these calculations, the PTO damping parameter is equal to  $R_m = 20.4$  kN.s/m

but on the maximum power. Without viscous damping, the maxima of the power is much higher than with the viscous damping.

Table (8) shows a comparison of the mean absorbed power by the small Bref-HB calculated without viscous damping with fixed length of the wire, with viscous damping with length of the wire adapted to the water depth and with viscous damping with fixed length of the wire.

Averaged on the whole year, one could conclude that the uncertainty on the mean absorbed wave power of the small Bref-HB from the modelling of the viscous damping and the length of wire is at most 30%.

However, let consider table (9). In this table, it is shown a comparison of the absorbed power at Yeu site without taking into account viscous damping, with taking into account viscous damping only in surge, in heave and along both degrees of freedom. Contrarily to the previous table, one can see that

$C_x$	$C_z$	Absorbed power [kW]
0	0	3.4
0.5	0	3.4
0.0	1	3.1
0.5	1	3.3

Table 9: Mean power without and with viscous damping at Yeu site. The length of the wire is equal to 39 m, and the PTO damping parameter is optimised for each sea state

Site	Mean power with	Mean power with	Difference
	fixed $R_m$ and $l_0 + 4 = h$ [kW]	$R_m$ optimised and $l_0 + 4 = h$ [kW]	
SEM-REV	1.1	N/A	N/A
EMEC	2.2	2.8	27
Yeu	2.5	3.3	32
Lisboa	2.4	3.5	46
Belmullet	3.4	N/A	N/A

Table 10: Comparison of the mean absorbed power with and without optimisation of the PTO damping coefficient

in this case, the mean absorbed power is roughly the same whatever the modelling of the viscous damping.

The reason is that in this second table, the PTO damping parameter is optimised for each state. It shows that even if the dynamic of the system is different because of different modelling of the viscous damping, the estimation of absorbed power is robust with errors in this modelling, provided that the PTO damping parameter is optimised.

Therefore, the uncertainty on the mean absorbed wave power from the modelling of the viscous damping and the length of wire is estimated to be small, about 10%.

Table (10) shows a comparison of the mean output power with optimisation and with the nominal value of the PTO damping coefficient ( $R_m = 20kN.s/m$ ). The PTO damping coefficient  $R_m$  was optimised in the range [10000, 100000]  $N.s/m$ .

One can see that optimising the PTO damping coefficient allows to increase significantly the mean absorbed wave power whatever the sea state. Depending on the wave resource, the gain is between 20 and 50%.

Hence, not to have considered the optimisation of the PTO damping coefficient in the calculation of the criteria of the small bottom-referenced heaving buoy would have introduced the largest uncertainty on the energy production.

Finally, to remain conservative, the uncertainty on the energy production

of the small Bref-HB is estimated to be about  $\pm 30\%$ .

### 4.3.3 Conclusion

- The mean absorbed wave power that one can expect from the small Bref-HB device is about 2 to 3 kW/m on a site on which the wave resource is higher than 20 kW/m.
- The uncertainty on the criteria of the small Bref-HB is about  $\pm 30\%$ . It comes from the uncertainties on the modelling of viscous effects and on the wire.

## 4.4 Parametric studies

### 4.4.1 Effect of the tide

Configuration	1	2	3
Tide [m]	-0.5	0	+0.5
$l$ [m]	21.5	22	22.5
$Z_0$ [m]	4.5	4	3.5

Table 11: Configurations considered for the assessment of the effect of the tide.

For studying the effect of tide on the performances of the device, we considered three scenarii. In the first one, the tide is -0.5 m, in the second one the water depth is nominal, and in the last one, the tide is +0.5 m. Table 11 summarises the parameters which were used.

$T_p$ [s]	$H_s$ [m]	$\gamma$	Absorbed power [kW]		
			1	2	3
4	1	1.	1.11	1.32	1.13
6	1.5	1.	2.53	2.4	2.11
8	2.0	3.3	2.11	2.1	1.47
10	3.0	3.3	2.89	2.86	2.09
12	7.5	3.3	6.48	6.07	4.95

Table 12: Results of the parametric study on the effect of the tide.

Five sea states, from light to severe conditions, were considered. Table (12) summarises the wave conditions and the results of wave power absorption in each tidal configuration. One can see that, except for the less energetic sea state, the best power absorption is achieved at low tide, whereas the worst power absorption is achieved at high tide. In comparison with no tide, low tide can lead to increase up to 8%, whereas high tide can lead to a reduction of 30%.

These results are probably linked with the high end stop. In the numerical simulations, it has been observed that the high end stop is more often used than the lower one, which provides an explanation. Hence, it might be possible to increase a bit the capture width of the small bottom-referenced heaving buoy by reducing the low end stop and increasing the high end stop.

#### 4.4.2 Effect of the scale

To assess the effect of scale, a calculation of the criteria of the small bottom-referenced heaving buoy was performed on a version at scale 2:1. All parameters were scaled up with respect to the Froude scale law, except the length of the wire (equal to 22 m)

Version		1:1	2:1	Ratio
Displacement	[m <sup>3</sup> ]	2.88	23.1	8.
Mean power	[kW]	2.5	13.2	5.3
Energy / Mass	[kWh/m <sup>3</sup> ]	718	467	0.65
Energy / Wetted surface	[kWh/m <sup>2</sup> ]	530	690	1.30
Energy / PTO force	[kWh/N]	3.1	3.0	1.0
Energy / Wave force	[kWh/N]	0.99	1.4	1.41

Table 13: Comparison of the criteria for scale 1:1 and 2:1.

Table (13) shows a comparison of the criteria of the small bottom-referenced heaving buoy at scale 1:1 and scale 1:2. One can see that the ratio of the power absorbed at a scale 2 is between  $2^2 = 4$  and  $2^3 = 8$ . Hence, if the cost is proportional to the mass of the system, it is not worth scaling up the system to decrease the cost of the energy. However, if the cost is proportional to the wetted surface, then the scaling up can decrease the cost of the energy by 30%.

Regarding the two other criteria - energy per PTO force and energy per wave force - it appears that up scaling is favourable.

#### 4.4.3 Effect of limitation of the maximal output power

In order to assess the effect of limiting the maximal output power, a calculation of mean annual power of the small Bref-HB on the Yeu site was performed with a threshold on the maximum instantaneous power production equal to 20 kW. It means that when the instantaneous power is greater than 20 kW, only 20 kW are taken into account for the calculation of the mean power. It is supposed that the power difference is dissipated by an inner device and that it does not affect the behaviour of the system.

Power matrix of the system with that limitation of the output power is plotted in figure (28). One can show that the mean power is very similar to the one without the limitation (figure (21) whereas the maximal absorbed

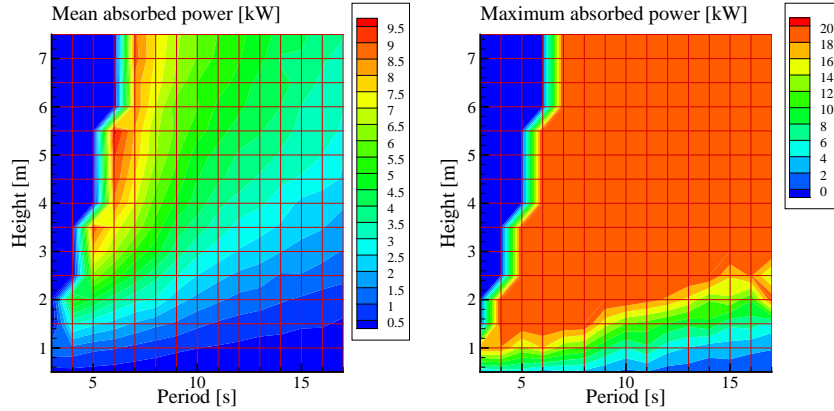


Figure 28: Power matrix of the small bottom-referenced heaving buoy device with limitation of the maximal output power at 20 kW. Left figure is the mean absorbed power and right figure is the maximum power.

power is limited. Using the wave statistics of Yeu, without limitation of the output power the mean annual power is 2.4 kW against 2.36 kW with the limitation, i.e a difference smaller than 2%. Hence, limitation on the output power to 10 times the mean annual power could be applied losing significant amount of power production.

#### 4.5 Power flow

One question for a wave-energy converter that moves in several degrees of freedom is how much energy is converted from each of the oscillation modes. As we have seen, the small bottom-referenced heaving buoy converter has a quite strong response in surge additional to the principal mode for wave energy extraction, which for this device is heave. It also interacts with the ocean through the pitch motion.

Figure 29 gives the average absorbed power (i.e. before subtracting the viscous loss) for a selection of seven sea states that cover the most relevant part of the scatter diagrams presented in Section 3. For each of these the relative contribution from the surge, heave and pitch motions are shown in Figure 30. It has been calculated as the difference between excitation power and radiated power,  $\bar{P}_a = \bar{P}_e - \bar{P}_r$  where the bar means time averaging.

The general result is that about 80 % of the absorbed power comes from the heave motion and the remaining 20 % comes primarily from surge. The tendency of a relatively larger contribution from surge for the sea states with peak period 8 to 10 s corresponds well to the observed maximum for the surge RAO around the same wave periods.

Looking further to Figure 31 we have decomposed the absorbed power into the three power sinks of the system: power extracted through the

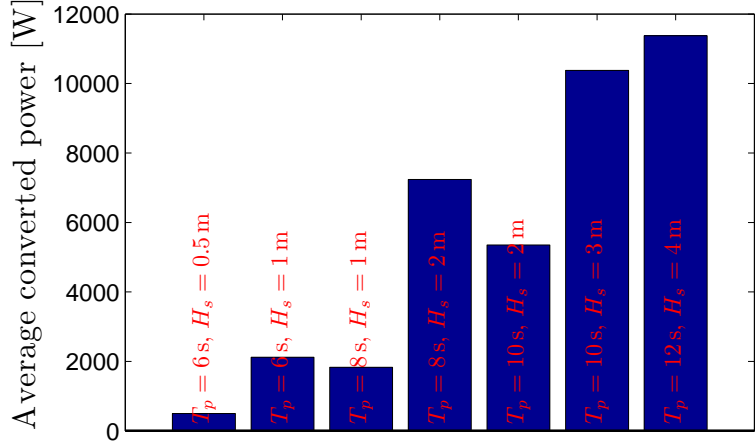


Figure 29: Average converted power using a linear damper as machinery. The power flow through the system has been analysed for seven representative sea states.

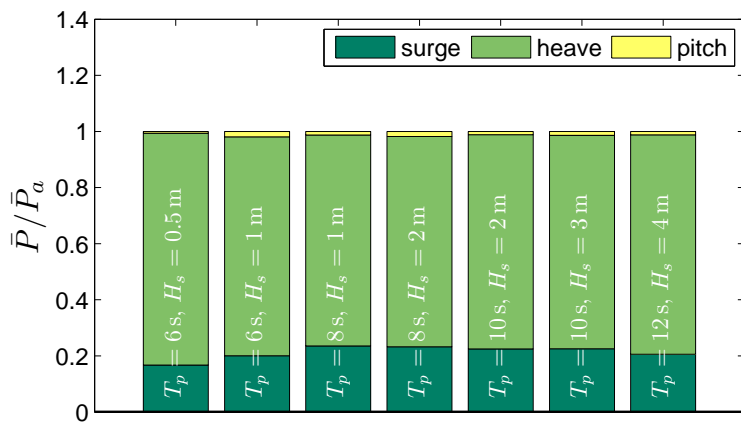


Figure 30: Average absorbed power for each oscillation mode given as fraction of the total absorbed power for the seven sea states assuming a linear damper characteristic for the machinery.

machinery, viscous loss and radiated power. The viscous power is a loss, whereas the radiated power is necessary for the wave absorption process (and thus appear above the value 1). Although the viscous power in principle is a pure loss, we have earlier seen (Section 4.2.3) that for the system studied here it has a beneficial effect in on range of wave periods and amplitudes due to the nonlinear influence of the end stop mechanism.

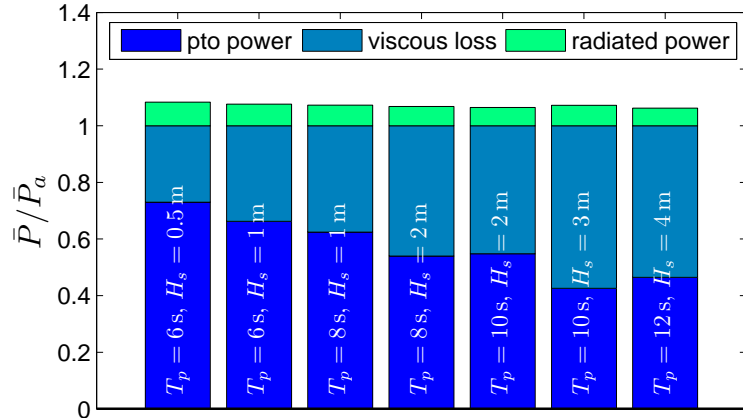


Figure 31: Average power converted by the PTO and viscous loss given as fraction of the absorbed power assuming a linear damper as machinery. The full length of the bars equals the total average excitation power, which differs from the absorbed power by an amount equal to the average radiated power.

The relative importance of viscous loss steadily increases as the significant wave height increases. For the weakest sea state with wave height 0.5 m, about 25 % of the absorbed power is lost through viscous dissipation according to our model. For the sea states with significant wave heights around 3-4 m, the share of viscous loss is about 50 %.

#### 4.6 Linear damper PTO vs. generator with DC-level control

Most of the results in this report has been derived assuming a linear damping characteristic for the machinery force. This is partly because it serves as a good reference for comparing with other systems, and partly because the details generator and power electronics design for our reference system, the Seabased, hasn't been known to us. However, in this section we we investigate the reponse of the system assuming a direct-coupled linear generator working in a fashion according to our best knowledge, which has been described in the modelling part, Section 2.4.

For the results presented here it has been assumed that the generator work in DC-level control mode. On the inverter side the controller has been defined with a quite strong controller to keep the DC-level constant. This

is demanding as the currents become very high once the machinery force “kicks in”. It should also be mentioned that the viscous force model has been simplified for these simulations as the second model implementation has been used (running on the 20-sim software package). In the current version of the model it does not have access to the relative velocity between the buoy and the water. Instead an equivalent linear damping force has been included for the surge motion only. The comparisons are made on equal basis, i.e. in this case also the linear damper machinery has been run with a model having a simplified viscous damping.

The average absorbed power is given by Figure 32, and a comparison of the converted useful power (after subtracting the viscous loss) is shown in Figure 33.

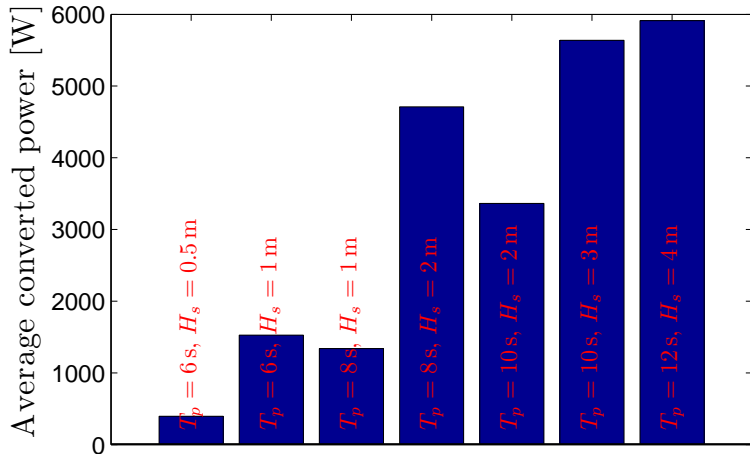


Figure 32: Average converted power for the seven sea states used in the investigation of power flow through the system.

The converted power is slightly reduced (5 to 20 %) for the generator as compared to a linear damper. In both cases the machinery parameters (DC-level setpoint and damping coefficient) have been optimised. Further detail on the decomposition into power sinks is given by Figure 34. It may be seen that the viscous power loss is about 30 % of the absorbed power for most of the sea states. (Remember that this is based on a simplified relation). What is more interesting to observe is however that the resistive loss due to the generator current is estimated to increase as the sea states become more rich on power. It goes from constituting about 20 % of the absorbed power for the weakest sea state, to about 40 % for the strongest sea states. The reason for these losses is the setup where the rectifier on the generator side works directly against a constant DC level. As already mentioned, if the inverter controller is run with a strong effort to keep the DC level constant, the resulting currents are large. An exert of time series

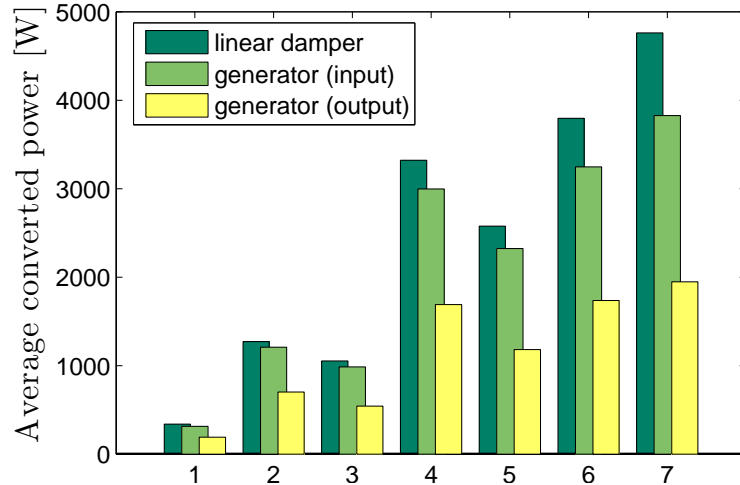


Figure 33: Comparison of the converted power for the system with two different alternatives for the PTO model: linear damper and linear generator. Power is lost in the generator due to high electric currents.

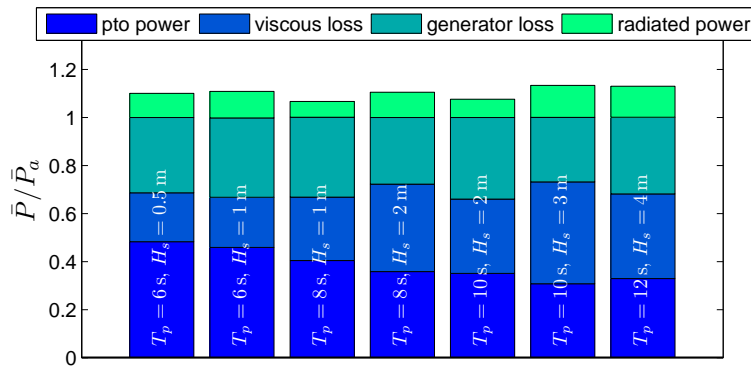


Figure 34: Average power converted by the linear generator, viscous loss and ohmic losses in the generator given as fraction of the absorbed power. The full length of the bars equals the total average excitation power, which differs from the absorbed power by an amount equal to the average radiated power.

for the DC-level voltage and generator current is shown in Figure 35.

It can be seen that even though the DC-level is still quite variable, the instantaneous current reaches relatively high values. A more constant DC value would require even higher currents. Reservations must be made that the machine may be somewhat undersized for this kind of sea states – as we can see, the relative importance of the generator losses become smaller for weaker sea states.

One effect of the sourcing the power through the DC-link is to smoothen the output power. A comparison between the power fed to the generator and that flowing through the inverter on the output side is shown in Figure 36.

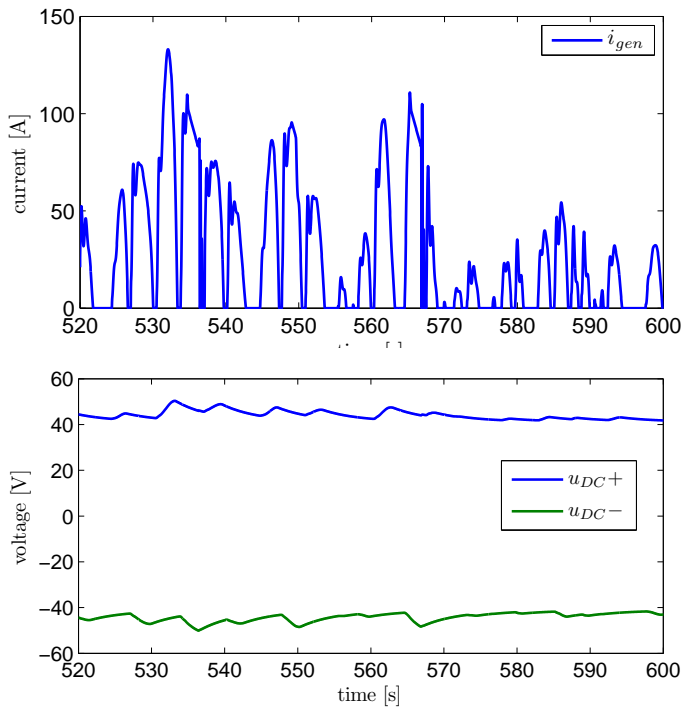


Figure 35: The voltages of the DC-link (upper) and the current through the generator (lower) in a seastate with  $H_s = 2$  m and  $T_p = 8$  s. The DC voltage setpoint was 41 V.

## 5 Conclusions and recommendations

From these results and the study, main conclusions are :

- The mean power level that one can expect from the small bottom-referenced heaving buoy WEC is about 2 to 3 kW on a site whose

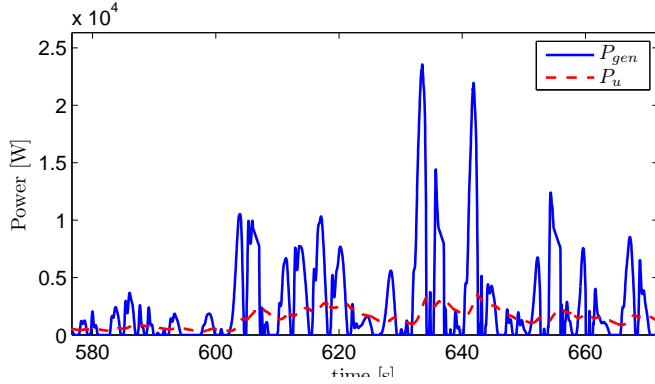


Figure 36: Mechanical power  $P_{gen}$  converted by the generator, and the delivered useful power  $P_u$  converted by the inverter after the DC link. The sea state has  $H_s = 2\text{ m}$  and  $T_p = 8\text{ s}$ .

wave resource is greater than 20 kW/m. The uncertainty is about  $\pm 30\%$ . It comes from:

- The modelling of the viscous losses and a dependence on the length of the wire.
- The modelling of the PTO and the value of the PTO damping coefficient in case of a linear damper.
- High tide leads to a reduction of the absorbed power up to 30%. Low tide might lead to an increase of the absorbed power up to 8%.
- A scaling up by a factor 2 of the system (displacement times 8) leads to an increase of the power by a factor 5.3 and a decrease of the criteria energy per PTO force and energy per wave force. Depending on how scale the costs, it could be beneficial to scale up the system in order to decrease the cost of energy.
- The output power could be limited to 10 times the mean annual power without losing a significant amount of energy production.
- The total absorbed energy is roughly due 20 % to the surge motion and 80 % to the heave motion. Of the absorbed energy, between 25 and 50 % is typically lost through viscous damping. For some operating conditions, however, the viscous damping has a positive influence on the power response by keeping the translator from getting stuck at the end stop.
- According to the model presented here, the linear generator run with optimised DC level control is able to absorb about 5 to 20 % less energy than an idealised linear damper. The main part of the results in this

report has been obtained assuming a linear damper characteristic for the power take-off.

## References

- [1] J. Falnes, 2002. Ocean waves and oscillating systems. Linear interactions including wave energy extraction. Cambridge university press.
- [2] M. Folley, T.W.T. Whittaker and J. van't Hoff, 2007. The design of small seabed-mounted bottom-hinged wave energy converters. Proceedings of the 7th European Wave and Tidal Energy Conference, Porto, Portugal.
- [3] B. King, 1987. Time-Domain Analysis of Wave Exciting Forces on Ships and Bodies. PhD thesis, the University of Michigan.
- [4] B. Molin, 2002. Hydrodynamique des structures offshore, Guides Pratiques sur Les Ouvrages En Mer, TECHNIP Eds.
- [5] A. Babarit, Achil3D v2.0 : User Manual, Laboratoire de Mécanique des Fluides, CNRS UMR6598, Ecole Centrale de Nantes, October, 2008.
- [6] Mikael Eriksson. *Modelling and experimental verification of direct drive wave energy conversion – Buoy-generator dynamics*. PhD thesis, Uppsala Universitet, 2007.
- [7] C. Bostrom, R. Waters, E. Lejerskog, O. Svensson, M. Stalberg, E. Stromstedt, and M. Leijon. Study of a wave energy converter connected to a nonlinear load. *Oceanic Engineering, IEEE Journal of*, 34(2):123 –127, april 2009.
- [8] R. Taghipour, T. Perez, and T. Moan. Hybrid frequency–time domain models for dynamic response analysis of marine structures. *Ocean Engineering*, 35(7):685–705, May 2008.
- [9] Tristan Perez and Thor I. Fossen. Time- vs. Frequency-domain Identification of Parametric Radiation Force Models for Marine Structures at Zero Speed. *Modeling, Identification and Control*, 29(1):1–19, 2008.
- [10] Rafael Waters. *Energy from Ocean Waves – Full Scale Experimental Verification of a Wave Energy Converter*. PhD thesis, Uppsala Universitet, 2008. ISSN 1651-6214, ISBN 978-91-554-7354-9.
- [11] C. Bostrom, E. Lejerskog, M. Stalberg, K. Thorburn, and M. Leijon. Experimental results of rectification and filtration from an offshore wave energy system. *Renewable Energy*, 34(5):1381 – 1387, 2009.
- [12] Simon Tyrberg, Magnus Stålberg, Cecilia Bostrom, R. Waters, O. Svensson, E. Stromstedt, A. Savin, J. Engstrom, Olivia Langhamer, Halvar Gravråkmo, Kalle Haikonen, J. Tedelid, J. Sundberg,

- and M. Leijon. The lysekil wave power project – status update. In *Proceedings of the 10th World Renewable Energy Conference (WREC)*, Glasgow, UK, 2008.
- [13] Ned Mohan, Tore Undeland, and William P. Robbins. *Power electronics – Converters, Applications and Design*. Number ISBN 0-471-58408-8. John Wiley & Sons, Inc., 1995.
  - [14] Jørgen Hals. *Modelling and phase control of wave-energy converters*. PhD thesis, Norges teknisk-naturvitenskapelige universitet, 2010. Doctoral theses at NTNU 2010:23, ISSN 1503-8181, ISBN 82-471-2003-3.
  - [15] *Bølgekraftprogram*. Afslutningsrapport 2002. Bølgekraftudvalgets Sekretariat, RAMBØLL, Teknikerbyen 31, 2830 Virum.

## Chapter 2

**A floating two-body  
heaving wave energy  
converter (F-2HB) inspired  
by the Wavebob device**

# Numerical estimation of energy delivery from a selection of Wave Energy Converters

## – Floating two-body heaving converter

Aurélien Babarit<sup>1</sup>, Jørgen Hals<sup>2</sup>

<sup>1</sup>Laboratoire de Mécanique des Fluides - CNRS UMR6598  
Ecole Centrale de Nantes, 1 rue de la Noe, 44300 Nantes, France

<sup>2</sup>Centre for Ships and Ocean Structures  
Norges teknisk-naturvitenskapelige universitet,  
Otto Nielsens V. 10, 7491 Trondheim, Norway

20 May 2011

## Summary

This document reports the study of a Floating two-body heaving converter (F-2HB) inspired by the Wavebob WEC in the frame of the project “Numerical estimation of energy production from a selection of Wave Energy Converters”. It contains a mathematical model and simulation results for the study of the Wavebob wave energy converter .

Results of the study are the following criteria:

- The annual mean power.
- The yearly energy output / displacement.
- The yearly energy output / wetted surface.
- The power per unit of significant machinery (or PTO) force.
- The power per unit of excitation force
- The duration curves.

These criteria were estimated for this floating two-body heaving converter using the mathematical model described in this report. Results are given in the following table and in figure (1).

From these results and the study, main conclusions are :

- The mean power level that one can expect from this floating two-body heaving converter is about 200 kW on a site whose wave resource is about 30 kW/m. The uncertainty is about [−20%, +40%]. It comes from the modelling of the viscous losses.

Parameter	Unit	SEM-REV	EMEC	Yeu	Lisboa	Bel-mullet	Danish site
$\gamma$		1	1	3.3	3.3	3.3	1
Wave en. trans.	[kW/m]						
Mean power	[kW]	78.8	127	191	199	373	116
$E_y / \text{Mass}$	[MWh/m <sup>3</sup> ]	0.139	0.225	0.338	0.351	0.660	0.205
$E_y / A_{\text{wet}}$	[MWh/m <sup>2</sup> ]	0.326	0.527	0.791	0.820	1.54	0.480
$E_y / \text{PTO frc.}$	[kWh/N]	1.20	1.66	2.03	2.03	2.67	1.60
$E_y / \text{Wave frc.}$	[kWh/N]	1.67	2.28	3.03	2.66	3.41	2.45

Table 1: Evaluation criteria for the floating two-body heaving converter. The parameters are calculated based on the yearly energy delivery  $E_y$ . The mass is taken as the total mass of the ballasted installed structure, not including the moorings, and  $A_{\text{wet}}$  is the wetted surface area of the structure. The uncertainty of these numbers is estimated to be in the range of  $[-20, +40]\%$ .

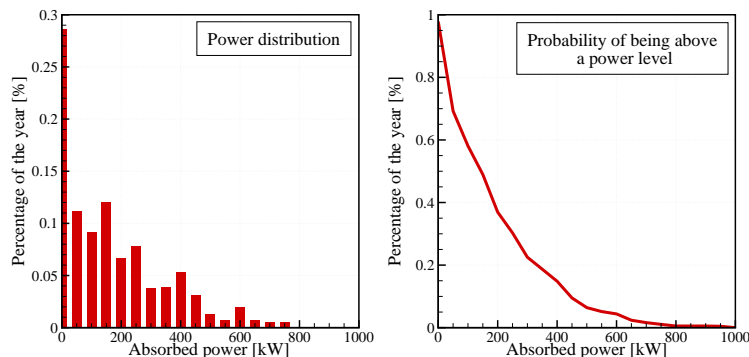


Figure 1: Distribution of the power production on a typical 30 kW/m wave site.

- Optimisation of the power take-off (PTO) parameters for each sea state increases the mean absorbed power by 17% in comparison with the best case without optimisation (one set of PTO parameters for every sea state).
- The output power could be limited to 1MW without losing a significant amount of energy production. Limitation of the instantaneous absorbed power to 10 times the mean output power (2MW) would reduce the mean absorbed power by only a small amount (6%).
- A scaling down by a factor 0.78 of the system (displacement divided by 2) leads to a decrease of the power by 30%. On the other side, doubling the displacement of the system increases the energy absorption by only 20%. This indicates that, depending on how the costs scale, it could be beneficial to scale down the system in order to decrease the cost of energy.
- The stroke length of the relative motion could be limited to 3 m without significant losses in the mean energy absorption.

# Contents

<b>1 System description - The floating two-body heaving converter</b>	<b>5</b>
1.1 Dimensions and mechanical parameters . . . . .	5
1.2 Power take-off and control . . . . .	8
1.3 Cost-related criteria . . . . .	9
1.3.1 Mass, displacement and wetted surface . . . . .	9
1.3.2 Significant forces . . . . .	9
1.4 Comment from the Wavestar developer . . . . .	9
<b>2 Equation of motion</b>	<b>9</b>
2.1 Kinematics . . . . .	10
2.2 Forces . . . . .	12
2.2.1 Hydrostatic forces . . . . .	12
2.2.2 Wave excitation and radiation forces . . . . .	13
2.2.3 Viscous damping forces . . . . .	13
2.2.4 Bearing and PTO forces . . . . .	14
2.2.5 End stops forces . . . . .	15
2.2.6 Mooring forces . . . . .	16
2.2.7 Other forces . . . . .	16
2.3 Equation of motion . . . . .	16
2.3.1 Frequency domain . . . . .	16
2.3.2 Time domain . . . . .	18
2.4 Implementation . . . . .	19
2.4.1 Calculation of the hydrodynamic coefficients and functions	19
2.4.2 Estimation of viscous damping coefficients . . . . .	23
2.4.3 W2W models . . . . .	23
<b>3 Simulation results and energy assessment</b>	<b>24</b>
3.1 Verification . . . . .	24
3.2 RAOs . . . . .	28
3.2.1 Maximisation of the power production (without constraints)	28
3.2.2 Optimisation of the PTO coefficients (without constraints)	31
3.2.3 Assessment of the influence of the viscous damping modelling	35
3.2.4 Assessment of the influence of the non linearities . . . . .	36
3.2.5 Optimisation of the PTO coefficients (with constraints) .	38
3.2.6 Conclusions . . . . .	39
3.3 Power matrix and criteria . . . . .	39
3.3.1 Power matrix of the F-2HB . . . . .	39
3.3.2 Assessment of the uncertainties . . . . .	43
3.3.3 Parametric studies . . . . .	46
<b>4 Conclusions and recommendations</b>	<b>47</b>

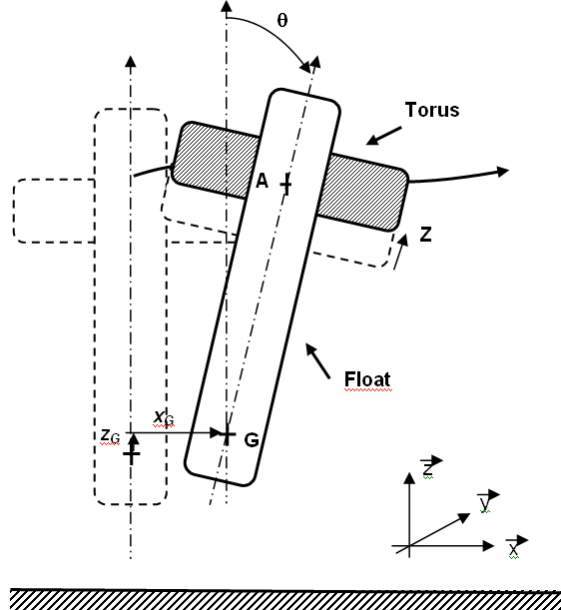


Figure 2: Sketch of the system.

## 1 System description - The floating two-body heaving converter

This device is an axi-symmetric, self-reacting point absorber, operating in the heave mode. It is composed of two bodies sliding along each other. A simplified sketch of the system is shown in figure (2). The bigger and deeper body is referenced as the Float while the shallower one is referenced as the Torus.

It was inspired by the Wavebob WEC which is currently in development in Ireland. Figure (3) shows a picture of the 1/4th scale model which was tested at sea in the Galway bay.

### 1.1 Dimensions and mechanical parameters

Dimensions of the system considered in this study were taken as similar as possible as the ones of the Wavebob WEC. Dimensions of the Wavebob were estimated from pictures or data found on the Internet of the Wavebob WEC. On Wavebob's website [6], it is specified that the diameter of the torus is about 20 meters. Using that length as a reference, other dimensions were estimated from pictures of the 1/17th scale model found on [7].

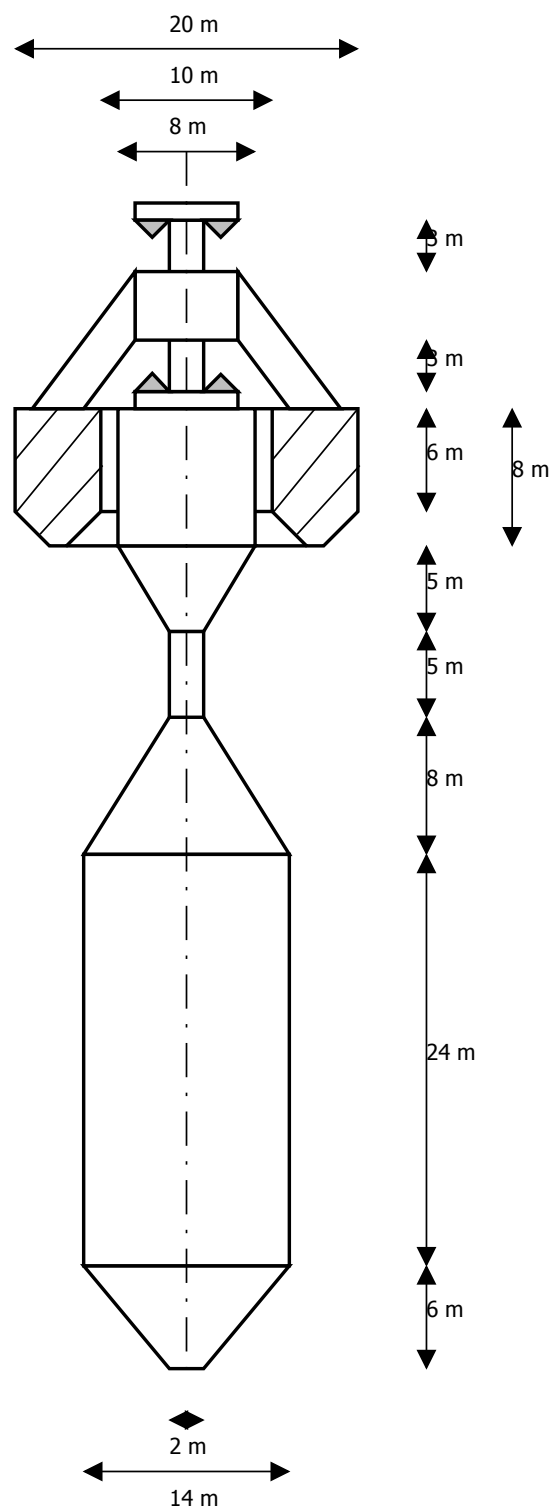
Figure (1.1) shows the dimensions that were used. One can notice that it is a rather deep device, with draft of about 50 meters. From these dimensions, mechanical parameters (masses, inertia) were estimated. They are summarised in table (1.1).



Figure 3: 1/4 scale model of the Wavebob WEC at sea.

<b>Property</b>	<b>Value</b>	<b>Unit</b>
<b>Torus</b>		
Outer diameter	20	m
Inner diameter	10	m
Draft	2	m
Height	8	m
Displacement	278	$\text{m}^3$
Mass	278	tons
Centre of mass	0	m below the free surface
Moment of inertia $I_{xx}$	12400	$\text{t} \cdot \text{m}^2$
Moment of inertia $I_{yy}$	12400	$\text{t} \cdot \text{m}^2$
Moment of inertia $I_{zz}$	16500	$\text{t} \cdot \text{m}^2$
Stroke length	6	m
Stiffness upper end stop spring	$10^6$	kN/m
Stiffness lower end stop spring	$10^6$	kN/m
<b>Float</b>		
Diameter at WL	8	m
Draft	50	m
Height	66	m
Displacement	4680	$\text{m}^3$
Mass	4680	tons
Centre of mass	-35.	m below the free surface
Moment of inertia $I_{xx}$	1740000	$\text{t} \cdot \text{m}^2$
Moment of inertia $I_{yy}$	1740000	$\text{t} \cdot \text{m}^2$
Moment of inertia $I_{zz}$	1510000	$\text{t} \cdot \text{m}^2$

Table 2: System parameters



## 1.2 Power take-off and control

In this study it was chosen to model the power take-off as a linear system. It was motivated by the fact that, although in the actual Wavebob the power take-off (PTO) is hydraulic [6] (for which a Coulomb damping model would be more suitable), in [8] many references to damping as in linear damping are made for the Wavebob. Therefore, it is most probable that the PTO is controlled in order to mimic a specified linear behaviour. One could note that it is common practice for wave energy converters. Moreover, it is not expected that this modelling choice would have a significant influence on the power absorption figures, as other studies performed in this project indicate (see Bottom-dixed Heave-buoy Array for example).

Let  $B_{PTO}$  and  $K_{PTO}$  be the damping and restoring coefficients of the PTO system, respectively. Usually,  $K_{PTO}$  is set to non-zero values to achieve tuning of the system response to the current sea state. Positive  $K_{PTO}$  can be achieved by including a simple physical spring in the PTO system. Therefore, it can be seen as a practical option. Negative  $K_{PTO}$  values are much more difficult to achieve. One would have to use an active component. As the power flowing through the machinery will be out of phase with the velocity, i.e. there will be reactive machinery power, the machinery will have to work partly as a generator and partly as a motor. The instantaneous reactive power may typically be typically 10 times larger than the average absorbed power [10]. Therefore all the benefit induced by adding the negative spring is likely to be lost in conversion efficiencies. This is why other control strategies based on passive components are often considered instead. Latching control is an example.

However, the situation is a bit different in the case of a floating two-body heaving converter, because it is a self-referenced system. Because of that property, the masses of torus and float do not have to balance their own displacement. The equilibrium position of both torus and float will not be affected, provided the PTO can deliver a static force compensating the difference between gravity and buoyancy forces. This can be achieved easily with a hydraulic PTO.

Let denote  $M_{PTO}$  the associated parameter: the difference between the actual mass of the torus and its displacement. In the equation of motion in frequency domain this parameter will appear on the left hand sign with a minus sign. Therefore, it will have the same effect as a negative spring in the PTO. Being a physical parameter, the negative spring effect will be achieved without reactive power.

This parameter can be adjusted to each sea state by transferring ballast from the float to the torus in one or the other way. Therefore, it is believed that this extra possibility of controlling the response of the system is an essential component of a floating two-body heaving converter. Actually, this could provide the explanation for one of the claims one can find on Wavebob's website: *The Wavebob has exceptional facilities for almost instantaneous tuning and longer period adjustment of natural frequencies and bandwidth.* Thus, this feature has been included in the analysis.

Criteria		unit
Significant wetted surface	2120	$\text{m}^2$
Significant mass	4958	tons

Table 3: Significant wetted surface and mass of the floating two-body heaving converter.

### 1.3 Cost-related criteria

#### 1.3.1 Mass, displacement and wetted surface

The wetted surface and mass are two of the relevant costs-related criteria which could be derived for any wave energy converter.

In the case of the considered floating two-body heaving converter, as it is a self - reacting device, only the two parts of the floating unit itself - the Torus and the Float - are taken into account. The weight of the moorings and anchors are neglected. They are expected to be small, because the moorings have to counteract only the drift forces.

The displacement of the torus is equal to 278 tons and the displacement of the float is 4680 tons. Hence, the overall significant mass is 4958 tons.

The wetted surface of the torus is about  $420 \text{ m}^2$ . The wetted surface of the float is about  $1700 \text{ m}^2$ . The total significant wetted surface considered here is then  $2120 \text{ m}^2$ .

#### 1.3.2 Significant forces

The two other cost criteria considered are the significant PTO force and the significant wave force. They both have zero mean values. So, the cost criteria are defined as the RMS value of the forces over the whole year.

### 1.4 Comment from the Wavestar developer

In working with this study we have been in contact with the developer of the Wavebob device. They have been informed about our study, and have received a draft copy of this report. We proposed to the developer to give comment for inclusion into the report, and this is the comment from the Wavebob team:

*Wavebob acknowledge the high quality and volume of the work produced. As the investigations are based on somewhat out-of-date public domain system information the analysis does not represent the full potential of current Wavebob WEC technology; this is primarily with respect to device geometry, PTO control and inherent tuning capability.*

## 2 Equation of motion

An actual floating two-body heaving converter has 7 degrees of freedom: 3 translations and 3 rotations for the float, plus one translation for the relative motion of the torus. In this study, the incident waves are assumed to be mono-directional and propagating in the positive  $x$  direction. The system being

axisymmetric, all motions remain in the ( $xOz$ ) plane. Therefore, only surge, heave and pitch of the float, and the motion of the torus relative to the float have been considered in this study.

Referring to Figure 2, let  $G$  be the gravity centre of the float. Let  $x_G$  and  $z_G$  be the surge and heave motion of the float and  $\theta$  be the pitch motion. At equilibrium, it is assumed that  $G$  and the origin of the Cartesian reference frame  $O$  are the same. Furthermore, let  $A$  be the gravity centre of the torus and  $Z$  be the excursion of the torus relative to the float. Then  $GA = d + Z$ , with  $Z = 0$  at equilibrium.

It is assumed that all motions are of small amplitude. Hence, second order effects will be neglected and equation of motion will linearised. From our experience, taking into account non linear effects would lead to a reduction in the power absorption figures. Therefore, this assumption is not seen as a problem as the aim of this study is to derive upper estimates for energy absorption.

## 2.1 Kinematics

In the Cartesian reference frame, the position of the torus' gravity centre is given by:

$$\overrightarrow{OA} = \overrightarrow{OG} + \overrightarrow{GA} \quad (1)$$

$$\overrightarrow{OA} = \begin{pmatrix} x_G + (d + Z) \sin \theta \\ z_G + (d + Z) \cos \theta \end{pmatrix}^0 \quad (2)$$

By time derivating this equation, one gets the velocity in the fixed reference frame:

$$\overrightarrow{V}(A) = \begin{pmatrix} u + \dot{Z} \sin \theta + (d + Z) \dot{\theta} \cos \theta \\ w + \dot{Z} \cos \theta - (d + Z) \dot{\theta} \sin \theta \end{pmatrix}^0 \quad (3)$$

In the body reference frame:

$$\overrightarrow{V}(A) = \begin{pmatrix} u \cos \theta - w \sin \theta + (d + Z) \dot{\theta} \\ u \sin \theta + w \cos \theta + \dot{Z} \end{pmatrix}^B \quad (4)$$

By time derivating once gain, one gets the acceleration. In the fixed reference frame:

$$\overrightarrow{\gamma}(A) = \begin{pmatrix} \dot{u} + \ddot{Z} \sin \theta + 2\dot{Z}\dot{\theta} \cos \theta + (d + Z)\ddot{\theta} \cos \theta - (d + Z)\dot{\theta}^2 \sin \theta \\ \dot{w} + \ddot{Z} \cos \theta - 2\dot{Z}\dot{\theta} \sin \theta - (d + Z)\ddot{\theta} \sin \theta - (d + Z)\dot{\theta}^2 \cos \theta \end{pmatrix}^0 \quad (5)$$

In the body reference frame:

$$\overrightarrow{\gamma}(A) = \begin{pmatrix} \dot{u} \cos \theta - \dot{w} \sin \theta + 2\dot{Z}\dot{\theta} + (d + Z)\ddot{\theta} \\ \dot{u} \sin \theta + \dot{w} \cos \theta + \ddot{Z} - (d + Z)\dot{\theta}^2 \end{pmatrix}^B \quad (6)$$

Let  $m'$  be the mass of the torus, and  $M'$  the mass of the float. If  $m$  and  $M$  are the masses of displaced water by the torus and float at equilibrium, then  $m' - m = M - M'$  is what we called  $M_{PTO}$  in section (1.2), i.e the amount of mass transferred from the float to the torus. Let  $I_T$  and  $I_F$  be the respective moments of inertia of torus and float for  $M_{PTO} = 0$ . When  $M_{PTO}$  is different

from 0, these moments of inertia will be different too. In a first approximation, it is supposed that they behave such as  $I'_T \simeq \frac{m'}{m} I_T$  and  $I'_F \simeq \frac{M'}{M} I_F$ .

At point  $G$ , the dynamic moment of the float is given by:

$$\vec{\delta}_F(G) = I'_F \ddot{\theta} \vec{y} \quad (7)$$

and the dynamic moment of the torus is

$$\vec{\delta}_T(G) = \vec{\delta}_T(A) + \vec{AG} \times m' \vec{\gamma}(A) \quad (8)$$

This moment works about the y-direction, which component is

$$\begin{aligned} \delta_T(G) &= I'_T \ddot{\theta} - m'(d+Z) \begin{pmatrix} \sin \theta \\ \cos \theta \end{pmatrix}^0 \times \\ &\quad \left( \begin{array}{l} \dot{u} + \ddot{Z} \sin \theta + 2\dot{Z}\dot{\theta} \cos \theta + (d+Z)\ddot{\theta} \cos \theta - (d+Z)\dot{\theta}^2 \sin \theta \\ \dot{w} + \ddot{Z} \cos(\theta) - 2\dot{Z}\dot{\theta} \sin(\theta) - (d+Z)\ddot{\theta} \cos \theta - (d+Z)\dot{\theta}^2 \cos \theta \end{array} \right)^0 \end{aligned} \quad (9)$$

$$\begin{aligned} \delta_T(G) &= [I'_T + m'(d+Z)^2]\ddot{\theta} + m'(d+Z) \cos \theta \dot{u} \\ &\quad - m'(d+Z) \sin \theta \dot{w} + 2m'(d+Z)\dot{Z}\dot{\theta} \end{aligned} \quad (10)$$

Linearised, the vectorial relations (2) to (6) read:

$$\vec{OA} = \begin{pmatrix} x_G + d\theta \\ z_G + d + Z \end{pmatrix}^{0,B} \quad (11)$$

$$\vec{V}(A) = \begin{pmatrix} u + d\dot{\theta} \\ w + \dot{Z} \end{pmatrix}^{0,B} \quad (12)$$

$$\vec{\gamma}(A) = \begin{pmatrix} \dot{u} + d\ddot{\theta} \\ \dot{w} + \ddot{Z} \end{pmatrix}^{0,B} = \begin{pmatrix} 1 & 0 & d & 0 \\ 0 & 1 & 0 & 1 \end{pmatrix} \vec{\mathbf{x}}. \quad (13)$$

with the state vector defined as  $\mathbf{X} = [x_G, z_G, \theta, Z]^T$ . Thus the linearised dynamic moments of the torus is found from Equations (8) and (13) to be

$$\begin{aligned} \delta_T(G) &= \left[ \frac{m + M_{PTO}}{m} I_T + (m + M_{PTO})d^2 \right] \ddot{\theta} + (m + M_{PTO})d\dot{u} \quad (14) \\ &= \left( \begin{array}{cccc} (m + M_{PTO})d & 0 & \frac{m + M_{PTO}}{m} I_T + (m + M_{PTO})d^2 & 0 \end{array} \right) \vec{\mathbf{x}} \end{aligned} \quad (15)$$

Then, one can write:

$$\begin{pmatrix} (m + M_{PTO}) \vec{\gamma}(A) \\ \vec{\delta}_T(G) \end{pmatrix} = \mathbf{m} \vec{\mathbf{x}} \quad (16)$$

for the torus, and

$$\begin{pmatrix} (M - M_{PTO}) \vec{\gamma}(G) \\ \vec{\delta}_F(G) \end{pmatrix} = \mathbf{M} \vec{\mathbf{x}} \quad (17)$$

for the float, with:

$$\mathbf{m} = \begin{pmatrix} m' & 0 & (m')d & 0 \\ 0 & m' & 0 & (m') \\ (m')d & 0 & \frac{m'}{m} I_T + (m')d^2 & 0 \end{pmatrix} \quad (18)$$

$$\mathbf{M} = \begin{pmatrix} M' & 0 & 0 & 0 \\ 0 & M' & 0 & 0 \\ 0 & 0 & \frac{M'}{M} I_F & 0 \end{pmatrix} \quad (19)$$

## 2.2 Forces

In the following, the generalised force at point  $P$  will be written  $\mathbf{F}(P)$ . It is composed of a reaction  $\mathbf{R}$  and a torque  $\mathbf{T}$ .

Let us first define the operator:

$$\overline{\overline{AG}} = \begin{pmatrix} 1 & 0 & 0 \\ 0 & 1 & 0 \\ (d+Z)\cos\theta & -(d+Z)\sin\theta & 1 \end{pmatrix} \quad (20)$$

It corresponds to the transfer of a generalised force  $\mathbf{F}$  from the point  $A$  to the point  $G$ .

When one transfers a force which is proportional to a first order quantity (such as velocity for example), only 0<sup>th</sup> order terms should be retained because of the linearisation:

$$\overline{\overline{AG}} = \begin{pmatrix} 1 & 0 & 0 \\ 0 & 1 & 0 \\ d & 0 & 1 \end{pmatrix} \quad (21)$$

### 2.2.1 Hydrostatic forces

- **Force on the torus:** At the gravity centre of the torus  $A$ , in the frame of linear theory, one can show that the effect of the generalised weight plus generalised Archimedes force reduces to a restoring force proportional to the motion of point  $A$  plus a constant (because the weight and the buoyancy can be different due to the mass transfer  $M_{PTO}$ )

$$\mathbf{F}_{HT}(A) = -\mathbf{K}_{HT} \Delta \mathbf{X}_A - M_{PTO} g \begin{pmatrix} 0 \\ 1 \\ 0 \end{pmatrix} \quad (22)$$

Here, only the two last diagonal coefficients of the matrix  $\mathbf{K}_{HT}$  are non zero, because the body we consider is axisymmetric:  $\mathbf{K}_{HT} = \text{diag}(0, K_{H,z}, K_{H,\theta})$

At point  $G$ , the generalised hydrostatic force is given by:

$$\mathbf{F}_{HT}(G) = -\overline{\overline{AG}} \mathbf{K}_{HT} \Delta \mathbf{X}_A - \overline{\overline{AG}} M_{PTO} g \begin{pmatrix} 0 \\ 1 \\ 0 \end{pmatrix} \quad (23)$$

By linearising, one can show:

$$\mathbf{F}_{HT}(G) = -\overline{\overline{AG}} \mathbf{K}_{HT} \overline{\overline{GA}} \mathbf{X} - \overline{\overline{AG}} M_{PTO} g \begin{pmatrix} 0 \\ 1 \\ 0 \end{pmatrix} \quad (24)$$

with the operator  $\overline{\overline{GA}}$  defined by:

$$\overline{\overline{GA}} = \begin{pmatrix} 1 & 0 & d & 0 \\ 0 & 1 & 0 & 1 \\ 0 & 0 & 1 & 0 \end{pmatrix} \quad (25)$$

Equation (24) can be further simplified as:

$$\mathbf{F}_{HT}(G) = -(\overline{\mathbf{AG}} \mathbf{K}_{HT} \overline{\mathbf{GA}} + \mathbf{K}_{PTOT}) \mathbf{X} - M_{PTO} g \begin{pmatrix} 0 \\ 1 \\ 0 \end{pmatrix} \quad (26)$$

with  $\mathbf{K}_{PTOT}$  equal to  $diag(0, 0, -M_{PTO}gd)$ .

From this last equation, one can see that transferring mass from the float to the torus decreases the hydrostatic stiffness of the system.

- **Force on the float:** For the float,

$$\mathbf{F}_{HF}(G) = -\mathbf{K}_{HF} \mathbf{X} + M_{PTO} g \begin{pmatrix} 0 \\ 1 \\ 0 \end{pmatrix} \quad (27)$$

### 2.2.2 Wave excitation and radiation forces

- **Force on the torus:** At the gravity centre of the torus A, in the frame of linear theory, the hydrodynamic forces read in the frequency domain:

$$\mathbf{F}_{DT}(A) = \mathbf{F}_{exT}(A) - \mathbf{C}_{MT} \ddot{\mathbf{X}}_A - \mathbf{C}_{AT} \dot{\mathbf{X}}_A \quad (28)$$

where  $\mathbf{C}_{MT}$  is the added mass matrix and  $\mathbf{C}_{AT}$  the radiation damping matrix for the torus. Linearised, the equation reads:

$$\mathbf{F}_{DT}(A) = \mathbf{F}_{exT}(A) - \mathbf{C}_{MT} \overline{\mathbf{GA}} \ddot{\mathbf{X}} - \mathbf{C}_{AT} \overline{\mathbf{GA}} \dot{\mathbf{X}} \quad (29)$$

At point G, it is given by:

$$\mathbf{F}_{DT}(G) = \overline{\mathbf{AG}} \mathbf{F}_{DT}(A) \quad (30)$$

which gives, once linearised:

$$\mathbf{F}_{DT}(G) = \overline{\mathbf{AG}} \mathbf{F}_{exT}(A) - \overline{\mathbf{AG}} \mathbf{C}_{MT} \overline{\mathbf{GA}} \ddot{\mathbf{X}} - \overline{\mathbf{AG}} \mathbf{C}_{AT} \overline{\mathbf{GA}} \dot{\mathbf{X}} \quad (31)$$

- **Force on the float:** At the gravity centre of the float G, the hydrodynamic forces reads in the frequency domain:

$$\mathbf{F}_{DF}(G) = \mathbf{F}_{exF}(G) - \mathbf{C}_{MF} \ddot{\mathbf{X}} - \mathbf{C}_{AF} \dot{\mathbf{X}} \quad (32)$$

where  $\mathbf{C}_{MF}$  is the added mass matrix and  $\mathbf{C}_{AF}$  the radiation damping matrix for the float.

### 2.2.3 Viscous damping forces

- **Force on the torus:** For the torus, the viscous damping force is modelled under the form of the Morison equation:

$$\mathbf{F}_{VT}(A) = -\frac{1}{2} \rho \mathbf{C}_{D,T} \left( \left( \vec{V}(A) - \vec{V}_0(A) \right) \frac{\| \vec{V}(A) - \vec{V}_0(A) \|}{\dot{\theta} |\dot{\theta}|} \right) \quad (33)$$

where:

- $\vec{V}_0(A)$  is the undisturbed flow velocity taken at the instantaneous position of the gravity centre of the torus  $A$ .
- $\mathbf{C}_{D,T}$  is the viscous damping coefficient matrix. Here, it is considered as a diagonal matrix with coefficients  $\text{diag}(C_{x,T}A_{x,T}, C_{z,T}A_{z,T}, C_{\theta,T}I_{\theta,T})$  with  $A_{x,T} = 40 \text{ m}^2$ ,  $A_{z,T} = 240 \text{ m}^2$  and  $I_{\theta,T} = 213000 \text{ m}^5$ .

At point G, it is given by:

$$\mathbf{F}_{VT}(G) = \overline{\mathbf{AG}} \mathbf{F}_{VT}(A) \quad (34)$$

- **Force on the float:** For the float, one can not neglect any more the variation of the velocity along the vertical axis. Hence, the viscous damping force on the float is written in the general case:

$$\begin{aligned} \mathbf{F}_{VF}(G) = -\frac{1}{2}\rho \int_{-D}^0 & \left( \begin{array}{c} C_{x,F}(z)A_{x,F}(z)\left(\vec{V}_x(z) - \vec{V}_{0,x}(z)\right) \\ C_{z,F}(z)A_{z,F}(z)\left(\vec{V}_z(z) - \vec{V}_{0,z}(z)\right) \\ z \times C_{x,F}(z)A_{x,F}(z)\left(\vec{V}_x(z) - \vec{V}_{0,x}(z)\right) \end{array} \right) \\ & \cdot \left\| \vec{V}(z) - \vec{V}_0(z) \right\| dz \end{aligned} \quad (35)$$

However, taking into account the shape of the system, viscous damping in heave will probably occur mostly around the wider and deeper part of the system. Hence, we assume that:

$$\begin{aligned} & \int_{-D}^0 C_{z,F}(z)A_{z,F}(z)\left(\vec{V}_z(z) - \vec{V}_{0,z}(z)\right) \left\| \vec{V}(z) - \vec{V}_0(z) \right\| dz \\ & \simeq C_{z,F}(G)A_{z,F}(G)\left(\vec{V}_z(G) - \vec{V}_{0,G}(G)\right) \left\| \vec{V}(G) - \vec{V}_0(G) \right\| \end{aligned} \quad (36)$$

with  $A_{z,F}(G) = 150 \text{ m}^2$ .

#### 2.2.4 Bearing and PTO forces

According to section (1.2), the PTO force is composed of three parts:

- A linear damping part proportional to the relative velocity  $\dot{Z}$ , whose coefficient is  $B_{PTO}$ . This part corresponds with the energy absorption.
- A linear spring part, proportional to the relative motion  $Z$ , whose coefficient  $K_{PTO}$  is supposed to be larger than 0. It can be achieved by means of controlling the PTO force, or by using a physical spring.
- A static part. It aims at compensating the static force in the torus and in the float, due to the unbalance of the buoyancy force and the gravity force. It is equal to  $M_{PTO}g$  in absolute value.

Hence, the associated generalised PTO force, on the torus, is:

$$\mathbf{F}_{\text{PTO}T}(A) = \begin{pmatrix} 0 \\ -B_{PTO} \dot{Z} - K_{PTO} Z + M_{PTO} g \\ 0 \end{pmatrix}^B \quad (37)$$

$$= \begin{pmatrix} (-B_{PTO} \dot{Z} - K_{PTO} Z + M_{PTO} g) \sin \theta \\ (-B_{PTO} \dot{Z} - K_{PTO} Z + M_{PTO} g) \cos \theta \\ 0 \end{pmatrix}^0 \quad (38)$$

The bearing between the float and torus is supposed to be ideal. Hence, the associated generalised force on the torus from the bearing is:

$$\mathbf{F}_{\mathbf{B}T}(A) = \begin{pmatrix} R \\ 0 \\ T \end{pmatrix}^B = \begin{pmatrix} R \cos \theta \\ -R \sin \theta \\ T \end{pmatrix}^0 \quad (39)$$

Using the reaction principle, the effect of the bearing (respectively PTO) on the float is opposite to the effect of the bearing (respectively PTO) on the torus. Hence:

$$\mathbf{F}_{\mathbf{B}F}(A) = -\mathbf{F}_{\mathbf{B}T}(A) \quad (40)$$

$$\mathbf{F}_{\text{PTO}F}(A) = -\mathbf{F}_{\text{PTO}T}(A) \quad (41)$$

### 2.2.5 End stops forces

The relative motion between the torus and the float has a limited stroke. In order to take into account that limit in the model, an additional restoring force with large restoring coefficients is added in the model in the link between the float and the torus. This force is applied only when the relative motion reaches the higher or lower end stop. On the torus, it reads:

$$\mathbf{F}_{\text{EST}}(A) = -K_{ES} \begin{pmatrix} 0 \\ (Z + Z_{ES}) u(-Z_{ES} - Z) + (Z - Z_{ES}) u(Z - Z_{ES}) \\ 0 \end{pmatrix}^B \quad (42)$$

in which :

- $u$  is the step function.
- $K_{ES}$  is a restoring coefficient.
- $Z_{ES}$  is the stroke limit.

The effect on the float is the opposite:

$$\mathbf{F}_{\text{EST}}(A) = -\mathbf{F}_{\text{ES}F}(A) \quad (43)$$

### 2.2.6 Mooring forces

Moorings are supposed to be slack. They are not supposed to have a significant impact on the dynamic response of the system. Hence, the effect of mooring is modelled by a simple restoring force proportional to the horizontal motions of the float, with a rather low coefficient. It is set equal to 100 kN/m.

$$\mathbf{F}_M(G) = \begin{pmatrix} -K_M & 0 & 0 \\ 0 & 0 & 0 \\ 0 & 0 & 0 \end{pmatrix}^0 \mathbf{X} = -\mathbf{K}_M \mathbf{X} \quad (44)$$

### 2.2.7 Other forces

In this study, other forces such as drift and/or current forces were not considered. It is because their effect is believed to be limited to a shift in the horizontal equilibrium position of the system. Moreover, they are horizontal forces whereas the device works with vertical motions. Thus the effect of the energy absorption is of second order.

## 2.3 Equation of motion

### 2.3.1 Frequency domain

In the frequency domain, the viscous forces and the end stops forces are not taken into account.

Let us first consider the system composed of the {float} + {torus}. By expressing Newton's law at point  $G$ , one can show:

$$\begin{aligned} (\mathbf{M} + \mathbf{C}_{MF} + \mathbf{m} + \overline{\mathbf{AG}} \mathbf{C}_{MT} \overline{\mathbf{GA}}) \ddot{\mathbf{X}} = \\ \mathbf{F}_{exF}(G) + \overline{\mathbf{AG}} \mathbf{F}_{exT}(A) \\ - (\mathbf{C}_{AF} + \overline{\mathbf{AG}} \mathbf{C}_{AT} \mathbf{GA}) \dot{\mathbf{X}} \\ - (\mathbf{K}_{HF} + \overline{\mathbf{AG}} \mathbf{K}_{HT} \overline{\mathbf{GA}} + \mathbf{K}_{PTO} + \mathbf{K}_M) \mathbf{X} \end{aligned} \quad (45)$$

Let us further consider the forces on the isolated torus. One can show that:

$$\begin{aligned} \left( \overline{\mathbf{AG}}^{-1} \mathbf{m} + \mathbf{C}_{MT} \overline{\mathbf{GA}} \right) \ddot{\mathbf{X}} = & \mathbf{F}_{exT} - \mathbf{C}_{AT} \overline{\mathbf{GA}} \dot{\mathbf{X}} \\ & - \mathbf{K}_{HT} \overline{\mathbf{GA}} \mathbf{X} + \mathbf{F}_{PTOT} + \mathbf{F}_{BT} \end{aligned} \quad (46)$$

From this last equation, one can calculate the loads on the bearing between the torus and the float.

By assembling all these equations, one can show that the whole system can be written, in frequency domain:

$$(\mathbf{M} + \mathbf{C}_M) \ddot{\mathbf{X}} + (\mathbf{B}_{PTO} + \mathbf{C}_A) \dot{\mathbf{X}} + (\mathbf{K} + \mathbf{K}_{PTO}) \mathbf{X} = \mathbf{F}_{ex} \quad (47)$$

with :

$$\mathbf{M} = \begin{pmatrix} m_{11} & 0 & m_{13} & 0 \\ 0 & m_{22} & 0 & m_{24} \\ m_{31} & 0 & m_{33} & 0 \\ 0 & m_{42} & 0 & m_{44} \end{pmatrix} \quad (48)$$

where

$$\begin{aligned}
m_{11} &= m_{22} = m + M \\
m_{31} &= m_{13} = (m + M_{PTO}) d \\
m_{42} &= m_{24} = m_{44} = (m + M_{PTO}) \\
m_{33} &= \frac{m + M_{PTO}}{m} I_T + (m + M_{PTO}) d^2 + \frac{M - M_{PTO}}{M} I_F
\end{aligned} \tag{49}$$

Furthermore, the assembled added mass matrix is composed in the following way

$$\mathbf{C}_M = \begin{pmatrix} c_{M,11} & 0 & c_{M,13} & 0 \\ 0 & c_{M,22} & 0 & c_{M,24} \\ c_{M,31} & 0 & c_{M,33} & 0 \\ 0 & c_{M,42} & 0 & c_{M,44} \end{pmatrix} \tag{50}$$

Here the matrix elements are

$$\begin{aligned}
c_{M,11} &= C_{M11,FF} + C_{M11,FT} + C_{M11,TF} + C_{M11,FF} \\
c_{M,22} &= C_{M33,FF} + C_{M33,FT} + C_{M33,TF} + C_{M33,TT} \\
c_{M,31} &= c_{M,13} \\
&= C_{M15,FF} + C_{M15,FT} + d(C_{M11,FT} + C_{M11,TT}) \\
&\quad + C_{M15,TF} + C_{M15,TT} \\
c_{M,33} &= C_{M55,FF} + C_{M55,FT} + d^2 C_{M11,TT} \\
&\quad + 2dC_{M15,TT} + dC_{M15,TF} + C_{M55,TF} + C_{M55,TT} \\
c_{M,42} &= c_{M,24} \\
&= C_{M33,TF} + C_{M33,TT} \\
c_{M,44} &= C_{M33,TT}
\end{aligned} \tag{51}$$

The assembled radiation resistance matrix is

$$\mathbf{C}_A = \begin{pmatrix} c_{A,11} & 0 & c_{A,13} & 0 \\ 0 & c_{A,22} & 0 & c_{A,24} \\ c_{A,31} & 0 & c_{A,33} & 0 \\ 0 & c_{A,42} & 0 & c_{A,44} \end{pmatrix} \tag{52}$$

where the matrix elements are given by

$$\begin{aligned}
c_{A,11} &= C_{A11,FF} + C_{A11,FT} + C_{A11,TF} + C_{A11,FF} \\
c_{A,22} &= C_{A33,FF} + C_{A33,FT} + C_{A33,TF} + C_{A33,TT} \\
c_{A,31} &= c_{A,13} \\
&= C_{A15,FF} + C_{A15,FT} + d(C_{A11,FT} + C_{A11,TT}) \\
&\quad + C_{A15,TF} + C_{A15,TT} \\
c_{A,33} &= C_{A55,FF} + C_{A55,FT} + d^2 C_{A11,TT} \\
&\quad + 2dC_{A15,TT} + dC_{A15,TF} + C_{A55,TF} + C_{A55,TT} \\
c_{A,42} &= c_{A,24} \\
&= C_{A33,TF} + C_{A33,TT} \\
c_{A,44} &= C_{A33,TT}
\end{aligned} \tag{53}$$

Finally, the machinery damping  $\mathbf{B}_{\text{PTO}}$ , machinery stiffness  $\mathbf{K}_{\text{PTO}}$ , hydrostatic stiffness  $\mathbf{K}$  and excitation force  $\mathbf{F}_{\text{ex}}$  matrices are

$$\mathbf{B}_{\text{PTO}} = \begin{pmatrix} 0 & 0 & 0 & 0 \\ 0 & 0 & 0 & 0 \\ 0 & 0 & 0 & 0 \\ 0 & 0 & 0 & B_{\text{PTO}} \end{pmatrix} \quad (54)$$

$$\mathbf{K}_{\text{PTO}} = \begin{pmatrix} 0 & 0 & 0 & 0 \\ 0 & 0 & 0 & 0 \\ 0 & 0 & -M_{\text{PTO}}gd & 0 \\ 0 & 0 & 0 & K_{\text{PTO}} \end{pmatrix} \quad (55)$$

$$\mathbf{K} = \begin{pmatrix} K_{M11} & 0 & 0 & 0 \\ 0 & K_{H33,F} + K_{H33,T} & 0 & K_{H33,T} \\ 0 & 0 & K_{H55,F} + K_{H55,T} & 0 \\ 0 & K_{H33,T} & 0 & K_{H33,T} \end{pmatrix} \quad (56)$$

$$\mathbf{F}_{\text{ex}} = \begin{pmatrix} F_{\text{ex}F1} + F_{\text{ex}T1} \\ F_{\text{ex}F3} + F_{\text{ex}T3} \\ F_{\text{ex}F5} + dF_{\text{ex}T1} + F_{\text{ex}T5} \\ F_{\text{ex}T3} \end{pmatrix} \quad (57)$$

In the equation (55), one can see that the mass transfer  $M_{\text{PTO}}$  from the float to the torus reduces the stability in pitch of the system. This effect limits the amount of transferable mass.

### 2.3.2 Time domain

In the time-domain model, viscous forces and forces from the end stops are included. The equation of motion then becomes:

$$\begin{aligned} (\mathbf{M} + \mu_{\infty}) \ddot{\mathbf{X}} + \mathbf{B}_{\text{PTO}} \dot{\mathbf{X}} + \int_0^t \mathbf{K}_{\text{rad}}(t - \tau) \dot{\mathbf{X}}(\tau) d\tau + (\mathbf{K} + \mathbf{K}_{\text{PTO}}) \mathbf{X} \\ = \mathbf{F}_{\text{ex}} + \mathbf{F}_{\text{viscous}} + \mathbf{F}_{\text{ES}} \end{aligned} \quad (58)$$

with:

$$\mu_{\infty} = \lim_{\omega \rightarrow +\infty} \mathbf{C}_M(\omega) \quad (59)$$

$$\mathbf{K}_{\text{rad}}(t) = \frac{2}{\pi} \int_0^{+\infty} \mathbf{C}_A(\omega) \cos \omega t d\omega \quad (60)$$

The vector of viscous forces is

$$\mathbf{F}_{\text{viscous}}(t, \mathbf{X}, \dot{\mathbf{X}}) = \begin{pmatrix} \mathbf{F}_{\mathbf{V}F}(G) + \mathbf{F}_{\mathbf{V}T}(G) \\ F_{VT,2} \end{pmatrix} \quad (61)$$

in which  $\mathbf{F}_{\mathbf{V}F}(G)$  and  $\mathbf{F}_{\mathbf{V}T}(G)$  are given by equations (35) and (34), and  $F_{VT,2}$  is the second element of vector  $\mathbf{F}_{\mathbf{V}T}(G)$ . The end stop force vector is

$$\mathbf{F}_{\text{ES}}(t, \mathbf{X}, \dot{\mathbf{X}}) = \begin{pmatrix} \mathbf{0}_{3 \times 1} \\ F_{ES,2} \end{pmatrix} \quad (62)$$

in which  $F_{ES,2}$  is the second line of vector  $\mathbf{F}_{\text{EST}}(A)$ .

## 2.4 Implementation

### 2.4.1 Calculation of the hydrodynamic coefficients and functions

The BEM code Aquaplus [4] (respectively Achil3D [3]) was used to calculate the hydrodynamic coefficients in the frequency domain (respectively in time domain). Figure (4) shows the meshes which were used. The first one is composed of 580 flat panels. The moonpool region between the torus and float was not modelled, because it is not expected to have a strong influence on the behaviour of the system as it is thin in comparison with the diameter of the torus. A finer mesh, composed of 1320 flat panels, was also considered.

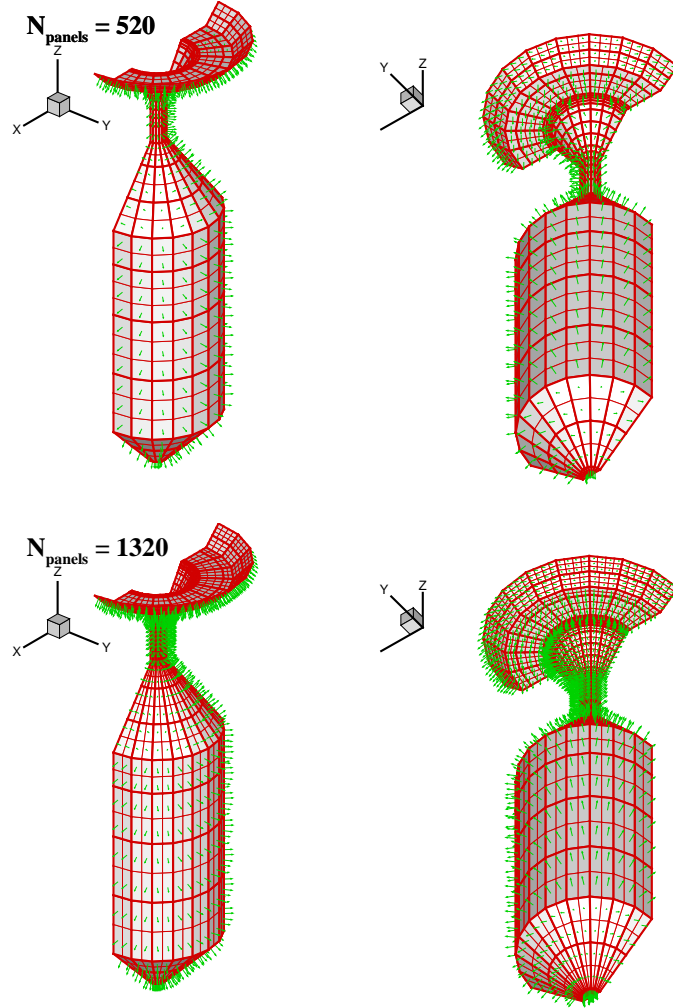


Figure 4: Meshes used for the the hydrodynamic calculations. The top one is composed of 580 flat panels. The bottom one is composed of 1320 panels.

Results of computation of added mass and radiation damping coefficients are plotted in figure (5). There are three sets of data, corresponding with three

different calculations. The solid lines have been obtained by Fourier Transform of the radiation impulse response functions calculated using Achil3D with the 580 panels composed mesh. The squares are results of the calculation with Aquaplus with the 580 panels composed mesh and the triangles are results of the calculation with Aquaplus with the fine mesh, which has 1320 panels.

One can see that the agreement between all these calculations is good. However, one can notice differences for coefficients corresponding with forces measured on body 1 (the float) when it moves (first column in figure (5)), particularly on the added mass coefficients. One can see that the agreement between the Achil3D calculation and the Aquaplus calculation is better with the fine mesh than with the coarse mesh for the added mass coefficients. This is rather surprising since the Achil3D calculation was done with the coarse mesh. However, one can notice that differences are small (about a few percents).

For the radiation damping coefficients, the agreement is found to be good in the range of the wave frequencies ([0.3, 1.] rad/s), except for coefficient  $CA33$ . For this coefficient, it seems that numerical issues in Aquaplus leads to oscillations around the Achil3D result and that increasing the number of panels does not improve the result. However, these coefficients are widely dominated by the other damping coefficients and the PTO damping forces, so it is not seen as a problem.

Wave excitation force coefficients computed in the frequency domain with Aquaplus are plotted in figure (6). One can see that there is a good agreement between the two meshes used.

Asymptotic values for the added mass coefficients  $\mu_\infty$  when  $\omega \rightarrow \infty$  were computed using Achil3D. Their values are:

$$\begin{aligned} \mu_{\infty, \text{FF}} &= \begin{pmatrix} 3.61 \cdot 10^6 & 0 & 0 & 0 & 1.57 \cdot 10^7 & 0 \\ 0 & 3.61 \cdot 10^6 & 0 & -1.57 \cdot 10^7 & 0 & 0 \\ 0 & 0 & 8.73 \cdot 10^5 & 0 & 0 & 0 \\ 0 & -1.57 \cdot 10^7 & 0 & 2.92 \cdot 10^8 & 0 & 0 \\ 1.57 \cdot 10^7 & 0 & 0 & 0 & 2.92 \cdot 10^8 & 0 \\ 0 & 0 & 0 & 0 & 0 & 0 \end{pmatrix} \\ \mu_{\infty, \text{FT}} &= \begin{pmatrix} 1.47 \cdot 10^4 & 0 & 0 & 0 & 4.74 \cdot 10^5 & 0 \\ 0 & 1.47 \cdot 10^4 & 0 & -4.74 \cdot 10^5 & 0 & 0 \\ 0 & 0 & 8.08 \cdot 10^4 & 0 & 0 & 0 \\ 0 & -3.28 \cdot 10^5 & 0 & 1.25 \cdot 10^7 & 0 & 0 \\ 3.28 \cdot 10^5 & 0 & 0 & 0 & 1.25 \cdot 10^7 & 0 \\ 0 & 0 & 0 & 0 & 0 & 0 \end{pmatrix} \\ \mu_{\infty, \text{TF}} &= \begin{pmatrix} 1.47 \cdot 10^4 & 0 & 0 & 0 & 3.27 \cdot 10^5 & 0 \\ 0 & 1.47 \cdot 10^4 & 0 & -3.27 \cdot 10^5 & 0 & 0 \\ 0 & 0 & 8.10 \cdot 10^4 & 0 & 0 & 0 \\ 0 & -4.76 \cdot 10^5 & 0 & 1.25 \cdot 10^7 & 0 & 0 \\ 4.76 \cdot 10^5 & 0 & 0 & 0 & 1.25 \cdot 10^7 & 0 \\ 0 & 0 & 0 & 0 & 0 & 0 \end{pmatrix} \\ \mu_{\infty, \text{TT}} &= \begin{pmatrix} 5.55 \cdot 10^4 & 0 & 0 & 0 & 6.12 \cdot 10^5 & 0 \\ 0 & 5.55 \cdot 10^4 & 0 & -6.12 \cdot 10^5 & 0 & 0 \\ 0 & 0 & 6.95 \cdot 10^5 & 0 & 0 & 0 \\ 0 & -6.12 \cdot 10^5 & 0 & 1.23 \cdot 10^7 & 0 & 0 \\ 6.11 \cdot 10^5 & 0 & 0 & 0 & 1.23 \cdot 10^7 & 0 \\ 0 & 0 & 0 & 0 & 0 & 0 \end{pmatrix} \end{aligned}$$

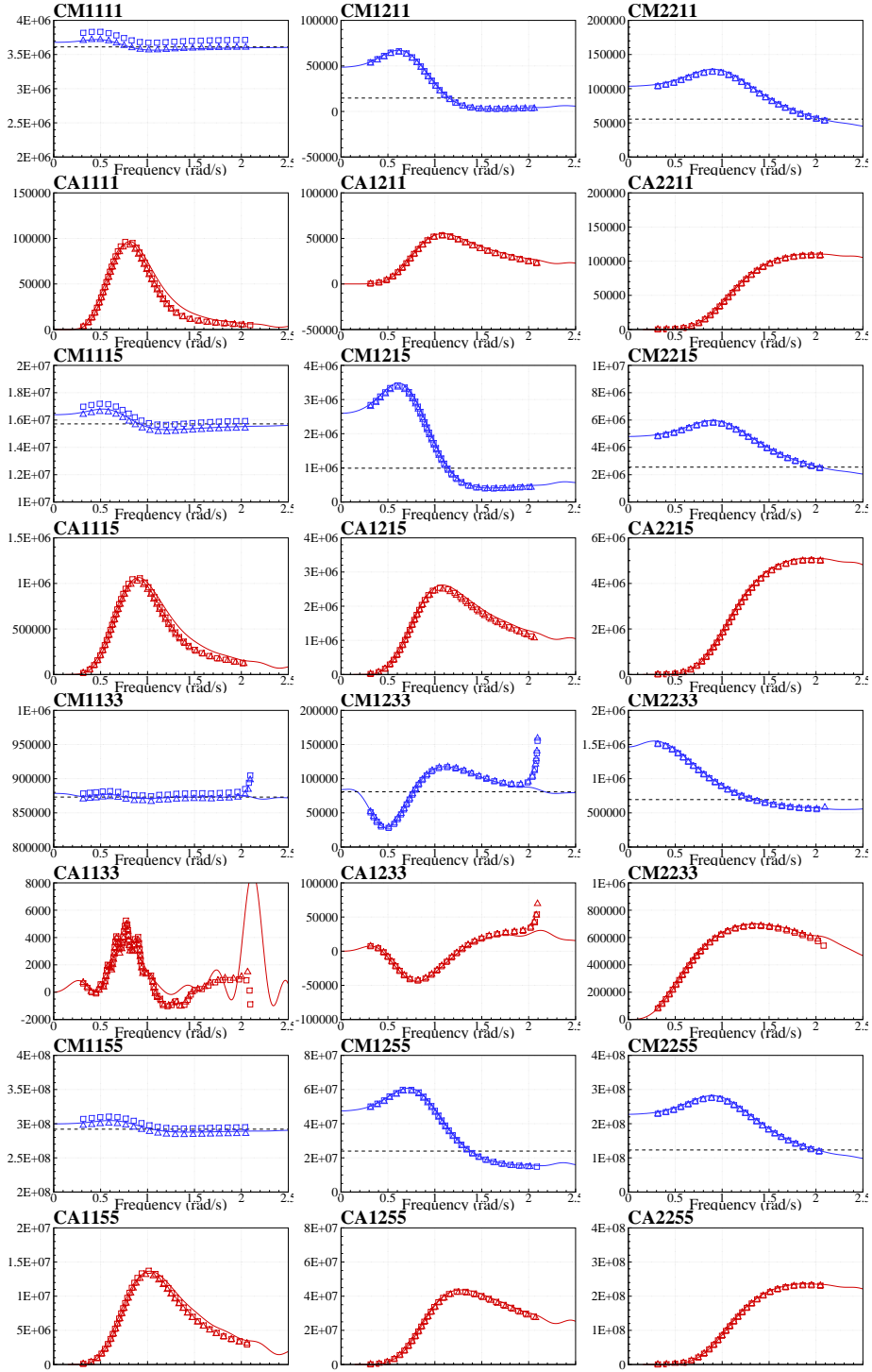


Figure 5: Hydrodynamic coefficients of the radiation force in frequency domain, computed with Aquaplus and Achil3D. Index  $cdij$  means force measured on axis  $i$  of body  $c$  associated with a motion of body  $d$  along axis  $j$ . 1 stands for surge motion or force on the  $x$  axis, 3 for heave motion or force on the vertical axis and 5 for pitch motion or moment force along the  $y$  axis.

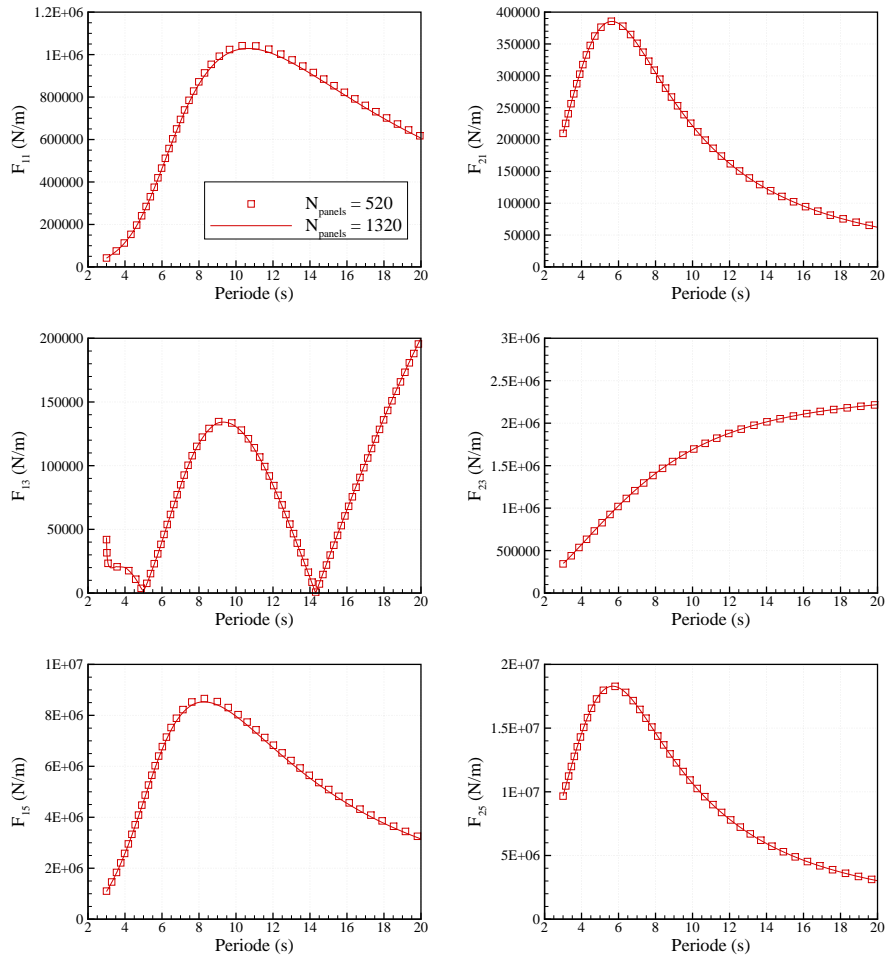


Figure 6: Wave excitation force coefficient in frequency domain computed with Aquaplus. Index  $ci$  means force measured on axis  $i$  of body  $c$ .

According to these results, in the following, the coarse mesh was used in time domain and the fine mesh in frequency domain.

#### 2.4.2 Estimation of viscous damping coefficients

- **Viscous forces on the torus:** The surge motion of the torus can be large or small depending on the mooring system. Since the mooring is supposed to be slack, one can expect large amplitude of the fluid motion relatively to the torus, typically of the order of magnitude of a few torus diameter. This leads to values of the Keulegan-Carpenter number in the range [6, 12].

From figure (16), one can see that the heave motion of the torus can possibly be up to 2 to 3 times the wave amplitude. In a wave of amplitude 1 meter, this means a Keulegan-Carpenter number about 6 – 12, because the draft of the torus is only 2 m.

Hence, according to [2], the viscous damping coefficients should be something between 0.5 and 1. In this study, they were chosen equal to  $C_{x,T} = C_{z,T} = 1$ .

According to the same author, chapter 5, page 224, the pitch damping coefficient is taken equal to 0.1.

- **Viscous forces on the float:** For the float, the Keulegan-Carpenter number for the surge motion will be even larger than for the torus, because the diameter of the float is smaller than the torus. Hence, whatever the depth,  $C_{x,F}$  was chosen equal to 0.5. However, for the heave motion, the Keulegan-Carpenter is as low as 0.5, because the draft of the float is large. Hence,  $C_{z,F}$  was taken equal to 1.

Practically, the integral in equation (35) was replaced by a sum of discrete contributions of cylinders of finite height, evaluated at different heights along the vertical axis of the float.

$$\int_{-D}^0 C_{x,F}(z) D_{x,F}(z) \left( \vec{V}_x(z) - \vec{V}_{0,x}(z) \right) \left\| \vec{V}(z) - \vec{V}_0(z) \right\| dz \simeq \quad (63)$$

$$\sum_{i=1}^N 0.5 A_i \left( \vec{V}_x(z_i) - \vec{V}_{0,x}(z_i) \right) \left\| \vec{V}(z_i) - \vec{V}_0(z_i) \right\| \quad (64)$$

Table (4) shows the parameters which were used in this last equation.

#### 2.4.3 W2W models

Based on equations (47) and (58), two numerical models were derived: one in the frequency domain and the other one in the time domain. They were implemented in Fortran90. The point with implementing separately a frequency domain model and a time domain model is that it allows to verify the implementations by comparing their results in regular waves of small amplitude. It has been found to be very useful for debugging.

i	$z_i$ (m)	$A_i$ ( $\text{m}^2$ )
1	-2	21
2	-9.5	5
3	-16	72
4	-24	112
5	-32	112
6	-38	112
7	-47	54

Table 4: Parameters used for the discretisation of the viscous forces on the float

### 3 Simulation results and energy assessment

When they are not explicitly specified, the parameters which were used in all the simulations presented here are the ones given in table (1.1).

#### 3.1 Verification

If PTO parameters are set to large values, the whole system behaves as one single body, whose natural period in heave is given by:

$$\omega_0 = \sqrt{\frac{K_{H33,F} + K_{H33,T}}{m + M + C_{M33,FF}(\omega_0) + C_{M33,FT}(\omega_0) + C_{M33,TF}(\omega_0) + C_{M33,TT}(\omega_0)}} \quad (65)$$

After a few iterations, one can get  $\omega_0 = 0.61$  rad/s from this last equation. The RAO in heave of the locked system (PTO coefficients set equal to  $10^{10}$ ) was calculated with the frequency domain model. Results are plotted in figure (7). One can see that the peak frequency matches the one calculated above.

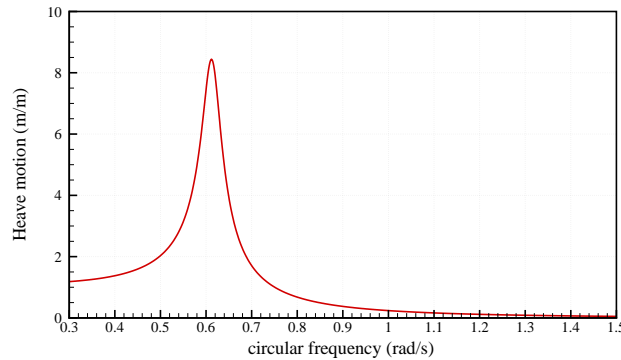


Figure 7: Heave motion of the system with large PTO coefficients ( $10^{10}$ ). Natural frequency appears to be about 0.61 rad/s

Figure (8) shows a decay test in heave (initial position is  $z_G = 1$  m) calculated with the time domain model. The PTO parameters are set to large

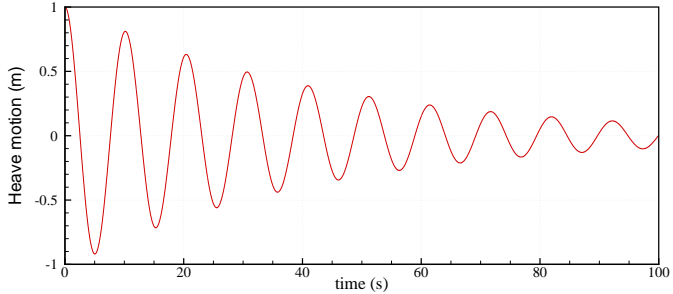


Figure 8: Decay test of the heave motion. Initial position is  $z_G = 1$  m,  $Z = 0$  m. The PTO parameters are set to  $10^8$ . Viscous damping is set to 0.

values ( $10^8$ ) in order to make the system behave like a single body. The viscous damping was set equal to 0.

The period of the response is equal to about 10.2 seconds, which matches with the natural period calculated with equation (65).

In figure (9), we plotted a comparison of the RAOs of the system, calculated with the frequency domain model and with the time domain model. The PTO parameters are set to  $B_{PTO} = 8.10^3$  kN/m.s and  $K_{PTO} = 0$ . Viscous damping was set equal to 0, and additional linear damping was added on the surge ( $10^3$  kN/m.s) and pitch ( $10^5$  kN/rad.s) modes of motion to get dissipation of the transients (otherwise, they are very long to dissipate because the natural frequencies of these modes is very low and there is very little radiation damping for these low frequencies).

In the time domain model, the calculation of the memory term is made through numerical integration. For this last model, what is plotted is the maximum of the motion over the simulation (600s), from which the transients have been removed.

One can see that the agreement between the two models is very good, which cross-validates the two implementations for the resolution of the equation of motion.

Figure (10) and (11) shows decay tests of the system in surge and pitch computed with the time domain model. As well as simulation results with nominal viscous damping (with parameters given in the previous sections), simulation with no and twice viscous damping are plotted.

One can see that without taking into account the viscous damping, the oscillations of the structure are almost not damped at all. With viscous damping, the motions are getting damped. But because of the quadratic nature of the damping, it would take long time before reaching equilibrium.

Figure (12) and (13) shows decay tests of the system in heave, for the float and for the torus. In these simulations, the PTO damping coefficients was taken equal to  $= 8.10^3$  kN/m.s.

One can see that the float behaves as an over damped oscillator, with a slow time constant. This makes sense if one recalls that the float has a large inertia and a small restoring force. The contrary is true for the torus, which has a rather small inertia and a large hydrostatic stiffness.

Here, it should be noticed that because of the large damping term associated

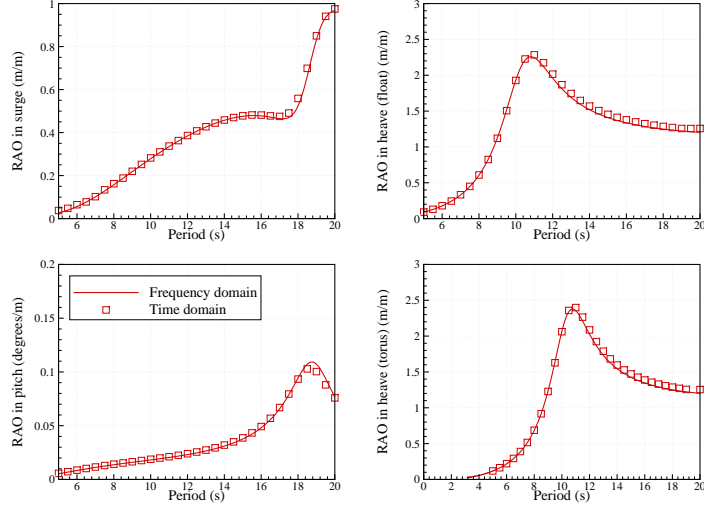


Figure 9: Comparison of RAOs calculated with the frequency domain model (red solid line) and with the time domain model (red square). The PTO parameters are set to  $B_{PTO} = 8.10^3$  kN/m.s and  $K_{PTO} = 8.10^6$ .

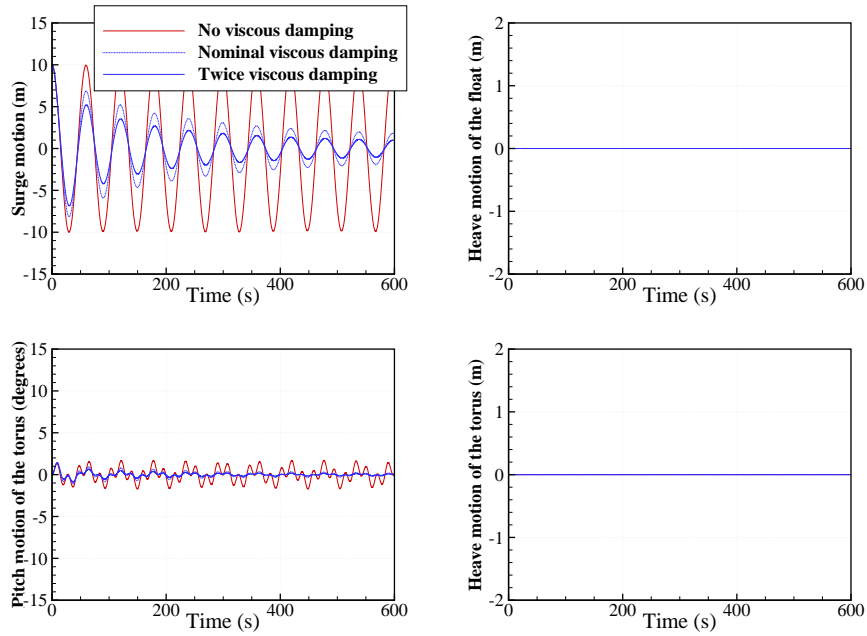


Figure 10: Decay tests in surge. The initial surge is 10 m.

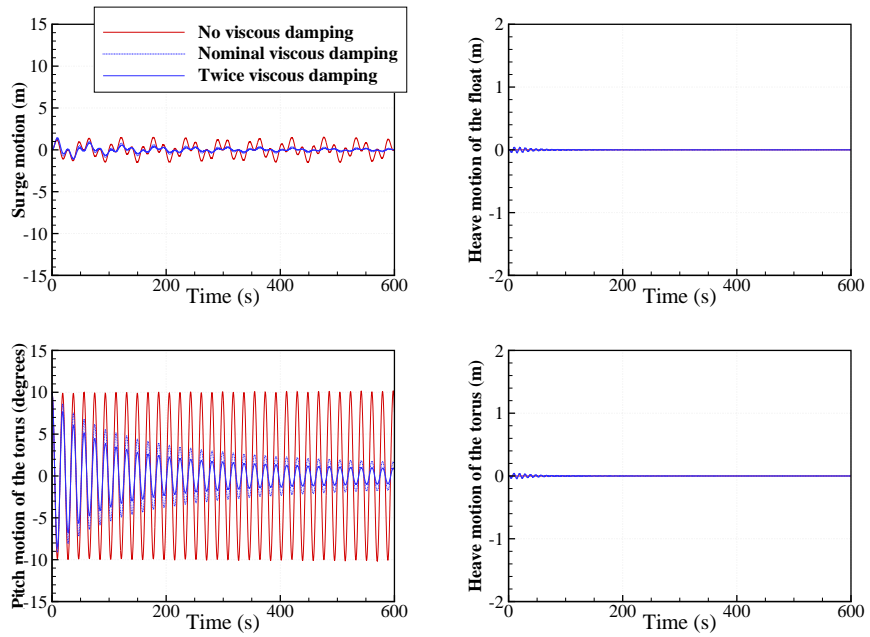


Figure 11: Decay tests in pitch. The initial pitch is 10 degrees.

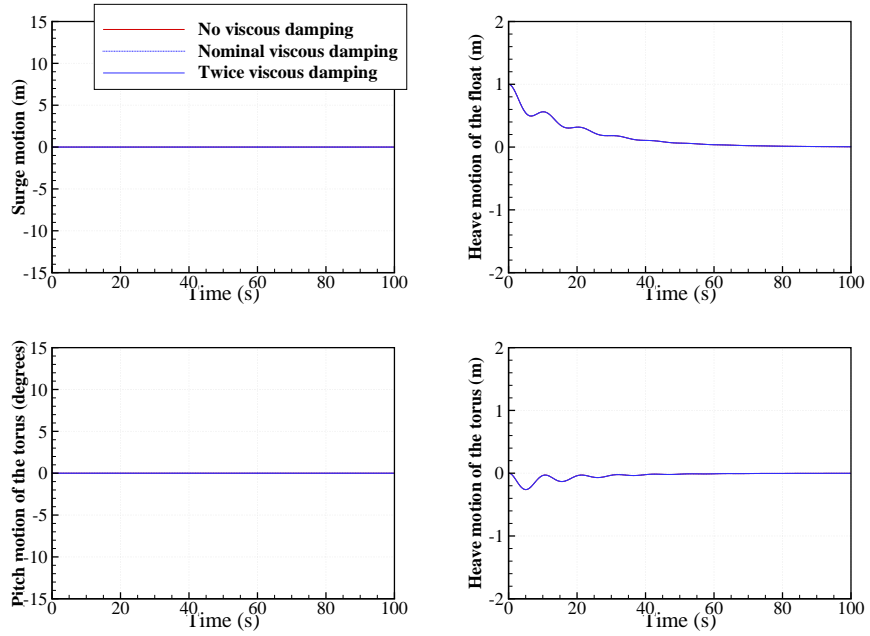


Figure 12: Decay tests in heave. The initial heave motion of the float is 1 m.

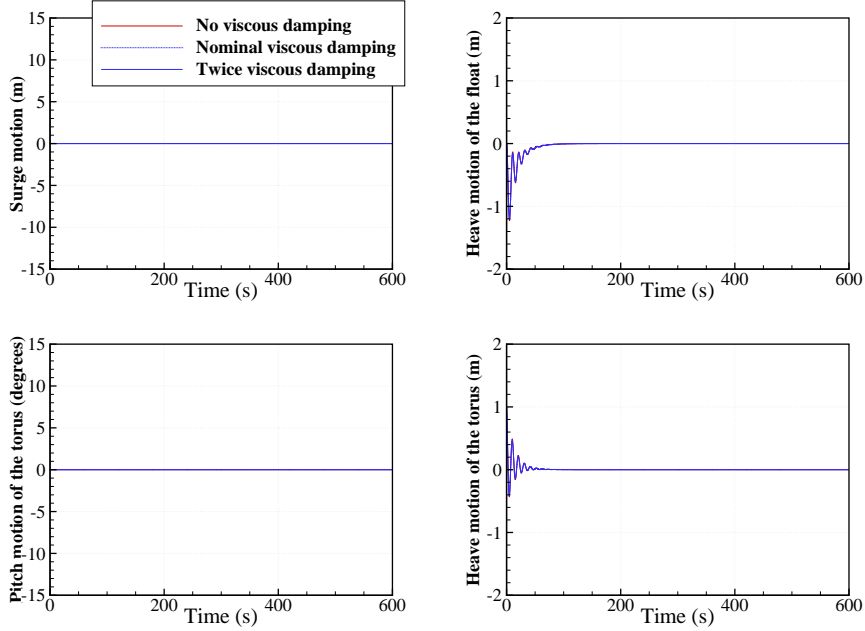


Figure 13: Decay tests in heave. The initial heave motion of the torus is 1 m.

with the PTO force, changing the intensity of the viscous damping terms does not affect the response of the system. Hence, the sensitivity of the results to the viscous damping model is very small.

Figure (14) shows a comparison of the motion of the F-2HB with and without a limit on the stroke of the relative motion between the float and the torus. The wave period is 10 seconds and the wave height 4 meters. The end stop restoring coefficient is set equal to  $2.10^8$  N/m. As the aim here is to verify that the implementation of the end stops model is correct, the stroke limit was set to a small value:  $\pm 0.5$ m.

On the bottom right plot, one can see that the system behaves as expected: with end stops the motion is limited to the strokes value. On the other plots, one can see how it affects the other degrees of freedom.

### 3.2 RAOs

#### 3.2.1 Maximisation of the power production (without constraints)

The floating two-body heaving converter is a two-bodies axisymmetric heaving point absorber similar to the one considered by Falnes in [5]. Then, following it, one can show that in regular waves, PTO coefficients can be selected such as they maximise the energy production. This is called optimal reactive control. Of course in this case, the PTO coefficients depend on the wave frequency.

$$\begin{aligned}
 M_{PTO} &= 0 \\
 B_{PTO} &= \Re(Z_i) \\
 K_{PTO} &= \Im(Z_i)
 \end{aligned} \tag{66}$$

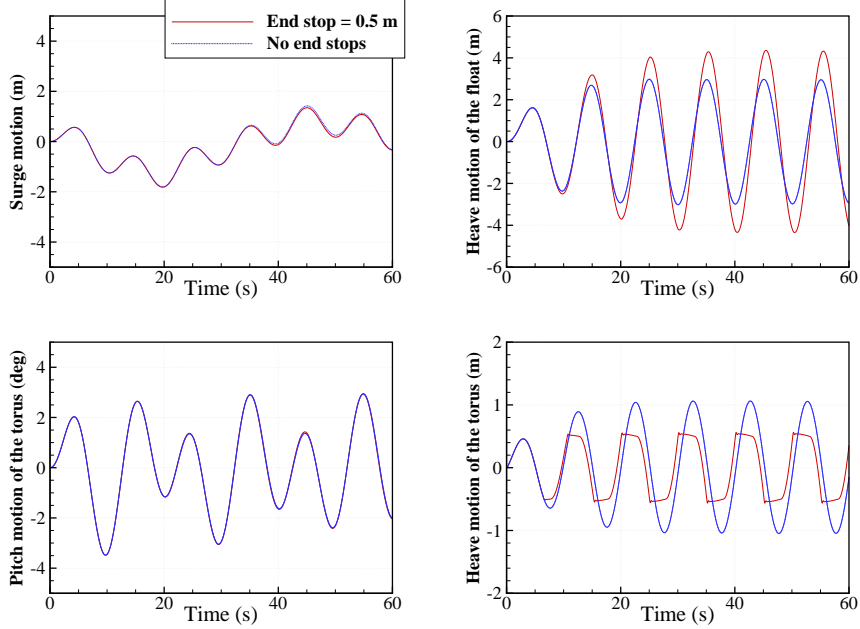


Figure 14: Simulation of the motion with and without end stops. The stroke limit is set equal to 0.5 m in this simulation.

with  $Z_i = Z_{44} - \frac{Z_{24}^2}{Z_{22}}$  is a complex number, in which:

- $Z_{22} = (m_{22} + c_{M,22}) i\omega + c_{A,22} - \frac{iK_{22}}{\omega}$
- $Z_{24} = (m_{24} + c_{M,24}) i\omega + c_{A,24} - \frac{iK_{24}}{\omega}$
- $Z_{44} = (m_{44} + c_{M,44}) i\omega + c_{A,44} - \frac{iK_{44}}{\omega}$

where the  $m_{ii}$ ,  $c_{rmM,ii}$  and  $c_{rmA,ii}$  are matrix elements from Equations (48), (50) and (52), and the  $K_{ii}$ 's are elements of the assembled stiffness matrix  $\mathbf{K}$ , Equation (56).

The instantaneous absorbed power  $P_a(t)$  may now be calculated as a function of the relative position  $Z$  between the two bodies:

$$P_a(t) = F_{\text{PTO}} \dot{Z} = B_{\text{PTO}} \dot{Z}^2 + K_{\text{PTO}} Z \dot{Z} \quad (67)$$

In regular waves with complex amplitude for the surface wave elevation equal to  $\hat{\eta}$  we may, for the linearised system, define the relative velocity response amplitude  $\hat{v}_{\text{rel}}$ , i.e.  $\dot{Z} = \Re\{\hat{v}_{\text{rel}} e^{i\omega t}\}$ . Then the time averaged absorbed power equals  $\bar{P}_a = 1/2 B_{\text{PTO}} |\hat{v}_{\text{rel}}|^2$ .

In figure (15), we have plotted the RAOs with optimal reactive control. We have also plotted the optimal PTO coefficients calculated according to equation (66), the power function  $P_a/|\hat{\eta}|^2$  and its comparison with the theoretical maximum for a heaving WEC ( $= \frac{1}{4} \rho g^3 |\hat{\eta}|^2 / \omega^3$ , see [1]).

One can see that the response amplitudes of the float in surge and pitch is small in the range of the most common wave periods ([5–15] seconds). However,

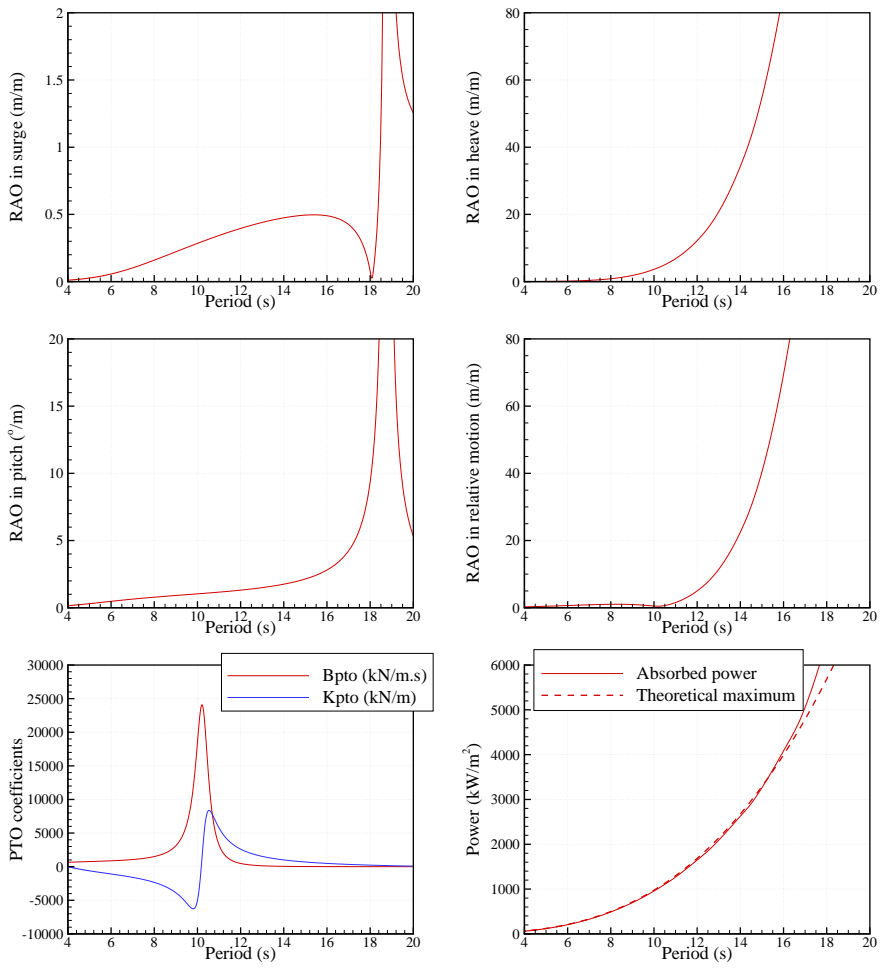


Figure 15: RAOs and power function of the motion with optimal reactive control.

there is a resonance for periods of about 19 seconds. This resonance comes from a resonance in the pitch motion.

Because of optimal reactive control, the mathematical model gives amplitudes of the motion in heave and of the relative motion that become unrealistically large at long wave periods. This means that the F-2HB will not be able to capture well these wave periods. However, one can see that for wave periods up to  $10 - 12$  seconds, the amplitude of the motion remains reasonable. Hence, the system should be able to efficiently capture waves up to these periods.

One can see on the plot showing the power function that the absorbed power matches the theoretical maximum only up to 16 seconds. For higher periods, the absorbed power predicted by the model is slightly larger than the theoretical maximum. This is due to small numerical errors. As this occurs only for very large periods, with unrealistically large amplitude of motion, this is not seen as a problem.

Unfortunately, PTO coefficients appear to be rapidly varying around the periods of interest ( $8 - 12$  seconds). It makes difficult to choose average values for these coefficients, which could have been used in irregular waves. One can say that their order of magnitudes should be about  $10^6 - 10^7$ .

### 3.2.2 Optimisation of the PTO coefficients (without constraints)

To get a better understanding of how these coefficients affect the power absorption of the F-2HB, we computed its power function with several sets of PTO coefficients. No negative value for the PTO restoring coefficient was selected, because it would mean that reactive power would need to be brought to the system during a cycle. Instead cases with  $M_{PTO} > 0$  were considered.

Table (5) summarises the set of PTO coefficients which were used. We plotted in figure (16), (18) and (19) the associated RAOs in vertical motion and power function.

Set number	$B_{PTO}$ (kN/m.s)	$K_{PTO}$ (kN/m)	$M_{PTO}$ (t)
1	500	0	0
2	1 000	0	0
3	2 000	0	0
4	4 000	0	0
5	8 000	0	0
6	12 000	0	0
7	16 000	0	0
8	4 000	1 000	0
9	4 000	2 000	0
10	4 000	3 000	0
11	4 000	4 000	0
12	4 000	0	200
13	4 000	0	400
14	4 000	0	600
15	4 000	0	800

Table 5: PTO settings

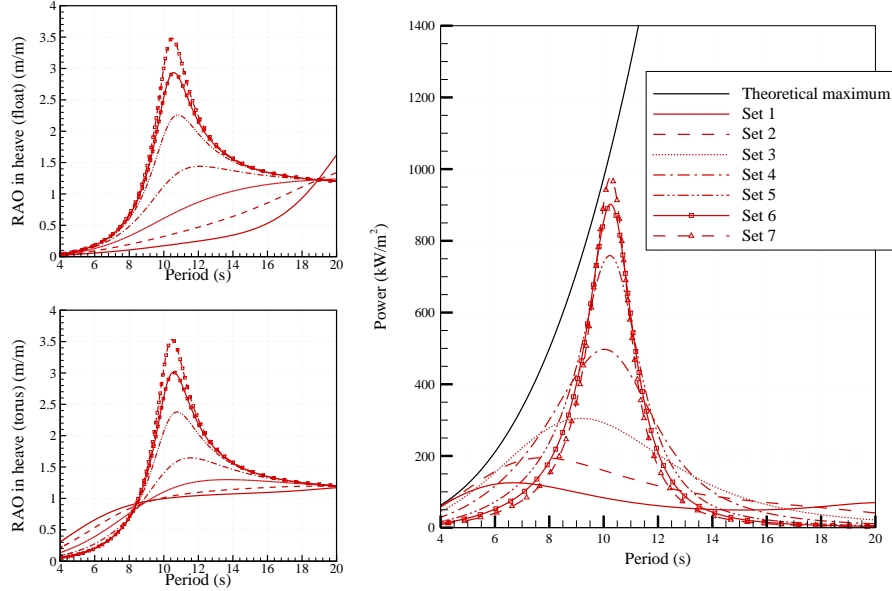


Figure 16: RAOs and power function of the motion of the F-2HB with PTO settings 1 to 7. In these settings, both  $K_{PTO}$  and  $M_{PTO}$  are equal to 0

In figure (16), we have plotted the RAOs and power function for PTO settings from 1 to 7. For these settings,  $K_{PTO}$  and  $M_{PTO}$  are equal to 0. One can see that, starting from the low values, the effect of increasing  $B_{PTO}$  is first to increase the peak of power absorption to higher wave periods and to higher levels of energy absorption. For values higher than  $8.10^3$  kN.m/s, one can see that increasing  $B_{PTO}$  does not increase the peak period anymore, but still increase the height of the peak. A maximum is reached for  $B_{PTO} \simeq 50.10^3$  kN.m/s (not plotted), from which it starts to decrease. One should notice that the power function is very peaky for such high PTO values.

One should notice also that each increase in  $B_{PTO}$  narrows the bandwidth of the system. Hence, since a WEC should be as broadband as possible, one can say that a nominal value for the  $B_{PTO}$  could be between  $4.10^3$  and  $8.10^3$  kN.m/s.

On the two other plots, one can see that the heave response of both bodies becomes large for large values of the  $B_{PTO}$  coefficient. For the float, it is not expected that large viscous effects will be induced, because this body is profiled and the Keulegan Carpenter is as low as 0.5 even with an amplitude of oscillation equal to 4 m.

However, it is another story for the torus. A KC number of 4 is reached as soon as the amplitude of the motion reached 2 meters, which is likely to happen for wave periods close to the resonance with large  $B_{PTO} = 8.10^3$  values. Moreover, the sharp corners on the torus will induce flow separation. Hence, viscous damping should have a large influence in the response of the torus. This will be investigated later in this report.

In figure (17), we plotted a comparison of the power functions we calculated in this study on a particular geometry and power functions of the Wavebob

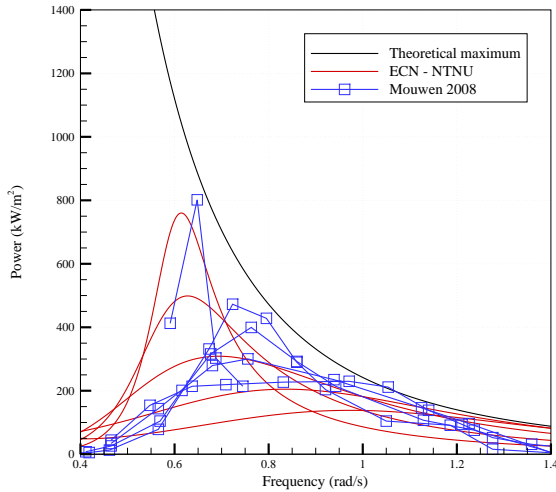


Figure 17: Comparison of power functions calculated with ECN-NTNU frequency domain model for the F-2HB, and results from Mouwen [8] for the Wavebob WEC. One can see that, except a shift in the frequencies, the trends are similar.

WEC, taken from [8]. One can see that, if one forgets for a moment the frequency shift between the two sets of plots, the power functions look like very much at each other, in trends as in levels of power absorption.

However, there is a frequency shift. The Wavebob system appears to respond at a bit higher frequencies, about 0.1 rad/s higher. This can probably be explained by the use of somewhat different geometries. However, the trends are similar which give confidence in the our modelling and understanding of this category of devices.

In figure (18), we have plotted the RAOs and power function for PTO settings from 8 to 11. One can see that an increase of the  $K_{PTO}$  increases both the peak period and the maximum of power absorption. However, it narrows the bandwidth. For large values of  $K_{PTO}$ , one can see that the peak period reaches a maximum at about 11.5 seconds.

One could say that the same effect can be obtained by increasing the damping coefficient  $B_{PTO}$ . This is partly true, but one should notice that increasing  $K_{PTO}$  allows to shift the maximum peak period to slightly higher values.

In figure (19), we have plotted the RAOs and power function for PTO settings from 12 to 15. One can see that an increase of the  $M_{PTO}$  results only in an increase of the maximum of power absorption.

From these results, one can conclude that it is probably beneficial for the F-2HB to adapt both the PTO parameters to each sea state, so they will have to be optimised in the calculation of the annual average power production.

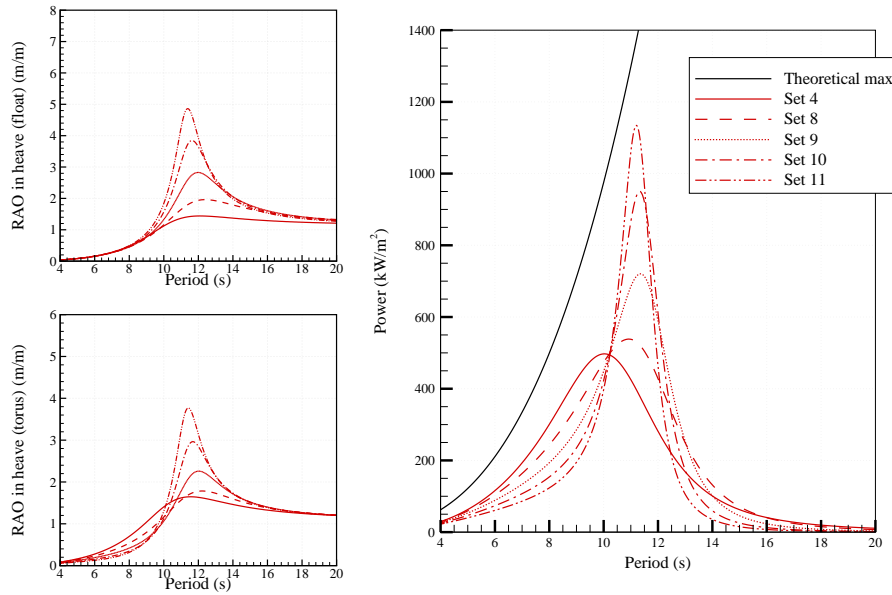


Figure 18: RAOs and power function of the motion with PTO settings 8 to 11. In these settings, the PTO damping coefficient is equal to  $4.10^3$  kN.m/s

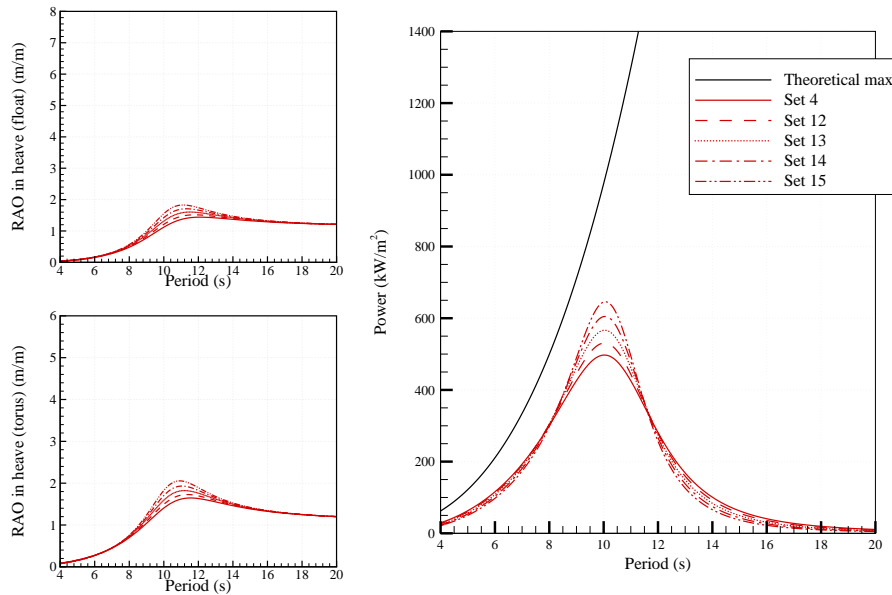


Figure 19: RAOs and power function of the motion with PTO settings 12 to 15. In these settings, the PTO damping coefficient is equal to  $4.10^3$  kN.m/s

### 3.2.3 Assessment of the influence of the viscous damping modelling

There is a rather large uncertainty on the value which should be used for the viscous damping coefficients. Hence, it is important to assess the sensitivity of the response of the system to the modelling of the viscous forces.

Figure (20) shows a comparison of the RAOs and power function of the system with different values for the viscous damping coefficients. In these calculations, the PTO damping coefficient was set equal to  $8 \cdot 10^3$  kN.m/s, and the wave amplitude was 2 meters. Other PTO coefficients were set equal to 0.

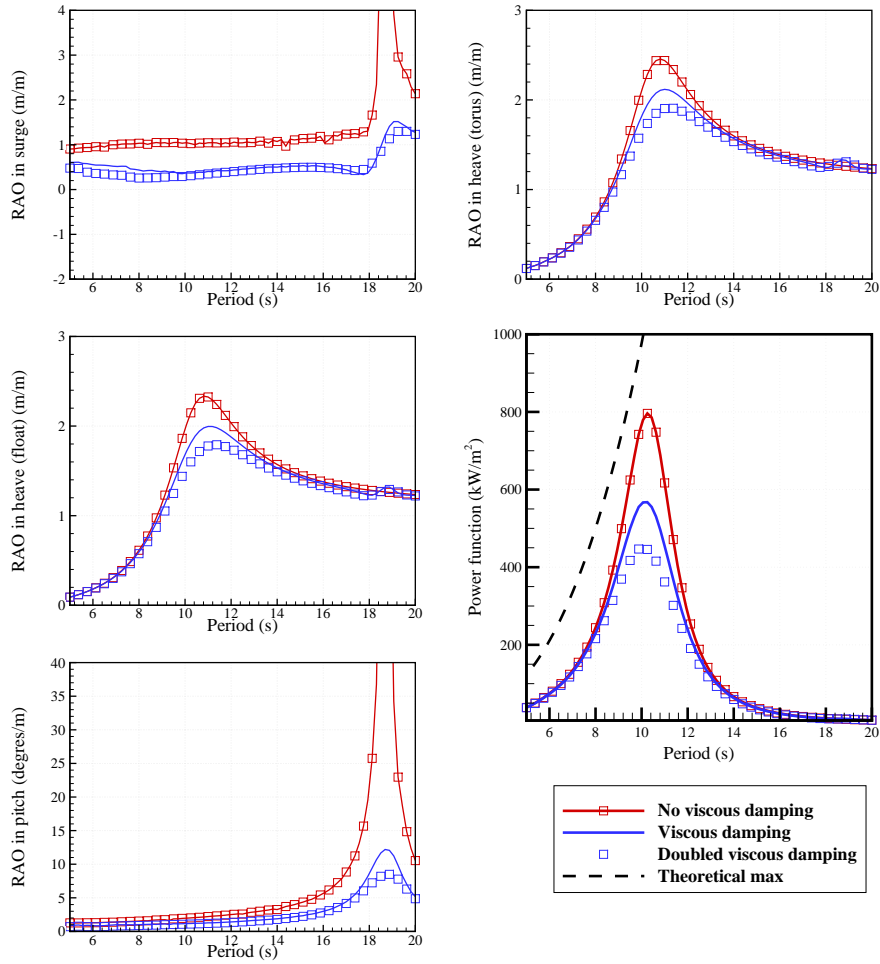


Figure 20: RAOs in surge, heave and pitch and power function of the system, calculated in regular waves with a wave amplitude of 2 m. The PTO damping coefficient is equal to  $8 \cdot 10^3$  kN.m/s.

As expected, the effect of viscous damping is strong for wave periods close to the resonance. With the set of values that we have selected as nominal, the absorbed power is reduced by 25% at resonance in comparison with the case without viscous damping. It turns to 40% if one doubles these coefficients.

Hence, one can see that the power absorption is sensitive to the modelling of the viscous damping. A parametric study should be conducted when calculating the annual energy production then.

For the sake of illustration, time domain recordings of the motion of the system have been plotted in figure (21). The wave amplitude is 2 meters and the wave period is 10 seconds, i.e the system is resonating.

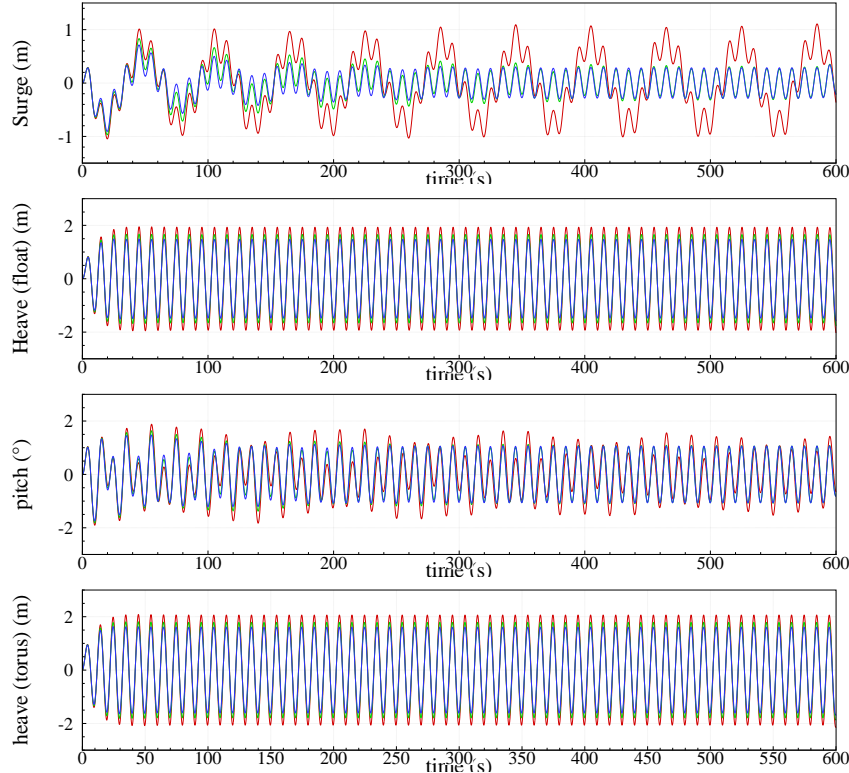


Figure 21: Simulation of the motion of the system in a regular wave, with three different values of the viscous damping coefficient. The wave period is equal to the resonance, i.e 10 s, and the wave height is 2 m. The PTO damping coefficient is equal to  $8.10^3$  kN.m/s.

Without viscous damping, one can see that steady state is not reached for the surge motion and hardly for the pitch motion, because the natural period for these motions is long. For the heave motion, one can see how the motion is decreased with the increase of the viscous damping coefficients.

### 3.2.4 Assessment of the influence of the non linearities

In order to check the level of non linearities (viscous damping and end stops) involved in the dynamic response of the system, comparison of RAOs and power function of the system have been plotted in figure (22) for several wave heights from 1 meter to 4 meters.

One can see that even for wave whose height is 4 meters, the effect of non

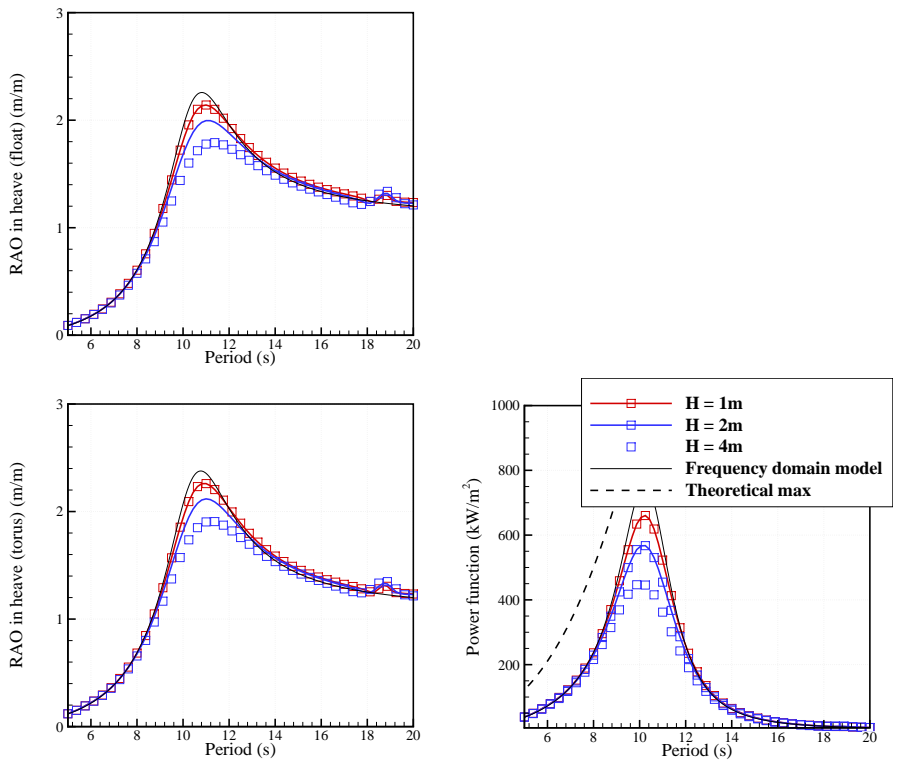


Figure 22: Comparison of the RAOs in heave and power function of the system with different wave amplitude, in regular waves. The PTO damping coefficient is equal to  $8.10^3 \text{ kN.m/s}$ .

linearities can be observed only for wave periods close to the resonance. Hence, one can conclude that non linearities are not very strong in this system when the wave period is far from the resonance. However, one can see that there is a difference between the frequency domain and the time domain model (non linear) even for small waves of amplitude 1 meter. It shows that viscous damping is strong at resonance.

### 3.2.5 Optimisation of the PTO coefficients (with constraints)

We have seen in section (3.2.1) that the value of PTO damping coefficients has an influence on the response of the system. This was shown in the frequency domain. Figure (23) shows a comparison of the power function and RAOs of the system with and without optimisation in the time domain of the  $B_{PTO}$  coefficient for each period, in order to maximise the energy absorption, as well as the optimal value of this coefficient.

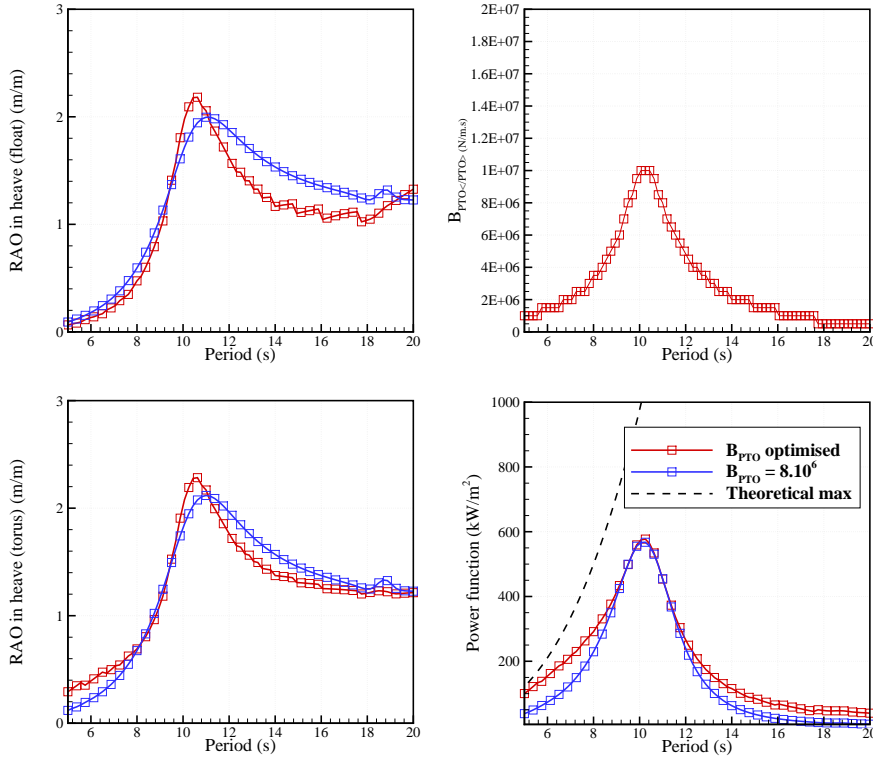


Figure 23: Comparison of the RAOs in heave and power function of the system with and without optimisation of the PTO damping coefficient. In these calculations, the wave amplitude is 2 m.

From these results, one can see that the improvement from optimising the PTO coefficient for each period is significant only for wave periods far from the resonance period. For small and high wave periods, the gain can be up to 100%, but if one refers to the power power absorption at resonance, it drops to less

than 15%.

### 3.2.6 Conclusions

From these results in regular waves, it appears that:

- The order of magnitude of absorbed power from this floating two-body heaving converter F-2HB is several hundreds of  $kW$  per square meters of wave amplitude in regular waves.
- The PTO parameters are the most relevant parameter to optimise in order to adapt the transfer functions to the wave spectrum (figure (9) and (23)). Optimisation of the PTO damping parameter improves the energy production in long wave periods and short wave periods by a factor about 2.
- The strongest non linear effect comes from the viscous damping. The modelling of this damping, via the choice of the viscous damping coefficients, has an influence on the level of energy absorption at resonance.

Hence, the estimation of the power absorption should be done with optimisation of the PTO parameters and the uncertainty on the results should be assessed by considering the effect of the viscous damping modelling.

## 3.3 Power matrix and criteria

In this section, all time domain simulations were performed in irregular waves using the JONSWAP spectrum. All quantities are derived from 1200s duration simulations, with a time step of  $0.05s$ . To remove the transient effects, the first  $15 \times T_p$  seconds of the simulations are not taken into account.

### 3.3.1 Power matrix of the F-2HB

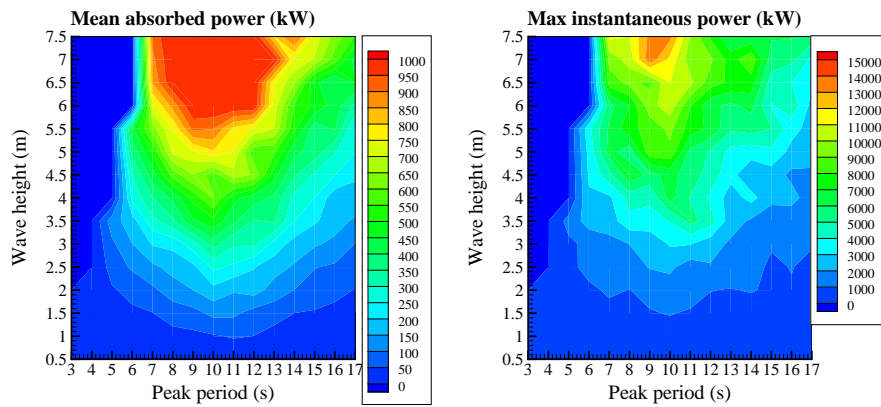


Figure 24: Power matrix of the F-2HB with optimised PTO coefficients. Left figure is the mean absorbed power and right figure is the maximum instantaneous power recorded during each simulation.

Figure (24) shows the power matrix of the F-2HB, calculated in deep water. Left figure is the mean absorbed power and right figure is the maximum recorded over the duration of the simulation for each sea state.

For each sea states, the set of PTO parameters were optimised numerically using a brute force approach. The range of optimisation of the PTO parameters are given in table (6). The maximum value for the  $M_{PTO}$  parameter can seem to be small, but it comes from the fact that the amount of transferred mass  $M_{PTO}$  has an effect on the hydrostatic stability of the device. For  $M_{PTO} > 8.10^5$  kg, the system becomes unstable in pitch and roll. Hence,  $M_{PTO}$  was optimised in the range  $[0, 6.10^5]$  kg.

	$B_{PTO}$ (kN/m.s)	$K_{PTO}$ (kN/m)	$M_{PTO}$ (t)
Minimum	500	0	0
Maximum	10 000	10 000	600

Table 6: Range of optimisation of the PTO parameters

The mean absorbed power is typically hundreds of kilowatts for typical sea states. Power absorption up to 1 megawatt is reached for the strongest sea states. As it was expected from the results in regular waves, the system exhibits the best efficiency for wave periods about 10 seconds.

The maximum absorbed power is typically about 13 times the mean power. It is very large. This might be a drawback of the system from the power electronics point of view.

Figure (25) shows the matrices of the optimised values of the PTO coefficients. One can see that they vary with the wave period but not so much with the wave height.

The optimal damping coefficient reaches a maximum of  $B_{PTO} = 8000$  kN/m.s at resonance (10-11 seconds) for small wave heights. It decreases rather rapidly as the wave peak period decreases (the optimal value is only 2000 kN/m.s as soon as the wave peak period is smaller than 8 seconds.) For larger periods, it is about 2000 kN/m.s.

Surprisingly, the optimal damping value decreases with the wave height. This effect is particularly clear at resonance. This was also reported in the study of the small bottom-referenced heaving buoy. The reason, still unclear, is probably related with the effect of quadratic viscous damping.

As one could have expected from figure (9), when the wave peak period is smaller than the resonance, optimal  $M_{PTO}$  is larger than 0. One can see that it reaches its maximum limit for wave periods between 6 and 10 seconds. For wave periods larger than the resonance, it is the turn of  $K_{PTO}$  to become non zero and to take its upper limit.

Figure (26) shows matrices of the RMS of the motion in surge, heave for the float and torus, and pitch.

One can see that the RMS in surge and pitch increase with the wave period and the wave height. However, they appear to be small, even in strong sea states.

As soon as the wave period is larger than 10 seconds, the significant heave motion of both the float and the torus seems to be almost independent of the wave period. One could say that it is about 1/4 of the significant wave height. In other words, the significant heave motion is the same order of the significant

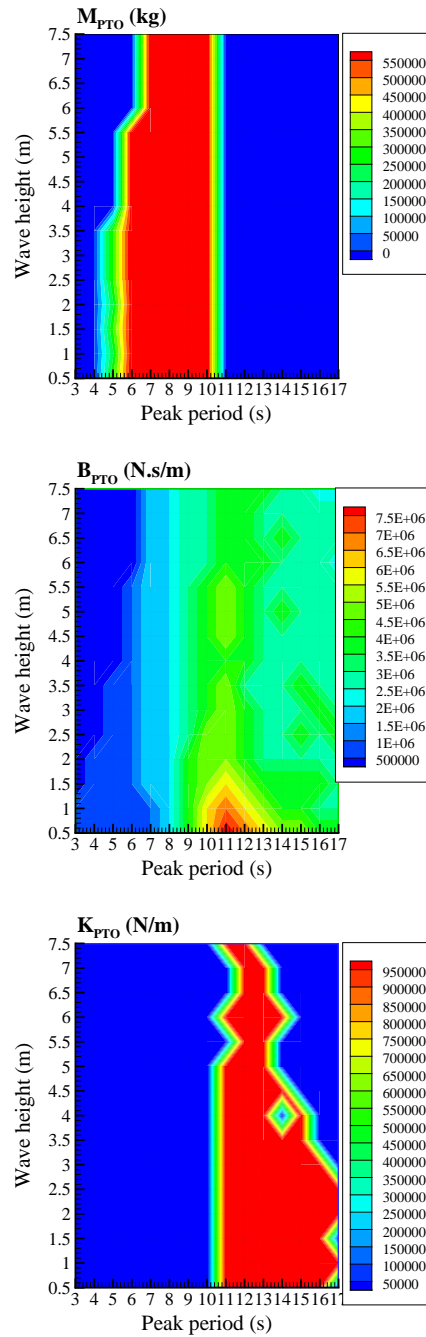


Figure 25: Optimised value of the PTO coefficients.

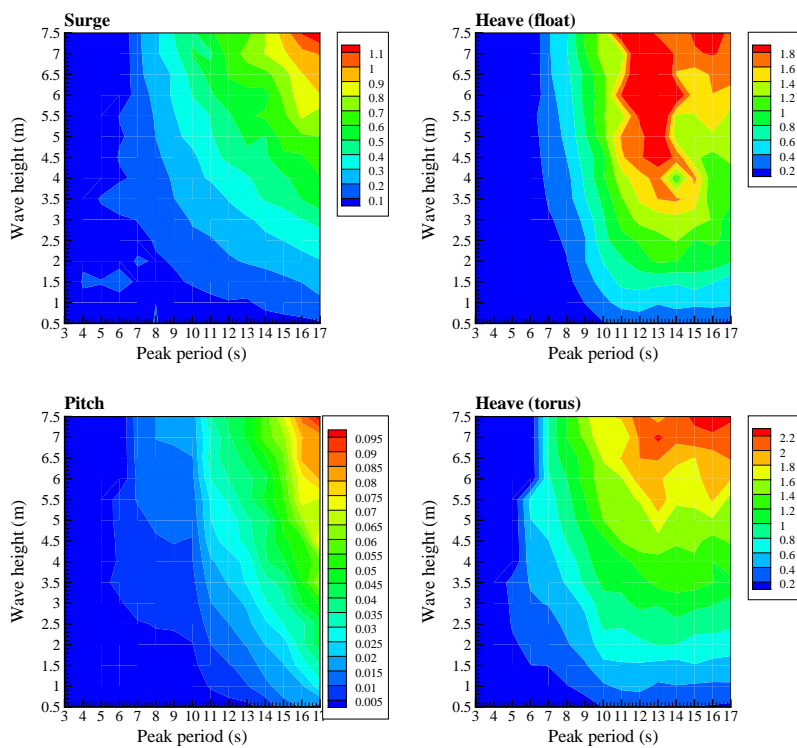


Figure 26: Matrices of the RMS of the motion of the F-2HB.

wave height. One can notice also that the heave motion of the torus seems to be a bit larger than the heave motion of the float.

By multiplying the power matrix with wave data statistics, one can calculate the annual energy absorption for each considered wave site. The values are reported in table (7) along with the other assessment criteria.

Parameter	Unit	SEM-REV	EMEC	Yeu	Lisboa	Bel-mullet	Danish study
$\gamma$		1	1	3.3	3.3	3.3	1
Wave en. trans.	[kW/m]	14.8	21.8	26.8	37.5	80.6	14.8
Mean power	[kW]	78.8	127	191	199	373	116
Capture width	[m]	5.32	5.82	7.12	5.30	4.62	7.83
$E_y / \text{Mass}$	[MWh/m <sup>3</sup> ]	0.139	0.225	0.338	0.351	0.660	0.205
$E_y / A_{\text{wet}}$	[MWh/m <sup>2</sup> ]	0.326	0.527	0.791	0.820	1.54	0.480
$E_y / \text{PTO frc.}$	[kWh/N]	1.20	1.66	2.03	2.03	2.67	1.60
$E_y / \text{Wave frc.}$	[kWh/N]	1.67	2.28	3.03	2.66	3.41	2.45

Table 7: Evaluation criteria for the F-2HB wave energy converter. The parameters are calculated based on the yearly energy delivery  $E_y$ . The mass is taken as the total mass of the ballasted installed structure, not including the moorings, and  $A_{\text{wet}}$  is the wetted surface area of the structure. By forces in the two last lines is meant significant forces, defined as the RMS value of the force over the whole year. The uncertainty of these numbers is estimated to be in the range of  $[-20, +40]\%$ , see following section.

One can see that the mean annual power resource that one can expect from this floating two-body heaving converter is about a few hundred of kilowatts. It goes from 78.8 kW for the SEM-REV site up to 373 kW for the highly energetic Belmullet site. For a typical wave resource about 30 kW/m, the typical absorbed wave power by the Seabased is about 200kW.

One can see that the typical mean capture width is about 6 meters. It is not totally independent on the site. A maximum of 7.12 meters is reached for Yeu site.

At the Danish site, the hydrodynamic efficiency <sup>1</sup> of the F-2HB is about 39%. This is higher than the best efficiency found in the results of the Bølgekraftprogram [9], in which hydrodynamic efficiencies of the considered devices were found to be 27% as a maximum.

Figure (27) shows the distribution of the absorbed power in function of the power level. The left-hand diagram shows the probability for the power production to be between two levels, and the right-hand figure shows the probability for the power to be larger than a given power level. It has been calculated with the wave statistics of the Yeu site. One can see the absorbed wave power is larger than the mean power only 40% of the year.

### 3.3.2 Assessment of the uncertainties

#### Viscous losses

To assess the uncertainty associated with the modelling of the viscous damping, the mean absorbed power of the F-2HB at Yeu site has been calculated for

---

<sup>1</sup>Defined as the ratio of the capture width divided by the diameter

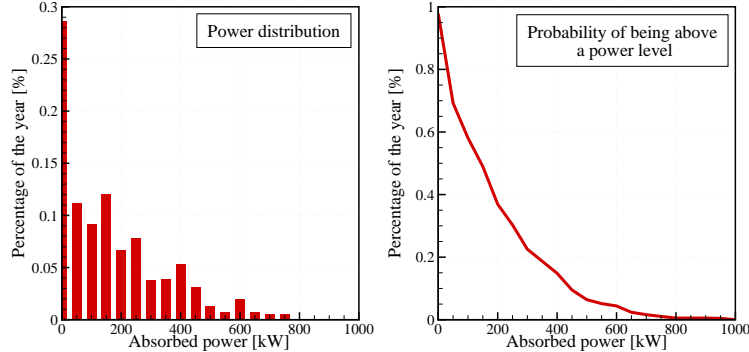


Figure 27: Distribution of the power production.

several different settings of the viscous damping coefficients. In all these calculations, the values of the PTO coefficients were optimised for each sea state. Figure (28) shows the results in function of the percentage of viscous damping coefficients with respect to the nominal values.

One can see that the modelling of the viscous damping has a large influence on the results of mean power. If viscous damping is set to 0, the mean absorbed power is 42% larger than the one with nominal values. If viscous damping is underestimated by a factor 2, then the absorbed power is over predicted by 21%.

It is worth noticing that the mean absorbed power figure obtained with the time domain model (274 kW) without viscous damping matches with the figure obtained with the frequency domain model (287 kW). This shows that the effect of the non linearities associated with the end stops is small. The small difference (5%) can be explained by numerical noise associated with non infinite duration simulations in the time domain.

### End stops

The nominal stroke of the F-2HB is uncertain. To assess this uncertainty, a calculation of the mean absorbed power at Yeu with twice the nominal stroke was performed, with all other parameters equal to their nominal values, and with optimisation of the PTO damping coefficient. The result is 178.8 kW, against 180 kW with nominal stroke. This small difference (-1%) comes from noise associated with non infinite duration simulations in the time domain. One can see that, as it was expected from previous results, the stroke is sufficiently long not to constrain the power absorption. Actually, this stroke might be reduced without much penalisation. This is investigated in the next section.

### Threshold on the mean absorbed power

In all the previous calculations, there was a threshold for the mean absorbed power at 1MW. It means that when the calculated value of the mean absorbed power is larger than 1MW, it is limited to 1MW in the power matrix. To assess the effect of this threshold on the mean power absorption, the calculations were redone at Yeu site with a 100MW threshold. The difference was found to be smaller than 3%. It is smaller than the noise coming from the time domain simulations, meaning that it does not penalise artificially the results.

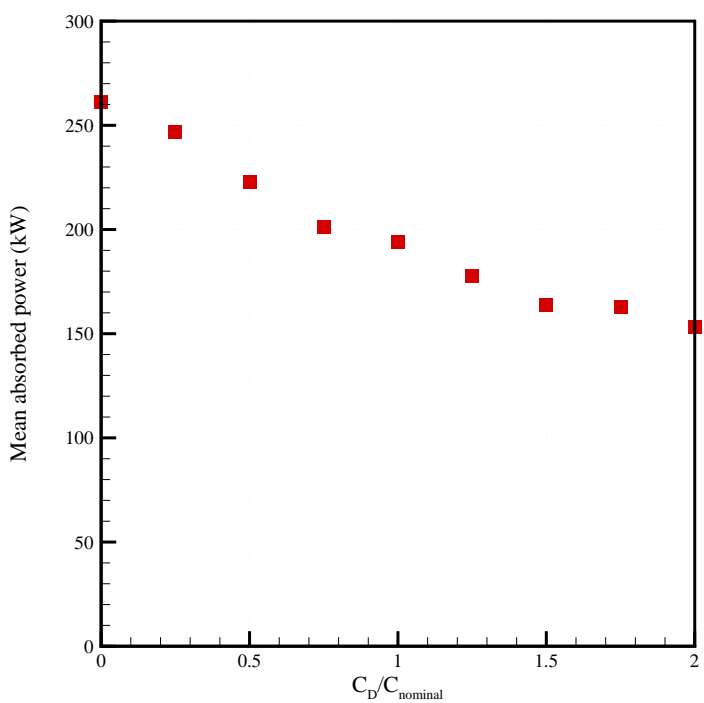


Figure 28: Mean absorbed power at Yeu in function of the percentage of viscous damping with respect to the nominal value.

$M_{PTO}$ (t)	$B_{PTO}$ (kN/m.s)	$K_{PTO}$ (kN/m)	Power (TD model) (kW)
Optimal	Optimal	Optimal	194
0	Optimal	0	176
0	$8.10^6$	0	166

Table 8: Mean absorbed power at Yeu for several PTO settings.

Threshold on the instantaneous power (kW)	Power (TD model) (kW)
Infinite	194
2000	182
1000	159

Table 9: Mean absorbed power at Yeu for several threshold of the instantaneous absorber power.

### 3.3.3 Parametric studies

#### Optimisation of PTO reactive coefficients

In table (8), the mean annual power absorption at Yeu is given for several scenarios of optimisation of PTO settings. If one considers the case without optimisation as the nominal case, one can see that optimising the PTO coefficient increases the mean energy absorption by 6% and that the full optimisation of the whole set of PTO parameters increases it by 17%.

In other words, a solution with only one set of PTO parameters for all sea states would perform only 17% less than a solution with full optimisation.

#### Threshold on the instantaneous absorbed power

In figure (24), it was seen that the instantaneous power is typically 13 times the mean power, and that it could reach very large values ( $> 10MW$ ). This is not favourable for the cost of the PTO system. So one can wonder how a threshold on the instantaneous power would affect the mean power absorption.

In table (9), one can see that limiting the instantaneous power to 2 MW (10 times the mean power) reduces the mean absorbed power by only 6%. It is small. However, a limit to 1MW reduces the power by 18%.

Hence, one can see that limiting the absorbed power to 10 times the mean absorbed power reduces the mean absorbed power by only a small amount.

#### Effect of scale

Figure (29) shows the effect of scaling on the mean power absorption of the F-2HB, at the Yeu site. This figure has been calculated using the frequency domain model. The  $B_{PTO}$  parameter is fixed for every sea state. It is taken equal to  $8.10^6$  N/m.s at scale 1, and it is scaled accordingly to Froude law for others scale. Other PTO parameters are set equal to 0.

One can see that the mean absorbed power is about linear with the displacement only for devices weighing less than 1000 t. For these small devices, the factor power to displacement is about 0.1 kW/t. As the displacement increases, the slope decreases. A mean wave power absorption of 350 kW seems to be an asymptotic limit.

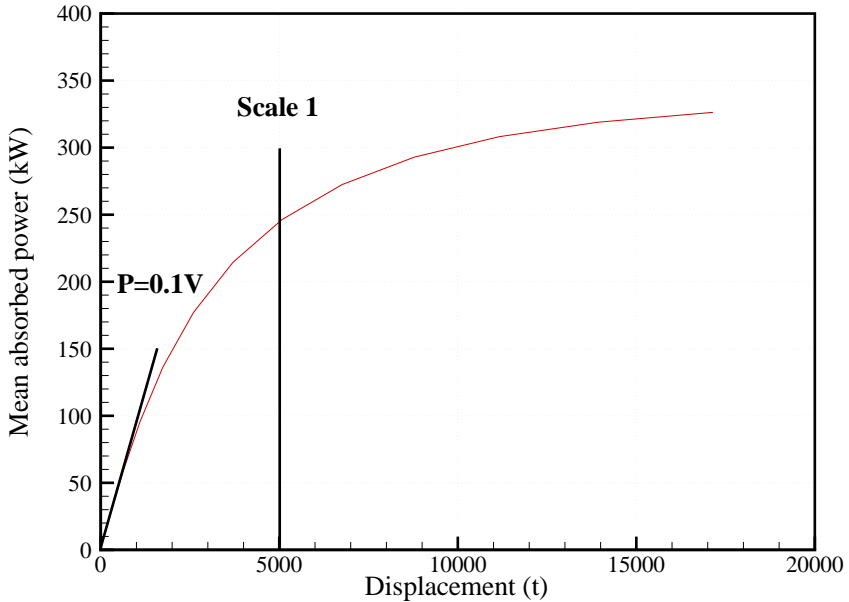


Figure 29: Influence of the scale on the mean power absorption of the F-2HB at Yeu.

One can see that a reduction of the mass by a factor 2 would lead to a reduction in power absorption by only 28%. As for the small bottom-reference heaving buoy, depending on how scales the cost, it could be worth considering a smaller version of this device.

#### Stroke

Finally, the mean absorbed power with half the nominal stroke (3 m instead of 6 m) for the relative motion was calculated. It was found that mean absorbed power was only 1% less than with the nominal stroke. It is smaller than the noise coming from the time domain simulations, meaning that a 3m stroke would be sufficient.

## 4 Conclusions and recommendations

From these results and the study, main conclusions are :

- The mean power level that one can expect from this floating two-body heaving converter is about 200 kW on a site whose wave resource is about 30 kW/m. The uncertainty is about  $[-20\%, +40\%]$ . It comes from the modelling of the viscous losses.
- Optimisation of the PTO parameters for each sea state increases the mean absorbed power by 17% in comparison with the best case without optimisation (same set of PTO parameters for all sea states).

- The output power of the F-2HB could be limited to 1MW without losing a significant amount of energy production. Limitation of the instantaneous absorbed power to 10 times the mean output power (2MW) would reduce the mean absorbed power by only a small amount (6%).
- A scaling down by a factor 0.78 of the system (displacement divided by 2) leads to a decrease of the power by 30%. On the other side, doubling the displacement of the system increases the energy absorption by only 20%. Depending on how scale the costs, it could be beneficial to the F-2HB to scale down the system in order to decrease the cost of energy.
- The stroke could be limited to 3 m without losses in the mean energy absorption.

## References

- [1] J. Falnes, 2002. Ocean waves and oscillating systems. Linear interactions including wave energy extraction. Cambridge university press.
- [2] B. Molin, 2002. Hydrodynamique des structures offshore, Guides Pratiques sur Les Ouvrages En Mer, TECHNIP Eds.
- [3] A. Babarit, Achil3D v2.0 : User Manual, Laboratoire de Mécanique des Fluides, CNRS UMR6598, Ecole Centrale de Nantes, October, 2008.
- [4] G. Delhommeau, 1997. Seakeeping Code Aquaplus
- [5] J. Falnes, 1999. Wave-energy conversion through relative motion between two single-mode oscillating bodies. Journal of Offshore Mechanics and Artic Engineeringm Vol. 121, 32–38.
- [6] <http://www.wavebob.com>. Accessed September, 9th, 2010.
- [7] <http://www.seapower.ie/news2.php>. Accessed September, 9th, 2010.
- [8] F. Mouwen, 2008. Presentation on Wavebob to Engineers Ireland. December, 9th, 2008. Downloaded from [www.engineersireland.ie](http://www.engineersireland.ie) the 10th of September 2010.
- [9] Bølgekraftprogram, Afslutningsrapport 2002. Bølgekraftudvalgets Sekretariat, RAMBØLL, Teknikerbyen 31, 2830 Virum.
- [10] J. Hals, T. Bjarte-Larsson, J. Falnes, Optimum reactive control and control by latching of a wave-absorbing semisubmerged heaving sphere. In Proc. of the 21st Offshore Mechanics and Artic Engineering Conference, pp. 1-9, 2002.

## Chapter 3

A floating three-body  
oscillating flap device  
(F-3OF) inspired by the  
Langley WEC

# Numerical estimation of energy delivery from a selection of Wave Energy Converters – Floating three-body oscillating flap device

Aurélien Babarit<sup>1</sup>, Jørgen Hals<sup>2</sup>

<sup>1</sup>Laboratoire de Mécanique des Fluides - CNRS UMR6598

Ecole Centrale de Nantes, 1 rue de la Noe, 44300 Nantes, France

<sup>2</sup>Centre for Ships and Ocean Structures

Norges teknisk-naturvitenskapelige universitet, Otto Nielsens V. 10, 7491 Trondheim, Norway

23 May 2011

## Summary

This document reports the study of a wave energy converter inspired by the Langlee device in the frame of the project “Numerical estimation of energy production from a selection of Wave Energy Converters”. It contains a mathematical model and simulation results for the study of this floating three-body oscillating flap device, which here will be abbreviated F-3OF device.

Results of the study are the following criteria:

- The annual mean power.
- The yearly energy output / displacement.
- The yearly energy output / wetted surface.
- The power per unit of significant PTO force.
- The power per unit of excitation force
- The duration curves.

These criteria were estimated using the mathematical model described in this report. Results are given in the following table and in figure (1). The main conclusions from the study are :

- The mean power level that one can expect from the FOF WEC is about 130 kW on a site whose wave resource is about 25 kW/m. The uncertainty is about [−25 %, +30 %], and comes mainly from the modelling of the viscous losses.
- A stiffer mooring in surge could significantly improve the energy absorption. In case the surge motion to be ideally restrained, the increase of energy absorption could be higher than 60 %.

- The output power of the FOF could be limited to 500 kW with only a small decrease in energy delivery. Limitation of the instantaneous absorbed power to 20 times the mean output power (1 MW) would not significantly reduce the mean absorbed power.

Parameter	Unit	SEM-REV	EMEC	Yeu	Lisboa	Bel-mullet	Danish study
$\gamma$		1	1	3.3	3.3	3.3	1
$J$	[kW/m]	14.8	21.8	26.8	37.5	80.6	14.8
Mean power	[kW]	52.3	112	131	104	145	112
Capture width	[m]	3.5	5.1	4.9	2.8	1.8	7.6
$E_y / \text{Mass}$	[MWh/m <sup>3</sup> ]	0.32	0.69	0.79	0.65	0.90	0.685
$E_y / A_{\text{wet}}$	[MWh/m <sup>2</sup> ]	0.21	0.46	0.51	0.42	0.59	0.453
$E_y / F_{\text{PTO}}^{\text{RMS}}$	[kWh/N]	1.09	1.43	1.64	1.55	1.53	1.25
$E_y / F_{\text{wave}}^{\text{RMS}}$	[kWh/N]	1.04	1.50	1.58	1.39	1.42	1.49

Table 1: Evaluation criteria for the FOF WEC for chosen sites having mean annual wave energy transport  $J$ , and where sea states are synthesized with a spectrum peakedness factor  $\gamma$ . The parameters are calculated based on the yearly energy delivery  $E_y$ . The mass is taken as the total mass of the ballasted installed structure, not including the moorings, and  $A_{\text{wet}}$  is the wetted surface area of the structure. Significant PTO force  $F_{\text{PTO}}^{\text{RMS}}$  and significant wave force  $F_{\text{wave}}^{\text{RMS}}$  are taken as the yearly RMS values. The uncertainty of  $E_y$  is estimated to  $[-25, 30]\%$ .

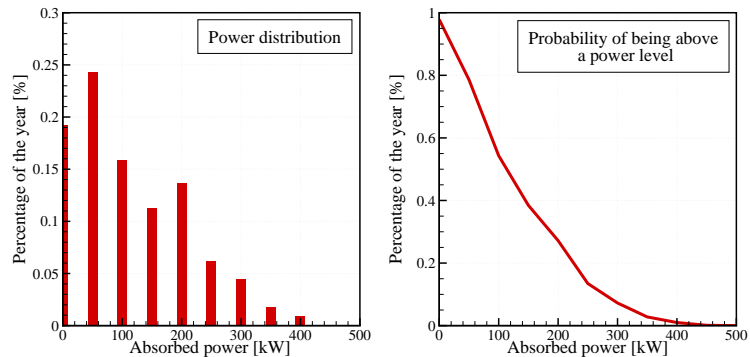


Figure 1: Distribution of the power production on a typical 25 kW/m wave site.

# Contents

<b>1 System description - The F-3OF wave energy converter</b>	<b>4</b>
1.1 Dimensions and mechanical parameters . . . . .	5
1.2 PTO and control . . . . .	5
1.3 Cost-related criteria . . . . .	6
1.3.1 Mass, displacement and wetted surface . . . . .	6
1.3.2 Significant forces . . . . .	7
<b>2 Equation of motion</b>	<b>7</b>
2.1 Kinematics . . . . .	8
2.2 Forces . . . . .	9
2.2.1 Hydrostatic forces . . . . .	9
2.2.2 Wave excitation and radiation forces . . . . .	10
2.2.3 Viscous damping forces . . . . .	11
2.2.4 PTO forces . . . . .	12
2.2.5 Mooring forces . . . . .	12
2.3 Equation of motion . . . . .	12
2.3.1 Frequency domain . . . . .	12
2.3.2 Time domain . . . . .	16
2.4 Implementation . . . . .	16
2.4.1 Calculation of the hydrodynamic coefficients and functions . . . . .	16
2.4.2 Estimation of viscous damping coefficients . . . . .	16
2.4.3 W2W models . . . . .	21
<b>3 Simulation results and energy assessment</b>	<b>21</b>
3.1 Verification tests . . . . .	21
3.2 RAOs . . . . .	24
3.2.1 Influence of the PTO coefficients . . . . .	27
3.2.2 Influence of the viscous damping on the RAOs . . . . .	31
3.2.3 Conclusions . . . . .	31
3.3 Power matrix and criteria . . . . .	33
3.3.1 Power matrix of the floating three-body oscillating flap device . . . . .	33
3.3.2 Assessment of the uncertainties . . . . .	38
3.4 Parametric studies . . . . .	39
3.4.1 Fixed platform vs Floating platform . . . . .	39
3.4.2 Threshold on the instantaneous absorbed power . . . . .	39
3.4.3 Threshold on the mean absorbed power . . . . .	40
3.4.4 Effect of scale . . . . .	40
<b>4 Conclusions and recommendations</b>	<b>41</b>

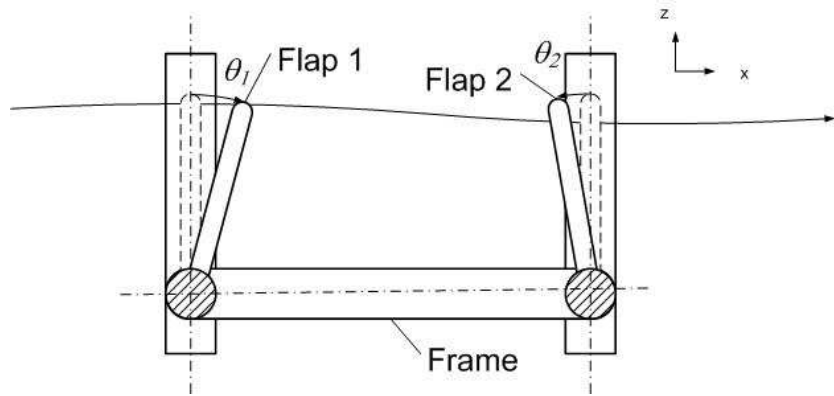


Figure 2: Sketch of the floating three-body oscillating flap device, which is inspired by the Langlee WEC.

## 1 System description - The F-3OF wave energy converter

The Langlee is a wave-energy converter operating in the pitch mode. It is composed of four hinged flaps, which are all connected to the same floating frame. Via a power take-off system (PTO), the relative motion between each flap and the main frame is converted into useful energy. Figure (3) shows an artist's view of a full scale Langlee WEC.



Figure 3: Picture of the Langlee Wave Energy Converter.

The Langlee WEC was the inspiration for the floating oscillating flaps device considered in this study. The device is sketched in figure (2). Flaps facing the waves are numbered with odd numbers (1-3) and flaps in the rear with even numbers.

In this picture, one can see that surface piercing flaps were considered whereas in the Langlee WEC they are completely submerged. Full submergence is expected to induce large energy losses due to massive vortex shedding, which is not good for the energy absorption. That's why they were chosen as surface-piercing in this study.

## 1.1 Dimensions and mechanical parameters

Dimensions of the system considered in this study were taken as similar as possible as the ones of the Langley WEC. Dimensions of the Langley WEC were obtained from [9] and from pictures and data found on the Internet [8]. In [9], wave tank experiments on a model scale are reported. There, the width of the model was equal to 1.25 m, and results are given at full scale for three scale ratios: 1:20, 1:30, 1:40, corresponding to full-scale widths of 25, 37.5 and 50 m. In this study, the smaller size was considered, i.e 25 m.

Figure (4) shows the dimensions which were used. From these dimensions, it has been possible to make estimations of the mechanical parameters of the system, assuming that the masses of each component is equal to its own displacement, and that all the masses are distributed on the surface. The geometric and dynamic parameters are summarised in table (2). One should notice that some of these estimates are rough, such as the inertia coefficients.

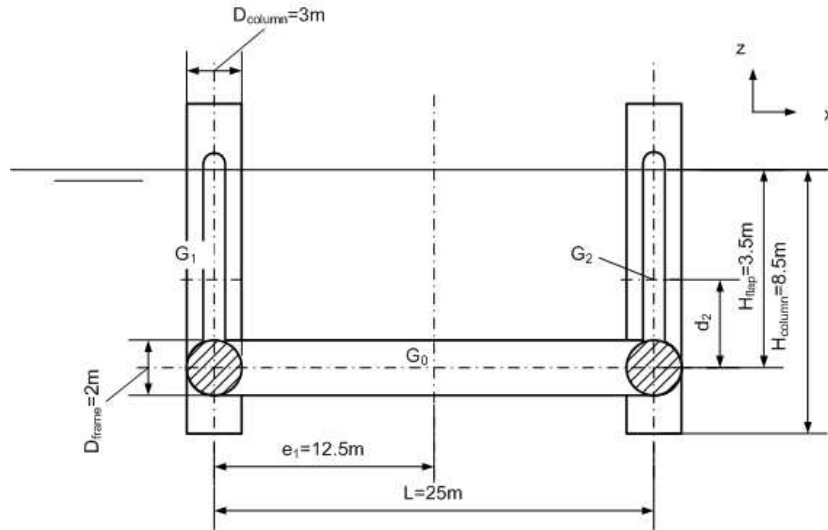


Figure 4: Notations and dimensions.

## 1.2 PTO and control

According to Langley's website [8], the power take-off system (PTO) is hydraulic. In this study, it is assumed that the PTO is controlled to behave like an ideal linear damper and spring system, with forces proportional to the relative velocity and relative motion, respectively.

Let  $B_{PTO}$  and  $K_{PTO}$  be the damping and restoring coefficients, respectively of the PTO system. Usually,  $K_{PTO}$  is set to non-zero values to achieve tuning of the system response to the current sea state. Positive  $K_{PTO}$  can be achieved by including a simple physical spring in the PTO system. Therefore, it can be seen as a practical option. Negative  $K_{PTO}$  values are much more difficult to achieve. One would have to use an active component. As the power flowing through the machinery will be out of phase with the velocity, i.e. there will be reactive machinery power, the machinery will have to work partly as as

Property	Value	Unit
<b>Flaps</b>		
Width	9.5	m
Draught	8.5	m
Thickness	2	m
Displacement	185	$\text{m}^3$
Wetted surface	230	$\text{m}^2$
Centre of mass	3.5	above hinge
Moment of inertia $I_{yy}$ at CoG	1300	$\text{t.m}^2$
Moment of inertia $I_{yy}$ at hinge	3560	$\text{t.m}^2$
<b>Frame</b>		
Length	25	m
Width	25	m
Draught	12	m
Diameter of columns	3	m
Diameter of other pipes	2	m
Displacement	673	$\text{m}^3$
Wetted surface	1240	$\text{m}^2$
Centre of mass	-8.5	m below the free surface
Moment of inertia $I_{yy}$	76300	$\text{t.m}^2$

Table 2: System parameters

a generator and partly as a motor. The instantaneous reactive power may typically be typically 10 times larger than the average absorbed power [2]. All the benefit induced by adding the negative spring is likely to be lost in conversion efficiencies. Therefore it seems that negative  $K_{PTO}$  values are non-practical options unless the machinery can be run with very high efficiency. This can possibly be remedied by making the strategies more sophisticated.

More sophisticated strategies are out of the scope of this study. That is why we choose to do one set of computations assuming no spring term, and one set with PTO spring term with positive values, where the spring coefficient is optimised for each sea state.

As the floating three bodies oscillating flap device is a self-referenced system, it is not necessary that the mass of each individual component of the system (flaps, frame) balances its own displacement. Only the overall mass and displacement must be balanced. It means that the flaps can have a positive buoyancy, if it is balanced by additional mass in the frame part of the system. It will be shown later that it provides a way of tuning the natural frequency in pitch of the flaps. This parameter is denoted  $M_{PTO}$ .

### 1.3 Cost-related criteria

#### 1.3.1 Mass, displacement and wetted surface

The wetted surface and mass are two relevant costs-related criteria that can be derived for any wave energy converter.

In the case of the F-3OF device, as it is supposed to be a self-reacting, the weight of the moorings and anchors are not taken into account in the derivation

Criterion	unit	
Significant wetted surface	2160	$\text{m}^2$
Significant mass	1410	tons

Table 3: Significant wetted surface and mass of the investigated F-3OF device.

of the mass of the system. This weight is expected to be small, because the moorings should counteract only the drift forces.

The displacement of each flap is equal to 185 tons and the displacement of the frame is 670 tons. Hence, the overall mass is 1410 tons. This is what in this report will be denoted significant mass.

The wetted surface of each flap is about 890  $\text{m}^2$ . The wetted surface of the float is about 1240  $\text{m}^2$ . The total wetted surface area here is then 2160  $\text{m}^2$ . This will in this report be denoted significant wetted area.

### 1.3.2 Significant forces

The two other cost criteria considered are the significant PTO force and the significant wave force. They both have zero mean values. So, they are defined as their RMS values over the whole year.

## 2 Equation of motion

Here, the incident waves are assumed to be mono-directional and propagating in the positive  $x$  direction. The system being symmetric about the  $xOz$  plane, all motions remain in this plane. Hence

- the motion of flap 1 (respectively 2) is equal to the motion of flap 3 (4).
- the sway, roll and yaw motion of the frame is equal to 0.

Under this assumption, the degrees of freedom of the F-3OF WEC are the surge, heave and pitch motion of the frame, and the relative motion of rotation of flaps 1 and 2.

Let  $G$  be the gravity centre of the frame. Let  $x_G$  and  $z_G$  be the surge and heave motion of the frame and  $\theta$  be the pitch motion. At equilibrium, it is assumed that  $G$  and the origin of the Cartesian reference frame  $O$  are the same.

Let  $G_i$  be the gravity centre of the flap number  $i$ . Let  $\theta_i$  be its relative pitch motion. Let  $\overrightarrow{GG_i} = e_i \vec{x} + d_i \vec{z}$  at rest.

It is assumed that all motions are of small amplitude. All second order effects are neglected and equation of motion will linearised. From our experience, taking into account non linear effects would lead to a reduction in the power absorption figures. Therefore, this assumption is not seen as a problem as the aim of this study is to derive upper estimates for energy absorption.

## 2.1 Kinematics

In the Cartesian reference frame, the position of the gravity centres of each flap is given by:

$$\overrightarrow{OG_i} = \overrightarrow{OG} + \overrightarrow{GG_i} \quad (1)$$

$$\overrightarrow{OG_i} = \begin{pmatrix} x_G + e_i \cos(\theta) + d_i \sin(\theta + \theta_i) \\ z_G - e_i \sin(\theta) + d_i \cos(\theta + \theta_i) \end{pmatrix}^0 \quad (2)$$

By time derivating this equation, one get the velocity in the fixed reference frame:

$$\overrightarrow{V}(G_i) = \begin{pmatrix} u - e_i \dot{\theta} \sin(\theta) + d_i (\dot{\theta} + \dot{\theta}_i) \cos(\theta + \theta_i) \\ w - e_i \dot{\theta} \cos(\theta) - d_i (\dot{\theta} + \dot{\theta}_i) \sin(\theta + \theta_i) \end{pmatrix}^0 \quad (3)$$

In the reference frame of the flap this becomes:

$$\overrightarrow{V}(G_i) = \begin{pmatrix} u \cos(\theta + \theta_i) - w \sin(\theta + \theta_i) + e_i \dot{\theta} \sin(\theta_i) + d_i (\dot{\theta} + \dot{\theta}_i) \\ u \sin(\theta + \theta_i) + w \cos(\theta + \theta_i) - e_i \dot{\theta} \cos(\theta_i) \end{pmatrix}^{B_i} \quad (4)$$

By time derivating once gain, one gets the acceleration. In the fixed reference frame:

$$\overrightarrow{\gamma(G_i)} = \begin{pmatrix} \dot{u} - e_i \ddot{\theta} \sin(\theta) - e_i \dot{\theta}^2 \cos(\theta) + d_i (\ddot{\theta} + \ddot{\theta}_i) \cos(\theta + \theta_i) - d_i (\dot{\theta} + \dot{\theta}_i)^2 \sin(\theta + \theta_i) \\ \dot{w} - e_i \ddot{\theta} \cos(\theta) + e_i \dot{\theta}^2 \sin(\theta) - d_i (\ddot{\theta} + \ddot{\theta}_i) \sin(\theta + \theta_i) - d_i (\dot{\theta} + \dot{\theta}_i)^2 \cos(\theta + \theta_i) \end{pmatrix}^0 \quad (5)$$

Again, in the reference frame of the flap:

$$\overrightarrow{\gamma(G_i)} = \begin{pmatrix} \dot{u} \cos(\theta + \theta_i) - \dot{w} \sin(\theta + \theta_i) + e_i \ddot{\theta} \sin(\theta_i) - e_i \dot{\theta}^2 \cos(\theta_i) + d_i (\ddot{\theta} + \ddot{\theta}_i) \\ \dot{u} \sin(\theta + \theta_i) + \dot{w} \cos(\theta + \theta_i) - e_i \ddot{\theta} \cos(\theta_i) - e_i \dot{\theta}^2 \sin(\theta_i) - d_i (\dot{\theta} + \dot{\theta}_i)^2 \end{pmatrix}^{B_i} \quad (6)$$

Let  $m'$  be the mass of each of the four flaps, and  $M'$  the mass of the frame. If  $m$  and  $M$  are the masses of displaced water by each flap and and by the frame at equilibrium, then  $(m - m') = \frac{M' - M}{2}$  is what we called  $M_{PTO}$  in section (1.2). Let  $I_{y,i}$  and  $I_y$  be the respective moments of inertia of the flap  $i$  and the frame for  $M_{PTO} = 0$ . When  $M_{PTO}$  is different from 0, these moments of inertia will be different too. In a first approximation, it is supposed that they behave such as  $I'_{y,i} \simeq \frac{m'}{m} I_{y,i}$  and  $I'_y \simeq \frac{M'}{M} I_y$ .

At point  $G$ , the dynamic moment of the frame is

$$\overrightarrow{\delta}(G) = I'_y \ddot{\theta} \overrightarrow{y}, \quad (7)$$

and of the flap  $i$  is

$$\overrightarrow{\delta_i}(G) = \overrightarrow{\delta_i}(G_i) + \overrightarrow{GG_i} \times m' \overrightarrow{\gamma(G_i)}. \quad (8)$$

$$\begin{aligned} \delta_i(G) &= I'_{y,i} (\ddot{\theta} + \ddot{\theta}_i) - m' \left( \begin{array}{c} e_i \cos \theta_i \\ e_i \sin \theta_i + d_i \end{array} \right)^{B_i} \times \\ &\quad \left( \begin{array}{c} \dot{u} \cos(\theta + \theta_i) - \dot{w} \sin(\theta + \theta_i) + e_i \ddot{\theta} \sin(\theta_i) - e_i \dot{\theta}^2 \cos(\theta_i) + d_i (\ddot{\theta} + \ddot{\theta}_i) \\ \dot{u} \sin(\theta + \theta_i) + \dot{w} \cos(\theta + \theta_i) - e_i \ddot{\theta} \cos(\theta_i) - e_i \dot{\theta}^2 \sin(\theta_i) - d_i (\dot{\theta} + \dot{\theta}_i)^2 \end{array} \right)^{B_i} \end{aligned} \quad (9)$$

$$\begin{aligned}\delta_i(G) = & [I'_{y,i} + m'(d_i^2 + e_i^2 + 2d_i e_i \sin \theta_i)]\ddot{\theta} + [I'_{y,i} + m'(d_i^2 + d_i e_i \sin \theta_i)]\dot{\theta}_i \\ & - m'[e_i \sin \theta_i - d_i \cos(\theta + \theta_i)]\dot{u} - m'[e_i \cos \theta_i + d_i \sin(\theta + \theta_i)]\dot{w} \\ & + m'd_i e_i(2\dot{\theta} + \dot{\theta}_i)\dot{\theta} \cos \theta_i\end{aligned}\quad (10)$$

Linearised, these equations read:

$$\overrightarrow{0G_i} = \begin{pmatrix} x_G + e_i + d_i(\theta + \theta_i) \\ z_G - e_i\theta + d_i \end{pmatrix}^{0,B_i} \quad (11)$$

$$\overrightarrow{V}(G_i) = \begin{pmatrix} u + d_i(\dot{\theta} + \dot{\theta}_i) \\ w - e_i\dot{\theta} \end{pmatrix}^{0,B} \quad (12)$$

$$\overrightarrow{\gamma(G_i)} = \begin{pmatrix} \dot{u} + d_i(\ddot{\theta} + \ddot{\theta}_i) \\ \dot{w} - e_i\ddot{\theta} \end{pmatrix}^{0,B} \quad (13)$$

$$\delta_i(G) = [I'_{y,i} + m'(d_i^2 + e_i^2)]\ddot{\theta} + [I'_{y,i} + m'd_i^2]\ddot{\theta}_i + m'd_i\dot{u} - m'e_i\dot{w} \quad (14)$$

## 2.2 Forces

In the following, the generalised force at point  $P$  will be written  $\mathbf{F}(P)$ . It is composed of a reaction  $\mathbf{R}$  and a torque  $\mathbf{T}$ .

Let us first define the operator:

$$\overline{\overline{GG_i}} = \begin{pmatrix} 1 & 0 & 0 \\ 0 & 1 & 0 \\ -e_i \sin \theta + d_i \cos(\theta + \theta_i) & -e_i \cos \theta - d_i \sin(\theta + \theta_i) & 1 \end{pmatrix} \quad (15)$$

It corresponds to the transport of a generalised force  $\mathbf{F}$  from the point  $G_i$  to the point  $G$ .

When one transports a force which is proportional to a first order quantity (such as velocity for example), only  $0^{th}$  order terms should be retained because of the linearisation:

$$\overline{\overline{GG_i}} = \begin{pmatrix} 1 & 0 & 0 \\ 0 & 1 & 0 \\ d_i & -e_i & 1 \end{pmatrix} \quad (16)$$

### 2.2.1 Hydrostatic forces

- **Force applying on flap  $i$ :** At the gravity centre of flap  $G_i$ , in the frame of linear theory, one can show that the effect of the generalised weight plus generalised Archimedes force reduces to a restoring force proportional to the motion of point  $G_i$  plus a constant (because the weight and the buoyancy can be different by  $M_{PTO}$ )

$$\mathbf{F}_{\mathbf{H}i}(G_i) = -\mathbf{K}_{\mathbf{H}i}\Delta\mathbf{X}_{\mathbf{G}_i} + M_{PTO}g \begin{pmatrix} 0 \\ 1 \\ 0 \end{pmatrix} \quad (17)$$

Here, only the two last diagonal coefficients of the matrix  $\mathbf{K}_{\mathbf{H}_i}$  are non zero, because the plane ( $yG_i z$ ) is a symmetry plane for the flap.

At point G, the generalised hydrostatic force is given by:

$$\mathbf{F}_{\mathbf{H}_i}(G) = -\overline{\mathbf{G}\mathbf{G}_i}\mathbf{K}_{\mathbf{H}_i}\Delta\mathbf{X}_{\mathbf{G}_i} + \overline{\mathbf{G}\mathbf{G}_i}M_{PTOG} \begin{pmatrix} 0 \\ 1 \\ 0 \end{pmatrix} \quad (18)$$

By linearising, one can show:

$$\mathbf{F}_{\mathbf{H}_i}(G) = -\overline{\mathbf{G}\mathbf{G}_i}\mathbf{K}_{\mathbf{H}_i}\overline{\mathbf{G}_i\mathbf{G}}\mathbf{X} + \overline{\mathbf{G}\mathbf{G}_i}M_{PTOG} \begin{pmatrix} 0 \\ 1 \\ 0 \end{pmatrix} \quad (19)$$

with  $\mathbf{X}$  defined by:

$$\mathbf{X} = (x_g \ z_g \ \theta \ \theta_1 \ \theta_2)^t \quad (20)$$

and operator  $\overline{\mathbf{G}_i\mathbf{G}}$  defined by:

$$\overline{\mathbf{G}_i\mathbf{G}} = \begin{pmatrix} 1 & 0 & d_i & d_i\delta_{i1} & d_i\delta_{i2} \\ 0 & 1 & -e_i & 0 & 0 \\ 0 & 0 & 1 & \delta_{i1} & \delta_{i2} \end{pmatrix} \quad (21)$$

Equation (19) can further be simplified as:

$$\mathbf{F}_{\mathbf{H}_i}(G) = -(\overline{\mathbf{G}\mathbf{G}_i}\mathbf{K}_{\mathbf{H}_i}\overline{\mathbf{G}_i\mathbf{G}} + \mathbf{K}_{\mathbf{PTO}_i})\mathbf{X} + M_{PTOG} \begin{pmatrix} 0 \\ 1 \\ -e_i \end{pmatrix} \quad (22)$$

with :

$$\mathbf{K}_{\mathbf{PTO}_i} = \begin{pmatrix} 0 & 0 & 0 & 0 & 0 \\ 0 & 0 & 0 & 0 & 0 \\ 0 & 0 & M_{PTOG}d_i & M_{PTOG}d_i\delta_{i1} & M_{PTOG}d_i\delta_{i2} \end{pmatrix} \quad (23)$$

From this last equation, one can see that increasing the buoyancy of the flaps increases the hydrostatic stability of the frame. It was expected since it corresponds to lower the vertical position of the overall gravity centre.

- **Force applying on the frame:** For the frame, it can be written:

$$\mathbf{F}_{\mathbf{H}}(G) = -\mathbf{K}_{\mathbf{H}}\mathbf{X} - M_{PTOG} \begin{pmatrix} 0 \\ 1 \\ 0 \end{pmatrix} \quad (24)$$

### 2.2.2 Wave excitation and radiation forces

- **Force applying on flap  $i$ :** At the gravity centre of the flap  $i$ , in the frame of linear theory, the hydrodynamic forces reads, in the frequency domain:

$$\mathbf{F}_{\mathbf{D}i}(G_i) = \mathbf{F}_{\mathbf{ex}i}(G_i) - \sum_{j=0}^2 \mathbf{C}_{\mathbf{M}ij} \ddot{\mathbf{X}}_{\mathbf{G}_j} - \mathbf{C}_{\mathbf{A}ij} \dot{\mathbf{X}}_{\mathbf{G}_j} \quad (25)$$

in which index 0 makes reference to the frame.

Linearised, it reads:

$$\mathbf{F}_{\mathbf{D}i}(G_i) = \mathbf{F}_{\mathbf{ex}i}(G_i) - \sum_{j=0}^2 \mathbf{C}_{\mathbf{M}ij} \overline{\mathbf{G}_j \mathbf{G}} \ddot{\mathbf{X}} - \mathbf{C}_{\mathbf{A}ij} \overline{\mathbf{G}_j \mathbf{G}} \dot{\mathbf{X}} \quad (26)$$

At point  $G$ , it is given by:

$$\mathbf{F}_{\mathbf{D}i}(G) = \overline{\mathbf{G} \mathbf{G}_i} \mathbf{F}_{\mathbf{D}i}(G_i) \quad (27)$$

which gives:

$$\mathbf{F}_{\mathbf{D}i}(G) = \overline{\mathbf{G} \mathbf{G}_i} \mathbf{F}_{\mathbf{ex}i}(A) - \overline{\mathbf{G} \mathbf{G}_i} \mathbf{C}_{\mathbf{M}ij} \overline{\mathbf{G}_j \mathbf{G}} \ddot{\mathbf{X}} - \overline{\mathbf{G} \mathbf{G}_i} \mathbf{C}_{\mathbf{A}ij} \overline{\mathbf{G}_j \mathbf{G}} \dot{\mathbf{X}} \quad (28)$$

- **Force applying on the frame:** At the gravity centre of the frame  $G$ , the hydrodynamic forces reads in the frequency domain:

$$\mathbf{F}_{\mathbf{D}}(G) = \mathbf{F}_{\mathbf{ex}}(G) - \sum_{j=0}^2 \mathbf{C}_{\mathbf{M}0j} \overline{\mathbf{G}_j \mathbf{G}} \ddot{\mathbf{X}} - \mathbf{C}_{\mathbf{A}ij} \overline{\mathbf{G}_j \mathbf{G}} \dot{\mathbf{X}} \quad (29)$$

### 2.2.3 Viscous damping forces

- **Force applying on flap  $i$ :** The viscous damping forces are modelled under the form of the Morison equation. In the general case:

$$\mathbf{F}_{\mathbf{V}i}(G) = -\frac{1}{2}\rho \int_{-D}^0 \left( \begin{array}{c} C_{x,i}(z) D_{x,i}(z) (V_x(z) - V_{0,x}(z))^{B_i} \\ C_{z,i}(z) D_{z,i}(z) \cos\theta (V_z(z) - V_{0,z}(z))^{B_i} \\ m_i \end{array} \right) \cdot \left\| \vec{V}(z) - \vec{V}_0(z) \right\| dz \quad (30)$$

with:

- $\vec{V}_0(z)$  the undisturbed flow velocity at the vertical position  $z$  along the flap  $i$ .
- $C_{x,i}(z)$  and  $C_{z,i}(z)$  are the viscous damping coefficients and  $D_{x,i}$  and  $D_{z,i}$  the characteristic dimensions along the x and z axis.
- $[m_i = (z - z_G) C_{x,i}(z) D_{x,i}(z) (V_x(z) - V_{0,x}(z))^{B_i} - e_i C_{z,i}(z) D_{z,i}(z) (V_z(z) - V_{0,z}(z))^{B_i}]$

Note that here, the force is expressed in the body reference frame.

- **Force applying on the frame:** Along the x direction, the viscous forces on the whole system will be dominated by the viscous forces on the flaps. Hence, the contribution of the frame can be neglected. Along the z axis,

it will be the sum of the contributions from each pipes from which the frame is made.

$$\begin{aligned} \mathbf{F}_V(G) = & \sum_{j=1}^N -\frac{1}{2} \rho C_z(P_j) D \begin{pmatrix} 0 \\ 1 \\ -(x(P_j) - x_G) \end{pmatrix} (V_z(P_j) - V_{0,z}(P_j))^B \\ & \cdot \left\| \vec{V}(P_j) - \vec{V}_0(P_j) \right\| \end{aligned} \quad (31)$$

Again, the force is expressed in the body reference frame.

#### 2.2.4 PTO forces

According to section (1.2), the PTO torque is modelled as a sum of two parts:

- A linear damping part proportional to the relative velocity  $\dot{\theta}_1$ , whose coefficient is  $B_{PTO}$ . This part corresponds with the energy absorption.
- A linear spring part, proportional to the relative motion  $\theta_1$ , whose coefficient  $K_{PTO}$  is supposed to be greater to 0. It can be achieved by means of controlling the PTO force, or by using a physical spring.

Hence, the PTO force applying on the flap  $i$  is:

$$\mathbf{F}_{PTOT}(G_i) = \begin{pmatrix} 0 \\ 0 \\ -B_{PTO}\dot{\theta}_i - K_{PTO}\theta_i \end{pmatrix}^0 \quad (32)$$

#### 2.2.5 Mooring forces

The moorings of the F-3OF device are supposed to be slack [8]. So, they are not supposed to have any significant impact on the dynamic response of the system. Hence, the moorings are modelled by a simple horizontal restoring force proportional to the surge motions of the float, with a small coefficient.

$$\mathbf{F}_M(G) = \begin{pmatrix} -K_M & 0 & 0 \\ 0 & 0 & 0 \\ 0 & 0 & 0 \end{pmatrix}^0 \mathbf{X} = -\mathbf{K}_M \mathbf{X} \quad (33)$$

### 2.3 Equation of motion

#### 2.3.1 Frequency domain

In the frequency domain, the viscous forces and the end stops forces are not taken into account.

By expressing Newton's law first for the system composed of the {Frame} + {Flaps} at point  $G$  and then for each system {Flap} at its hinge, one can write the equation of motion for the FOF in the frequency domain under the form:

$$(\mathbf{M} + \mathbf{C}_M) \ddot{\mathbf{X}} + (\mathbf{B}_{PTO} + \mathbf{C}_A) \dot{\mathbf{X}} + (\mathbf{K} + \mathbf{K}_{PTO}) \mathbf{X} = \mathbf{F}_{ex} \quad (34)$$

with :

$$\mathbf{M} = \begin{pmatrix} m_{11} & 0 & m_{13} & m_{14} & m_{15} \\ 0 & m_{22} & m_{23} & 0 & 0 \\ m_{31} & m_{32} & m_{33} & m_{34} & m_{35} \\ m_{41} & 0 & m_{43} & m_{44} & 0 \\ m_{51} & 0 & m_{53} & 0 & m_{55} \end{pmatrix} \quad (35)$$

where

$$\begin{aligned} m_{11} &= m_{22} = 2m + M \\ m_{31} &= m_{13} = (m - M_{PTO})(d_1 + d_2) \\ m_{32} &= m_{23} = -(m - M_{PTO})(e_1 + e_2) \\ m_{41} &= m_{14} = (m - M_{PTO})d_1 \\ m_{51} &= m_{15} = (m - M_{PTO})d_2 \\ m_{43} &= m_{34} = \frac{m - M_{PTO}}{m} I_{y,1} + (m - M_{PTO})d_1^2 \\ m_{53} &= m_{35} = \frac{m - M_{PTO}}{m} I_{y,2} + (m - M_{PTO})d_2^2 \\ m_{33} &= \frac{M + M_{PTO}}{M} I_y + \frac{m - M_{PTO}}{m} (I_{y,1} + I_{y,2}) + (m - M_{PTO})(d_1^2 + e_1^2 + d_2^2 + e_2^2) \\ m_{44} &= \frac{m - M_{PTO}}{m} I_{y,1} + (m - M_{PTO})d_1^2 \\ m_{55} &= \frac{m - M_{PTO}}{m} I_{y,2} + (m - M_{PTO})d_2^2 \end{aligned} \quad (36)$$

Furthermore, the assembled added mass matrix is composed in the following way

$$\mathbf{C}_M = \sum_{i=0}^2 \sum_{j=0}^2 \begin{pmatrix} c_{M,11} & 0 & c_{M,13} & c_{M,14} & c_{M,15} \\ 0 & c_{M,22} & c_{M,23} & 0 & 0 \\ c_{M,31} & c_{M,32} & c_{M,33} & c_{M,34} & c_{M,35} \\ c_{M,41} & 0 & c_{M,43} & c_{M,44} & c_{M,45} \\ c_{M,51} & 0 & c_{M,53} & c_{M,54} & c_{M,55} \end{pmatrix} \quad (37)$$

Here the matrix elements are

$$\begin{aligned}
c_{M,11} &= C_{M11ij} \\
c_{M,22} &= C_{M33ij} \\
c_{M,33} &= C_{M55ij} + d_j C_{M51ij} + d_i C_{M15ij} + d_j d_i C_{M11ij} + e_j e_i C_{M33ij} \\
c_{M,44} &= \delta_{i1} \delta_{j1} (C_{M55ij} + d_j C_{M51ij} + d_i C_{M15ij} + d_j d_i C_{M11ij}) \\
c_{M,55} &= \delta_{i2} \delta_{j2} (C_{M55ij} + d_j C_{M51ij} + d_i C_{M15ij} + d_j d_i C_{M11ij}) \\
c_{M,31} &= C_{M51ij} + d_i C_{M11ij} \\
c_{M,13} &= C_{M15ij} + d_j C_{M11ij} \\
c_{M,32} &= -e_i C_{M33ij} \\
c_{M,23} &= -e_j C_{M33ij} \\
c_{M,41} &= \delta_{i1} (d_1 C_{M11ij} + C_{M51ij}) \\
c_{M,14} &= \delta_{j1} (d_j C_{M11ij} + C_{M15ij}) \\
c_{M,43} &= \delta_{i1} (C_{M55ij} + d_j C_{M51ij} + d_i C_{M15ij} + d_j d_i C_{M11ij}) \\
c_{M,34} &= \delta_{j1} (C_{M55ij} + d_j C_{M51ij} + d_i C_{M15ij} + d_j d_i C_{M11ij}) \\
c_{M,51} &= \delta_{i2} (d_1 C_{M11ij} + C_{M51ij}) \\
c_{M,15} &= \delta_{j2} (d_j C_{M11ij} + C_{M15ij}) \\
c_{M,53} &= \delta_{i2} (C_{M55ij} + d_j C_{M51ij} + d_i C_{M15ij} + d_j d_i C_{M11ij}) \\
c_{M,35} &= \delta_{j2} (C_{M55ij} + d_j C_{M51ij} + d_i C_{M15ij} + d_j d_i C_{M11ij}) \\
c_{M,54} &= \delta_{i2} \delta_{j1} (C_{M55ij} + d_j C_{M51ij} + d_i C_{M15ij} + d_j d_i C_{M11ij}) \\
c_{M,45} &= \delta_{i1} \delta_{j2} (C_{M55ij} + d_j C_{M51ij} + d_i C_{M15ij} + d_j d_i C_{M11ij})
\end{aligned} \tag{38}$$

Correspondingly, the assembled radiation resistance matrix is

$$\mathbf{C}_A = \sum_{i=0}^2 \sum_{j=0}^2 \begin{pmatrix} c_{A,11} & 0 & c_{A,13} & c_{A,14} & c_{A,15} \\ 0 & c_{A,22} & c_{A,23} & 0 & 0 \\ c_{A,31} & c_{A,32} & c_{A,33} & c_{A,34} & c_{A,35} \\ c_{A,41} & 0 & c_{A,43} & c_{A,44} & c_{A,45} \\ c_{A,51} & 0 & c_{A,53} & c_{A,54} & c_{A,55} \end{pmatrix} \tag{39}$$

where the matrix elements are given by

$$\begin{aligned}
c_{A,11} &= C_{A11ij} \\
c_{A,22} &= C_{A33ij} \\
c_{A,33} &= C_{A55ij} + d_j C_{A51ij} + d_i C_{A15ij} + d_j d_i C_{A11ij} + e_j e_i C_{A33ij} \\
c_{A,44} &= \delta_{i1} \delta_{j1} (C_{A55ij} + d_j C_{A51ij} + d_i C_{A15ij} + d_j d_i C_{A11ij}) \\
c_{A,55} &= \delta_{i2} \delta_{j2} (C_{A55ij} + d_j C_{A51ij} + d_i C_{A15ij} + d_j d_i C_{A11ij}) \\
c_{A,31} &= C_{A51ij} + d_i C_{A11ij} \\
c_{A,13} &= C_{A15ij} + d_j C_{A11ij} \\
c_{A,32} &= -e_i C_{A33ij} \\
c_{A,23} &= -e_j C_{A33ij} \\
c_{A,41} &= \delta_{i1} (d_1 C_{A11ij} + C_{A51ij}) \\
c_{A,14} &= \delta_{j1} (d_j C_{A11ij} + C_{A15ij}) \\
c_{A,43} &= \delta_{i1} (C_{A55ij} + d_j C_{A51ij} + d_i C_{A15ij} + d_j d_i C_{A11ij}) \\
c_{A,34} &= \delta_{j1} (C_{A55ij} + d_j C_{A51ij} + d_i C_{A15ij} + d_j d_i C_{A11ij}) \\
c_{A,51} &= \delta_{i2} (d_1 C_{A11ij} + C_{A51ij}) \\
c_{A,15} &= \delta_{j2} (d_j C_{A11ij} + C_{A15ij}) \\
c_{A,53} &= \delta_{i2} (C_{A55ij} + d_j C_{A51ij} + d_i C_{A15ij} + d_j d_i C_{A11ij}) \\
c_{A,35} &= \delta_{j2} (C_{A55ij} + d_j C_{A51ij} + d_i C_{A15ij} + d_j d_i C_{A11ij}) \\
c_{A,54} &= \delta_{i2} \delta_{j1} (C_{A55ij} + d_j C_{M51ij} + d_i C_{A15ij} + d_j d_i C_{A11ij}) \\
c_{A,45} &= \delta_{i1} \delta_{j2} (C_{A55ij} + d_j C_{M51ij} + d_i C_{A15ij} + d_j d_i C_{A11ij})
\end{aligned} \tag{40}$$

Finally, the machinery damping  $\mathbf{B}_{\text{PTO}}$ , machinery stiffness  $\mathbf{K}_{\text{PTO}}$ , hydrostatic stiffness  $\mathbf{K}$  and excitation force  $\mathbf{F}_{\text{ex}}$  matrices are

$$\mathbf{B}_{\text{PTO}} = \begin{pmatrix} 0 & 0 & 0 & 0 & 0 \\ 0 & 0 & 0 & 0 & 0 \\ 0 & 0 & 0 & 0 & 0 \\ 0 & 0 & 0 & B_{\text{PTO}} & 0 \\ 0 & 0 & 0 & 0 & B_{\text{PTO}} \end{pmatrix} \tag{41}$$

$$\mathbf{K}_{\text{PTO}} = \begin{pmatrix} 0 & 0 & 0 & 0 & 0 \\ 0 & 0 & 0 & 0 & 0 \\ 0 & 0 & M_{\text{PTO}}g(d_1 + d_2) & M_{\text{PTO}}gd_1 & M_{\text{PTO}}gd_2 \\ 0 & 0 & M_{\text{PTO}}gd_1 & M_{\text{PTO}}gd_1 + K_{\text{PTO}} & 0 \\ 0 & 0 & M_{\text{PTO}}gd_2 & 0 & M_{\text{PTO}}gd_2 + K_{\text{PTO}} \end{pmatrix} \tag{42}$$

$$\mathbf{K} = \sum_{i=0}^2 \begin{pmatrix} \delta_{i1} K_{M11} & 0 & 0 & 0 & 0 \\ 0 & K_{H33,i} & -e_i K_{H33,i} & 0 & 0 \\ 0 & -e_i K_{H33,i} & K_{H55,i} + e_i^2 K_{H33,i} & \delta_{i1} K_{H55,i} & \delta_{i2} K_{H55,i} \\ 0 & 0 & \delta_{i1} K_{H55,i} & \delta_{i1} K_{H55,i} & 0 \\ 0 & 0 & \delta_{i2} K_{H55,i} & 0 & \delta_{i2} K_{H55,i} \end{pmatrix} \tag{43}$$

$$\mathbf{F}_{\text{ex}} = \sum_{i=0}^2 \begin{pmatrix} F_{ex,i1} \\ F_{ex,i3} \\ F_{ex,i5} + d_i F_{ex,i1} - e_i F_{ex,i3} \\ \delta_{i1} (F_{ex,i5} + d_i F_{ex,i1}) \\ \delta_{i2} (F_{ex,i5} + d_i F_{ex,i1}) \end{pmatrix} \tag{44}$$

### 2.3.2 Time domain

In time domain, viscous forces may be included. The equation of motion is:

$$(\mathbf{M} + \mu_\infty) \ddot{\mathbf{X}} + \mathbf{B}_{\text{PTO}} \dot{\mathbf{X}} + \int_0^t \mathbf{K}_{\text{rad}}(t-\tau) \dot{\mathbf{X}}(\tau) d\tau + (\mathbf{K} + \mathbf{K}_{\text{PTO}}) \mathbf{X} = \mathbf{F}_{\text{ex}} + \mathbf{F}_{\text{viscous}} \quad (45)$$

where:

$$\mu_\infty = \lim_{\omega \rightarrow +\infty} \mathbf{C}_M(\omega) \quad (46)$$

$$\mathbf{K}_{\text{rad}}(t) = \frac{2}{\pi} \int_0^{+\infty} \mathbf{C}_A(\omega) \cos \omega t d\omega \quad (47)$$

$$\mathbf{F}_{\text{viscous}}(t, \mathbf{X}, \dot{\mathbf{X}}) = \begin{pmatrix} \sum_{i=0}^2 \mathbf{F}_{V_i}(G) \\ T_{V1}(G) \\ T_{V2}(G) \end{pmatrix} \quad (48)$$

and in which  $\mathbf{F}_{V_i}(G)$  and  $T_{V1}$  are given by equation (30).

## 2.4 Implementation

### 2.4.1 Calculation of the hydrodynamic coefficients and functions

The BEM code Aquaplus [6] was used to calculate the hydrodynamic coefficients in the frequency domain. Figure (5) shows the meshes which were used. The first one is composed of 858 flat panels. A finer mesh, composed of 1890 flat panels, was also considered.

Results of computation of added mass and radiation damping coefficients are plotted in figure (6) and (7). The solid lines are results of calculation with Aquaplus with the 858 panels composed mesh and the square are results of the calculation with Aquaplus with the fine mesh, which has 1890 panels.

Overall, one can see that the agreement is very good. One can notice that there are differences for the added mass coefficients of body 0 (the frame) when it moves in heave and in pitch(first column in figure (6)). However, these differences are smaller than 3%, so they are not seen as a problem. Therefore, calculations for the hydrodynamic coefficients are considered as converged.

One can observe regularly located peaks in all the hydrodynamic coefficients related with horizontal motion. They corresponds with resonance of the fluid which is contained between the flaps and above the supporting structure.

The wave excitation force coefficients were computed in the frequency domain with Aquaplus, and are plotted in figure (8). Again, one can see that there is a good agreement between the two meshes used.

### 2.4.2 Estimation of viscous damping coefficients

- **Viscous forces on flap  $i$ :** Along the z direction, the viscous damping of the flaps will be dominated by the one of the frame. Hence, it can be neglected, i.e  $C_{z,i} = 0$ . Along the x direction, the flaps look like plates. Hence, according to [3] and [4],  $C_{x,i}$  is taken equal to 8 and  $D_{x,i} = B$ .

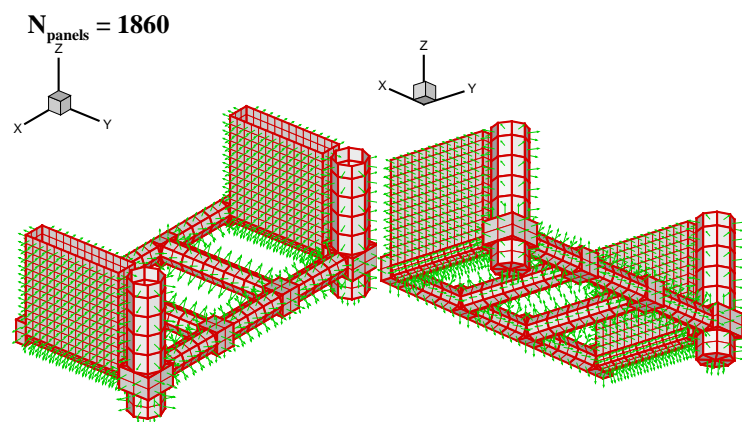
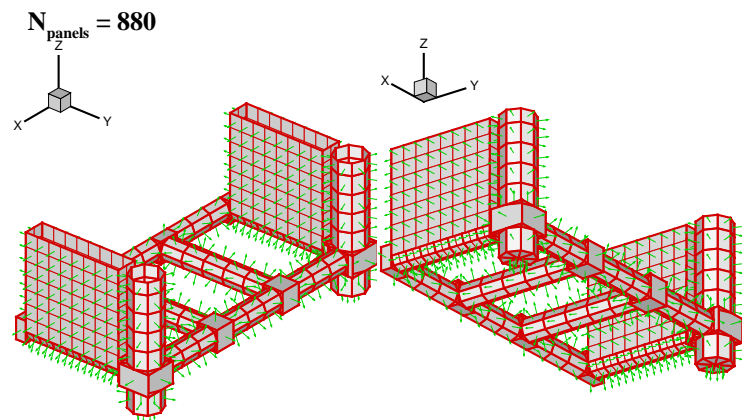


Figure 5: Meshes used for the hydrodynamic calculations. The top one is composed of 858 flat panels. The bottom one is composed of 1890 panels.

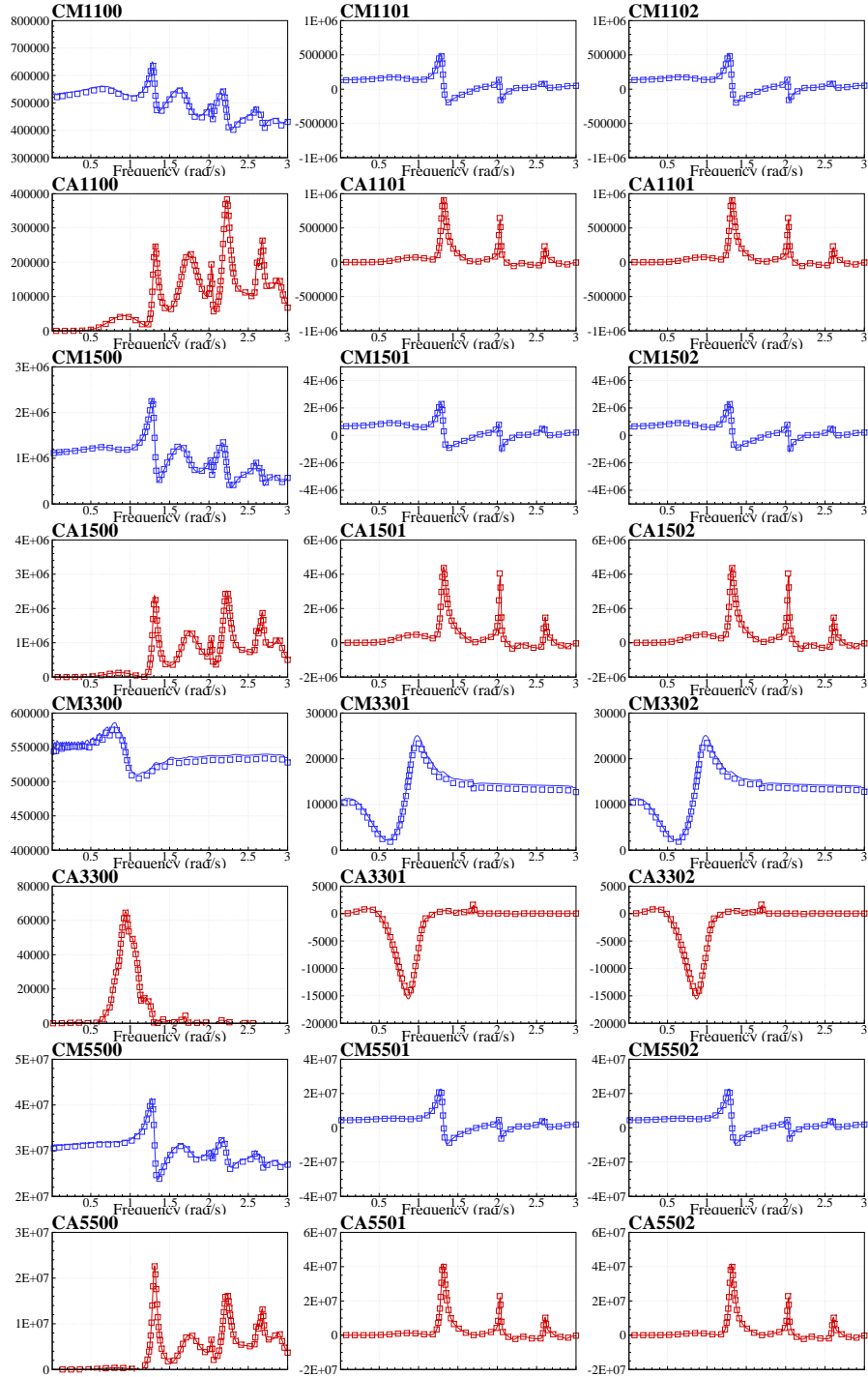


Figure 6: Hydrodynamic coefficients for the radiation force in the frequency domain, computed with Aquaplus. Index  $ijcd$  means the force measured on axis  $i$  of body  $c$  associated with a motion of body  $d$  along axis  $j$ . Solid lines are results of computation with the coarse mesh and the squares give the results for the finer mesh. Continued in Figure 7.

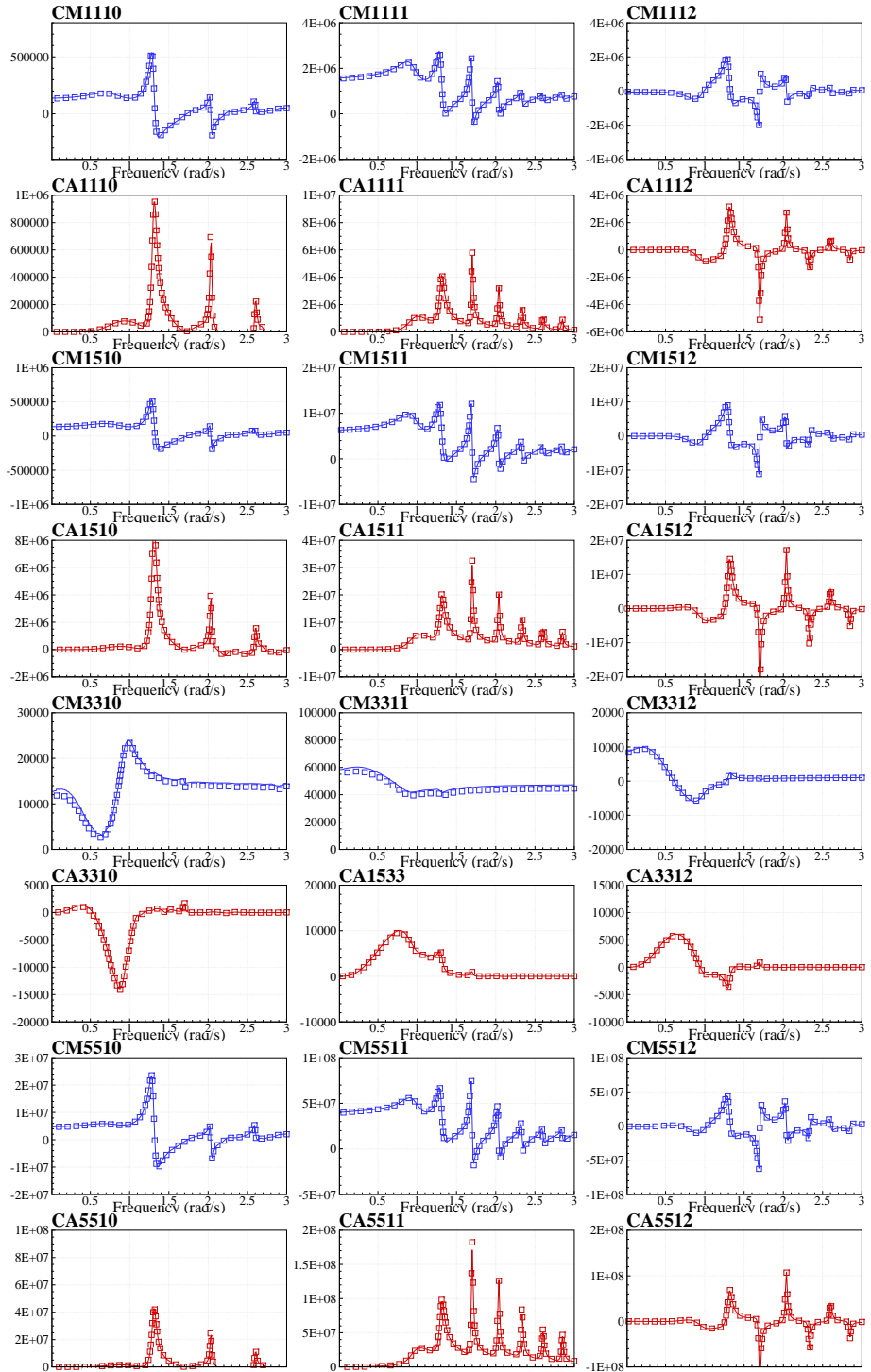


Figure 7: Continued from Figure 6.

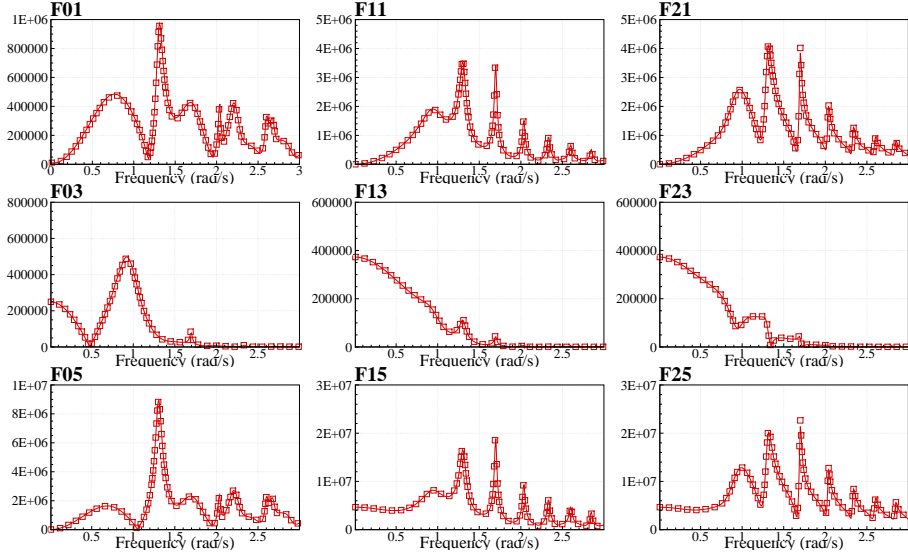


Figure 8: Wave excitation force coefficients in the frequency domain computed with Aquaplus. Index  $ci$  means force measured on axis  $i$  of body  $c$ . Solid lines are results of computation with the coarse mesh and the squares give the results for the finer mesh.

Therefore, equation (30) becomes:

$$\mathbf{F}_{\mathbf{V}i}(G) = -\frac{1}{2}\rho \int_{-D}^0 \begin{pmatrix} C_{x,i}B(V_x(z) - V_{0,x}(z))^{B_i} \\ 0 \\ (z - z_G) \times C_{x,i}B(\vec{V}_x(z) - \vec{V}_{0,x}(z))^{B_i} \end{pmatrix} (49)$$

$$\cdot \left\| \vec{V}(z) - \vec{V}_0(z) \right\| dz$$

For convenience, the integral in this last equation is replaced by a sum of discrete contributions, evaluated at different heights along the vertical axis of the float:

$$\mathbf{F}_{\mathbf{V}i}(G) = -\frac{1}{2}\rho \sum_{i=k}^N \begin{pmatrix} C_{x,i}B(V_x(z_k) - V_{0,x}(z_k))^{B_i} \\ 0 \\ (z_k - z_G) \times C_{x,i}B(V_x(z_k) - V_{0,x}(z_k))^{B_i} \end{pmatrix} (50)$$

$$\cdot \left\| \vec{V}(z_k) - \vec{V}_0(z_k) \right\| \frac{D}{N+1}$$

with  $z_k$  given by  $z_k = -\frac{D}{2(N+1)} + k\frac{D}{N+1} - D$ . In this study,  $N$  was set equal to 8.

- **Viscous forces on the frame:** The frame is composed of 13 pipes whose diameter is 2 meters. The amplitude of the relative heave motion of the platform with respect to the wave is expected to be smaller than or about equal to the amplitude of the waves. Hence the KC number for the pipes of the frame should not be greater than 6. According to [3], the coefficient  $C_z$  is taken equal to 1.

Table (4) shows the parameters which were used in equation (31).

$P_j$	$x(P_j) - x_G$ (m)	$z(P_j) - z_G$ (m)	$A_j$ ( $\text{m}^2$ )
1	-8.5	0	17.
2	0	0	17.
3	8.5	0	17.
4	-8.5	0	17.
5	0	0	17.
6	8.5	0	17.
7	-8.5	0	17.
8	0	0	17.
9	8.5	0	17.
10	-4	0	36.
11	4	0	36.
12	-4	0	36.
13	4	0	36.

Table 4: Parameters used for the calculation of the viscous forces on the float

#### 2.4.3 W2W models

Based on equations (34) and (45), two numerical models were derived: one in the frequency domain and the other one in the time domain. They were implemented for solution in Fortran90. Purpose of implementing separately a frequency domain model and a time domain model is that it allows to verify the implementations by comparing their results in regular waves of small amplitude. It has been found to be very useful in the debugging stage.

### 3 Simulation results and energy assessment

When they are not explicitly specified, the parameters which were used in all the simulations presented here are the ones given in table (2).

#### 3.1 Verification tests

If PTO parameters are set to large values, the whole system behaves as one single body, whose natural period in heave is given by:

$$\omega_{0,z} = \sqrt{\frac{K_{22}}{M_{22} + C_{M22}(\omega_{0,z})}} \quad (51)$$

and in pitch by:

$$\omega_{0,\theta} = \sqrt{\frac{K_{33}}{M_{55} + C_{M33}(\omega_{0,\theta})}} \quad (52)$$

with  $\mathbf{K}$  and  $\mathbf{K}'$  as in equation (34).

Solving Equations (51) and (52) numerically, one gets after a few iterations that  $\omega_{0,z} = 0.67$  rad/s and  $\omega_{0,\theta} = 0.67$ . The RAO in heave and pitch of the locked system (PTO coefficients  $K_{PTO}$  and  $B_{PTO}$  set equal to  $10^{12}$  and mooring

stiffness equal to  $10^9$ ) was calculated with the frequency domain model. Results are plotted in figure (9). One can see that the peak frequencies matches the ones calculated above.

In [9], table 4 gives the measured resonance period of the system in heave and pitch. At 1/25 scale, it is 2.13s in heave and 2.1s in pitch. At full scale, it means about 0.6 rad/s. It is close to the natural frequencies which are found in this study. It gives us confidence in the modelling and the dimensions and mechanical parameters which were used here.

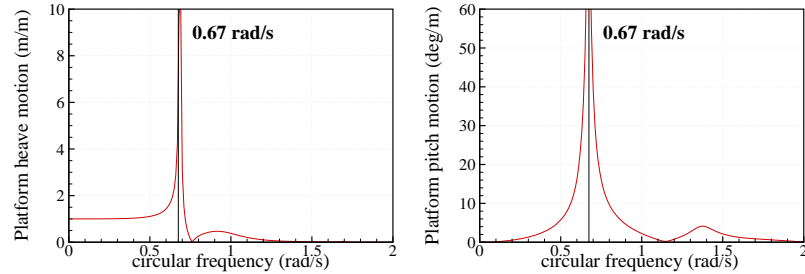


Figure 9: RAOs of heave (left) and pitch motion (right) of the system with flaps in locked mode.

We consider now the case of the fixed platform. Additional stiffness is added in the surge, heave and pitch motion of the platform ( $10^9$ ,  $10^9$  and  $10^{12}$  respectively). Figure (10) shows the RAOs in pitch of the front and rear flaps, and the associated power functions. In these figures,  $M_{PTO} = 10^5$  kg,  $B_{PTO} = 10^4$  kN.m.s and  $K_{PTO} = 0$ .

Starting from the low frequencies, one can see that the amplitude of motion increases first up to a maximum about  $10^\circ/\text{m}$  for both the front and the rear flaps, achieved at the frequency about 0.35 rad/s. It is close to the natural frequency of an isolated flap: 0.32 rad/s. The difference comes from the hydrodynamic coupling between the two flaps. Then, the amplitude decreases steadily for the rear flap with the increase of the frequency, whereas the amplitude of the motion of the front flap shows a wavy behaviour, which is thought to be due to trapped modes between the two rows of flaps.

On the right figures, one can see the absorbed power by the flaps in function of the wave frequency. The two first local maxima for the front flap are reached for  $\omega \approx 0.9$  rad/s and  $\omega \approx 1.1$  rad/s, and are shifted from the maxima of the rear flap.

For the front flap, the troughs in the power function matches with the harmonic of the modes trapped between the rows of flaps. By comparing the two power functions, one can see that they reach the same level at these frequencies. The power function of the first flap has a larger value when the wavelength is not in tune with the length of the system. In other words, it means that the wave interactions between the two flaps are positive when the wavelength does not match the length of the device.

Decay tests of the pitch motion of the flaps on a fixed platform have been plotted in figure (11) and (12). The PTO settings were set to  $M_{PTO} = 10^5$  kg,  $B_{PTO} = 10^4$  kN.m.s and  $K_{PTO} = 0$ . The initial pitch angle was set equal to 10

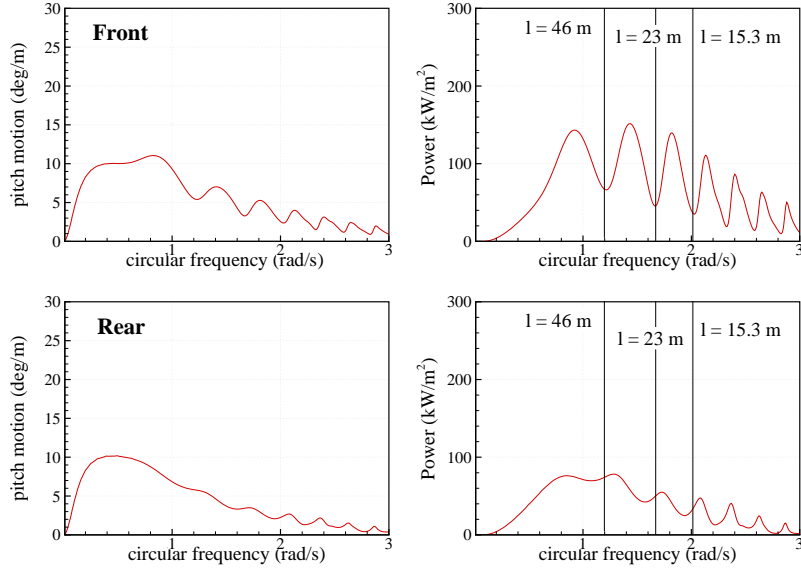


Figure 10: RAOs and power functions of the flaps mounted on a fixed platform. Here, the PTO parameters were set equal to  $M_{PTO} = 10^5$  kg,  $B_{PTO} = 10^4$  kN.m.s and  $K_{PTO} = 0$ .

degrees for the rear flap (figure (11)), and -10 degrees for the front flap (figure (12)).

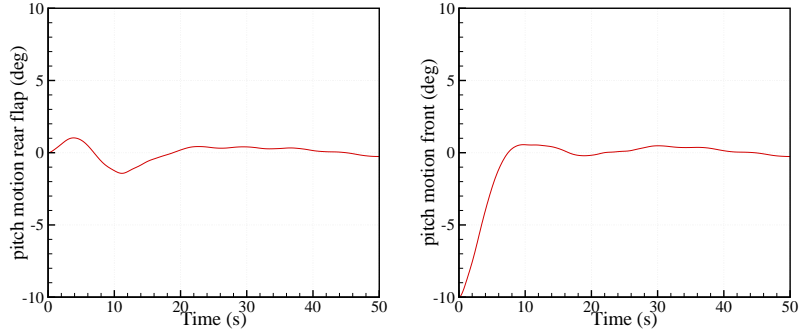


Figure 11: Pitch decay test of the rear flap. The PTO parameters were set equal to  $M_{PTO} = 10^5$  kg,  $B_{PTO} = 10^4$  kN.m.s and  $K_{PTO} = 0$ .

With this PTO configuration, the natural period of the flaps is 19.5 seconds. Although it is highly damped, one can see that the first half oscillation lasts in about 10 seconds, which matches with half the natural period. As expected, one can see that wave radiation by the rear flap creates a wave which makes the front flap move.

As expected, the pitch decay test of the front flap is symmetrical with the rear flap.

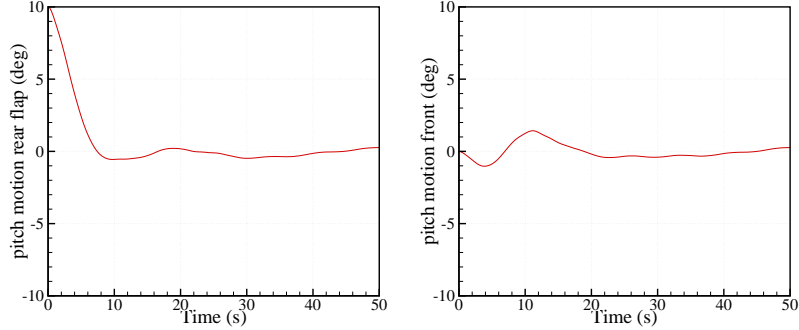


Figure 12: Pitch decay test of front flap. The PTO parameters were set equal to  $M_{PTO} = 10^5$  kg,  $B_{PTO} = 10^4$  kN.m.s and  $K_{PTO} = 0$ .

Figure (13) shows a comparison of the transfer and power functions of the system with all 5 DoFs computed with the frequency and the time domain model. Viscous damping was set to 0 in the time domain model. Artificial supplementary damping was added on the surge and heave motion of the frame for the duration of the simulation to damp the initial transient motion ( $10^6$  N/m.s). Same damping was added in the frequency domain model. The PTO parameters were set to  $M_{PTO} = 2 \cdot 10^5$  kg,  $B_{PTO} = 3 \cdot 10^4$  kN.m.s and  $K_{PTO} = 0$ .

The agreement between the two models is good except for a narrow range of periods around 7 seconds. It is thought to come from the truncation of the memory function in the radiation convolution product<sup>1</sup>. However, it will be seen below that it does not affect much the results in irregular waves because the range of period for which the time domain model is inaccurate is narrow.

### 3.2 RAOs

Figure (14) shows the RAOs and power functions of the F-3OF device calculated with the frequency domain model. The PTO parameters were set to :  $M_{PTO} = 2 \cdot 10^5$  kg,  $B_{PTO} = 4 \cdot 10^4$  kN.m.s and  $K_{PTO} = 0$ .

One can see that the RAO of the platform in surge has two peaks. The first one, at very low frequency (0.15 rad/s), is associated with the moorings resonance. Its amplitude is very large, as there is almost no hydrodynamic linear damping for the lowest frequencies. However, there is no wave energy at this frequency at first order, so it is not seen as a problem. The other peak, whose amplitude is smaller, is associated with the resonance in pitch, since the pitch and surge motion are coupled.

The platform responds in surge with an amplitude about the wave amplitude for the frequencies between these two peaks. For higher or lower frequencies, one can see that the platform does not move much in surge.

The frequency domain model predicts a large resonance in heave. It occurs at 0.67 rad/s, i.e in the middle of wave frequencies. In linear theory, heave

---

<sup>1</sup>Because the flaps are facing each other, there exist trapped modes in the region in between. It causes the memory function to last for very long time. It was truncated at 200 seconds. It is very long, but one can see here that it is still not sufficient to have a perfect agreement between the time and the frequency domain model

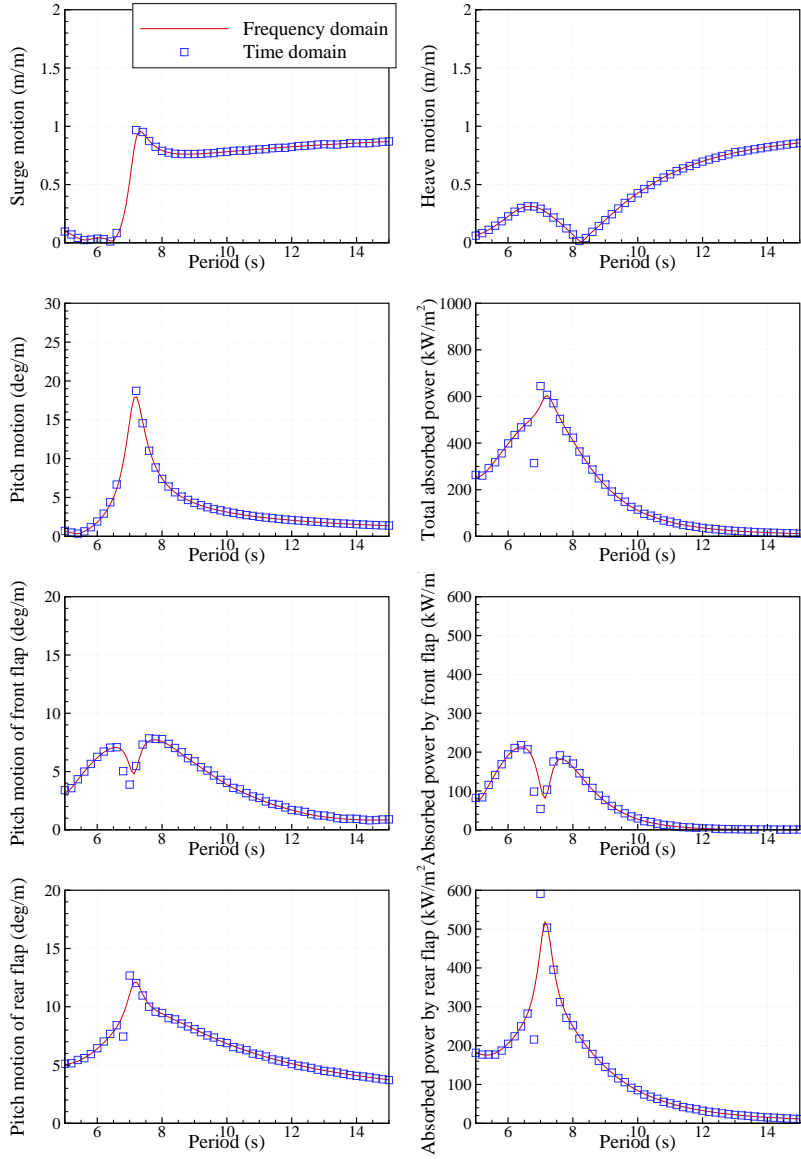


Figure 13: Comparison of RAOs of the 5 DoFs system computed with the frequency and the time domain model. The PTO parameters were set equal to  $M_{PTO} = 2 \cdot 10^5$  kg,  $B_{PTO} = 3 \cdot 10^4$  kN.m.s and  $K_{PTO} = 0$ .

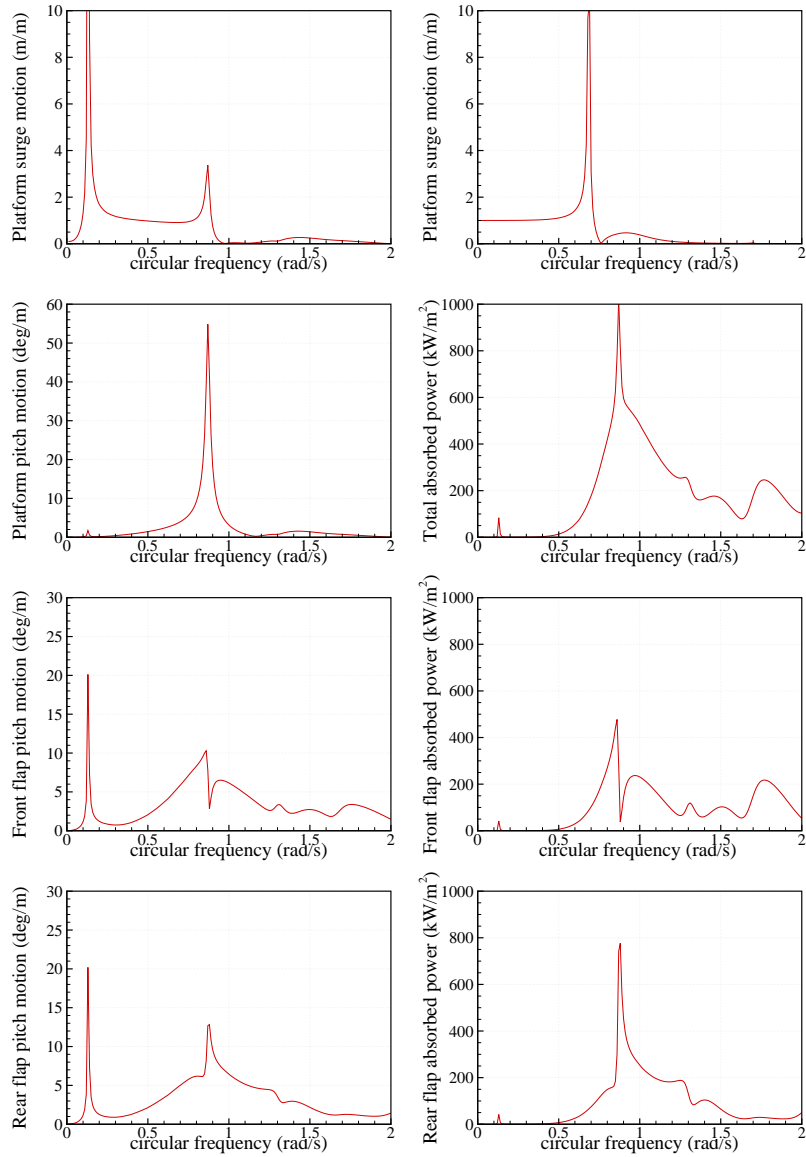


Figure 14: RAOs and power functions of the FOF WEC. The PTO parameters were set equal to  $M_{PTO} = 2 \cdot 10^4$  kg,  $B_{PTO} = 4 \cdot 10^4$  kN.m.s and  $K_{PTO} = 0$ .

motion is decoupled with the other modes of motion so it is not a problem. But in reality, one can wonder what would be the implications of such resonance. In particular, it might increase the fatigue in the mooring system.

The resonance in pitch of the platform occurs at 0.85 rad/s, i.e in the middle of wave frequencies. Again, one can see that the predicted amplitude is very large. As for the heave motion, this could be an issue for the mooring system. Out of resonance, one can see that the response of the platform in pitch decreases rapidly.

Except at the resonance frequency of the platform in pitch, both the front and rear flaps have similar responses in terms of relative pitch motion: they have a large peak in their response at the surge resonance frequency because of the coupling between pitch and surge and a wide bandwidth response of about 5 deg/m for wave frequencies between 0.7 and 1.2 rad/s. At the pitch resonance frequency of the platform, one can see that they have a different behaviour. The front flap's pitch response has a trough for that frequency, whereas there is a peaky maximum for the rear flap.

Obviously, these features appear also on the power function of the system. The absorbed power by the front and rear flaps is about the same in the range of typical wave frequencies, except at the pitch resonance, where the front flap has a minimum and the rear flap a maximum. However, one can see that the sum of the absorbed power from the front and the rear flap shows a maximum at the pitch frequency of the platform.

This last result shows that the pitch motion of the platform is beneficial to the energy absorption. However, we saw on the platform pitch motion that it corresponds with a very large amplitude response. It is most likely that viscous effects will much reduce this effect.

### 3.2.1 Influence of the PTO coefficients

The PTO coefficients naturally have an influence on the power absorption of the F-3OF device. To understand this influence, we computed its power function with several sets of PTO coefficients.

Table (5) summarises the set of PTO coefficients which were used. We plotted in figures (15), (16) and (17) the associated RAOs in pitch motions and the associated power functions.

In figure (15), we have plotted the RAOs and power function for PTO settings from 1 to 8. For these settings,  $K_{PTO}$  is equal to 0 and  $M_{PTO}$  is equal to  $2 \cdot 10^5$  kg. One can see that, starting from the low values of  $B_{PTO}$ , the effect of increasing this parameter is first to increase the peak of power absorption and to enlarge the bandwidth of the system. For frequencies smaller than the natural frequency, a maximum of power absorption is reached for  $B_{PTO} = 20$  MN.m.s. For greater frequencies, the optimal is higher, about 60 MN.m.s.

On the pitch motions, the effect of increasing the PTO damping coefficient is to increase the amplitude of the motion, whereas the motions of the front and rear flaps relative to the platform are reduced.

In figure (16), we have plotted the RAOs and power function for PTO settings 6, 10 and 11. As it was expected, one can see that an increase of the  $M_{PTO}$  essentially shifts the resonance frequency in pitch of the platform to higher periods. On the total absorbed power plot, one can see that the levels of absorbed power is not much affected.

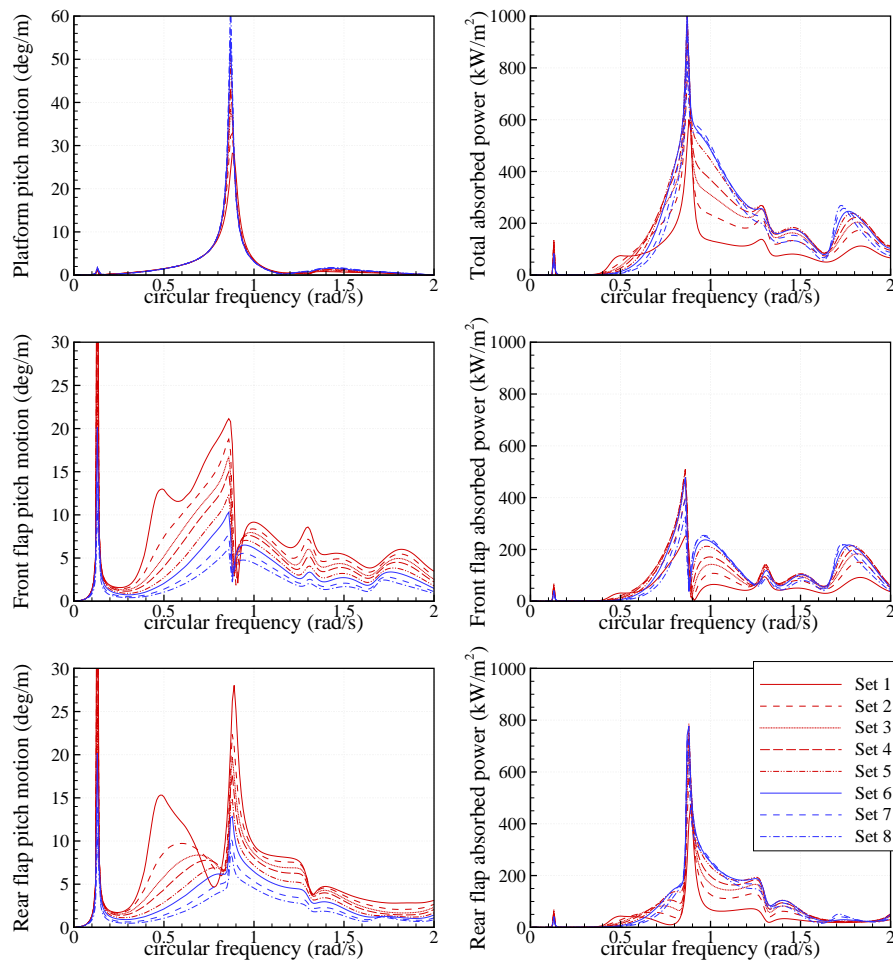


Figure 15: RAOs and power function of the motion with PTO settings 1 to 8. In these settings,  $K_{PTO}$  is equal to 0 and  $M_{PTO}$  is equal to  $2 \cdot 10^5$  kg.

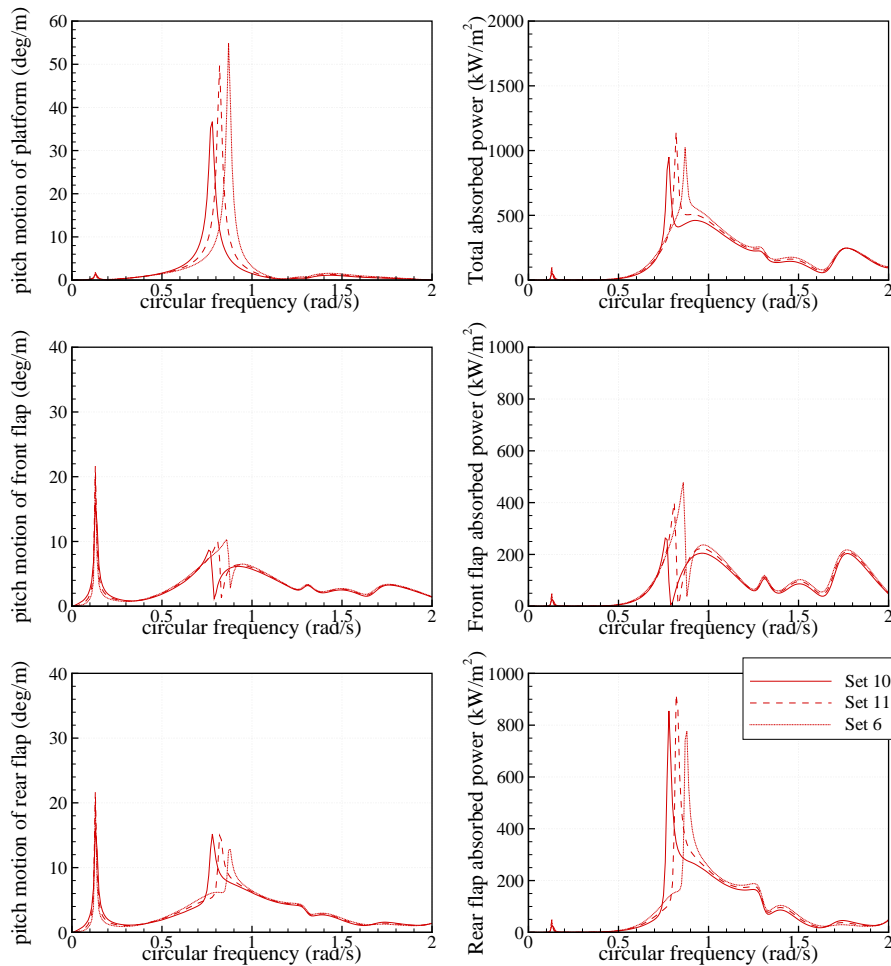


Figure 16: RAOs and power function of the motion with PTO settings 10 to 11. In these settings, the PTO damping coefficient is equal to 40 MN.m.s

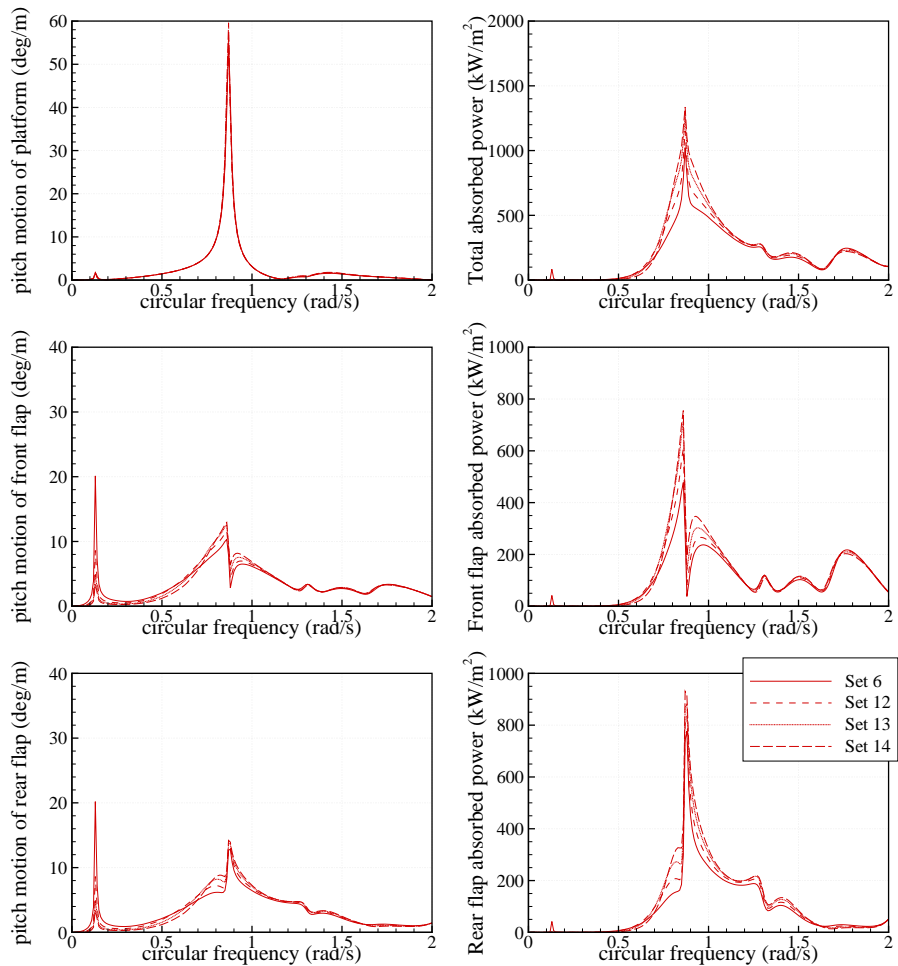


Figure 17: RAOs and power function of the motion with PTO settings 12 to 15. In these settings, the PTO damping coefficient is equal to 40 MN.m.s

Set number	$B_{PTO}$ (MN.m.s)	$K_{PTO}$ (MN.m)	$M_{PTO}$ ( $10^3$ kg)
1	5	0	200
2	10	0	200
3	15	0	200
4	20	0	200
5	30	0	200
6	40	0	200
7	60	0	200
8	80	0	200
9	100	0	200
10	40	0	0
11	40	0	100
12	40	10	200
13	40	20	200
14	40	30	200
15	40	40	200

Table 5: PTO settings

In figure (16), we have plotted the RAOs and power function for PTO settings from 12 to 15. One can see that an increase of the  $K_{PTO}$  coefficient does not significantly change the bandwidth of the motion response, but it results in an increase of the energy absorption.

From these results, one can conclude that it is probably beneficial for the F-3OF device to adapt the PTO parameters to each sea state, so they will have to be optimised in the calculation of the annual average power production.

### 3.2.2 Influence of the viscous damping on the RAOs

In frequency domain, the numerical model predicts very large response at resonance in pitch and heave, see figure (14). This large response is not realistic, since it will be limited by viscous effects.

Figure (18) shows a comparison of the RAOs and power function of the system computed with the frequency domain model, and with the time domain model including viscous damping. For the time domain model, two wave amplitudes were considered, 1 and 2 meters. The PTO parameters were set equal to setting 6 (see table (5)).

One can see that viscous damping has an important effect. Not only the amplitude of the responses of the system at resonances are reduced, but also the amplitude of motion of the flaps for period between 7 and 10 seconds. It leads to a reduced energy absorption.

One can see also peaks and troughs in the response in surge and pitch of the frame, and in the motion of the flaps. It is thought to come from the truncation in the memory term of the radiation force.

### 3.2.3 Conclusions

From these results in regular waves, it appears that:

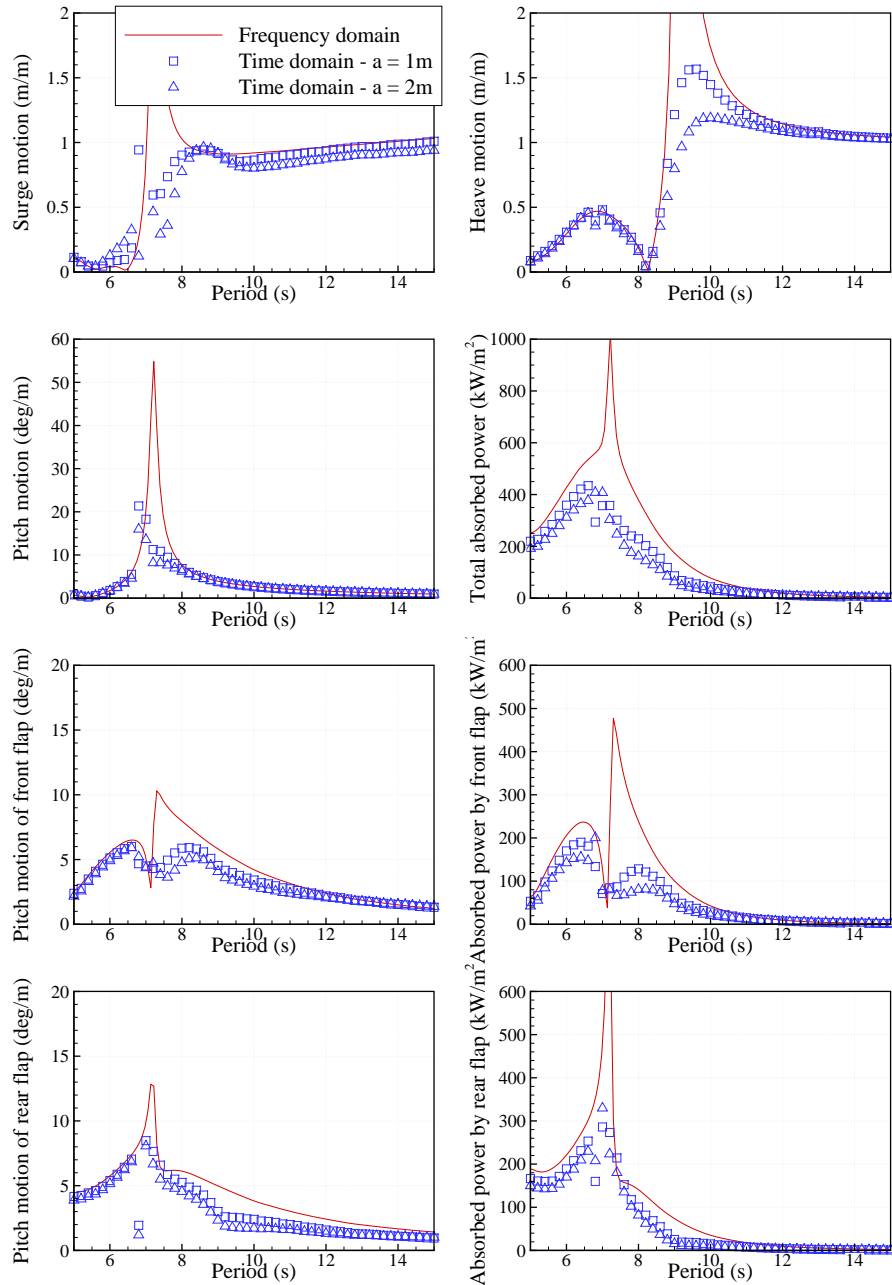


Figure 18: Comparison of RAOs and power functions with and without viscous damping. The PTO setting is number 6.

- The order of magnitude of absorbed power from the F-3OF device is several hundreds of kW per square meters of wave amplitude in regular waves.
- The PTO parameters have a large influence on the transfer functions of the F-3OF device.
- Viscous damping reduces the energy absorption. Influence of the modelling of this damping, via the choice of the viscous damping coefficients, must be assessed.

Hence, the estimation of the power absorption should be done with optimisation of the PTO parameters and the uncertainty on the results should be assessed by considering the effect of the viscous damping modelling.

### 3.3 Power matrix and criteria

In this section, all time domain simulations were performed in irregular waves using the JONSWAP spectrum. All quantities are derived from 1200 s duration simulations, with a time step of 0.05 s. To remove the transient effects, the first  $15 \times T_p$  seconds of the simulations are not taken into account.

#### 3.3.1 Power matrix of the floating three-body oscillating flap device

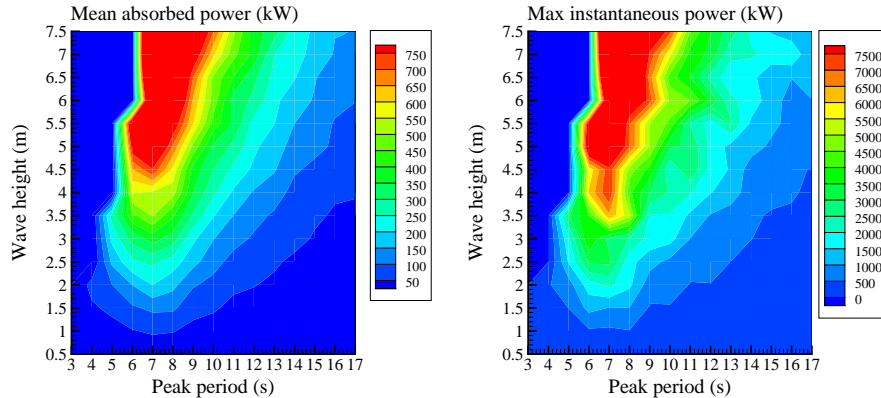


Figure 19: Power matrix with optimised PTO coefficients. The left-hand figure is the mean absorbed power and the right-hand figure is the maximum recorded over the duration of the simulation for each sea state.

Figure (19) shows the power matrix of the F-3OF device in deep water. The left-hand figure is the mean absorbed power and the right-hand figure is the maximum recorded over the duration of the simulation for each sea state.

For each sea state, the set of PTO parameters ( $B_{PTO}, K_{PTO}$ ) were optimised whereas  $M_{PTO}$  was fixed at  $2 \cdot 10^5$  kg. The range of values for optimisation of the PTO parameters is given in table (6).

For a typical sea state of 9 s wave peak period and 2.5 m significant wave height, the mean absorbed power is 170 kW. A mean power absorption higher than 500 kW is reached for the strongest sea states. As expected from the

	$B_{PTO}$ (kN.m.s/rad)	$K_{PTO}$ (kN.m/rad)
Minimum	5 000	0
Maximum	100 000	50 000

Table 6: Range of values for optimisation of the PTO parameters

results in regular waves, the system exhibits the best efficiency for wave periods about 7-8 seconds.

The maximum instantaneous machinery power is typically about 10 times the mean power. It is very large. This might be a drawback of the system from the power electronics point of view. The effect of limiting the instantaneous power is investigated later.

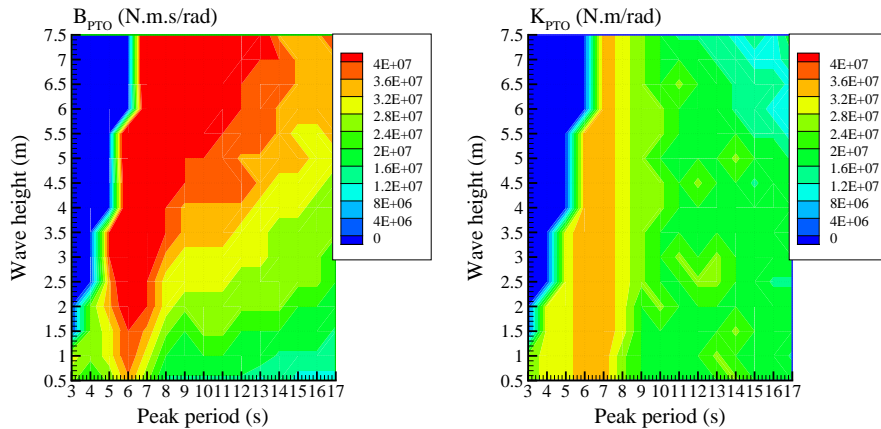


Figure 20: Optimised value of the PTO coefficients.

Figure (20) shows the matrices of the optimised values of the PTO coefficients. One can see that they vary with the wave period and with the wave height.

For a fixed wave height, the optimal damping coefficient reaches a peaky maximum at resonance (5-7 seconds). It decreases rapidly as the wave peak period decreases. For a fixed wave period, the optimal damping coefficient increases with the wave height. As an average, one can say that the nominal value of  $B_{PTO}$  should be about 20 MN.m.s/rad.

The optimal stiffness coefficient also reaches a maximum for wave periods of about 5-7 seconds. One can see that the optimal value does not depend on the wave height. As an average,  $K_{PTO}$  should be about 20 MN.m/rad.

Figure (21) shows the ratio of the power absorbed by the rear flap divided by the power absorbed by the front flap. One can see that for most sea states, it is rather balanced, only with a slightly higher absorption (about 10 to 20 %) for the rear flap than for the front flap.

Figure (22) shows matrices of the RMS values for the motion in surge, heave and pitch of the supporting structure, and the relative pitch of the front and rear flaps. Let us first consider the surge and heave motion, which are quite similar. One can see that for wave periods smaller than 7 seconds, there is little

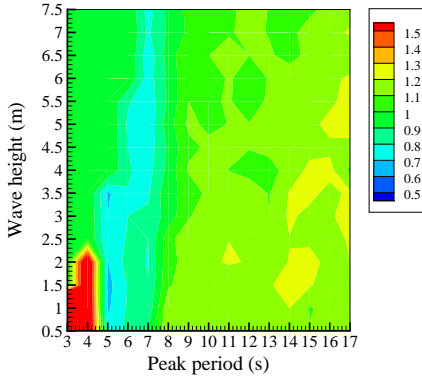


Figure 21: Ratio of the power absorbed by the rear flap to the power absorbed by the front flap, with optimised PTO coefficients.

response of the platform along these degrees of freedom. For periods higher than 7 seconds, the RMS value is about a quarter of the significant wave height, whatever the wave period. Hence, the platform follows the wave.

The maximum for the pitch response of the platform is found at 7 seconds. The RMS values of the angular excursion is up to about 10 degrees for typical sea states. The pitch responses of the front and rear flaps relative to the platform are similar. Their maxima are found for wave peak periods of around 8-9 seconds. The flaps pitch response are smaller than the pitch response of the platform.

By multiplying the power matrix with wave data statistics, one can calculate the annual energy absorption for each considered wave site. The values are reported in table (7) together with the assessment criteria.

Parameter	Unit	SEM-REV	EMEC	Yeu	Lisboa	Bel-mullet	Danish study
$\gamma$		1	1	3.3	3.3	3.3	1
$J$	[kW/m]	14.8	21.8	26.8	37.5	80.6	14.8
Mean power	[kW]	52.3	112	131	104	145	112
Capture width	[m]	3.5	5.1	4.9	2.8	1.8	7.6
$E_y / \text{Mass}$	[MWh/m <sup>3</sup> ]	0.32	0.69	0.79	0.65	0.90	0.685
$E_y / A_{\text{wet}}$	[MWh/m <sup>2</sup> ]	0.21	0.46	0.51	0.42	0.59	0.453
$E_y / F_{\text{PTO}}^{\text{RMS}}$	[kWh/N]	1.09	1.43	1.64	1.55	1.53	1.25
$E_y / F_{\text{wave}}^{\text{RMS}}$	[kWh/N]	1.04	1.50	1.58	1.39	1.42	1.49

Table 7: Evaluation criteria for the floating three-body oscillating flap device for chosen sites having mean annual wave energy transport  $J$ , and where sea states are synthesized with a spectrum peakedness factor  $\gamma$ . The parameters are calculated based on the yearly energy delivery  $E_y$ . The mass is taken as the total mass of the ballasted installed structure, not including the moorings, and  $A_{\text{wet}}$  is the wetted surface area of the structure. Significant PTO force  $F_{\text{PTO}}^{\text{RMS}}$  and significant wave force  $F_{\text{wave}}^{\text{RMS}}$  are taken as the yearly RMS values. The uncertainty of  $E_y$  is estimated to  $[-25, 30]\%$ .

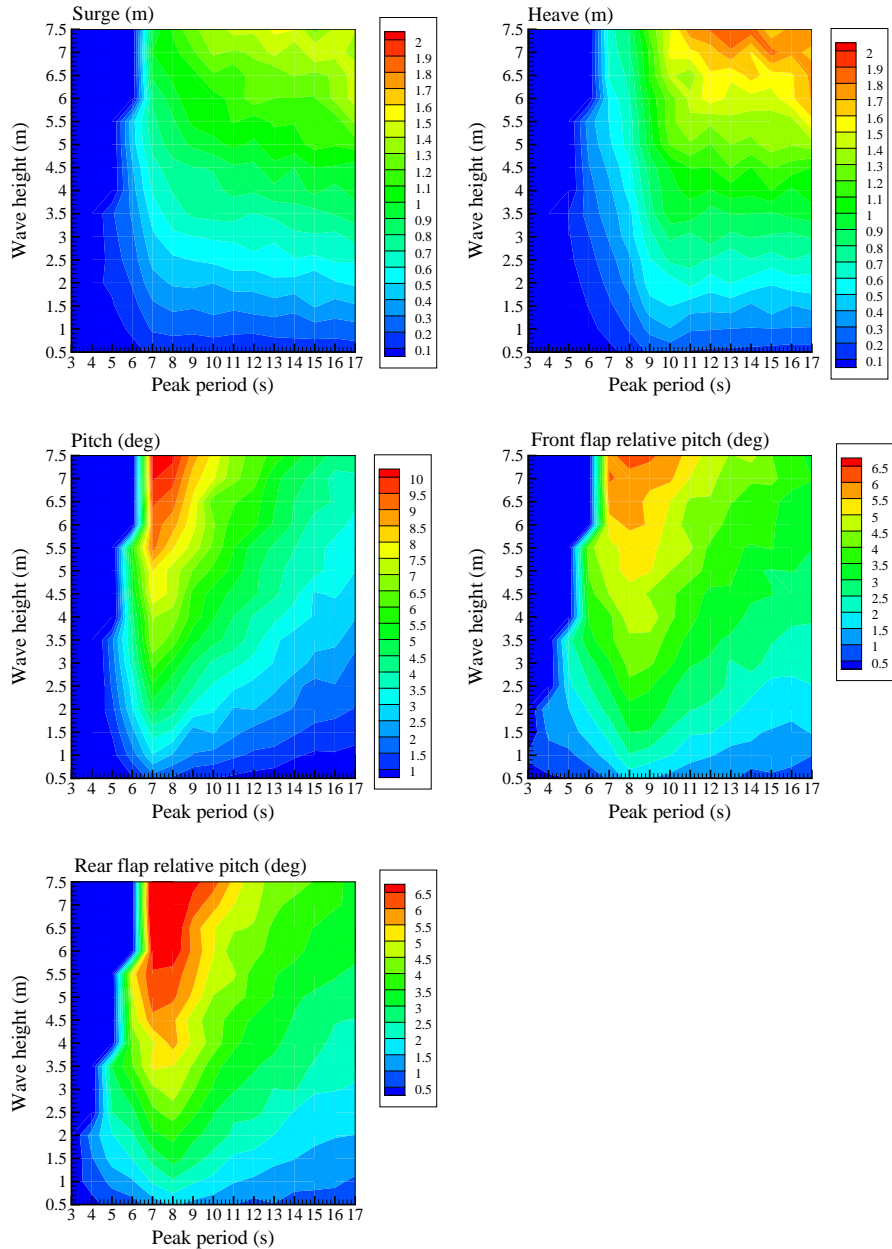


Figure 22: Matrices of the RMS values for the motion of the FOF device.

One can see that the mean annual power delivery that one can expect from the F-3OF device is about one hundred kilowatts. It ranges from 52 kW for the SEM-REV site up to 145 kW for the highly energetic Belmullet site. For a typical wave resource of about 30 kW/m, the typical absorbed wave power by the FOF device is about 130kW. The typical mean capture width is about 4 to 5 meters, depending on the site. One can see that the capture width is much larger at the Danish site. This is not surprising as the device is rather small, thus more suitable for short waves.

At the Danish site, the capture width ratio<sup>2</sup> is about 30 %. This is much higher than the capture width ratio of 14-18 % reported by Pecher *et al.* in [9]. But it is in range with what is reported by Folley in [11] and Henry in [12] (efficiencies between 8-41 % and 30-70 % respectively).

The discrepancy with the experiment by Pecher *et al.* may be explained by differences in the geometry of the system and different PTO parameters. In these experiments, the PTO parameters were not optimised for each sea state and it seems there was no additional stiffness provided by the PTO. Calculation of energy absorption without optimisation of the PTO parameters was carried out at Yeu site with PTO setting 5. Mean annual absorbed power is equal to 102 kW, 25 % less than with optimisation of the PTO parameters. It corresponds with a capture width ratio of 0.22, more in range with the result presented by Pecher *et al.*. The geometry is also different, with surface piercing flaps which are expected to suffer less viscous damping.

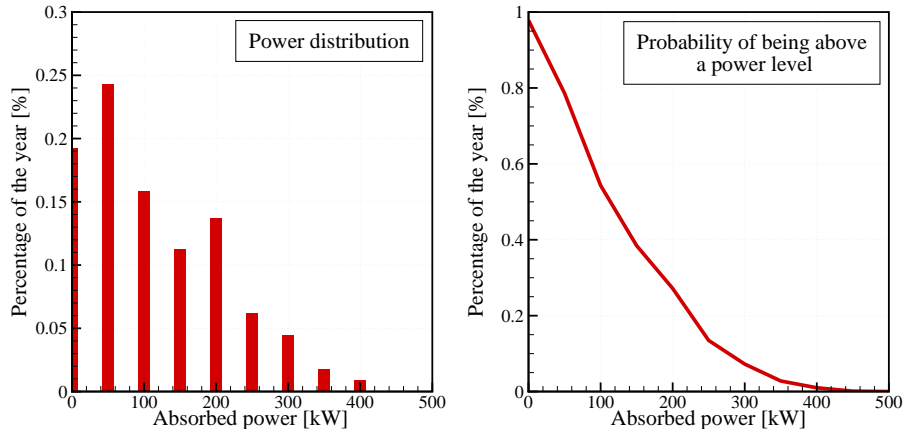


Figure 23: Distribution of the power delivery for the FOF device placed at Yeu off the French coast.

Figure (23) shows the distribution of the absorbed power in function of the power level. The left figure shows the probability for the power production to be between two levels and right figure shows the probability for the power to be greater than a given power level. It has been calculated with the wave statistics of the Yeu site. One can see the absorbed wave power is greater than the mean power 40 % of the year.

<sup>2</sup>Defined as the ratio of the capture width divided by the width

### 3.3.2 Assessment of the uncertainties

#### Viscous losses

To assess the uncertainty associated with the modelling of the viscous losses, the mean annual absorbed power at the Yeu site was calculated with different values of the viscous coefficients. Calculations were made with optimisation of the PTO parameters. Figure (24) shows the results in function of the percentage of viscous damping coefficients with respect to the nominal values.

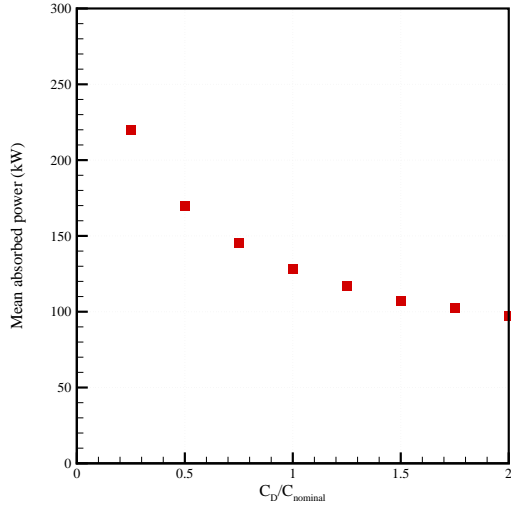


Figure 24: Mean absorbed power at Yeu in function of the percentage of viscous damping with respect to the nominal value. PTO parameters are optimised for each sea state.

One can see that the modelling of the viscous damping has an influence on the results of mean power. If viscous damping is set to half its nominal value, the mean absorbed power is 30 % greater than the one with nominal values. If viscous damping is underestimated by a factor 2, then the absorbed power is over predicted by 25 %.

It is worth noticing that if the viscous damping is set to 0, the mean power predicted by the numerical model is going as high as 580 kW. It shows how the viscous effect are dominant in the case of this particular device.

Therefore, the retained uncertainty associated with the modelling of viscous damping is assumed to be within  $[-25 \%, +30 \%]$ .

#### Mooring stiffness

To get an estimate of the uncertainty associated with the modelling of the mooring lines, the mean annual absorbed power at the Yeu site was calculated with different values of the mooring stiffness coefficient. Calculations were made with PTO setting number 5 and the frequency domain model. Results are shown in table (8). The difference on the absorbed power is smaller than 2 %.

Mooring stiffness coefficient in surge (kN/m)	Mean annual absorbed power (kW)
0	129
100 (nominal)	131
200	125
300	125

Table 8: Mean annual absorbed power at Yeu in function of the mooring stiffness coefficient in surge.

### 3.4 Parametric studies

#### 3.4.1 Fixed platform vs Floating platform

Mooring stiffness coefficient in surge (kN/m)	Resonance period in surge (s)	Mean annual absorbed power (kW)
100 (nominal)	40	131
1000	12	129
10000	4	207

Table 9: Mean annual absorbed power at Yeu in function of the mooring stiffness coefficient in surge.

Table (9) shows the mean absorbed power at Yeu in function of the mooring stiffness coefficient in surge. The PTO coefficients were optimised for each sea state. The first case (100 kN/m) corresponds with a slack mooring. In the last case (10000kN/m), the platform is almost fixed in surge.

One can see that large mooring stiffness coefficients are beneficial to the energy absorption of the F-3OF device. In other words, it would be possible to significantly increase the energy absorption by using a taught mooring instead of a slack mooring. However, a very stiff horizontal mooring system may be difficult to achieve in practice.

#### 3.4.2 Threshold on the instantaneous absorbed power

Table (10) shows the mean absorbed power at Yeu in function of a threshold on the instantaneous power. It means that the maximum of instantaneous power is limited to this threshold. The difference between the available instantaneous power and the maximum is lost.

Max. instantaneous absorbed power (kW)	Mean annual absorbed power (kW)
500	108
1000	122
2000	128
No	131

Table 10: Mean annual absorbed power at Yeu in function of the threshold of maximum instantaneous absorbed power. The PTO coefficients were optimised for each sea state.

One can see that the instantaneous power can be limited to a maximum of 2MW with negligible losses in the mean annual absorbed power.

### 3.4.3 Threshold on the mean absorbed power

A calculation of the mean annual power at Yeu site was performed with limiting the mean output power for each sea state to 500 kW. The resulting reduction in the mean annual power was found to be smaller than 2 %. It is smaller than the noise coming from the time domain simulations. It means that the F-3OF WEC could be rated at 1MW without losing energy.

### 3.4.4 Effect of scale

Figure (25) shows the effect of geometric scaling on the mean power absorption of the F-3OF device, at the Yeu site. This figure has been calculated using the frequency domain model. The PTO parameters are fixed for every sea state. They are taken equal to setting 5 at scale 1, and it is scaled accordingly to Froude law for others scale.

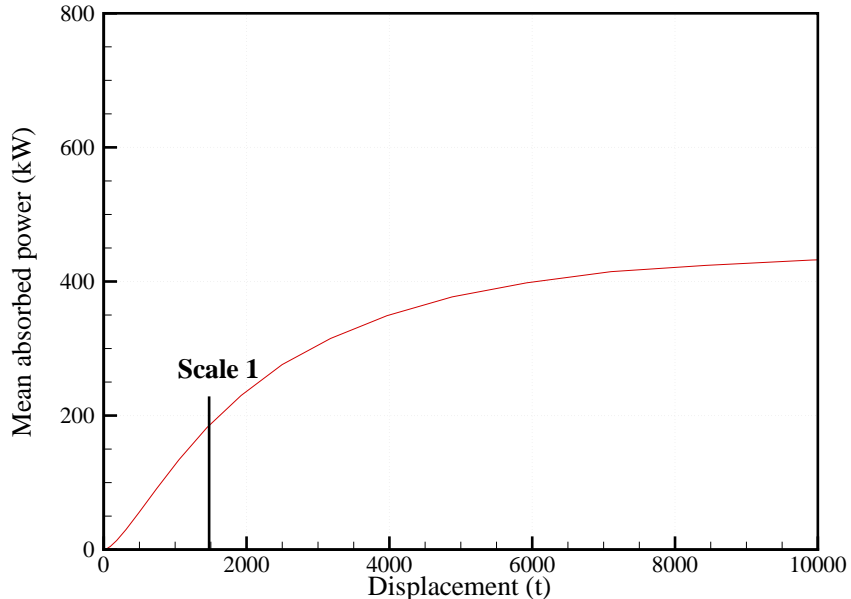


Figure 25: Influence of the scale on the mean power absorption at Yeu.

One can see that the mean absorbed power grows very fast with the displacement for small devices. As the displacement increases, the slope decreases. It seems that there exist an asymptotic limit for large displacement devices of about 430 kW.

For a displacement twice the nominal displacement of the F-3OF device, one can see that the increase in power absorption is about 60 %. In the same time, the increase in the wetted surface is 58 %. Therefore, depending on how scale the cost, it is possible that scaling up the platform would improve its economics.

## 4 Conclusions and recommendations

From these results and the study, the main conclusions are :

- The mean power level that one can expect from the FOF WEC is about 130 kW on a site whose wave resource is about 30 kW/m. The uncertainty is about [-25 %, +30 %], and comes mainly from the modelling of the viscous losses.
- A stiffer mooring in surge could significantly improve the energy absorption. In case the surge motion to be ideally restrained, the increase of energy absorption could be higher than 60 %. However, a stiff horizontal mooring may be impractical, or very expensive.
- The output power of the F-3OF device could be limited to 500 kW without decreasing the energy delivery. Limitation of the instantaneous absorbed power to 20 times the mean output power (2 MW) would not significantly reduce the mean absorbed power either.

## References

- [1] J. Falnes, 2002. Ocean waves and oscillating systems. Linear interactions including wave energy extraction. Cambridge university press.
- [2] J. Hals, T. Bjarte-Larsson, J. Falnes, 2002. Optimum reactive control and control by latching of a wave-absorbing semisubmerged heaving sphere. In Proc. of the 21st Offshore Mechanics and Arctic Engineering Conference, pp. 1-9.
- [3] B. Molin, 2002. Hydrodynamique des structures offshore, Guides Pratiques sur Les Ouvrages En Mer, TECHNIP Eds.
- [4] P.W. Bearman, M.J. Downie, J.M.R. Graham, E.D. Obasaju, 1985. Forces on cylinders in viscous oscillatory flow at low Keulegan-Carpenter numbers, Journal of Fluid Mechanics, Vol. 154, pp. 337-356.
- [5] A. Babarit, Achil3D v2.0 : User Manual, Laboratoire de Mécanique des Fluides, CNRS UMR6598, Ecole Centrale de Nantes, October, 2008.
- [6] G. Delhommeau, 1997. Seakeeping Code Aquaplus
- [7] J. Falnes, 1999. Wave-energy conversion through relative motion between two single-mode oscillating bodies. Journal of Offshore Mechanics and Arctic Engineeringm Vol. 121, 32–38.
- [8] [www.langleewavepower.com](http://www.langleewavepower.com) Accessed November, 1st, 2010.
- [9] A. Pecher, J.P. Kofoed, J. Espedal, S. Hagberg 2010. Results of an Experimental study of the Langley Wave Energy Converter. In Proc. of the 20<sup>th</sup> International Offshore and Polar Engineering Conference, Beijing, China, June 20-25.
- [10] Bølgekraftprogram, Afslutningsrapport 2002. Bølgekraftudvalgets Sekretariat, RAMBØLL, Teknikerbyen 31, 2830 Virum.
- [11] M. Folley, T.J.T. Whittaker, A. Henry 2006. The effect of water depth on the performance of a small surging wave energy converter. Ocean Engineering, Vol. 34(8-9), pp 1265-1274.
- [12] A. Henry, K. Doherty, L. Cameron, T. Whittaker, R. Doherty 2010. Advances in the design of the Oyster wave energy converter. In Proc. Of the Royal Institution of Naval Architects Marine and Offshore Renewable Energy Conference, London, UK, April.

## Chapter 4

# A floating oscillating water column (F-OWC) inspired by the OEBuoy WEC

Numerical estimation of energy production from  
a selection of Wave Energy Converters  
– Study of a floating oscillating water column

Aurélien Babarit<sup>1</sup>, Adi Kurniawan<sup>2</sup>, Jørgen Hals<sup>2</sup>

<sup>1</sup>Laboratoire de Mécanique des Fluides - CNRS UMR6598  
Ecole Centrale de Nantes, 1 rue de la Noe, 44300 Nantes, France

<sup>2</sup>Centre for Ships and Ocean Structures  
Norges teknisk-naturvitenskapelige universitet, Otto Nielsens V. 10, 7491  
Trondheim, Norway

August 2, 2011

## Summary

This document reports the study of a floating oscillating water column (F-OWC) wave energy device in the frame of the project “Numerical estimation of energy production from a selection of Wave Energy Converters.” It contains a mathematical model and simulation results for the estimation of power delivery and dynamic performance.

The characteristics of the studied wave energy converter is expressed through the following criteria:

- The annual mean power.
- The yearly energy output per displacement.
- The yearly energy output per wetted surface.
- The power per unit of significant PTO force.

These criteria were estimated for the F-OWC using the mathematical model described in this report. Results are given in Table 1. The main conclusions from the study are as follows:

- The mean power level that one can expect from the F-OWC is about 340 kW on a site whose wave resource is about 25 kW/m. The uncertainty is about [-25%, +25%], and comes mainly from the modelling of the viscous losses.
- The yearly energy delivery per mass is about 1.6 kWh/kg, and the yearly energy delivery per wetted surface area is about 0.45 MWh/m<sup>2</sup> for the Yeu site which may be taken to represent typical European wave conditions.

Table 1: Evaluation criteria for the F-OWC WEC for chosen sites.

	Unit	SEM-REV	EMEC	Yeu	Lisboa	Belmullet
Mean power	[kW]	147	262	337	367	745
Capture width ratio	%	41	50	52	41	38
Energy/Mass	[kWh/kg]	0.7	1.3	1.6	1.8	3.6
Energy/Wetted surf.	[MWh/m <sup>2</sup> ]	0.19	0.35	0.45	0.49	1.0
Energy/PTO force	[kWh/N]	3.42	4.28	5.17	5.94	8.29

A paper version of this report, titled Modelling and Simulation of a Floating Oscillating Water Column, has been published in the Proceedings of the 30th International Conference on Ocean, Offshore and Arctic Engineering, 2011.

## Contents

<b>1 System description - The F-OWC</b>	<b>4</b>
<b>2 Mathematical model</b>	<b>5</b>
2.1 Computation of hydrodynamic parameters . . . . .	5
2.2 Time-domain model . . . . .	8
2.2.1 Time-domain impulse response functions . . . . .	8
2.2.2 Excitation force and excitation volume flow . . . . .	9
2.2.3 System dynamics . . . . .	9
2.3 Frequency-domain model . . . . .	11
<b>3 Simulation results and energy assessment</b>	<b>13</b>
3.1 Frequency domain . . . . .	13
3.2 Time domain . . . . .	17
<b>4 Conclusions and recommendations</b>	<b>17</b>

## 1 System description - The F-OWC

The system considered in this study is a particular type of oscillating water column (OWC) device known as the backward bent duct buoy (BBDB), first proposed by Masuda [1]. It is a floating OWC with a submerged opening aligned downstream of the incident wave propagation direction. It has a single air chamber and is free to move in six degrees of freedom. The device is constructed of thin steel walls enclosing the water column. The power conversion is provided by means of an air turbine connected to an electric generator. The motion of the water column relative to the OWC body creates oscillating pressure in the chamber and air flow through the turbine. Compared to its axisymmetric counterpart (see, e.g. [2]), a BBDB seeks to utilise its surge and pitch motions in addition to its heave to maximize the swept volume flow of the water column relative to the OWC body.

The considered geometry is inspired by the OEBuoy, shown in Fig. 1, which is developed by Ocean Energy Ltd. in Ireland [3]. The system will here be referred to as a floating oscillating water column (F-OWC). The device is assumed to operate in deep water.



Figure 1: OEBuoy (1:4 scale) at sea, courtesy of Wave Energy Centre.

The main device dimensions, the significant wetted surface, and mass are listed in Table 2. The latter two are chosen as two relevant cost-related measures that can be derived for any WEC. Another cost measure that is used in this study is the root mean square PTO force, defined as the pressure in the chamber times the internal free surface area.

The air turbine usually has an approximately linear pressure-flow relationship, hence the power take-off is modelled in this study as a simple linear damping.

Table 2: Main device dimensions, significant wetted surface, and mass.

Property	Value	Unit
Length	50	m
Width	24	m
Draft	13	m
Height of submerged opening	10	m
Significant wetted surface	6500	$\text{m}^2$
Significant mass	1800	tons

## 2 Mathematical model

Two models are available to represent the hydrodynamics of an OWC device, viz. the massless piston model [4] and the pressure distribution model [5, 6]. In the massless piston model, the internal free surface is assumed to behave as a massless rigid piston, and the internal free-surface condition is satisfied approximately. In the pressure distribution model the internal free-surface condition and the spatial variation of the internal free surface is represented accurately, and the hydrodynamics is described in terms of the dynamic air pressure in the chamber. The latter model is used in this study. The analysis is based on linear potential flow theory.

### 2.1 Computation of hydrodynamic parameters

We adopt a right-handed Cartesian coordinate system, with the  $x$ -axis pointing toward the submerged opening of the OWC and  $z$ -axis pointing upward.

WAMIT [7] is used for computing the hydrodynamic parameters. Multi-Surf [8] is used to prepare the body geometry, where it is only necessary to model the submerged body surface. The thin walls are assumed to have negligible thickness, and are represented using dipoles. Modelling them as walls with finite thickness and representing them using conventional source elements would otherwise require very small panels to avoid numerical problems. Due to transverse symmetry (about  $y = 0$ ), only half of the body ( $y \geq 0$ ) is panelled. The whole submerged body geometry is shown in Fig. 2.

Convergence studies are first carried out to investigate the effects of panel size and panel size distributions, as well as the effect of using low- or higher-order methods. Low- and higher-order refer to the method for representation of the body surface and solution. In the low-order method the body surface is discretized using flat quadrilateral elements, and the solutions for the velocity potential are approximated by piecewise constant values on each element. The higher-order method, on the other hand, is based on B-splines to represent the body surface, velocity potential, and pressure on the body surface. The presence of irregular frequency effects is also examined. Based on these studies, we decide to use a higher-order panel method with ‘cosine spacing’ for better accuracy close to the corners, and with option for removal of irregular frequency effects. The higher-order panel method is confirmed to be computationally more efficient and accurate than the low-order one.

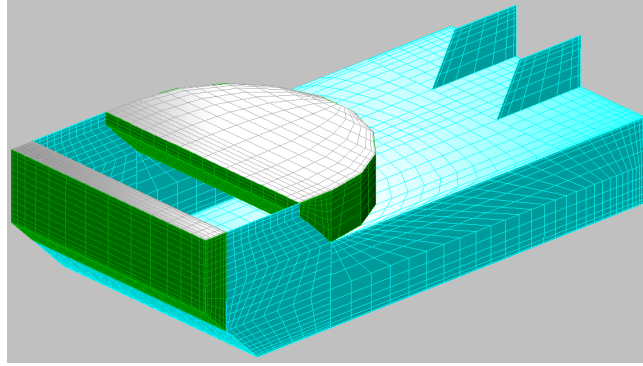


Figure 2: Submerged body geometry, showing source surfaces (green), dipole surfaces (cyan), and interior surfaces for removal of irregular frequency effects (grey).

We assume that the OWC is free to move in six degrees of freedom. Following the notations of [9], in the frequency domain the total hydrodynamic force acting on the body in  $j$ -direction can be written as

$$F_j = f_j A - \sum_{j'} Z_{jj'} u_{j'} - H_j^p p, \quad j = 1, \dots, 6, \quad (1)$$

where  $f_j$  is the excitation force coefficient,  $A$  is the undisturbed incident wave amplitude at origin,  $Z_{jj'}$  is the radiation impedance defined as the force on the body in  $j$ -direction induced by a unit velocity of the body in mode  $j'$ ,  $u_{j'}$  is the body velocity in mode  $j'$ , and  $H_j^p$  is the coupling coefficient defined as the force on the body in  $j$ -direction induced by a unit pressure  $p$  on the internal free surface. Likewise, the total volume flow through the internal free surface is expressed as

$$Q = qA - Yp - \sum_j H_j^u u_j, \quad (2)$$

where  $q$  is the excitation volume flow coefficient,  $Y$  is the radiation admittance defined as the volume flow induced by a unit pressure  $p$  on the internal free surface, and  $H_j^u$  is the coupling coefficient defined as the volume flow induced by a unit velocity of the body in mode  $j$ . It is understood that all these hydrodynamic parameters, also the wave amplitude, body velocities, and dynamic pressure are complex quantities, where the factor  $e^{i\omega t}$  applies.

In mathematical notations, the (frequency-dependent) hydrodynamic coefficients  $f_j$ ,  $Z_{jj'}$ ,  $H_j^p$ ,  $q$ ,  $Y$ , and  $H_j^u$  are defined as follows:

$$f_j = -i\omega\rho \frac{1}{A} \iint_{S_b} n_j \phi_d dS \quad (3)$$

$$Z_{jj'} = i\omega\rho \iint_{S_b} n_j \varphi_{j'} dS \quad (4)$$

$$H_j^p = i\omega\rho \iint_{S_b} n_j \varphi dS \quad (5)$$

$$q = \frac{1}{A} \iint_S \frac{\partial \phi_d}{\partial z} dS \quad (6)$$

$$Y = - \iint_S \frac{\partial \varphi}{\partial z} dS \quad (7)$$

$$H_j^u = - \iint_S \frac{\partial \varphi_j}{\partial z} dS, \quad (8)$$

where  $\rho$  is the water density,  $\phi_d$  is the diffraction potential, defined as the sum of the incident and scattered potentials,  $S_b$  is the mean body surface,  $S$  is the mean internal free surface,  $\mathbf{n}$  is the unit normal vector pointing out of the fluid domain, and we have denoted the radiation potential due to a unit velocity of the body in mode  $j$  as  $\varphi_j$  and the radiation potential due to a unit pressure on the internal free surface as  $\varphi$ .

The added mass and radiation damping terms, whose sum is the radiation impedance  $Z_{jj'}$ , and also the excitation force coefficient  $f_j$  are standard outputs of WAMIT. The excitation volume flow coefficient  $q$  can also be obtained quite straightforwardly by integrating the vertical diffraction velocity output by WAMIT over the internal free surface. This is done by distributing field points uniformly over the internal free surface and computing the velocity at each point. The integral is then approximated in a discrete manner. The coupling coefficient  $H_j^u$  can be obtained similarly.

It remains to evaluate the coefficients  $H_j^p$  and  $Y$  where three options are available [10]. In the first option special coding is required to modify the dynamic boundary condition on the internal free surface. It is then possible to evaluate the radiation potential due to the applied air pressure  $\varphi$  explicitly. The second option uses the concept of generalised modes [11]. The radiation potential due to the applied pressure is expressed as a superposition of modes of prescribed vertical velocity on the internal free surface. The internal free surface condition is then satisfied in an approximate manner. In the third option  $H_j^p$  and  $Y$  are evaluated using reciprocity relations, without solving for any additional potentials. The third option is used in this study and is described in the following.

The radiation conductance  $G = \Re\{Y\}$ , is related to the excitation volume flow coefficient  $q$  by the following reciprocity relation:

$$G = \frac{k}{8\pi\rho gv_g} \int_{-\pi}^{\pi} |q(\beta)|^2 d\beta = \frac{k}{4\pi\rho gv_g} \int_0^\pi |q(\beta)|^2 d\beta, \quad (9)$$

where  $k$  is the wave number,  $v_g$  is the group velocity, and  $\beta$  is the incident wave propagation direction. The last equality follows from transverse symmetry of the device. For deep water the equation further reduces to

$$G = \frac{\omega^3}{2\pi\rho g^3} \int_0^\pi |q(\beta)|^2 d\beta. \quad (10)$$

The radiation susceptance  $B = \Im\{Y\}$ , is related to  $G$  by the Kramers-Kronig relation, which takes the following form based on the discussion in the next subsection:

$$B(\omega) = -\frac{2\omega}{\pi} \int_0^\infty \frac{G(y)}{\omega^2 - y^2} dy, \quad (11)$$

where the integral is to be understood in the principal value sense. Lastly, it can be shown that  $H_j^p = -H_j^u$  [9, p. 250]. Hence, all the hydrodynamic parameters can be obtained without explicitly solving for  $\varphi$ .

The computations are performed for wave frequencies from 0 to 2.5 rad/s, in the interval of 0.01 rad/s. Computations are also performed for zero and infinite frequency limits. We assume infinite water depth and consider the case where the incident wave propagates in the direction of the positive  $x$ -axis. In our evaluation of the integrals in Eqns. (6) and (8), a total of 192 field points with uniform spacings are distributed over the internal free surface. The integral in Eqn. (10) is approximated by a sum over a discrete set of incident wave propagation directions. Here we use  $\beta = \pi/16, 3\pi/16, 5\pi/16, \dots, 15\pi/16$ . The principal value integral in Eqn. (11) is evaluated numerically using the Maclaurin's formula described in [12].

## 2.2 Time-domain model

### 2.2.1 Time-domain impulse response functions

Taking into account the frequency dependency of the hydrodynamic parameters and the nonlinear air compressibility, valve characteristics, and losses, we should use a time-domain model to describe the device dynamics. The equations of motion are in the form of integro-differential equations, where the frequency-dependent hydrodynamic parameters are taken up into convolution integrals. Equations (1) and (2) then take the following form:

$$\begin{aligned} F_j(t) &= \int_{-\infty}^{\infty} f_j(t - \tau) A(\tau) d\tau \\ &\quad - \sum_{j'} \left[ a_{jj'}(\infty) \dot{u}_{j'} + \int_{-\infty}^t k_{jj'}(t - \tau) u_{j'}(\tau) d\tau \right] \\ &\quad + C_j(\infty) p + \int_{-\infty}^t k_j^u(t - \tau) p(\tau) d\tau, \quad j = 1, \dots, 6, \end{aligned} \quad (12)$$

$$\begin{aligned} Q(t) &= \int_{-\infty}^{\infty} q(t - \tau) A(\tau) d\tau - \int_{-\infty}^t y(t - \tau) p(\tau) d\tau \\ &\quad - \sum_j \left[ C_j(\infty) u_j + \int_{-\infty}^t k_j^u(t - \tau) u_j(\tau) d\tau \right], \end{aligned} \quad (13)$$

where we have expressed  $Z_{jj'}$  and  $H_j^u$  as

$$Z_{jj'} = R_{jj'} + i\omega[a - a(\infty)] + i\omega a(\infty) \quad (14)$$

$$H_j^u = C_j(\infty) + [C_j - C_j(\infty)] + iJ_j, \quad (15)$$

and defined  $K_{jj'}$  and  $K_j^u$  as

$$K_{jj'} = R_{jj'} + i\omega[a - a(\infty)] \quad (16)$$

$$K_j^u = [C_j - C_j(\infty)] + iJ_j. \quad (17)$$

The time-domain IRFs  $f_j(t)$  and  $q(t)$  are non-causal, and therefore the range of integration is from  $-\infty$  to  $\infty$  as opposed to the causal IRFs  $k_{jj'}(t)$ ,  $y(t)$ , and  $k_j^u(t)$ , where the range of integration is from  $-\infty$  to  $t$ . If the input is also

causal, the lower integration limit of the integrals in Eqns. (12) and (13) is zero [9]. Based on the discussion in the preceding section, we take  $C_j(\infty)$  as non-zero, evaluated from the computed value of  $\Re\{\partial\varphi_j/\partial z\}$  for  $\omega \rightarrow \infty$ .

The IRFs  $f_j(t)$ ,  $k_{jj'}(t)$ ,  $q(t)$ ,  $y(t)$ ,  $k_j^u(t)$  and the frequency-dependent coefficients  $f_j(\omega)$ ,  $K_{jj'}(\omega)$ ,  $q(\omega)$ ,  $Y(\omega)$ ,  $K_j^u(\omega)$  are Fourier transform pairs. The radiation IRFs  $k_{jj'}(t)$ ,  $y(t)$ , and  $k_j^u(t)$  can be evaluated by either the cosine transform of the real part, or the sine transform of the imaginary part, of the corresponding frequency-dependent coefficients. The IRFs obtained from the cosine transform are compared with those obtained from the sine transform, where the two should give the same result. Good agreement is found only for certain mode combinations, however. Discrepancies appear to be due firstly to truncation error where usually the most significant truncation error is associated with the transform of the parameter having non-zero value at infinite frequency limit, and secondly to integration over the peak frequencies. Since the added mass does not usually go to zero at infinite frequency limit while the radiation damping does, we use the latter to evaluate the radiation impedance IRFs  $k_{jj'}(t)$ . Likewise, we use the transform of  $J_j(\omega)$  to evaluate the radiation coupling IRFs  $k_j^u(t)$ . On the behaviour of the IRFs, some of them are found to decay slowly, unlike those for conventional rigid bodies.

### 2.2.2 Excitation force and excitation volume flow

In Eqns. (12) and (13), the excitation force and the excitation volume flow are expressed as convolution integrals, i.e.,  $F_j^{\text{exc}}(t) = \int_{-\infty}^{\infty} f_j(t - \tau) A(\tau) d\tau$  and  $Q^{\text{exc}}(t) = \int_{-\infty}^{\infty} q(t - \tau) A(\tau) d\tau$  with the wave amplitude  $A(t)$  as input. As an alternative, we may treat these quantities themselves as input in the following way. First, we obtain the spectral density of the desired quantity as follows (shown here for  $F_j^{\text{exc}}(t)$ , likewise for  $Q^{\text{exc}}(t)$ ):

$$S_{F_j^{\text{exc}}}(\omega) = |f_j(\omega)|^2 S(\omega), \quad (18)$$

where  $S(\omega)$  is the wave spectrum. The excitation force is then given as

$$\begin{aligned} F_j^{\text{exc}}(t) &= \sum_{n=0}^{N/2} (a_{nj} \cos \phi_{nj} + b_{nj} \sin \phi_{nj}) \cos \omega_n t \\ &\quad + \sum_{n=0}^{N/2} (-a_{nj} \sin \phi_{nj} + b_{nj} \cos \phi_{nj}) \sin \omega_n t, \end{aligned} \quad (19)$$

where  $a_{nj}$  and  $b_{nj}$  are generated from a Gaussian distribution with variance  $S_{F_j^{\text{exc}}}(\omega_n) \Delta \omega$  [14]. Here,  $N$  is the number of values in the time series, determined by the required length of the series  $T$  and the time interval between values  $\Delta t$ . Also,  $\omega_n = n \Delta \omega$ , where  $\Delta \omega = 2\pi/T$ . In addition,  $\phi_{nj}$  is the phase (in radians) of  $f_j(\omega_n)$ . An inverse Fast Fourier Transform produces result identical to the sum in Eqn. (19), at a fraction of computer time, and thus is implemented in the simulation.

### 2.2.3 System dynamics

The dynamics of the whole system is modelled using the bond graph approach. A bond graph representation of the system, including hydrodynamic interac-

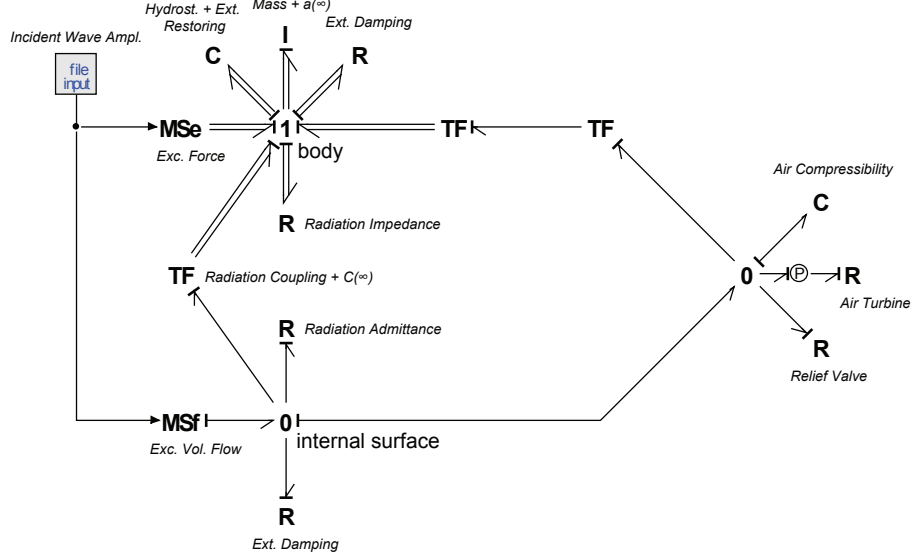


Figure 3: Bond graph model of the F-OWC.

tions, losses, air compressibility, relief valve, and air turbine, is shown in Fig. 3. Equations (12) and (13) are represented nicely in the bond graph structure. The force balance involving Eqn. (12) is represented by the multibonds connected to the 1-junction labelled ‘body,’ and the volume flow balance involving Eqn. (13) is represented by bonds connected to the 0-junction labelled ‘internal surface.’ The hydrodynamic coupling between the two is taken care of by the  $TF$  element connecting them. The first  $TF$  element to the right of ‘body’ 1-junction carries out the transformation required to obtain the vertical velocity of the body at the centre of the mean internal free surface, according to

$$u_b = \mathbf{T}^T \mathbf{u}, \quad (20)$$

where  $u_b$  is the vertical velocity of the body at the centre of the mean internal free surface and  $\mathbf{T}$  is the transformation vector given as

$$\mathbf{T} = (0, 0, 1, 0, -x_b, 0)^T, \quad (21)$$

where  $x_b$  is the  $x$ -coordinate of the centre of the mean internal free surface. The second  $TF$  element converts the force-velocity pair to pressure-volume flow pair with the internal mean free surface area as the transformation factor. The two branches, one from the ‘body’ 1-junction and the other from the ‘internal surface’ 0-junction, meet at a 0-junction, since it is the relative volume flow between the body and the internal free surface that is used for power conversion.

Due to air compressibility, the volume flow through the air turbine is less than the swept volume flow of the internal free surface. The air compressibility

can be modelled according to this nonlinear relationship:

$$p_0 + p = p_0 \left( \frac{V_0}{V_0 - \Delta V} \right)^\gamma, \quad (22)$$

where  $p_0$  is the atmospheric pressure and  $V_0$  is the average air volume in the chamber. The volume change due to compressibility is denoted by  $\Delta V$ . The specific heat ratio  $\gamma$  depends on whether the expansion and compression occur rapidly or slowly. The value  $\gamma = 1.4$  is usually adopted. This air compressibility relationship is contained in the bond graph element  $C$  labelled ‘Air Compressibility’ in Fig. 3.

A relief valve provides a way to keep the pressure in the air chamber within acceptable limits to prevent the turbine from stalling [15]. The excess volume flow passes through the valve to the atmosphere. A suitable model for the valve is given as conditional equations which determine the flow  $Q_v$  through the valve depending on the pressure difference across it:

$$Q_v = \begin{cases} \frac{p}{p_{cl}} Q_{cl} & \text{if } |p| < p_{cl} \\ \operatorname{sgn}(p) \left[ Q_{cl} + \frac{|p| - p_{cl}}{p_{op} - p_{cl}} (Q_{op} - Q_{cl}) \right] & \text{if } p_{cl} \leq |p| \leq p_{op} \\ C_d A_{\max} \sqrt{\frac{2}{\rho_a} |p|} \operatorname{sgn}(p) & \text{if } |p| > p_{op}, \end{cases} \quad (23)$$

where

$$Q_{cl} = C_d A_{\min} \sqrt{\frac{2}{\rho_a} p_{cl}} \quad (24)$$

$$Q_{op} = C_d A_{\max} \sqrt{\frac{2}{\rho_a} p_{op}}. \quad (25)$$

In the above,  $C_d$  is the discharge coefficient,  $\rho_a$  is the air density,  $A_{\min}$  is the leakage area, while  $A_{\max}$  is the fully open flow area. The pressures  $p_{cl}$  and  $p_{op}$  are reference pressures for the closing and opening of the valve. The valve is closed if  $|p| < p_{cl}$ , and is fully open if  $|p| > p_{op}$ . To be realistic, the leakage area  $A_{\min}$  is introduced to model leakage when the valve is closed. The  $R$  element labelled ‘Relief Valve’ in Fig. 3 is used to represent the relationship described in Eqns. (23) to (25).

The  $R$  elements labelled ‘Ext. Damping’ in Fig. 3 represent losses arising from viscous effects and mooring damping, for instance. These losses will reduce the body motions and the volume flow available to the turbine. External restoring forces are contributed by moorings, whose contribution we shall assume to be a small stiffness in surge. In this study we shall assume a linear pressure-volume flow relationship for the air turbine, where it is possible to tune the load resistance of the turbine.

### 2.3 Frequency-domain model

With the fact that an OWC device is usually fitted with a Wells turbine, which has approximately linear pressure-volume flow characteristics, it is appropriate to develop an alternative linear frequency-domain model of the device. A linear

frequency-domain model may be developed by assuming linear losses and linear air compressibility relationship as was done in [16], as well as assuming that there is no limit for the pressure in the air chamber.

Observing the bond graph structure (Fig. 3), we can write

$$\begin{pmatrix} \mathbf{f} \\ q \end{pmatrix} A = \begin{pmatrix} \mathbf{Z}_i & -\mathbf{H}_i \\ \mathbf{H}_i^T & Y_i + 1/R_L \end{pmatrix} \begin{pmatrix} \mathbf{u} \\ p \end{pmatrix}, \quad (26)$$

where

$$\mathbf{Z}_i = \mathbf{R} + \mathbf{R}_e + i\omega \left( \mathbf{M} + \mathbf{a} - \frac{\mathbf{K} + \mathbf{K}_e}{\omega^2} \right) \quad (27)$$

$$\mathbf{H}_i = \mathbf{H}^u + \mathbf{T}S \quad (28)$$

$$Y_i = Y + \frac{1}{R_f} + i\omega \frac{V_0}{\gamma p_0}. \quad (29)$$

In the above,  $\mathbf{f}$  is the excitation force coefficient vector,  $q$  is the excitation volume flow coefficient,  $A$  is the undisturbed incident wave amplitude at origin,  $\mathbf{u}$  is the body velocity vector,  $p$  is the air pressure in the chamber,  $R_L$  is the load resistance (assumed to be constant),  $\mathbf{R}$  is the radiation damping matrix,  $\mathbf{R}_e$  is the external damping matrix,  $\mathbf{M}$  is the inertia matrix,  $\mathbf{a}$  is the added mass matrix,  $\mathbf{K}$  is the hydrostatic stiffness matrix,  $\mathbf{K}_e$  is the external stiffness matrix,  $\mathbf{H}^u$  is the radiation coupling vector,  $\mathbf{T}$  is the transformation vector given previously in Eqn. (21),  $S$  is the internal free surface area,  $Y$  is the radiation admittance,  $R_f$  is the external damping related to the volume flow of the water column, and the last term in Eqn. (29) is the linearised air compressibility coefficient. For simplicity, we shall assume a diagonal  $\mathbf{R}_e$  matrix with constant values over the whole frequency range, as well as a constant  $R_f$ . It should be noted that the way the equation is rendered, the effect of  $R_f$  is such that smaller  $R_f$  results in greater loss of volume flow.

The linear system of equations contained in the matrix form (26) can be solved for  $\mathbf{u}$  and  $p$ . Knowing  $\mathbf{u}$  and  $p$ , the volume flow  $Q_L$  through the turbine can then be obtained from

$$Q_L = qA - Y_i p - \mathbf{H}_i^T \mathbf{u} \quad (30)$$

or, alternatively,

$$Q_L = \frac{p}{R_L}. \quad (31)$$

The instantaneous converted power  $P_u(t)$  is given by

$$P_u(t) = p(t)Q_L(t) = R_L Q_L^2(t), \quad (32)$$

and the mean converted power  $P_u$  by

$$P_u = R_L \sigma_{Q_L}^2, \quad (33)$$

where  $\sigma_{Q_L}^2$  is the variance of the volume flow through the turbine, which for harmonic oscillation is equal to  $|Q_L|^2/2$ .

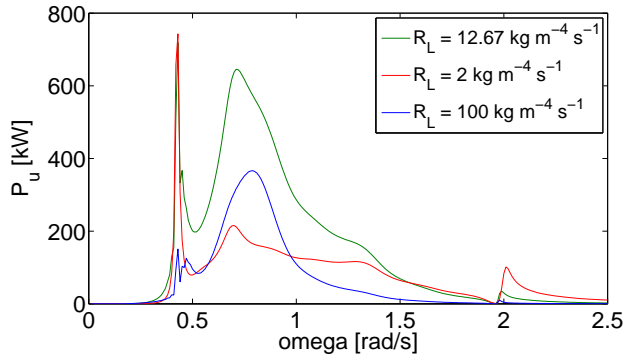


Figure 4: Converted power for a unit incident wave amplitude, for various values of load resistance.

### 3 Simulation results and energy assessment

#### 3.1 Frequency domain

For a given set of external stiffness and damping coefficients, the variation of converted power  $P_u$  with wave frequency  $\omega$  for a unit incident wave amplitude is plotted in Fig. 4 for different values of load resistance  $R_L$ , which is set to be constant over the whole frequency range. It should be noted that although we have included linear losses by the parameters  $\mathbf{R}_e$  and  $R_f$  in the frequency-domain model, we have assumed 100% turbine efficiency. An optimum constant  $R_L$  which maximizes the area below the power curve was found to be  $12.670 \text{ kg m}^{-4} \text{ s}^{-1}$ . It is shown that the device has good performance over a range of relevant wave frequencies occurring at sea, from 0.4 to 1.5 rad/s (equivalent to a range of wave periods from 4.2 s to 15.7 s). The displacements of the body, plotted against wave periods, are shown in Fig. 5. The variation of capture width  $d_a$  with wave frequency for  $R_L = 12.670 \text{ kg m}^{-4} \text{ s}^{-1}$  is plotted in Fig. 6 together with, for comparison, the maximum capture width  $d_{a\text{MAX}} = 3/k$  for an axisymmetric body oscillating in surge, heave, and pitch [17], where  $k$  is the wave number.

From the frequency-domain model we can also obtain the mean converted power for a given sea state, which is described by a combination of significant wave height  $H_s$  and peak period  $T_p = 2\pi/\omega_p$ . Here we shall use the JONSWAP spectrum to model a given sea state:

$$S(\omega) = \frac{\alpha g^2}{\omega^5} \exp\left(-1.25 \frac{\omega_p^4}{\omega^4}\right) \gamma^{a(\omega)}, \quad (34)$$

where

$$a(\omega) = \exp\left(-\frac{(\omega - \omega_p)^2}{2\sigma^2\omega_p^2}\right) \quad (35)$$

$$\sigma = \begin{cases} 0.07 & \text{for } \omega \leq \omega_p \\ 0.09 & \text{for } \omega > \omega_p \end{cases} \quad (36)$$

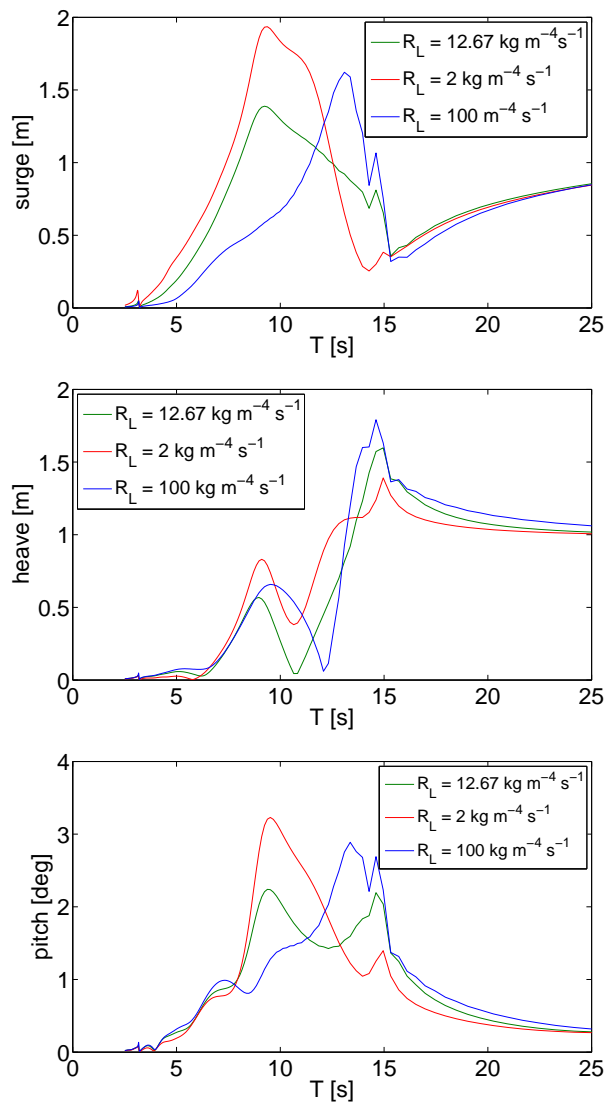


Figure 5: Body displacements for a unit incident wave amplitude, for various values of load resistance.

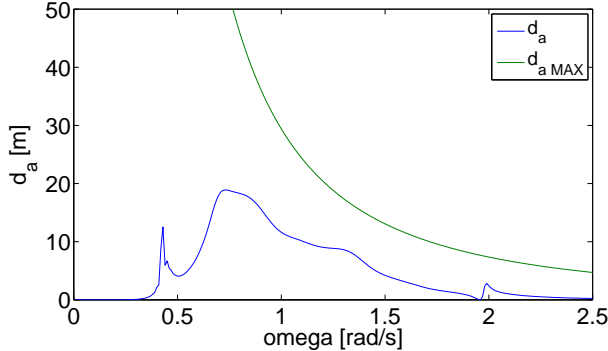


Figure 6: Capture width for  $r_l = 12.670 \text{ kg m}^{-4} \text{ s}^{-1}$ .

$$\alpha = 5.058 \frac{H_s^2}{T_p^4} (1 - 0.287 \ln \gamma) \quad (37)$$

The peakedness parameter  $\gamma$  is chosen to be 3 in this study. Following [18], the mean converted power for a given sea state can be obtained from

$$P_u = R_L \int_0^\infty \left| \frac{Q_L}{A} \right|^2 S(\omega) d\omega, \quad (38)$$

where the quantity  $Q_L/A$  is the frequency response function of the volume flow through the turbine. For a given sea state, there is a constant load resistance that maximizes the mean converted power. A matrix of these optimum constant load resistance together with a matrix of the corresponding mean converted power for a set of sea states ( $T_p = 3$  to 17 s,  $H_s = 0.5$  to 7.5 m) are shown in Fig. 7. With the scatter diagram of any given site available, the mean annual power output at that site can be obtained.

The mean annual power outputs at selected sites in Europe together with other evaluation criteria calculated from this frequency-domain model are summarized in Table 3. In the last criteria, the root mean square PTO force is given as

$$F_{\text{PTO rms}} = R_L \sigma_{Q_L} S, \quad (39)$$

where  $\sigma_{Q_L}$  is the standard deviation of  $Q_L$ :

$$\sigma_{Q_L}^2 = \int_0^\infty \left| \frac{Q_L}{A} \right|^2 S(\omega) d\omega. \quad (40)$$

The mean power per root mean square PTO force for each sea state is therefore

$$\frac{P_u}{F_{\text{PTO rms}}} = \frac{\sigma_{Q_L}}{S}. \quad (41)$$

As mentioned earlier, losses are taken into account through the addition of linear damping terms. They are applied to the body by introducing a diagonal damping matrix with constant values over the whole frequency range, taken as a

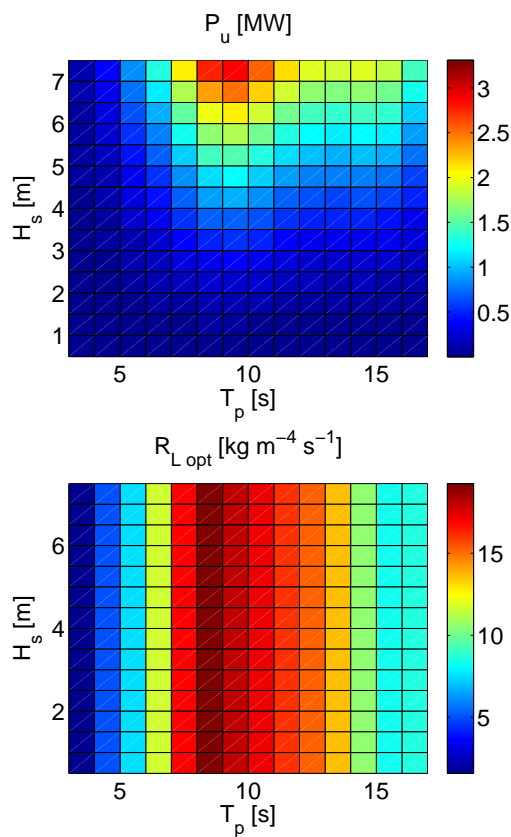


Figure 7: Matrices of mean converted power (top) and optimum constant load resistance (bottom), obtained from frequency-domain model.

certain percentage of the radiation damping. This has the effect of reducing the body motions. Another damping coefficient is also introduced with the effect of reducing the volume flow through the mean internal water surface. Uncertainty limits are obtained by taking these damping coefficients to be zero and twice the nominal values. They are found to be about [-25,+25] %.

Table 3: Evaluation criteria for the F-OWC WEC for chosen sites, obtained from frequency-domain model.

	Unit	SEM-REV	EMEC	Yeu	Lisboa	Belmullet
Mean power	[kW]	147	262	337	367	745
Capture width ratio	%	41	50	52	41	38
Energy/Mass	[kWh/kg]	0.7	1.3	1.6	1.8	3.6
Energy/Wetted surf.	[MWh/m <sup>2</sup> ]	0.19	0.35	0.45	0.49	1.0
Energy/PTO force	[kWh/N]	3.42	4.28	5.17	5.94	8.29

### 3.2 Time domain

The time-domain simulation is performed using an improved Euler method with a fixed step of 0.004 s, where the convolution terms are evaluated directly by trapezoidal integration at every time step. After numerical experimentation with several combinations of integration methods and step size, this combination of integration method and step size is found to yield acceptable results in the shortest time for this particular model. The integration methods considered are the Euler, improved Euler, and Runge-Kutta 4 methods.

Illustrative time histories of the device displacements, chamber dynamic pressure, and converted power for  $T_p = 8$  s,  $H_s = 3$  m, and  $R_L = 15$  kg m<sup>-4</sup> s<sup>-1</sup>, are shown in Fig. 8, for the cases where the pressure is unlimited (no relief valve) and where the pressure is limited by the operation of a relief valve. It is clear from Fig. 8 that the use of relief valve reduces the ratio of peak-to-average power.

## 4 Conclusions and recommendations

From these results and the study, the main conclusions are :

- The mean power level that one can expect from the F-OWC is about 340 kW on a site whose wave resource is about 25 kW/m. The uncertainty is about [-25%, +25%], and comes mainly from the modelling of the viscous losses.
- The yearly energy delivery per mass is about 1.6 kWh/kg, and the yearly energy delivery per wetted surface area is about 0.45 MWh/m<sup>2</sup> for the Yeu site which may be taken to represent typical European wave conditions.
- State-space representation of the convolution terms is necessary in order to accelerate the simulation time of the time-domain model.

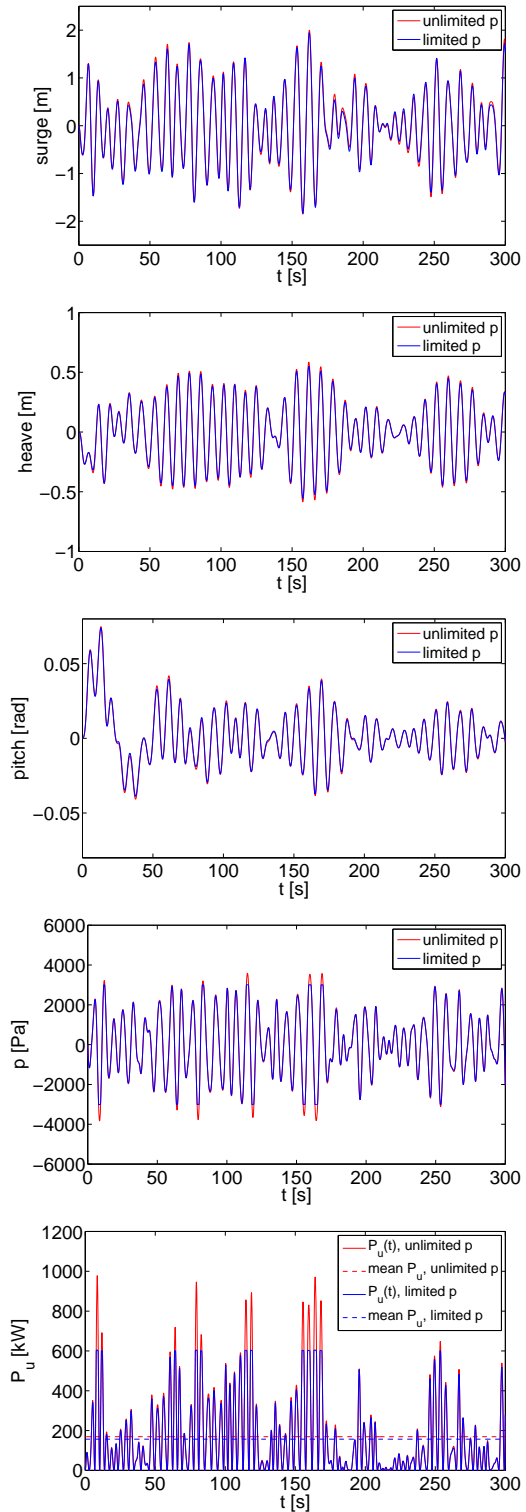


Figure 8: Time histories of device displacements, chamber dynamic pressure, and converted power, from time-domain model.

## References

- [1] Y. Masuda, H. Kimura, X. Liang, X. Gao, R. M. Mogensen, and T. Anderson. Regarding BBDB wave power generating plant. In G. Elliot and K. Diamantaras, editors, *Proceedings of the Second European Wave Power Conference*, pages 69–76, Lisbon, Portugal, 1996.
- [2] M. E. McCormick. A modified linear analysis of a wave-energy conversion buoy. *Ocean Engineering*, 3:133–144, 1976.
- [3] <http://www.oceanenergy.ie>.
- [4] D. V. Evans. The oscillating water column wave-energy device. *J. Inst. Maths Applics.*, 22:423–433, 1978.
- [5] D. V. Evans. Wave-power absorption by systems of oscillating surface pressure distributions. *Journal of Fluid Mechanics*, 114:481–499, 1982.
- [6] A. J. N. A. Sarmento and A. F. de O. Falcão. Wave generation by an oscillating surface-pressure and its application in wave-energy extraction. *Journal of Fluid Mechanics*, 150:467–485, 1985.
- [7] WAMIT. WAMIT, Inc., Chestnut Hill, MA, 2008. Version 6.4.
- [8] MultiSurf. AeroHydro, Inc., Southwest Harbor, Maine, 2009. Version 7.0.
- [9] J. Falnes. *Ocean Waves and Oscillating Systems*. Cambridge University Press, 2002.
- [10] C.-H. Lee and F. G. Nielsen. Analysis of oscillating-water-column device using a panel method. In V. Bertram, editor, *Proceedings of the 11th International Workshop on Water Waves and Floating Bodies*, pages 1–4, Hamburg, Germany, 1996.
- [11] C.-H. Lee, J. N. Newman, and F. G. Nielsen. Wave interactions with an oscillating water column. In *Proceedings of the 6th International Offshore and Polar Engineering Conference*, pages 82–90, Los Angeles, USA, 1996.
- [12] K. Ohta and H. Ishida. Comparison among several numerical integration methods for Kramers-Kronig transformation. *Applied Spectroscopy*, 42(6):952–957, 1988.
- [13] E. R. Jefferys. Device characterisation. In *Power from Sea Waves*, pages 413–438. 1980.
- [14] M. J. Tucker, P. G. Challenor, and D. J. T. Carter. Numerical simulation of a random sea: a common error and its effect upon wave group statistics. *Applied Ocean Research*, 6(2):118–122, 1984.
- [15] A. F. de O. Falcão, L. C. Vieira, P. A. P. Justino, and J. M. C. S. André. By-pass air-valve control of an OWC wave power plant. *Journal of Offshore Mechanics and Arctic Engineering*, 125:205–210, 2003.
- [16] A. Brendmo, J. Falnes, and P. M. Lillebekken. Linear modelling of oscillating water columns including viscous loss. *Applied Ocean Research*, 18(2-3):65–75, 1996.

- [17] J. N. Newman. The interaction of stationary vessels with regular waves. In *Eleventh Symposium on Naval Hydrodynamics*, pages 491–501, London, 1976.
- [18] R. Taghipour and T. Moan. Efficient frequency-domain analysis of dynamic response for the multi-body wave energy converter in multi-directional waves. In *Proceedings of the 18th International Offshore and Polar Engineering Conference*, pages 357–365, Vancouver, Canada, 2008.
- [19] A. Babarit, J. Hals, A. Kurniawan, T. Moan, and J. Krokstad. Power absorption measures and comparisons of selected wave energy converters. In *Proceedings of the 30th International Conference on Ocean, Offshore and Arctic Engineering*, Rotterdam, The Netherlands, 2011.

## **Chapter 5**

# **A floating heave-buoy array (F-HBA) inspired by the Pontoon wave energy converter**

# Numerical estimation of energy production from a selection of Wave Energy Converters – Pontoon Power Converter (PPC)

Made Jaya Muliawan<sup>1</sup>, Aurelien Babarit<sup>2</sup>, Jørgen Hals<sup>1</sup>

<sup>1</sup>Centre for Ships and Ocean Structures

Norges teknisk-naturvitenskapelige universitet, Otto Nielsens V. 10, 7491 Trondheim, Norway

<sup>2</sup>Laboratoire de Mecanique des Fluides – CNRS UMR6598

Ecole Centrale de Nantes, 1 rue de la Noe, 44300 Nantes, France

April 29, 2011

## Summary

This document reports the study of the Pontoon Power Converter (PPC) in the frame of the project "Numerical estimation of energy production from a selection of Wave Energy Converters". It contains a mathematical model and simulation results for the study of the PPC.

Results of the study are the following measures:

- The annual mean power.
- The yearly energy output / displacement.
- The yearly energy output / wetted surface.
- The duration curves.

These measures were estimated for the PPC using the mathematical model described in this report. Results are given in the following Table 1 and in Figure 1.

From these results and the study, main conclusions are:

- The mean power level that one can expect from the PPC with 10 pontoons is about 400 kW or averagely 40 kW per pontoon on a site whose wave resource is about 27 kW/m and with a PPC orientation of 90 degrees to the incoming wave. The uncertainty is about [-10%, +25%]. It comes from the modelling of the viscous losses.
- Aligning the WEC in the direction of incoming waves significantly changes the distribution of the power absorbed by each pontoon and the mean power absorption. It shows that an orientation of 90 degrees to the incoming waves (i.e. waves with wave crests alongside the Bridge) gives the largest power conversion. Decreasing the orientation angle from 90 degrees to 45 degrees will decrease the power about [-3%, -30%] and from 90 deg to 0 deg will decrease the power about [-10%, -50%].

- With structure properties as specified in the present study, slacks on the wires that connect the Bridge and the Ballast Basket easily occur. Larger pre-tension, optimization on the overall structure properties or other re-design is needed to eliminate this problem. However, this has not been covered in the present study. This study assumes that the wires are strong enough to face the slack behaviour.

Table 1. Estimated values for the evaluation criteria for the PPC with 10 pontoons.

Site		SEM-REV	EMEC	Yeu	Lisboa	Belmullet
$\gamma$		1	1	3.3	3.3	3.3
Mean Power	[kW]	224	326	409	317	417
Wave pow. Resources	[kW/m]	14.8	21.8	26.8	37.5	80.6
Capture width	[m]	15.1	15.0	15.2	8.4	5.2
Energy/mass	[kWh/kg]	0.42	0.62	0.77	0.6	0.78
Energy/Wetted surface	[MWh/m <sup>2</sup> ]	0.43	0.63	0.79	0.61	0.80

The uncertainty is estimated to [-10, +25]%

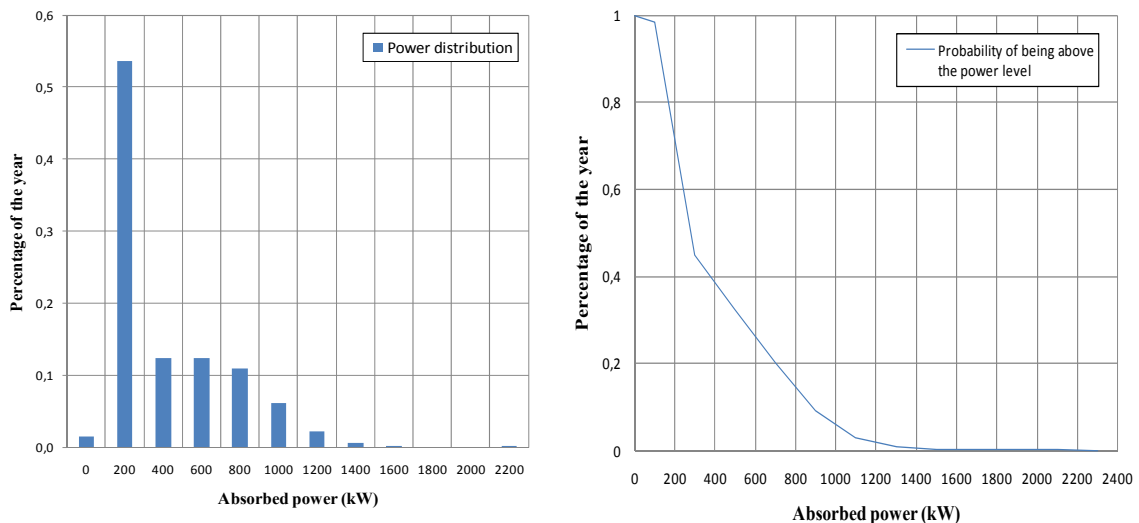


Figure 1. Distribution of the absorbed power on a typical 27 kW/m wave site.

- The output power of the PPC with 10 pontoons could be rated to 1.4 MW without losing a significant amount of production. Limitation of the instantaneous absorbed power to 10 times the mean output power (4 MW) would not significantly reduce the mean absorbed power.

## Contents

1	System description – The Pontoon Power Converter (PPC).....	4
1.1	Dimensions and mechanical parameters .....	4
1.2	PTO and control.....	6
1.3	Cost related criteria.....	7
1.4	Comments from the Pontoon developer .....	7
2	Modelling.....	8
2.1	Calculation of hydrodynamic coefficients and functions .....	8
2.2	Power take-off system .....	9
2.2.1	PTO force distribution .....	9
2.2.2	End stops .....	10
2.3	Wires and mooring system.....	11
2.4	Viscous damping forces.....	11
3	Simulation results and energy assessment .....	12
3.1	Static condition.....	12
3.2	Optimisation of the PTO force (without constrains) and assessment of the effect of wave height, period and direction on the output power .....	12
3.3	Negative tension (slack) on the wire – an observation .....	20
3.4	Assessment of the influence from the viscous damping.....	21
3.5	Optimisation of the PTO force (with constrains) .....	23
3.6	Power matrix and criteria .....	24
4	Conclusions and recommendations .....	27

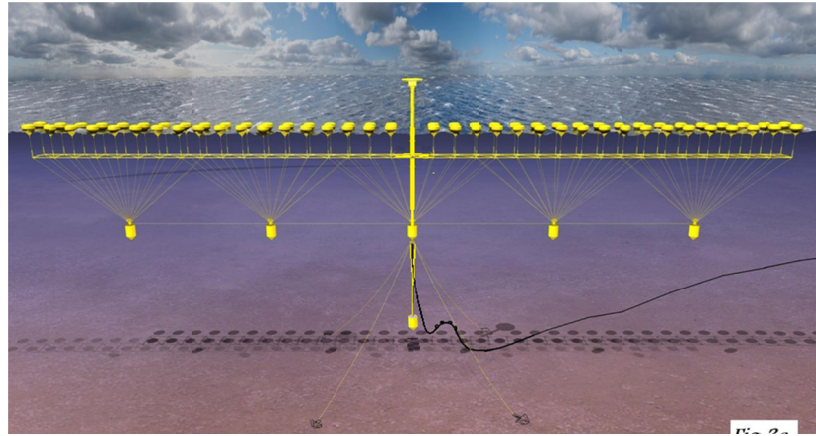


Figure 2. Artistic view of the PPC

## 1 System description – The Pontoon Power Converter (PPC)

The PPC is a multibody floating wave energy converter that in full scale will have 73 pontoons (floating buoys) connected a submerged structure called “the Bridge”, and five “Ballast Baskets” as illustrated in Fig. 2. The wave energy absorbed by the PPC will come from the motions of each pontoon relative to the point on the Bridge where it is pinned. The total net buoyancy force of the Pontoons will be balanced by net gravity forces of the Bridge and the Ballast Baskets. The Bridge and the Ballast Baskets are connected by wires which get their pre-tension from the net gravity force of the Ballast Baskets.

### 1.1 Dimensions and mechanical parameters

In the present study, where the model consists only of 10 pontoons, a Bridge of reduced size and 2 Ballast Baskets is modelled. It is expected to be a simpler but good alternative to the full system that will be able to indicate the overall behaviour of the PPC and its ability to absorb wave power. The sketch of the modelled PPC is shown in Fig. 3, and the parameters of the system are summarised in Table 2, which are given by the PPC’s concept owner. The parameters result from merely downscaling according to the reduced number of buoys (i.e. a factor of 10/73), except that that a higher moment of inertia for the Bridge is applied in the model in order to make the Bridge more stable and thus more similar to the full size behaviour.

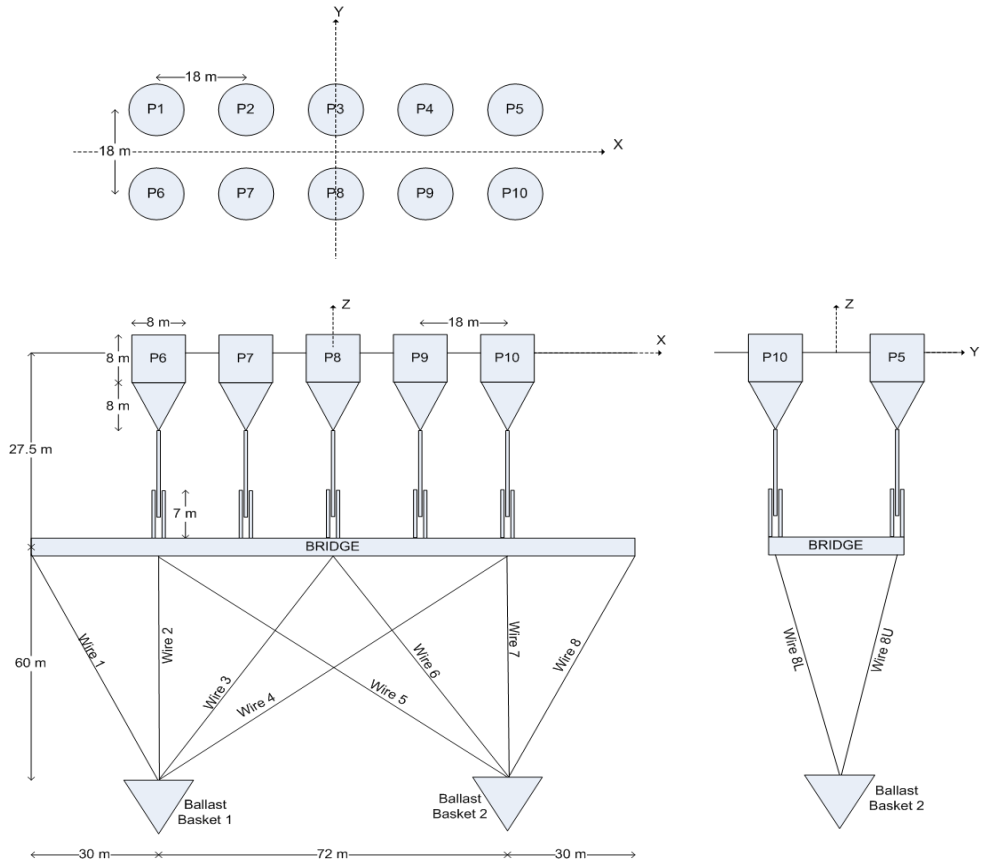


Figure 3. Sketch of the PPC modelled in the present study.

Table 2. System parameters of the modelled PPC.

Property	Value	Unit
<i>Pontoon</i>		
Diameter at WL	8	m
Draft	13.4	m
Height	16	m
Displacement	406.15	$\text{m}^3$
Mass	364.26	Tonnes
Centre of mass	0.6	m below the free surface
Moment of inertia $I_{xx}$	$2.1 \times 10^4$	$\text{t.m}^2$
Moment of inertia $I_{yy}$	$2.1 \times 10^4$	$\text{t.m}^2$
Moment of inertia $I_{zz}$	$4.5 \times 10^3$	$\text{t.m}^2$
Distance between pontoons	18	m (centre to centre)
<i>Bridge (for 10 pontoons)</i>		
Outer diameter of the member	0.5	m
Length	132	m
Width	18	m
Displacement (including PTO)	272.2	$\text{m}^3$
Mass (including PTO)	467.3	Tonnes
Centre of mass	27.5	m below the free surface
Moment of inertia $I_{xx}$	$7.4 \times 10^4$	$\text{t.m}^2$
Moment of inertia $I_{yy}$	$1.9 \times 10^5$	$\text{t.m}^2$
Moment of inertia $I_{zz}$	$1.3 \times 10^5$	$\text{t.m}^2$

Property	Value	Unit
<b>Ballast Basket</b>		
Diameter	15	m
Height	17.5	m
Displacement	148.5	$\text{m}^3$
Mass	318.2	Tonnes
Centre of mass	96	m below the free surface
Moment of inertia $I_{xx}$	$1.8 \times 10^7$	$\text{t.m}^2$
Moment of inertia $I_{yy}$	$1.8 \times 10^7$	$\text{t.m}^2$
Moment of inertia $I_{zz}$	$5.9 \times 10^4$	$\text{t.m}^2$
<b>Power take-off machinery</b>		
Stroke length	7	m
Average force	510.5	kN
Stiffness end stops	$10^6$	kN/m

## 1.2 PTO and control

According to the information from the concept owner, the PPC will use a hydraulic power take-off (PTO) machinery. The hydraulic PTO is modelled as a coulomb damping force acting in opposite direction of the relative velocity  $v_{rel}$  between the Pontoon and the Bridge's pinned joint. The PTO force for this type of machinery can be written as:  $F_{PTO} = F_{mean} - dF_{PTO} \operatorname{sign}(v_{rel})$ , where  $F_{mean}$  is the force that is needed to hold the bridge and the ballast baskets (or actually 1/10<sup>th</sup> of this force as we have 10 buoys). See illustration in Fig. 4 below. Further,  $dF_{PTO}$  is the half of force difference (pressure difference times the piston area) set in the hydraulic circuit connected to the cylinders.

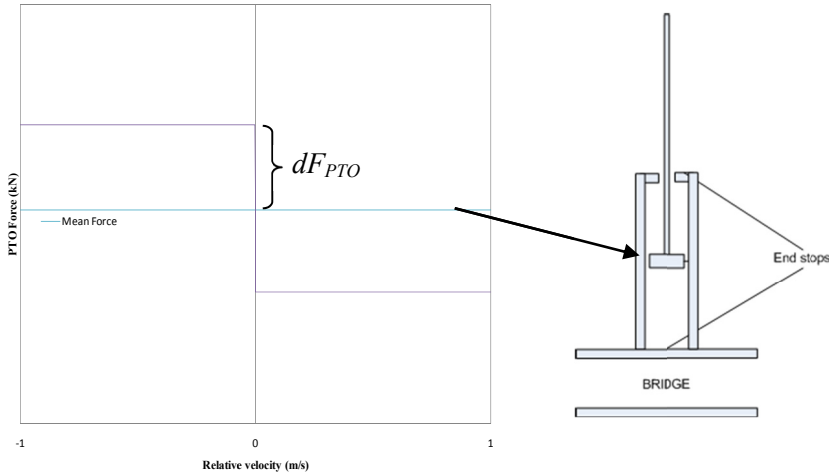


Figure 4. Coulomb damping of the PTO.

The PTO force will be optimised by adjusting the value of  $dF_{PTO}$  such as to maximise the power output.

### **1.3 Cost related criteria**

The wetted surface and mass are two parameters relevant for the cost of energy provided by any wave energy converter.

In the case of the PPC, as it is a self-reacting device, all thirteen parts of the system - 10 pontoons, a Bridge and 2 Basket Ballasts – are included in the definition of the PPC significant wetted surface and significant mass. The weight and surface of the wires and mooring system are not taken into account. They are expected to be small. The totals of the significant wetted surface and mass of the modelled PPC are presented in Table 3.

Table 3. Significant wetted surface and significant mass of the modelled PPC wave energy converter.

Criteria	unit
Significant wetted surface	$\text{m}^2$
Significant mass	tonnes

### **1.4 Comments from the Pontoon developer**

In working with this study we have been in contact with the developer of the Pontoon device. They have been informed about our study, and have also contributed with comments and specifications for the setup of the mathematical model for which we are grateful. After having received a draft version of this report the developer was invited to give a written comment to be included in the report, which we cite below:

1        *General comment about Energy/mass ratio, ref Tables 7 and 8:*

*The energy/mass ratio for the PPC is calculated using the gross mass. For the PPC model that consists of 10 pontoons, more than 3000 tonnes of this mass was intended to be water ballast in the pontoons, which is almost 2/3 of the total mass of 4746 tonnes in Table 3. The energy/mass ratio for the PPC would thus look better if the dry mass was applied. However, this may be the case also for the other WEC concepts that are compared, so we cannot indicate how a similar comparison based on dry mass will change the PPC's competitiveness. However, we believe that the ratio energy to dry mass could be a better indicator for how economical the power production will be.*

*As mentioned in the report, a significant amount of the PPC's dry mass is cheap stone material, so the expensive part of the mass is even less. Therefore, the ratio of energy to steel mass could probably be an even better indicator for comparing the concepts.*

2        *Effect of orientation angle and ballast basket geometry for PPC.*

*In the study, three orientation angles of the bridge are considered; 0°, 45° and 90°. The energy absorption has been found to highest at 90°, and is found to be lower at 45° and lowest at 0°. The first pontoons typically have a higher power output than the pontoons further down the row, although the degree of reduction differs from case to case. The main explanation for*

this we believe is that the shielding effect is becoming increasingly dominant as the angle becomes low. It is an important result that the optimum power output is found at the high angle. However, we think that there may be some optimum angle that is missed in the study, as there is no angle studied between  $90^\circ$  and  $45^\circ$ .

The basic idea behind the bridge concept is that its x axis can span over a certain distance in the wave direction in order to have pontoons working in different phase along the length axis of the bridge. We believe that an optimum can be found when the orientation is changed a relatively small angle (perhaps between  $5^\circ$  to  $25^\circ$ ) away from the  $90^\circ$  direction. Then a certain effect of the different phases (the “bridge effect”) is achieved while the angle is still high enough to maintain a relatively low shielding effect.

We believe that the “bridge effect” at an angle different from  $90^\circ$  may lead to improvement in the PPC’s energy uptake especially for long waves (typical for the Lisboa site) compared to the calculated results PTO for  $90^\circ$  angle to the wave.

### 3 Conclusion

From the considerations about angles we believe there is a potential for increasing the PPC’s energy conversion compared to the results in the study. However, we believe that the study in general gives a mainly correct indication of the PPC’s energy harvesting capability, and that it will be interesting to see how future tests with a physical model will compare to the results from this study.

09.11.2011

Nils Myklebust

## 2 Modelling

### 2.1 Calculation of hydrodynamic coefficients and functions

To perform hydrodynamic analysis, the panel models of each parts of the PPC used in the study shown in Fig. 5 were developed using GeniE [1]. Further, the hydrodynamic properties of each part of the PPC were estimated in frequency domain using HydroD [2]. Hydrodynamic interaction between the Pontoons is included in the study. However, the effects of the Bridge and the Ballast Basket motions on the Pontoons hydrodynamic properties are neglected. Fig. 6 illustrates how the panel model is applied in the hydrodynamic analysis of the multibody system in HydroD.

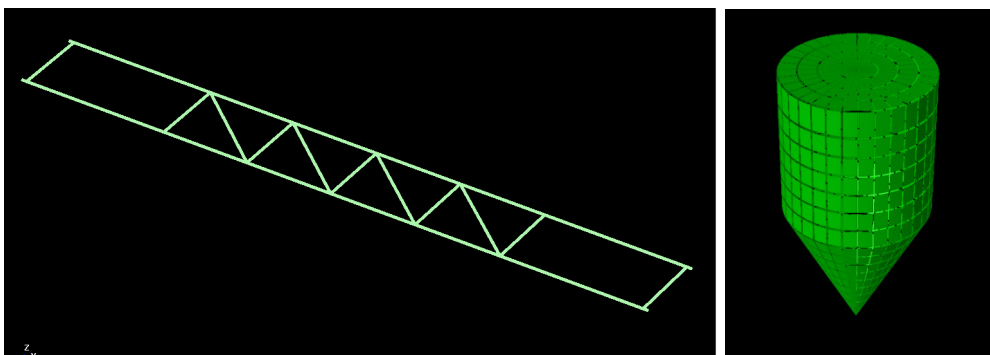


Figure 5. Panel models of the Bridge and the Pontoon in the study.

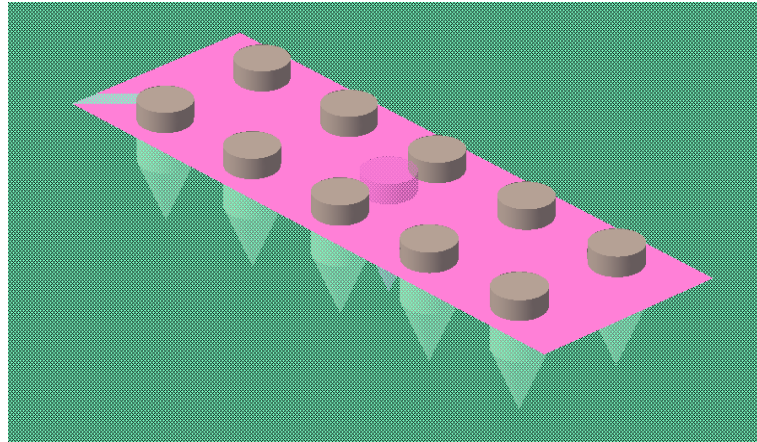


Figure 6. Ten Pontoon panel models are included to estimate the hydrodynamic properties of the full system, including hydrodynamic interaction. Computations are made using the HydroD software [2].

## 2.2 Power take-off system

### 2.2.1 PTO force distribution

The hydraulic PTO system is modelled as a coulomb damping term that can be written as:

$$F_{PTO} = F_{mean} - dF_{PTO} \operatorname{sign}(v_{rel}) \quad (1)$$

The mean force  $F_{mean}$  for the specified PPC properties can be calculated by considering static position of the system as illustrated in Fig. 7.

$$\begin{aligned} F_{mean} &= \text{net buoyancy of the Pontoon} - (\text{net gravity of the Bridge} + \text{net gravity of the Ballast Basket}) \\ &= (((406.15 \text{ m}^3 \cdot \rho_{\text{salt water}}) - 364.3 \text{ kg}) - ((467.3 \text{ kg} - (272.2 \text{ m}^3 \cdot \rho_{\text{salt water}})) / 10) \\ &\quad - ((318.2 - (148.5 \cdot \rho_{\text{salt water}})) / 5)) \cdot g \\ &= 510.5 \text{ kN} (= 42.75 \text{ bar with the piston of 39 cm in diameter}) \end{aligned}$$

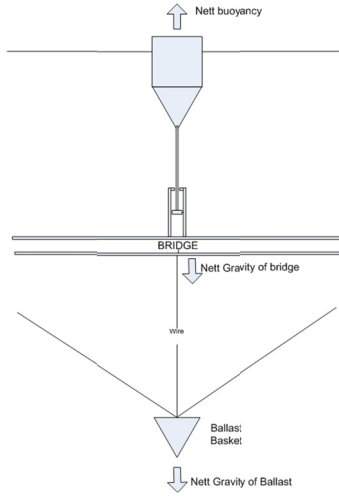


Figure 7. Static position of the system.

Values of  $dF_{PTO}$  are varying from 50 kN up to 500 kN in the study. Consider diameter of the piston of 39 cm, 50 kN will refer to 4.1 bar of the pressure in the PTO, which is small enough. The  $dF_{PTO}$  of 500 kN is chosen as the maximum limit to avoid the negative PTO force that will result to negative tension of the PTO lines. Some PTO force distributions in this study are shown in Fig 8.

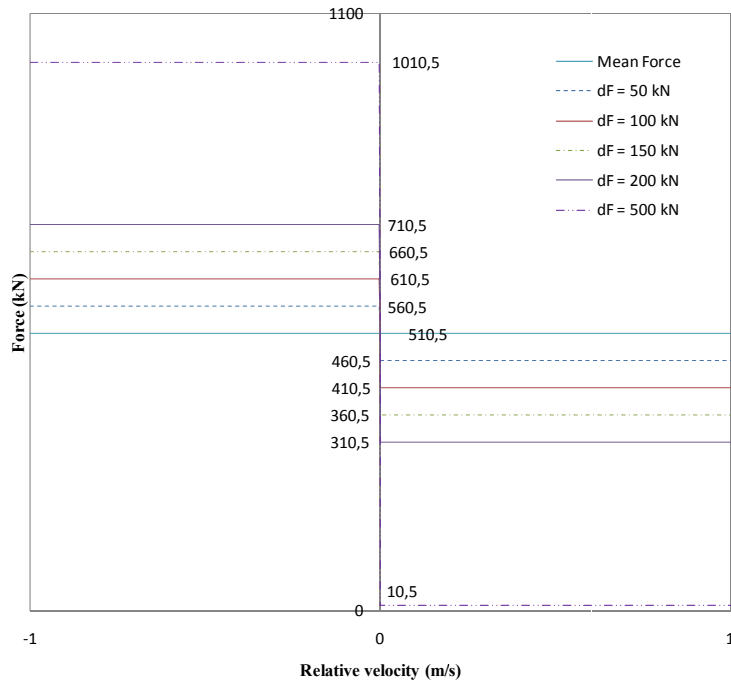


Figure 8. Distribution of the PTO forces.

### 2.2.2 End stops

Fender feature in SIMO [3] is applied to model the end stops. In the study, the stiffness of  $10^6$  kN/m is used in each fender and the total stroke before end stops are engaged is set to be 7 m as illustrated in Fig 4.

## 2.3 Wires and mooring system

Wires that connect the Bridge and the Ballast Baskets are simply modelled as a linear spring that has axial stiffness  $EA$ . The connection between the wire and the structure is considered flexible (pin joints). No negative tension on the wire is set during the simulation.  $EA$  of  $10^6$  kN/m is used for each wire for all simulation performed in this study.

There is no mooring line model included in the simulation. However, a linear stiffness of  $10^3$  kN/m is introduced on the Ballast Baskets in the horizontal (x and y) directions in order to keep the system in place.

## 2.4 Viscous damping forces

Viscous damping forces have been included and modelled under the form of the Morison equation, given by:

$$\vec{F}_{viscous} = -\frac{1}{2}\rho C_d A (\vec{V}_G - \vec{V}_0) |\vec{V}_G - \vec{V}_0|, \quad (2)$$

where:

- $\vec{V}_0$  is the undisturbed flow velocity taken at the instantaneous position of the gravity centre of the moving body.
- $\vec{V}_G$  is the velocity of the structure
- $C_d$  is the viscous coefficient on the specific direction that has projection area  $A$ .
- $\rho$  is the sea water density

**Viscous forces on the Pontoons and the Ballast Basket:** In surge and sway, the Keulegan-Carpenter number  $KC_{x,y}$  is expected to be in the range [0,4]. In heave,  $KC_z$  is in the range [0,1]. Considered as small KC, the drag coefficient can be estimated around 0.2 KC for cylinder as given in [4]. Viscous drag coefficient then should be between 0.2 and 0.8. In this study, they were chosen equal to  $C_{dx}=C_{dy}=C_{dz}=0.5$  as nominal viscous damping coefficient both for the Pontoon and the Ballast Basket.

**Viscous forces on the Bridge:** The Bridge consists of pipe elements. The nominal viscous drag coefficient for pipes is commonly set to around 0.7 in the transversal direction. This value could be doubled if the roughness of the pipe surface changes from smooth to rough. In this study,  $C_d = 0.7$  is chosen for transversal direction. Due to long structure, one cannot neglect the variation of the velocity along the members. Hence, the viscous damping force on the Bridge is estimated by a sum of discrete contributions found by sectioning of the Bridge structure. In this study, each discrete section of the Bridge is chosen to be 3 m. This means that the viscous force on the Bridge is calculated by sum of 154 discrete sections' contribution.

### 3 Simulation results and energy assessment

All simulations in this study are performed in time domain using the SIMO software [3], and the results are post-processed using Matlab [5]. Unless otherwise specified, the parameters given in Table 1 were used in all the simulations presented here.

#### 3.1 Static condition

The static condition of the system is estimated by applying small amplitude waves on the model. This is needed to see whether the model has the appropriate properties as specified. Some of the results that represent static conditions are presented in Fig. 9. The model is able to give appropriate PTO forces during this static condition, i.e. it is equal to mean force (510.5 kN). The tensions of the wires are also seen to be reasonable. The wire tension during static condition is the initial tension of the wire. It depends on the net gravity forces of the Ballast Baskets. This test confirms that the model is able to present the correct properties of the system.

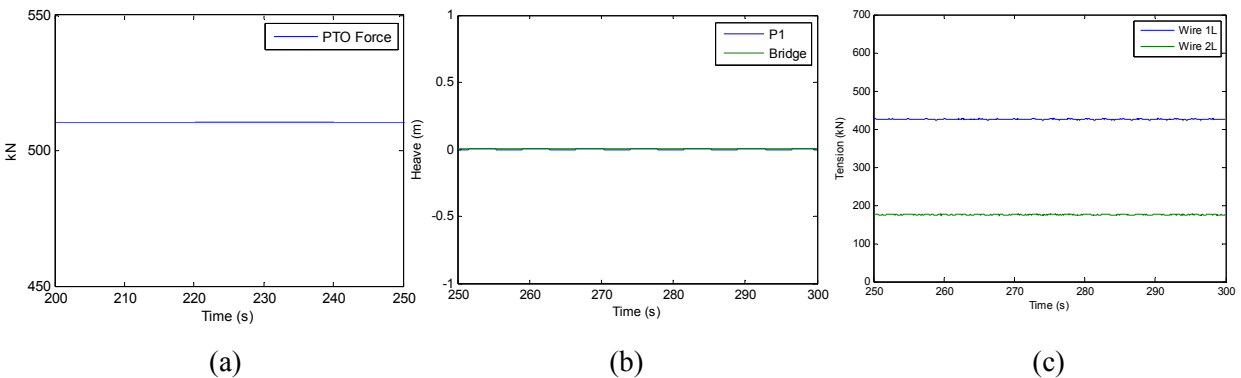


Figure 9. Results of applying small waves on the model to represent static conditions of the system; (a) PTO force, (b) heave motion of Pontoon P1 and the Bridge and (c) tension of wires 1L and 2L.

#### 3.2 Optimisation of the PTO force (without constrains) and assessment of the effect of wave height, period and direction on the output power

To get a better understanding of how the PTO force setting affects the power absorbed by the PPC, the power function ( $p(T) = P_a(T)/A$ , average absorbed power as a function of wave period divided by incident wave amplitude) is calculated for several different PTO force settings. As described before, only  $dF_{PTO}$  has been varied in the present study. The effects of the incoming wave height and direction on the power function are also assessed. Table 4 shows the simulation cases with varying sea state and PTO force conditions. All simulations in this table are performed with regular waves and viscous forces have been neglected in the model. Fig. 10 illustrates the three incoming wave directions specified in the Table 4.

Table 4. PTO Force and waves properties setting.

Case number	Wave Direction	Wave Height (m)	$dF_{\text{PTO}}$ (kN)	$C_d/C_{d,\text{nominal}}$
1a	0	1	50	0
2a	0	1	100	0
3a	0	1	150	0
4a	0	1	200	0
5a	0	2	100	0
6a	0	3	100	0
1b	45	1	50	0
2b	45	1	100	0
3b	45	1	150	0
4b	45	1	200	0
5b	45	2	100	0
6b	45	3	100	0
1c	90	1	50	0
2c	90	1	100	0
3c	90	1	150	0
4c	90	1	200	0
5c	90	2	100	0
6c	90	3	100	0

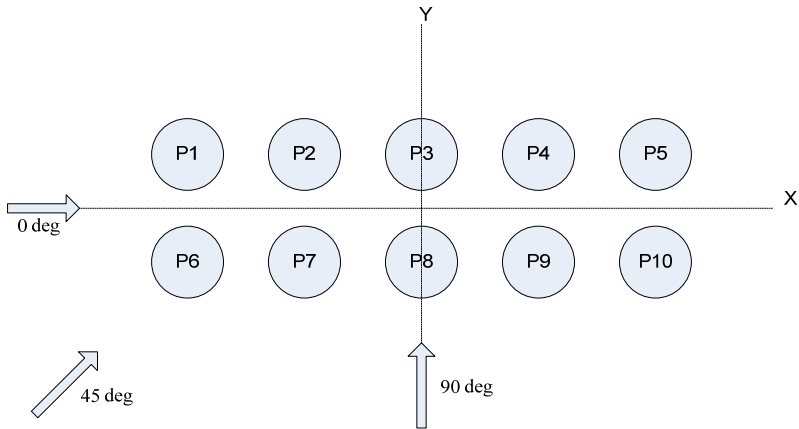


Figure 10. Three different wave directions considered in the simulations.

#### Wave direction: 0 deg (cases 1a – 6a)

Fig. 11 shows the power function computed for cases 1a – 6a, which apply a wave direction of 0 degrees. One can see that starting from the low value, the effect of increasing  $dF_{\text{PTO}}$  is first to shift the peak of absorbed power to higher wave periods and to decrease the maximum power absorption. From the same figure, we also can see that the bandwidth of the system becomes narrower when  $dF_{\text{PTO}}$  is increased.

An opposite trend is observed from Fig. 11 (b) when wave height is increased while keeping  $dF_{\text{PTO}}$  constant. Increasing the wave height results in shifting the peak of power absorption to lower wave period and increasing the maximum power. Broader bandwidth of the system occurs when wave height is increased.

Comparing Figs. 11 (a) and (b), one can understand that the observed trends are related to each other. Knowing that the PTO force setting is varied as indicated in Fig. 8, where the direction of the

force is changing but the magnitude  $dF_{PTO}$  of the opposing force is kept constant, it is understood that the effect of increasing  $dF_{PTO}$  and keeping the wave height constant will have the same effect on the power function as decreasing the wave height and keeping  $dF_{PTO}$  constant.

The setting of the  $dF_{PTO}$  parameter has two effects: (i) it decides when the check external forces on the buoy is large enough make it move (corresponding to the threshold pressure for the check valve), and (ii) it sets the magnitude of the resistance that the machinery yields on the buoy when it moves. In this way this one control parameter influences both the phase of the buoy oscillation and its amplitude. Ideally, one would like to control both of these (phase and amplitude) independently.

This may be achieved with a more sophisticated hydraulic machinery than projected here.

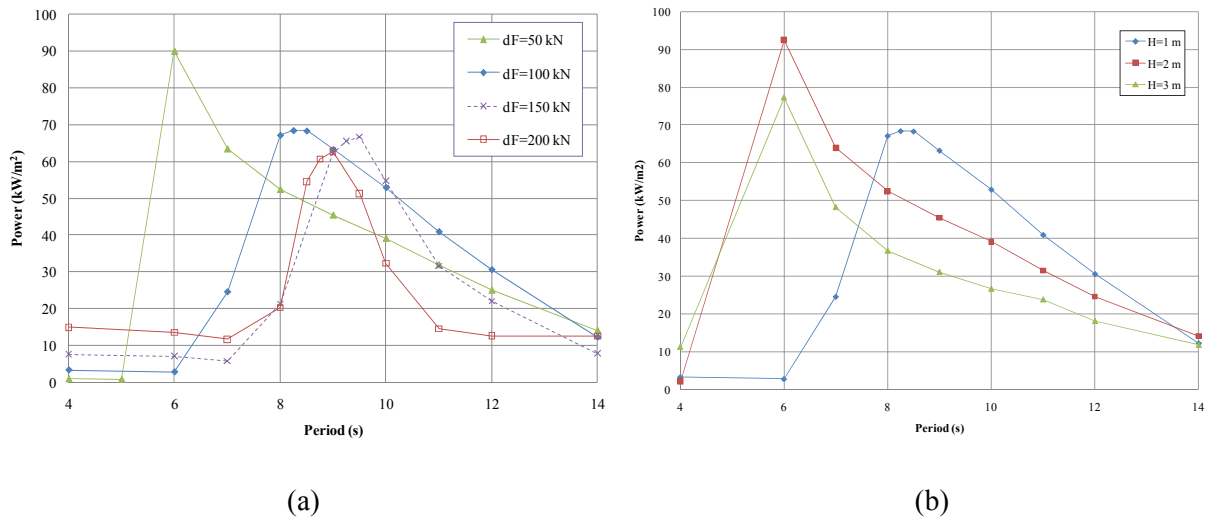
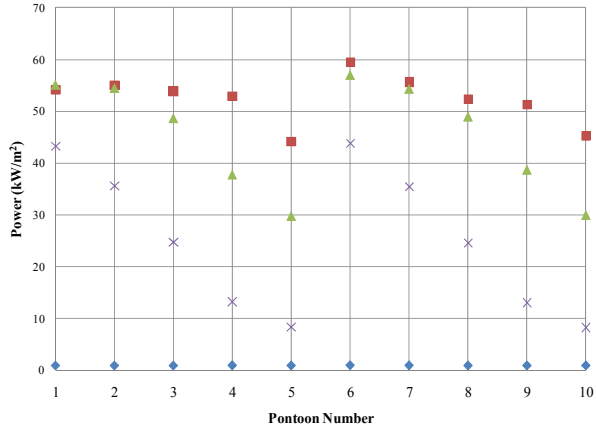


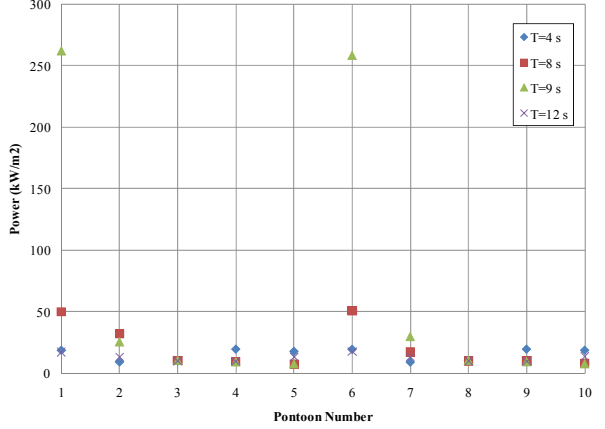
Figure 11 The power functions (average per Pontoon) for (a) cases 1a-4a and (b) cases 2a, 5a, 6a.

Distribution of the mean power absorbed by each Pontoon is plotted in Fig. 12. One will expect that with 0 deg wave direction, symmetrical distribution of P1-5 and P6-10 will be produced. This is confirmed by the results. Some small differences are observed but it is considered as a small and negligible simulation error.

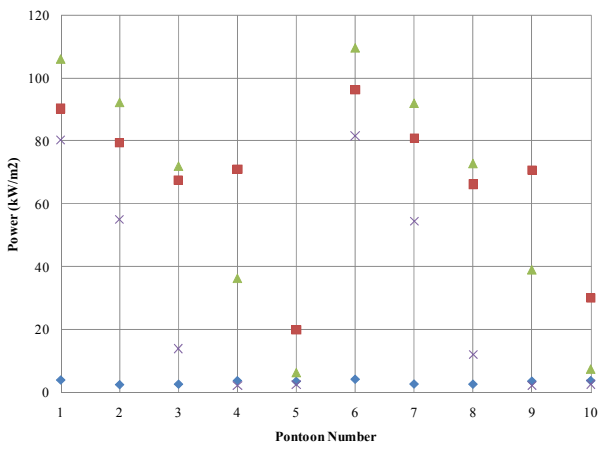
The contribution of the each pontoon to the total absorbed power is varying with the sea state and with PTO force setting. However, one can see that in most of the cases with 0 degree wave direction, P1-2 and P6-7 are the pontoons that most contribute to the absorbed power. Compared to those pontoons, significant reduction on mean power is observed for the pontoons P3-5 and P8-9. In some specific cases such as cases 3(a) and 4(a), the contributions from P3-5 and P8-9 are almost negligible. This is something that should be avoided in the WEC operation as it results in poorly exploitation of the installed equipment. It may be concluded that the influence of size of the pontoons and the distance between them should be studied more carefully in order to ensure efficient use of the equipment. With the configuration specified in this study the distance seems too narrow compared to the size of the Pontoon. The situation is expected to be even worse if the number of pontoons is increased as specified in the full size PPC. Optimization of the properties of the system is needed especially if PPC is expected to work with the orientation of 0 deg to the incoming waves.



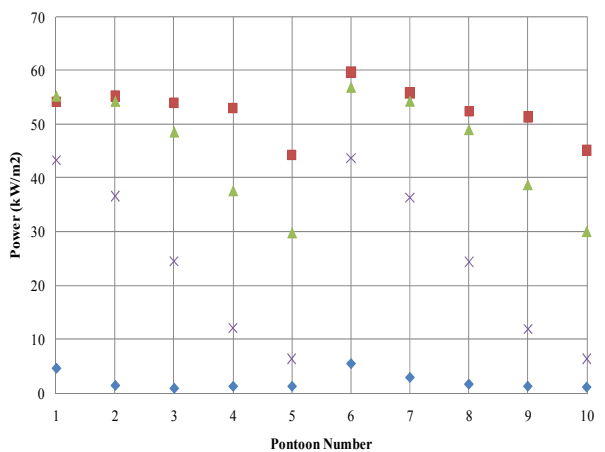
(a)



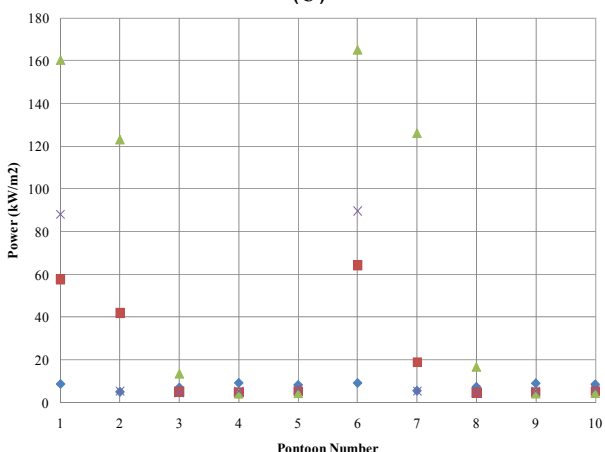
(d)



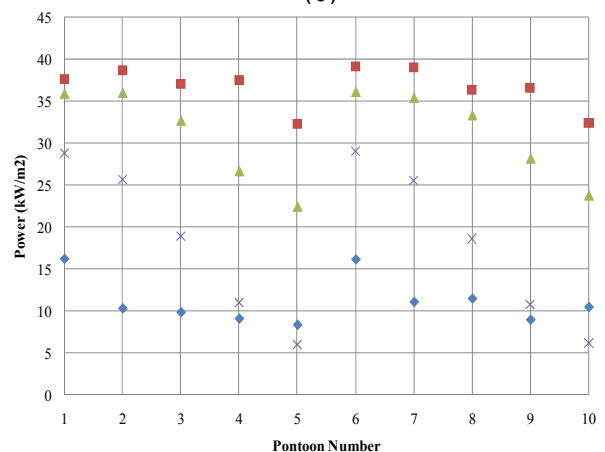
(b)



(e)



(c)



(f)

Figure 12 Distributions of power absorbed by each Pontoon for cases (a) 1a, (b) 2a, (c) 3a, (d) 4a, (e) 5a and (f) 6a, respectively.

### Wave direction: 45 deg (cases 1b – 6b)

Fig. 13 shows the power function resulting from cases 1b – 6b, which apply a wave direction of 45 degrees. The effect of increasing  $dF_{PTO}$  is to shift the peak of power absorption to higher wave periods. This is similar to what observed for the 0 degree cases. However, in the case of 45 degrees wave direction, increasing  $dF_{PTO}$  results in increased maximum power absorption. From the same figure, we can see that narrower bandwidth of the system also occurs when  $dF_{PTO}$  is increased.

As before, an opposite trend is observed from Fig. 13 (b) when wave height is increased while keeping  $dF_{PTO}$  constant. Increasing the wave height both shifts the peak of power absorption to lower wave period and also decreases the maximum power. Broader bandwidth of the system occurs when wave height is increased.

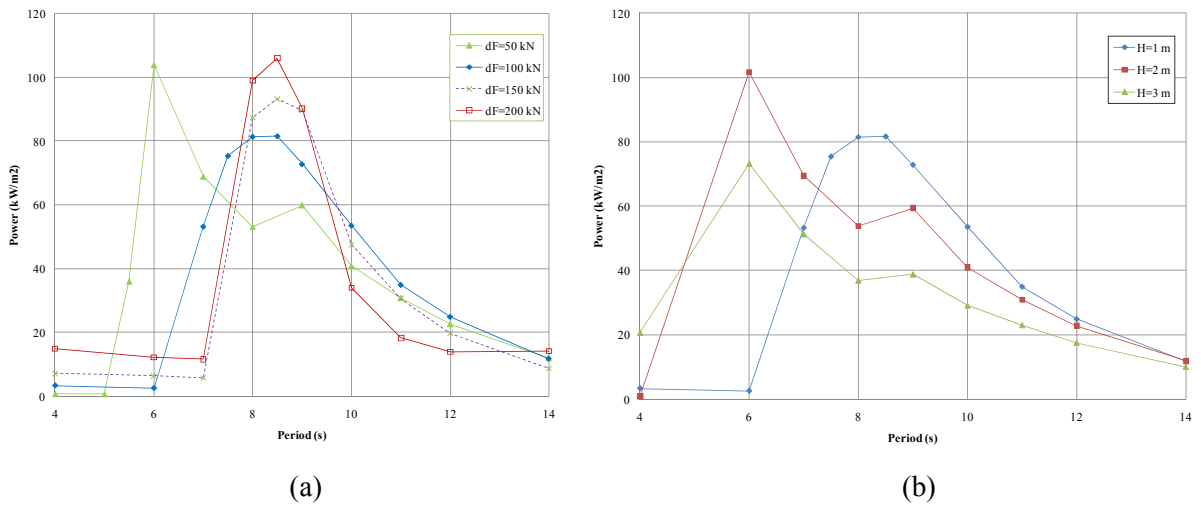


Figure 13 The power functions (average per Pontoon) for (a) cases 1b-4b and (b) cases 2b, 5b, 6b

Distribution of the mean absorbed power by each Pontoon in specified cases are plotted in Fig. 14. The contribution of the each pontoon to the total absorbed power is varying with the wave condition and PTO force setting for the simulation. However, one can see that in most of the cases with 45 deg wave direction, Pontoons P6-10 and P1-2 are the Pontoons that contribute the most to the total absorbed power. Pontoons P3-5 contributes considerably less. Given that 45 deg waves can be represented by a linear summation of incoming wave from 0 and 90 degrees, one can expect that distribution of absorbed power among pontoons for 45 degrees wave direction equals the average between the cases of 0 and 90 degrees wave direction. For the 45 degrees cases that have been described previously, P1-2 and P6-7 are the largest contributors to the total power. Compared to those, P3-5 and P8-10 absorb less power. For the cases of 90 deg waves that will be explained later on in this report, one can expect that P6-10 will be the most contributors since they are located in the first row to face the incoming wave. Summation of those contributions will go to the explanation why Pontoons P6-10 and P1-2 are the Pontoons that contribute the most to the absorbed power, while Pontoons P3-5 give less absorption.

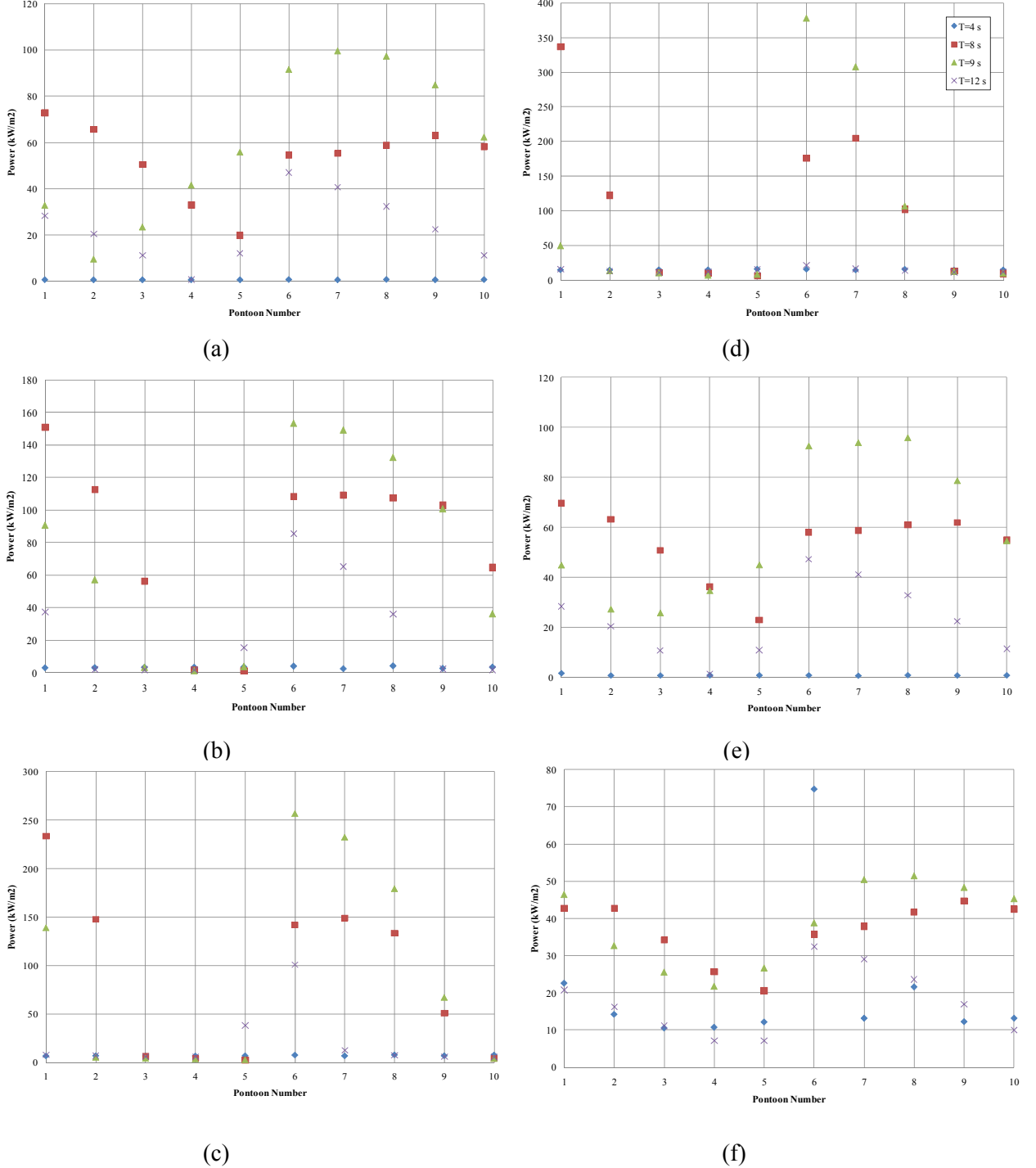


Figure 14 Distributions of power absorbed by each Pontoon for cases (a) 1b, (b) 2b, (c) 3b, (d) 4b, (e) 5b and (f) 6b, respectively.

#### Wave direction: 90 deg (cases 1c – 6c)

Fig. 15 shows the power function estimated for cases 1c – 6c, which apply a wave direction of 90 degrees. The effect of increasing  $dF_{PTO}$  is to increase the maximum power absorption just like for the two other wave directions considered. However, no shifting of the peak of power absorption is

observed here. From the same figure, we can see that narrower bandwidth of the system also occur when the  $dF_{PTO}$  is increased.

As before, an opposite trend is observed in Fig. 15 (b) when wave height is increased while keeping  $dF_{PTO}$  constant. Increasing the wave height results in decreasing the maximum power. Broader bandwidth of the system occurs when wave height is increased.

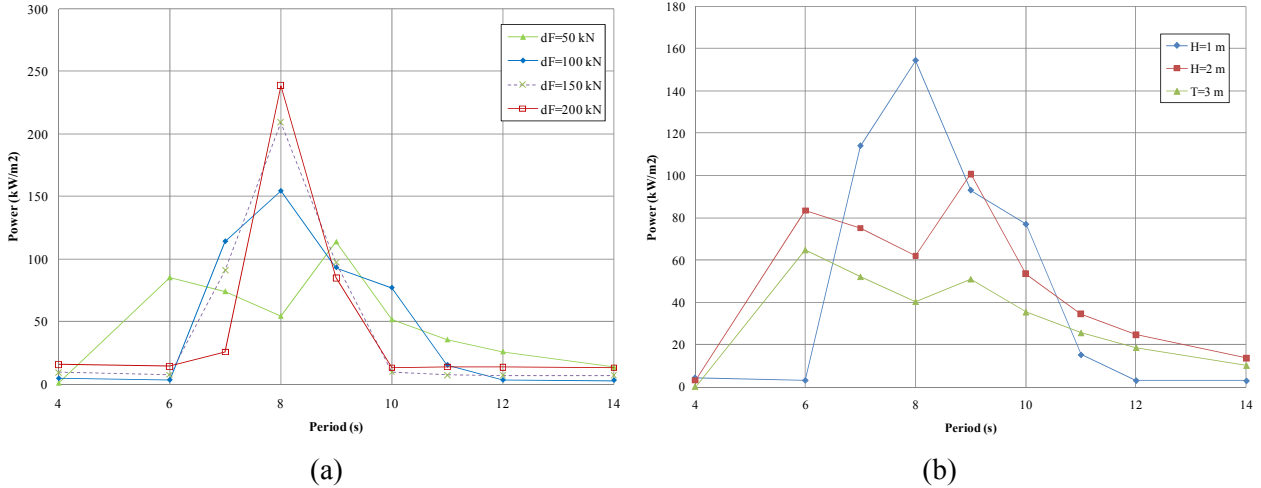


Figure 15 The power functions (average per Pontoon) for (a) cases 1c-4c and (b) cases 2c, 5c, 6c

The distribution of the mean absorbed power by each Pontoon in specified cases is plotted in Fig. 16. The contribution of each pontoon to the absorbed power is varying with the wave condition and PTO force setting. However, one can see that in most of the cases with 90 deg wave direction, the mean power of Pontoons P6-10 is in average higher than the power of P1-5. This is as expected, since the first-row pontoons, which are facing the incoming wave, will have higher power.

The overall effect of the WEC orientation on the absorbed power is summarized in Fig. 17. Changing the orientation angle significantly changes the distribution of the power absorbed by each pontoon and the mean power absorption. It shows that a PPC orientation of 90 degrees to the incoming waves (i.e. waves with wave crests alongside the Bridge) gives the largest power production. Decreasing the orientation angle from 90 degrees to 45 degrees will decrease the power about [-3%, -30%] and from 90 deg to 0 deg will decrease the power about [-10%, -50%].

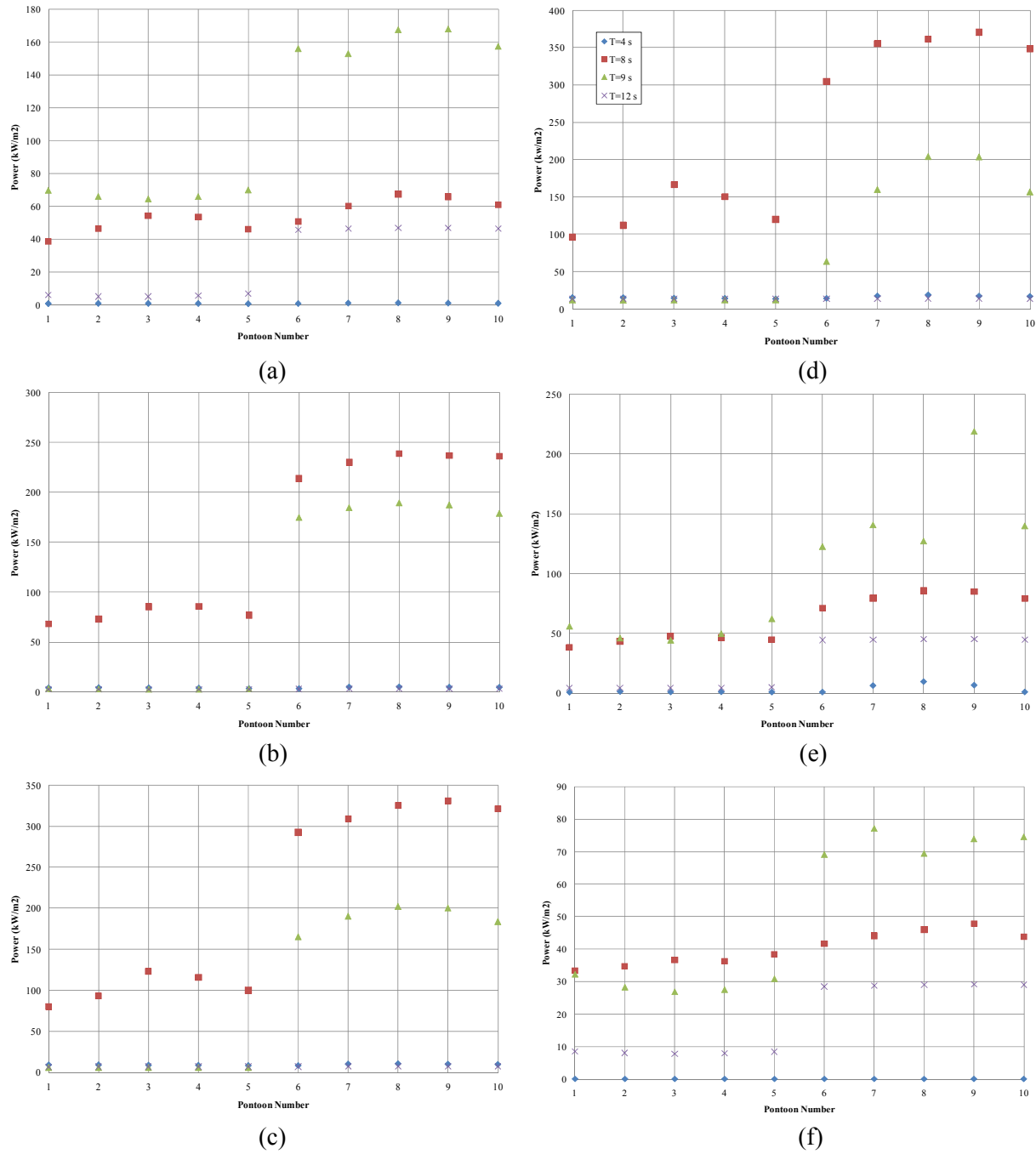


Figure 16 Distributions of power absorbed by each Pontoon for cases (a) 1c, (b) 2c, (c) 3c, (d) 4c, (e) 5c and (f) 6c, respectively.

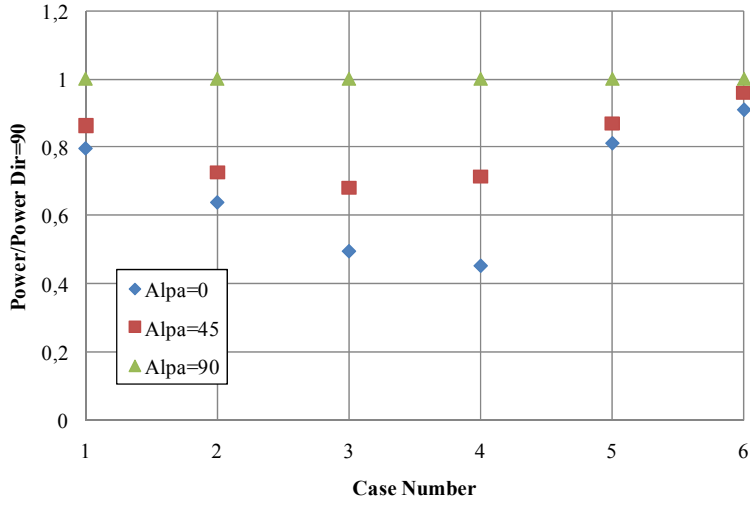


Figure 17. Comparison of the total mean absorbed power for three different wave directions.

### 3.3 Negative tension (slack) on the wire - an observation

The present study's focus is to see the behaviour of the PPC system with regard to the energy absorption, using only the system properties specified by the developer. No optimisation of the PPC system properties that relate to the integrity of the structure has been carried out in this work. However, during simulations the wire tension has been monitored and the results are reported in Table 5. A sample of time series for the wire tension is presented in Fig. 18.

Simulations results indicate that negative tension on one or more wires easily occur with the PPC properties specified for this study. The initial tension of the wires, which is governed by the net gravity forces on the Ballast Basket, is not sufficient to accommodate the reduced tension caused by the motions. The initial tension of the wire could be increased by applying heavier Ballast Baskets (combined with a lighter Bridge in order to keep the total net weight constant). How this would change the overall PPC properties discussed further in this report. A different strategy would be to do more investigation on the motions of each body, such as to come up with other possible solution to minimize the wire tensions. Again, this is not included in the present study.

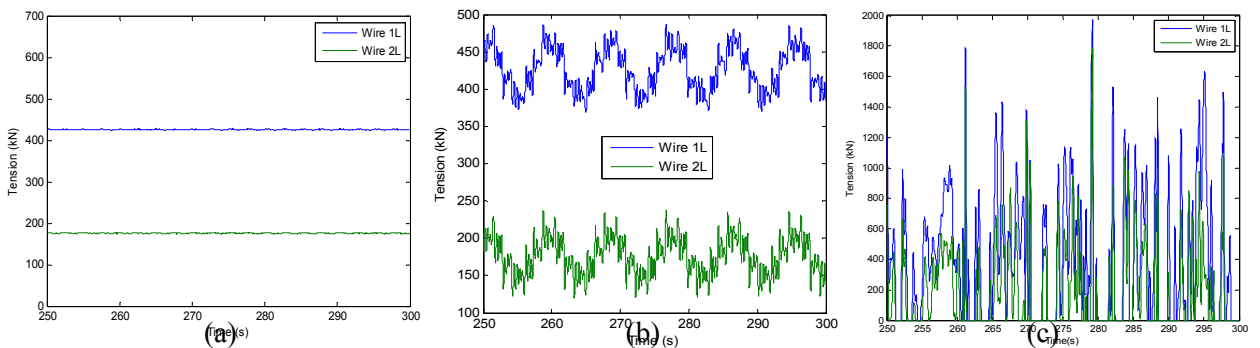


Figure 18 Time series for tensions on wire 1L and 2L from (a) static position, (b) case 2a and (c) case 5b, respectively.

Table 5. Slack-event observations from the simulation -  $\bullet$  indicates that negative tension is observed in one or more wires.

Dir=0	H=1 m				H=2 m	H=3 m
	T (s)	dF=50 kN	dF=100 kN	dF=150 kN	dF=200 kN	dF=100 kN
4	-	-	-	-	-	-
6	-	-	-	-	$\bullet$	$\bullet$
7	-	-	-	-	-	$\bullet$
8	-	-	-	-	-	$\bullet$
9	-	-	-	-	-	$\bullet$
10	-	-	-	-	-	$\bullet$
11	-	-	-	-	$\bullet$	$\bullet$
12	-	-	-	-	$\bullet$	$\bullet$
14	-	-	-	-	$\bullet$	-

Dir=45	H=1 m				H=2 m	H=3 m
	T (s)	dF=50 kN	dF=100 kN	dF=150 kN	dF=200 kN	dF=100 kN
4	-	-	-	-	-	$\bullet$
6	-	-	-	-	$\bullet$	$\bullet$
7	-	-	-	-	$\bullet$	$\bullet$
8	-	-	-	-	$\bullet$	$\bullet$
9	-	-	-	-	$\bullet$	$\bullet$
10	-	-	-	-	$\bullet$	$\bullet$
11	-	-	-	-	$\bullet$	$\bullet$
12	-	-	-	-	$\bullet$	$\bullet$
14	-	-	-	-	$\bullet$	$\bullet$

Dir=90	H=1 m				H=2 m	H=3 m
	T (s)	dF=50 kN	dF=100 kN	dF=150 kN	dF=200 kN	dF=100 kN
4	-	-	-	-	$\bullet$	$\bullet$
6	-	-	-	-	$\bullet$	$\bullet$
7	-	-	$\bullet$	$\bullet$	$\bullet$	$\bullet$
8	-	-	$\bullet$	$\bullet$	$\bullet$	$\bullet$
9	$\bullet$	$\bullet$	$\bullet$	$\bullet$	$\bullet$	$\bullet$
10	$\bullet$	$\bullet$	$\bullet$	$\bullet$	$\bullet$	$\bullet$
11	-	-	-	-	$\bullet$	$\bullet$
12	-	-	-	-	$\bullet$	$\bullet$
14	-	-	-	-	$\bullet$	$\bullet$

### 3.4 Assessment of the influence from the viscous damping

There is a rather large uncertainty on the value used for the viscous damping coefficients. Hence, it is important to assess the sensitivity of the system responses to variations in this coefficient. Table 6 summarises the simulation cases done in the present study to assess the influence that the uncertainty of the viscous damping coefficients has on the PPC's power production.

Fig. 20 shows a comparison of power functions per pontoon for the simulations cases specified in Table 6. It shows that the application of higher values for the viscous damping coefficient results in decreasing the value of the power function. One can see that compared to 0 and 45 degrees waves cases, a stronger effect of viscous damping is observed in cases with 90 degrees waves. The absolute decrease in power output is in general larger from the case of no viscous loss to the case of nominal viscous loss than from the case of nominal viscous loss to the case of double nominal viscous loss.

Comparisons of the mean power for each case with different viscous damping coefficients are presented in Fig. 19. It indicates that the uncertainty of power output resulting from the modelling of viscous losses will be about [-10%, +25%].

Table 6.  $C_d$  setting

Case number	Wave Direction	Wave Height (m)	dF (kN)	$C_d/C_{d \text{ nominal}}$
7a	0	1	100	0
8a	45	1	100	0
9a	90	1	100	0
10a	90	2	100	0
11a	90	3	100	0
7b	0	1	100	1
8b	45	1	100	1
9b	90	1	100	1
10b	90	2	100	1
11b	90	3	100	1
7c	0	1	100	2
8c	45	1	100	2
9c	90	1	100	2
10c	90	2	100	2
11c	90	3	100	2

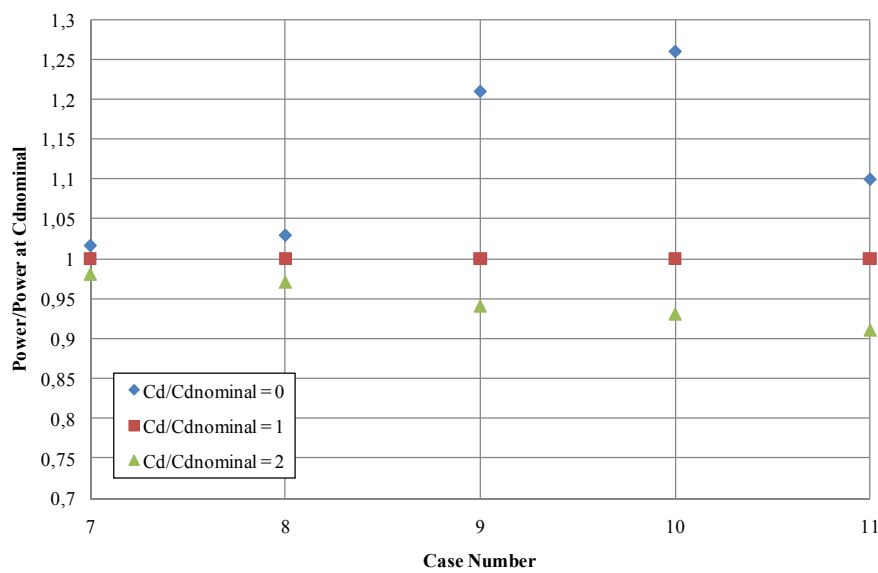


Figure 19 Comparison of the mean power absorption in different viscous damping coefficients.

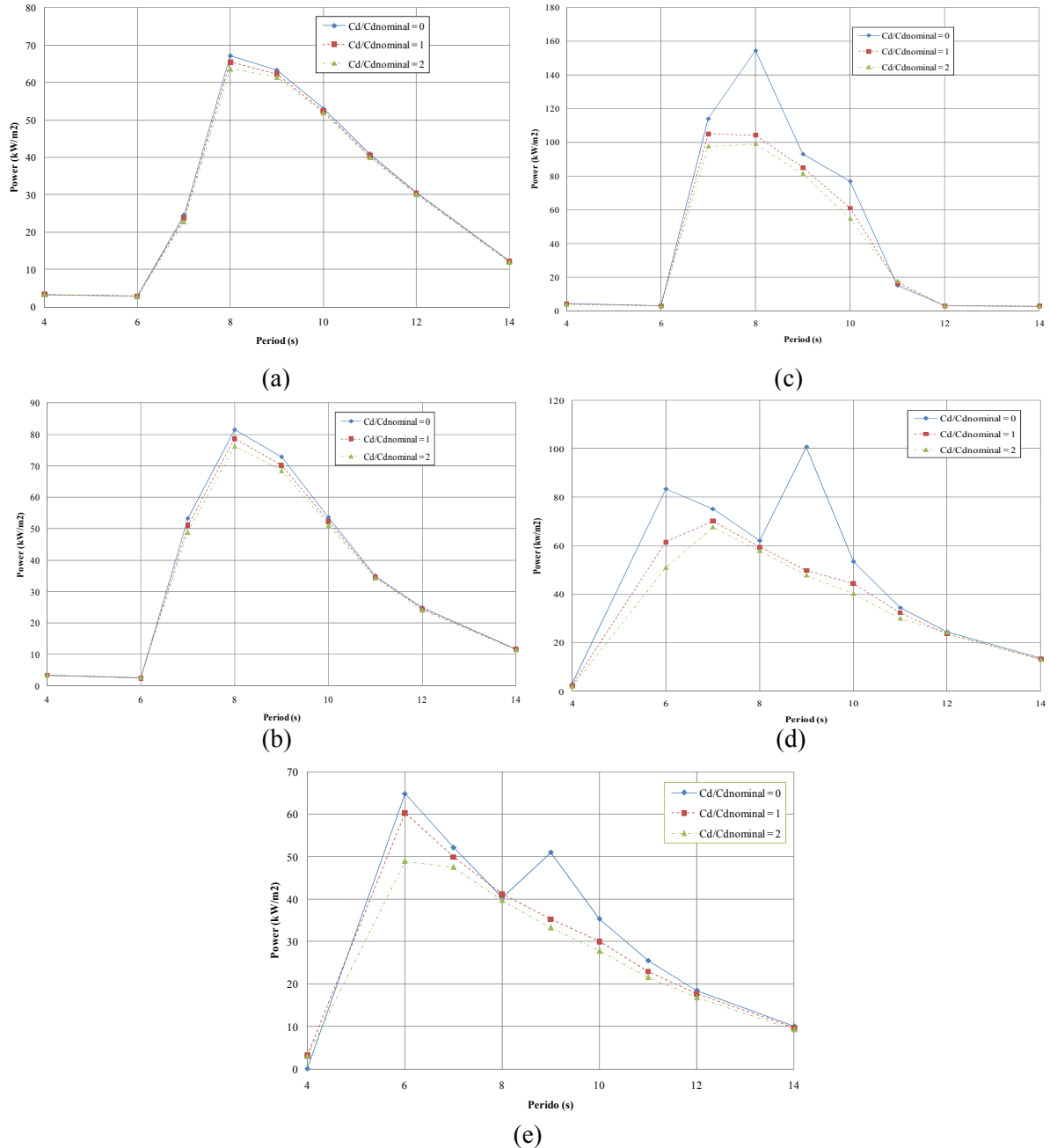


Figure 20 The power functions (average power per pontoon) for cases (a) 1a-c, (b) 2a-c, (c) 3a-c, (d) 4a-c and (e) 5a-c, respectively.

### 3.5 Optimisation of the PTO force (with constraints)

Assessment of the effect of the value of  $dF_{\text{PTO}}$  to the response of the system has been described in section 3.2. It shows that the power functions are varying with  $dF_{\text{PTO}}$  value, wave period, wave height and incoming wave direction. It is expected that there will be a value of  $dF_{\text{PTO}}$  that gives maximum power for each sea state. For that purpose, the optimisation of  $dF_{\text{PTO}}$  value within its possible range is performed. As described in section 2.2, the possible range of  $dF_{\text{PTO}}$  values considered in this study is

from 50 kN to 500 kN. The optimisation is done only for the case where the orientation angle of the PPC to the incoming wave is 90 degrees since it is considered that this case will give maximum power production. Due to restricted computational resources, only regular waves have been applied on the optimization process as this is less time consuming. The results are summarized in Fig. 21. The application of these values for  $dF_{PTO}$  is to maximise the mean power output for each combination of wave height and wave period in regular waves.

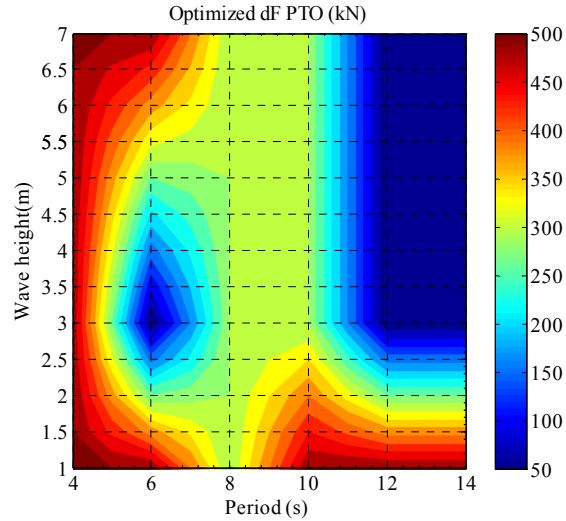


Figure 21 Matrix of the optimized values of  $dF_{PTO}$  in the orientation angle of 90 degrees between the PPC and the incoming waves.

### 3.6 Power matrix and criteria

In order to estimate the power matrix for the PPC, time domain simulations were performed in irregular wave using the JONSWAP spectrum. All quantities are derived from 1200s duration simulations, with a time step of 0.01s. To remove the transient effects, the first  $15 \times T_p$  and the last  $1 \times T_p$  seconds are not taken into account in the calculation of absorbed power.

Fig. 22 shows the power matrix of the PPC studied in this report. Fig. (a) is the mean absorbed power per pontoon and (b) is the maximum instantaneous power recorded over the duration of the simulation for each sea state.

The power matrix in Fig. 22 is derived considering only 90 degrees wave incidence angle. The choice of using only 90 degrees is because we would like to see the possible maximum power produced by the system and to be able to estimate the production from the full size PPC, which will use 73 pontoons. From the distribution of power at each pontoon served in section 3.2, it is understood that each pontoon in the same row will contribute about the same power when 90 deg waves are applied. Some side effects are observed but consider to be small. Therefore, once the mean absorbed power per pontoon is estimated, the power output from the full size PPC with 73 pontoons can be found. However, this would not be the case if 0 and 45 degrees are applied, as for these the hydrodynamic coupling and attenuation of the power gives a more complex situation. However, the effect of the orientation angle assessed for regular waves (Section **Error! Reference source not found.**) may be taken as an indication of how the situation may be also for the full-size device.

For each sea states, the optimized value of  $dF_{PTO}$  shown in Fig. 21 is applied, using significant wave height and peak period instead of wave height and period given for the regular wave. Direct application of the  $dF_{PTO}$  values optimised for regular waves also in irregular waves, will create an uncertainty in the results. The values of wave height and wave period for regular waves are not directly transferable to irregular waves, and therefore it is not clear how to choose the  $dF_{PTO}$  setting for irregular waves based on the regular wave results. However, based on experience and on results from other studies that are part of the same project as this study, it is expected that the error introduced by this practice will be small. This is related to the fact that this system most of the time is operated far from resonance for the oscillating buoys. Then optimal machinery damping will be much larger than the hydrodynamic damping of the system, and the response less sensitive to variation in the machinery damping. In cases where the system operates at or close to resonance, the optimal machinery damping will be similar to the hydrodynamic damping, and then the response will be much more sensitive to variation in this parameter, especially if, at the same time, the viscous losses are small.

On this background, the application of  $dF_{PTO}$  values optimised for regular waves is considered to be sufficient. The uncertainty from this practice is expected to be smaller than the one that come from viscous damping model.

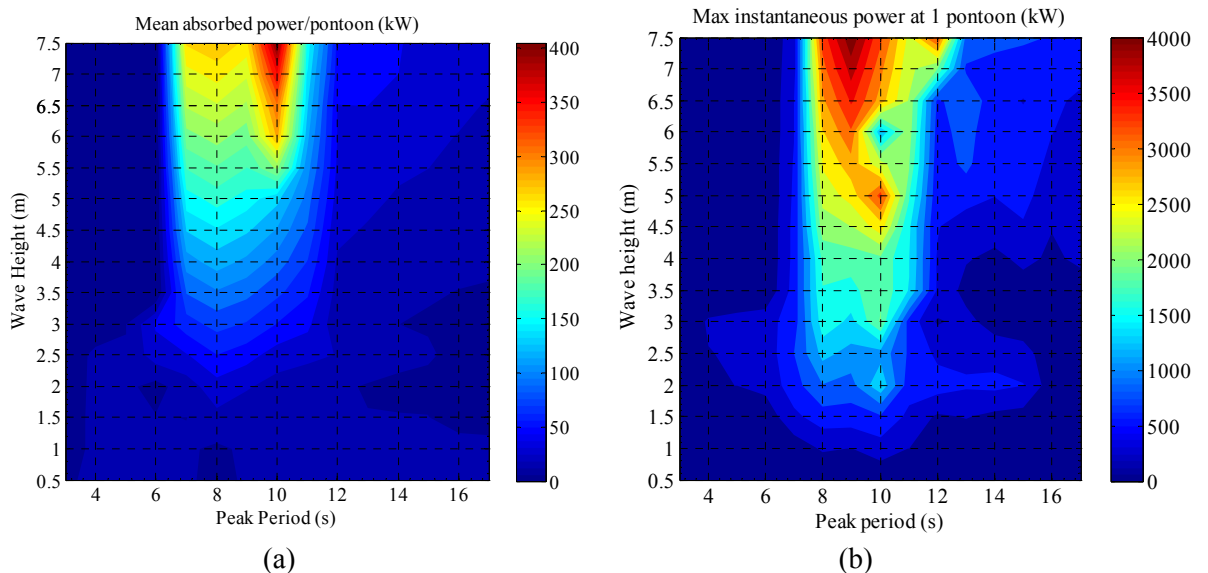


Figure 22 (a) Matrix for the mean absorbed power per pontoon and (b) matrix for the maximum instantaneous power at Pontoon 1. The horizontal axis gives the peak period and the vertical axis the significant wave height of each sea state. The  $dF_{PTO}$  values used were optimised for regular waves.

From Figures 22 (a) and (b) it is observed that the maximum instantaneous absorbed power typically is about 10 times the mean power. It means that the PTO system has to deal with large peaks of instantaneous power. This is a drawback that most of the proposed WECs have to face. However, in the case of the PPC, one should notice that by changing the orientation of the device and operating the hydraulic system properly, it is possible to smooth the power such that the high values of instantaneous power do not feed through to the electric generator.

By multiplying the power matrix with wave data statistics, one can calculate an estimate for the annual energy delivery from the PPC placed at different offshore sites. Estimates for the sites included in this project are reported in Table 7 along with derived measures for the assessment criteria.

Table 7. The power delivery and performance criteria for 10 pontoon PPC device.

Site		SEM-REV	EMEC	Yeu	Lisboa	Belmullet
$\gamma$		1	1	3.3	3.3	3.3
Mean Power	[kW]	224	326	409	317	417
Wave pow. Resources	[kW/m]	14.8	21.8	26.8	37.5	80.6
Capture width	[m]	15.1	15.0	15.2	8.4	5.2
Energy/mass	[kWh/kg]	0.42	0.62	0.77	0.6	0.78
Energy/Wetted surface	[MWh/m <sup>2</sup> ]	0.43	0.63	0.79	0.61	0.80

One can see that the mean annual power that one can expect from the specified PPC goes from 224 kW for SEM-REV site up to 417 kW for the highly energetic Belmullet site. For a typical wave resource of about 27 kW/m, the typical absorbed power by the PPC is about 400 kW. However, a decrease in power output to 300 kW is observed at the Lisboa site where the mean wave power resource is 37.5 kW/m. The reason for this is that the distribution of the sea states at Lisboa is dominated by sea states with higher wave periods as compared to others sites. This doesn't fit well with the PPC power matrix, which has the best efficiency for wave period around 7 to 10 s.

The typical mean capture width of the PPC with 10 pontoons is about 15 meters for three sites of lowest mean annual power level, and is considerably lower for the sites of Lisboa and Belmullet. It indicates that the capture width depends on the site. A maximum of 15.2 meters is reached for Yeu site.

Table 8 shows the comparison of the performance criteria for the studied PPC device with some others devices considered for the Yeu site.

One can see that PPC has an average hydrodynamic efficiency compared to others. The ratio of energy per mass of the PPC is also in the average range. However, it has a high value for the ratio of energy per wetted surface, which is equal to that found for the F-2HB (floating two-body heave-buoy inspired by Wavebob) but smaller than that found for the F-OF (floating oscillating flap device inspired by Langlee). In this respect it should be noted that for the PPC, the mass is mostly due to the Ballast Baskets, which will contain cheap ballast, such as stone.

Table 8. Comparison of performance measures for the PPC and others WEC designs at the Yeu site. The other WECs are the floating oscillating flap device (F-3OF) inspired by Langlee, the floating two-body heaving device (F-2HB) inspired by Wavebob, the bottom-reference heaving buoy (Bref-HB) inspired by Seabased and the bottom-standing heave-buoy array (BF-HBA) inspired by Wavestar.

Technology		PPC	F-OF	F-2HB	Bref-HB	B-HBA
Mean Power	[kW]	409	219	191	3.3	190
Capture width	[m]	15.2	8.17	7.12	0.12	8.08
Hydrodynamic Eff	[%]	19	33	36	6	11
Energy/mass	[kWh/kg]	0.77	1.36	0.338	0.92	1.04
Energy/Wetted surface	[MWh/m <sup>2</sup> ]	0.79	0.89	0.79	0.68	0.383

Fig. 23 shows the distribution of the absorbed power in function of the power level. Left figure shows the probability for the power production to be between two levels and right figure shows the probability for the power to be greater than a given power level. It has been calculated with wave statistics of the Yeu site. One can see the absorbed power is greater than the mean power only 37.5% of the year.

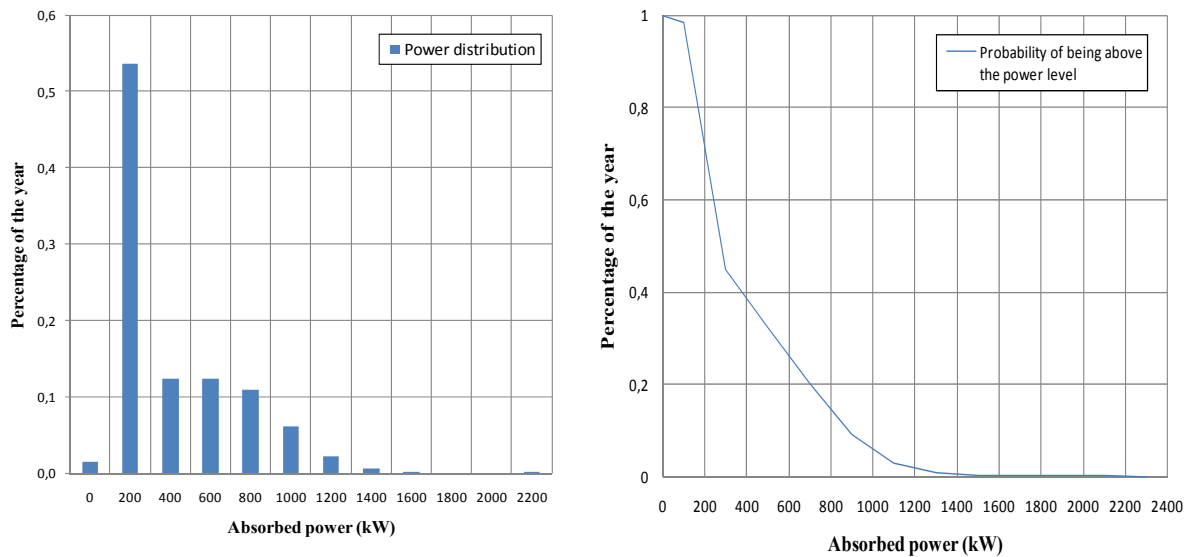


Figure 23 Distribution of the power production.

## 4 Conclusions and recommendations

From these results and the study, the main conclusions are:

- The mean power level that one can expect from the PPC with 10 pontoons is about 400 kW or averagely 40 kW per pontoon on a site whose mean annual wave power level is about 27 kW/m with the PPC orientation of 90 degrees (wave crests parallel to the bridge). The uncertainty of the power estimate is about [-10%, +25%]. It comes from the modelling of the viscous losses.
- Changing in the WEC orientation relative to the direction of incoming waves significantly changes the distribution of the power absorbed by each pontoon and the mean power absorption. It shows that PPC orientation of 90 degrees to the incoming waves (wave crests parallel to the Bridge) give the largest power output. Decreasing the orientation angle from 90 degrees to 45 degrees will decrease the power about [-3%, -30%] and from 90 degrees to 0 degrees will decrease the power about [-10%, -50%].
- With the configuration used in the present study, slack easily occurs on the wires that connect the Bridge and the Ballast Basket. Larger pre-tension or optimization on the overall structure properties to reduce the bridge and basket motions is needed. However, this has not been studied any further in the present study. Here it has been assumed that the wires are strong enough to face the slack behaviour.
- The output power of the PPC with 10 pontoons could be rated to 1.4 MW without losing a significant amount of production. Limitation of the instantaneous absorbed power to 10 times the mean output power (4 MW) would not significantly reduce the mean absorbed power.

## References

- [1] DNV. *GeniE user manual –version 4.0, June 2008.*
- [2] DNV. *HydroD user manual – program version 1.1-01, 2004.*
- [3] Marintek. *SIMO user manual – program version 3.6/August 2008.*
- [4] Faltinsen O.M. (1990). *Sea loads on Ships and Offshore Structures*, Cambridge University Press.
- [5] Matlab. *User's Guide*. [www.mathworks.com](http://www.mathworks.com), 2011.

## Chapter 6

# A bottom-fixed oscillating flap device (B-OF) inspired by the Oyster2 WEC

# Numerical estimation of energy delivery from a selection of Wave Energy Converters

## – Study of a bottom-standing oscillating flap

Aurélien Babarit<sup>1</sup>, Jørgen Hals<sup>2</sup>

<sup>1</sup>Laboratoire de Mécanique des Fluides - CNRS UMR6598

Ecole Centrale de Nantes, 1 rue de la Noe, 44300 Nantes, France

<sup>2</sup>Centre for Ships and Ocean Structures

Norges teknisk-naturvitenskapelige universitet, Otto Nielsens V. 10, 7491 Trondheim, Norway

September 2011

## Summary

This document reports the study of a bottom standing oscillating flap (B-OF) made for wave energy conversion in the frame of the project “Numerical estimation of energy production from a selection of Wave Energy Converters”. It contains a mathematical model and simulation results for the estimation of power delivery and dynamic performance.

The characteristics of the studied wave energy converter is expressed through the following criteria:

- The annual mean power.
- The yearly energy output / displacement.
- The yearly energy output / wetted surface.
- The power per unit of significant PTO force.
- The power per unit of excitation force
- The duration curves.

These criteria were estimated for the B-OF using the mathematical model described in this report. Results are given in the following table and in Figure 1. The main conclusions from the study are :

- The mean power level that one can expect from the B-OF WEC is about 440 kW on a shallow-water site whose off-shore wave resource is about 30 kW/m. The uncertainty is about [-4 %, +30 %], and comes mainly from the modelling of the viscous losses.

- The yearly energy delivery per mass is about 1 kWh/kg, and the yearly energy delivery per wetted surface area is about 2 kWh/m<sup>2</sup> for the Yeu site which may be taken to represent typical European wave conditions.
- The rated power output power (i.e. the maximum average delivered power during each sea state) of the B-OF could be limited to 2 MW with only a small decrease in energy delivery. Limitation of the instantaneous absorbed power to 10 times the mean output power (4 MW) would not significantly reduce the mean absorbed power.
- Viscous losses may be important for the dynamics of this type of device, and should thus be thoroughly considered in mathematical modelling of such systems.

Parameter	Unit	SEM-REV	EMEC	Yeu	Lisboa	Bel-mullet	Danish study
$\gamma$		1	1	3.3	3.3	3.3	1
$J$	[kW/m]	13.3	19.6	23.5	33.7	72.5	12.0
Mean power	[kW]	211	348	440	513	981	243
Capture width	[m]	15.8	17.8	18.7	15.2	13.5	20.0
$E_y$ / mass	[kWh/kg]	0.49	0.80	1.0	1.2	2.3	0.56
$E_y$ / $A_{\text{wet}}$	[MWh/m <sup>2</sup> ]	0.92	1.5	1.9	2.2	4.2	2.0
$E_y$ / $F_{\text{PTO}}^{\text{RMS}}$	[kWh/N]	N/A	1.1	1.4	1.6	2.1	0.97
$E_y$ / $F_{\text{wave}}^{\text{RMS}}$	[kWh/N]	N/A	3.4	4.1	4.8	6.6	2.8

Table 1: Evaluation criteria for the B-OF WEC for chosen sites having mean annual wave energy transport  $J$ , and where sea states are synthesised with a spectrum peakedness factor  $\gamma$ . The parameters are calculated based on the yearly energy delivery  $E_y$ . The mass is taken as the total mass of the ballasted installed structure and its concrete gravity base, and  $A_{\text{wet}}$  is the total wetted surface area of the structure (flap, barrier and base). Significant PTO force  $F_{\text{PTO}}^{\text{RMS}}$  and significant wave force  $F_{\text{wave}}^{\text{RMS}}$  are taken as the yearly RMS values. The uncertainty of the numbers is estimated to  $[-4, 30]\%$ .

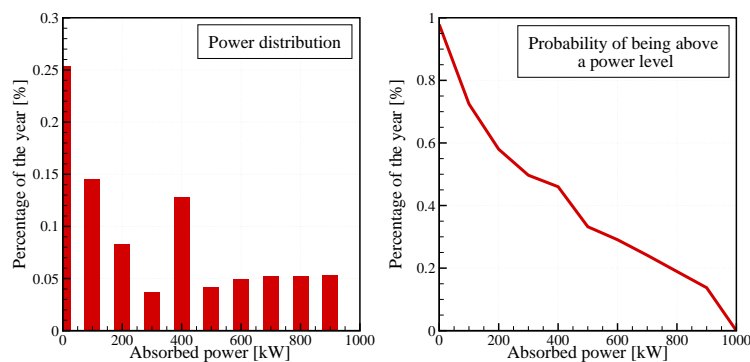


Figure 1: Distribution of the power production on a typical 25 kW/m wave site.

# Contents

<b>1 System description - The B-OF wave energy converter</b>	<b>4</b>
1.1 Dimensions and mechanical parameters . . . . .	4
1.2 Power take-off system and control . . . . .	5
1.3 Location and scaling of wave power resources . . . . .	7
1.4 Cost-related criteria . . . . .	7
1.4.1 Mass, displacement and wetted surface . . . . .	7
1.4.2 Significant forces . . . . .	8
1.5 Comment from the Oyster developer . . . . .	8
1.6 Physical rationale for studying bottom-hinged flap devices . . . . .	8
<b>2 Mathematical description</b>	<b>9</b>
2.1 Bond graph for the dynamic system . . . . .	10
2.2 Equations for the constrained system . . . . .	11
2.3 Frequency domain . . . . .	12
2.4 Time domain . . . . .	12
2.5 Implementation . . . . .	12
2.5.1 Calculation of the hydrodynamic coefficients and functions	12
2.5.2 Hydrodynamic parameters transferred to pivot axis . . . . .	13
2.5.3 Estimation of viscous damping coefficients . . . . .	13
2.5.4 W2W models . . . . .	19
<b>3 Simulation results and energy assessment</b>	<b>19</b>
3.1 Verification and initial analysis . . . . .	19
3.1.1 Decay tests and responses in regular waves . . . . .	19
3.1.2 Influence of PTO parameter variations . . . . .	21
3.1.3 Effect of quadratic damping . . . . .	24
3.1.4 Conclusions from verification tests . . . . .	24
3.2 Power matrix and criteria . . . . .	24
3.2.1 Power matrix of the B-OF . . . . .	26
3.2.2 Assessment of the uncertainties . . . . .	29
3.3 Parametric studies . . . . .	29
3.3.1 Threshold on the instantaneous absorbed power . . . . .	29
3.3.2 Threshold on the mean absorbed power . . . . .	31
3.3.3 Effect of scale . . . . .	31
<b>4 Conclusions and recommendations</b>	<b>32</b>

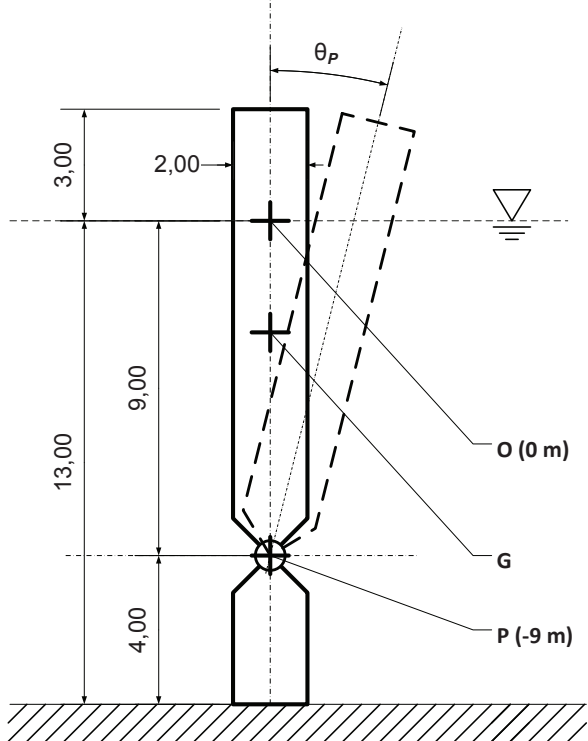


Figure 2: Side view sketch of the geometry that is analysed in this report. The oscillating flap is 26 m wide. Note the point O where hydrodynamic forces have been evaluated, and point P about which the flap oscillates. The rotation angle is called  $\theta_P$ .

## 1 System description - The B-OF wave energy converter

A simplified sketch of the system studied in this report is shown in Figure 2. It is a simple pitching flap, oscillating about a fixed axis close to the sea bottom, and is so suitable for shallow and intermediate water depth. It will here be referred to as a bottom-standing oscillating flap (B-OF). The device is inspired by the Oyster800 wave energy converter under development by Aquamarine Power in Scotland, which is made for a nominal water depth of 13 m. Figure 3 shows a 3D rendering of the Oyster800 geometry. Investigations of this system and issues related to it have been reported in several papers by authors at Queen's University Belfast and associates, see [1, 2, 3, 4, 5, 6]

### 1.1 Dimensions and mechanical parameters

Figure 2 shows the geometry of the studied device. It is based on information from the developers of the Oyster800. The overall dimensions are the same as for the Oyster, but the geometry has been simplified. From these dimensions,



Figure 3: Picture of the Oyster800 wave energy converter.

mechanical parameters have been calculated as shown in Table 2, and hydrodynamic parameters have been estimated, cf. Section 2.5.1. As we shall see, the simplification of the geometry has little influence on the parameters used in this study.

According to staff at Aquamarine Power, the mass of the flap is between 100 and 200 tonnes. Assuming that 15 mm steel has been used, the structural mass of the flap is about 87.5 tonnes. In this study it was chosen to add a point mass of 62.5 tonnes at  $\mathbf{x}=(0,0,-6.0)$ , such that the total mass of the flap is 150 tonnes.

The flap pivot axis is located 4.0 m above the sea bottom, and the passage below the flap is closed by a barrier. Assuming the same material for this part, the total mass of the flap and barrier is about 122.5 tonnes. It gives an excess buoyancy of about  $500 \text{ m}^3$ . Thus total ballast of 678 tonnes (63 tonnes for the flap and 615 tonnes for the barrier) has been assumed, yielding a total mass of 800 tonnes for the device. This corresponds to numbers given for the Oyster device, although Aquamarine power (who is developing the Oyster) hopes that these numbers can be reduced to some extent.

## 1.2 Power take-off system and control

The Oyster is planned for a hydroelectric machinery system, where a pump placed at the rotating shaft pumps pressurised hydraulic oil<sup>1</sup> to a shoreline station. There the hydraulic energy is used to drive an electric generator. According to Cameron *et al.* [5], the distance from the 13 m contour to shore in British and Irish waters typically varies from a couple of hundred meters to a couple of kilometres, which signifies the order of length needed for the hydraulic transmission.

It can be beneficial to ballast some water in it in order to decrease the

---

<sup>1</sup>Future versions of the Oyster device will use a closed-loop fresh water hydraulic system in order to reduce the risk of environmental damage

Property	Measure	Unit
<b>Overall</b>		
nominal water depth	13.0	m
mass of steel	122 500	kg
mass of ballast	678 000	kg
mass of concrete	3 000 000	kg
mass flap+barrier+ballast	800 000	kg
<b>mass including gravity base</b>	<b>3 800 000</b>	<b>kg</b>
submerged volume, flap+barrier	624	$\text{m}^3$
wetted surface, flap+barrier	1039	$\text{m}^2$
<b>significant wetted surface</b>	<b>2030</b>	<b><math>\text{m}^2</math></b>
<b>Flap</b>		
width	26	m
freeboard (MWL to top of flap)	3.0	m
hinge height from seabed	4	m
flap height	12.0	m
flap thickness	2.0	m
steel thickness	15	mm
mass off steel	87 500	kg
ballast mass (as point in (0,0,-6))	62 500	kg
mass, including ballast	150 000	kg
centre of gravity (CG), z-coord	-2.74	m
moment of inertia (about CG) $I_{yy}$	$2.24 \cdot 10^6$	$\text{kg m}^2$
pivot axis (P) z-coordinate	-9.0	m
water-plane area	52	$\text{m}^2$
submerged volume	442	$\text{m}^3$
significant wetted surface	744	$\text{m}^2$
<b>Barrier</b>		
width	26.0	m
height	4.0	m
thickness	2.0	m
mass of steel	35 000	kg
mass of ballast	615 000	kg
mass including ballast	650 000	kg
submerged volume	182	$\text{m}^3$
significant wetted surface	296	$\text{m}^2$
<b>Gravity base</b>		
width	26.0	m
length	26.0	m
thickness	2.0	m
mass of concrete	3 000 000	kg
significant wetted surface	$\approx 1000$	$\text{m}^2$

Table 2: System parameters

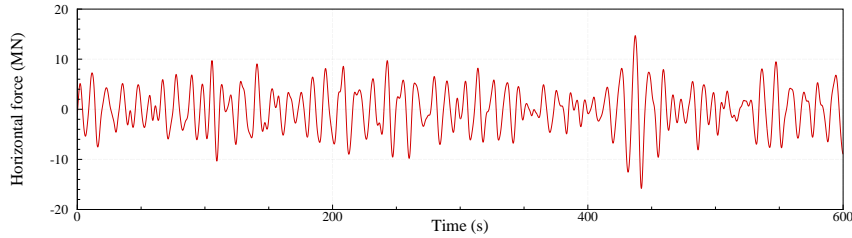


Figure 4: Time series of horizontal force

stiffness and increase its inertia, in order to tune its dynamic response. The corresponding parameter is called  $M_{PTO}$ , taking into account the mass of additional water ballasted in the flap. It is assumed that it applies at the gravity centre of the flap, and that it has no specific inertia.

To model power absorption, a resistive machinery loading will be considered. It is believed that it will give a good estimate of the potential for power absorption by this kind of device. Additionally, a spring term  $K_{PTO}$  is added in the PTO force as a tuning parameter to improve the power absorption.

### 1.3 Location and scaling of wave power resources

The Oyster device is designed for a nominal water depth of 13 m, and this is also used throughout this study for the B-OF. In order to be able to compare the results obtained in this study with results for other devices studied within the frame of the same project, it was decided to assume the same offshore wave power resource for all studies. For shallow-water devices the waves are assumed to propagate into shallow water according to linear refraction, but with an energy loss of 10 % for each and every wave component in the wave spectrum. This is described more in detail in a separate note [7].

### 1.4 Cost-related criteria

#### 1.4.1 Mass, displacement and wetted surface

The wetted surface and mass are chosen here as two relevant costs-related measures that can be derived for any wave energy converter.

As discussed above, the total mass of the bottom-standing oscillating flap is assumed to be about 800 tonnes. Additionally we need an estimate for the mass of the anchoring system. Figure (4) shows a time series of the horizontal wave force that this anchoring system would have to deal with. It was obtained through numerical simulation, using the time domain model which is detailed further in this report. The sea state parameters are  $T_p = 12$  seconds,  $H_s = 5$  meters, and  $\gamma = 3.3$ . It is a strong sea state, but likely to happen several times a year.

One can see that the typical order of magnitude of this force is about 10 MN. In this simulation, one can see that there is a peak at 15 MN. Let assume the flap is fixed on a gravity based structure. Let assume that for stronger sea states, the system is in safe mode, such a way that 15 MN is never exceeded. Assuming a friction coefficient of 0.5 (concrete on wet sand 0.4, on wet rock 0.5), the weight

of the gravity based structure should be 3000 tonnes. Assuming a contact surface of about twice the vertical crosssectional area of the flap ( $26\text{ m} \times 26\text{ m}$ ) and concrete as material, the height of the gravity base is 2 m.

Eventually, the overall significant mass of the buoy plus mooring is estimated to be about 3800 tonnes and the total wetted surface of the flap and barrier and anchoring system is about  $2030\text{ m}^2$ , including the part of the flap that pierces the water surface. This will in this report be chosen as the significant wetted area.

#### 1.4.2 Significant forces

The two other cost related measures considered here are the significant PTO force and the significant wave force. They both have zero mean values. So, they are defined as the RMS values over the whole year.

### 1.5 Comment from the Oyster developer

In working with this study we have been in contact with the developer of the Oyster device. They have been informed about our study, and have received a draft copy of this report. We proposed to the developer to give comment for inclusion into the report, and this is the comment from the Oyster team:

*Aquamarine Power Ltd. would like to recognise the excellent efforts made by Dr. Babarit and Dr. Hals during this investigation. Performing a detailed and fair comparison of numerous devices with diverse and unique operational characteristics is certainly challenging. This has compelled the authors to make some necessary assumptions to achieve a comparison. In our review of the Bottom Standing Oscillating Flap (B-OF) concept, which is representative of the Oyster® technology developed by Aquamarine Power Ltd., we note that a gravity base foundation solution is assumed. Aquamarine Power Ltd. have found that a piled foundation concept is a much more cost effective solution. The use of a piled foundation significantly reduces the overall mass and cost of the device with the most recent full scale Oyster 800 steel device being over 3 times lighter than the mass estimate of the B-OF concept. Our next generation machine is expected to weigh even less, improving further the power to mass ratio of the Oyster device.*

### 1.6 Physical rationale for studying bottom-hinged flap devices

Arguments for pursuing the development of bottom hinged flap devices as the one studied here include the following:

- The shoaling effect of ocean wave entering shallow water makes that energy is transferred from vertical to horizontal water motion. This tends to increase the surge forces relative to the heave forces. As long as the water depth is not too shallow, this more than outweighs the reduction in wave power level due to dissipation as the wave travels into shallower water.
- The distance to shore is short, and hence also the costs for energy transport.

- The bottom-hinged flaps naturally have a high bandwidth, so there is no need for phase control (hence no handling of reactive power flow).
- There is no end-stop challenge with the pitching flaps, as they will lose the excitation force when the amplitude gets too large.
- Survival in storm conditions can be facilitated by swinging the flap and keeping it close to the bottom.

## 2 Mathematical description

Here, the incident waves are assumed to be mono-directional and propagating in the positive  $x$  direction. As the flap is pivoting about a fixed axis, the system has only one degree of freedom: pitch. It is assumed that all motions are of small amplitude and all second order effects are neglected.

The forces that determine the dynamics of the device are

**Excitation forces:** The flap will experience a torque from the hydrodynamic pressure due to the incident and diffracted waves. This is labelled the excitation torque  $\tau_{\text{ex}}$ .

**Hydrodynamic forces:** As the flap moves it feels the pressure generated in the water it moves. This sums up to a radiation torque, which will conventionally be divided in added mass and radiation terms;  $\tau_A(\omega) = A(\omega) \ddot{\theta}_P$  and  $\tau_B = B(\omega) \dot{\theta}_P$  (here assuming that the system is excited by a regular wave of angular frequency  $\omega$ ).

**Hydrostatic forces:** The flap feels a hydrostatic force  $\tau_C = C \theta_P$ , where the hydrostatic coefficient  $C$  is equal to the sum of:

- the hydrostatic stiffness coefficient  $C_{55}$  of the flap if it would be neutrally buoyant. It is a function of the mass of the flap (and its distribution) and the water plane area.
- the product of net buoyancy force  $g(\rho V - M)$  times the vertical height  $d$  from the hinge to the gravity centre of the flap.
- minus the product of the additional ballasted mass  $M_{PTO}$  force times the vertical height  $d$ .

**Viscous damping forces:** The viscous torque  $\tau_v$  on the flap is estimated by dividing the flap in ten horizontal sections and computing the viscous force  $F_{v,i}$  on each section by taking into account the relative motion between the flap section and the surrounding water (corresponding to the undisturbed wave). This gives the following expression:

$$\tau_v = \sum_{i=1}^9 \overrightarrow{PM_i} \times \overrightarrow{F_{v,i}}(M_i) \quad (1)$$

with:

$$\overrightarrow{PM_i} = [x_i, y_i, z_i - z_P] \quad (2)$$

$$\overrightarrow{F_{v,i}}(M_i) = -C_v A_i (\overrightarrow{V}(M_i) - \overrightarrow{V}_0(M_i)) \|\overrightarrow{V}(M_i) - \overrightarrow{V}_0(M_i)\| \quad (3)$$

Here  $M_i = (x_i, y_i, z_i)$  is the middle point of section  $i$ ,  $z_P$  is the vertical coordinate of the shaft,  $C_v$  is the drag coefficient,  $A_i$  is the crossectional area of section  $i$ ,  $\vec{V}(M_i)$  is the velocity of section  $i$  and  $\vec{V}_0(M_i)$  is the water velocity of the undisturbed incident wave.

**PTO forces:** As mentioned (Section 1.2), the PTO torque is assumed to be linear;  $\tau_{\text{PTO}} = -I_{\text{PTO}} \ddot{\theta} - B_{\text{PTO}} \dot{\theta} - K_{\text{PTO}} \theta$ , where  $I_{\text{PTO}} = M_{\text{PTO}} d$  is the machinery inertia,  $B_{\text{PTO}}$  is the machinery resistance and  $K_{\text{PTO}}$  is the coefficient for the machinery spring effect.

## 2.1 Bond graph for the dynamic system

A bond graph for the system can be drawn simply as shown in Figure 5. It includes the forces listed above along with the inertia forces. The transformer is needed because the hydrodynamic forces are evaluated in the Cartesian coordinate system with  $z = 0$  at the mean surface level. It corresponds to a conventional change of coordinate systems known from classical mechanics. A simpler bond graph can be made to represent the system, where the hydrodynamic parameters are transformed to rotation about the point P, see Figure 6.

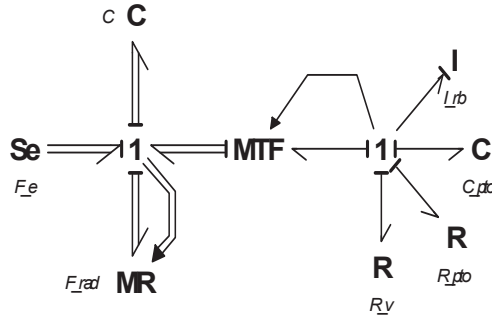


Figure 5: Bond graph for hydrodynamic description with six degrees of freedom.

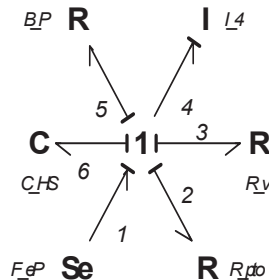


Figure 6: Bond graph for system with hydrodynamic parameters transformed to rotation about point P.

## 2.2 Equations for the constrained system

According to the last bond graph, the state-space equation for the system is simply

$$\dot{q}_6 = f_6 = p_4/I_4 \quad (4)$$

$$\dot{p}_4 = e_4 = e_1 - e_2 - e_3 - e_5 - e_6 = \tau_{\text{ex}} - \tau_{\text{PTO}} - \tau_v - \tau_B - q_6/C_6 \quad (5)$$

where  $q_6 = \theta_P$  and  $p_4 = I_4 \dot{\theta}_P$ . Further  $1/C_6 = C$ , the hydrostatic stiffness.

Now as the hydrodynamic parameters are evaluated for a coordinate system at point G, we need the transformation  $\mathbf{T}$  that converts between the angular speed  $\dot{\theta}_P$  around the pivot axis P and the motion  $\dot{\eta}_G$  about point G:

$$\dot{\eta}_G = \mathbf{T} \dot{\theta}_P \quad (6)$$

By considering the following relations between the motion  $\dot{\eta}_G$  of point G and the angular velocity  $\dot{\theta}_P$  of point P,

$$\dot{x}_G = |\vec{PG}| \cos \theta_P \dot{\theta}_P \quad (7)$$

$$\dot{z}_G = -|\vec{PG}| \sin \theta_P \dot{\theta}_P \quad (8)$$

$$\dot{\theta}_G = \dot{\theta}_P \quad (9)$$

we see that the transformation matrix is given by

$$\mathbf{T} = \begin{bmatrix} |\vec{PG}| \cos \theta_P \\ -|\vec{PG}| \sin \theta_P \\ 1 \end{bmatrix} \quad (10)$$

In accordance with classical mechanics, the parameters needed for solution of the system equations (4) and (5) can now be found as

$$A(\omega) = I_4 - (I_P + I_{\text{PTO}}) = \mathbf{T}^T \mathbf{A}_G(\omega) \mathbf{T} \quad (11)$$

$$B(\omega) = R_5 = \mathbf{T}^T \mathbf{B}_G(\omega) \mathbf{T} \quad (12)$$

$$C_{\text{HS}} = 1/C_6 = \mathbf{T}^T \mathbf{C}_G(\omega) \mathbf{T} + g (\rho V - M - M_{\text{PTO}}) d + K_{\text{PTO}} \quad (13)$$

where  $\mathbf{A}_G$ ,  $\mathbf{B}_G$  and  $\mathbf{C}_G$  are added mass, radiation resistance and hydrostatic stiffness coefficient matrices evaluated with reference to a coordinate system centred at point G, and containing elements only for the surge, heave and pitch modes. Furthermore,  $I_P = \mathbf{T}^T \mathbf{M}_G(\omega) \mathbf{T}$  is the rigid-body mass matrix  $\mathbf{M}_G$  transferred to rotation about point P. Equations (4) and (5) can now be written out as

$$\dot{\theta}_P = w_\theta \quad (14)$$

$$\dot{w}_\theta = \frac{1}{I_P + I_{\text{PTO}} + A(\omega)} (\tau_{\text{ex}} - \tau_{\text{PTO}} - \tau_B - \tau_v - q_6/C_6) \quad (15)$$

$$= \frac{1}{I_P + I_{\text{PTO}} + A(\omega)} (\tau_{\text{ex}} - B_{\text{PTO}} w_\theta - B(\omega) w_\theta - \tau_v - C_{\text{HS}} \theta_P) \quad (16)$$

As there are frequency dependent parameters involved, this equation system is only valid for excitation with one frequency (monochromatic wave). If linearised (see Section 2.3) it can be solved in the frequency domain, otherwise

the frequency-dependent terms must be resolved as convolution integrals (see Section 2.4).

Equivalently to equations (14) and (15), the equation of motion may be written in the more conventional way as

$$(I_P + I_{PTO} + A(\omega)) \ddot{\theta}_P(t) + (B(\omega) + B_{PTO}) \dot{\theta}(t) + \tau_v + C_{HS} \theta(t) = \tau_{ex} \quad (17)$$

### 2.3 Frequency domain

Now, if we disregard the viscous forces and linearise the transform matrix of equation (10),

$$\mathbf{T} = \begin{bmatrix} |\vec{PG}| \\ 0 \\ 1 \end{bmatrix}, \quad (18)$$

the whole model may be represented by the second-order ordinary differential equation

$$(I_y + (M + M_{PTO}) d^2 + A(\omega)) \ddot{\theta} = \tau_{ex} - B(\omega) \dot{\theta} - B_{PTO} \dot{\theta} - (C_{55,P} + g(\rho V - M - M_{PTO}) d + K_{PTO}) \theta \quad (19)$$

with  $I_y$  being the inertia of flap at the centre of gravity (point G), and the distance  $d = |\vec{PG}|$ . This equation is that of a damped harmonic oscillator. As viscous forces are usually significant in flap-type wave energy conversion systems [3], equation (19) is not expected to give a realistic solution for the dynamic response, but it will be used as a check for the time-domain model.

### 2.4 Time domain

As the parameters of equation (15) involves frequency-domain parameters, convolution integrals occur for the added mass and damping terms when the input is polychromatic. In the time-domain solver routine, these are solved by direct numerical integration. The transformation matrix  $\mathbf{T}$  is still linearised in order to be consistent with the linear hydrodynamic theory used. Now with, with an estimate of viscous losses included, the model reads

$$(I_y + (M + M_{PTO}) d^2 + \mu_\infty) \ddot{\theta} = \tau_{ex} - \int_0^t K(t - \tau) \dot{\theta}(\tau) d\tau - B_{PTO} \dot{\theta} - (C_{55} + g(\rho V - M - M_{pto}) d + K_{PTO}) \theta + \tau_v \quad (20)$$

### 2.5 Implementation

#### 2.5.1 Calculation of the hydrodynamic coefficients and functions

Frequency-dependent hydrodynamic parameters were computed both by use of the BEM code Aquaplus and the Wadam software provided by DNV. Figures 7 to 8 shows the meshes used for computations both on the simplified geometry used in this study and on more refined geometries closer to the geometry of the Oyster800. In Figures 9 to 11 the convergence of the parameters can be assessed.

For comparison, the hydrodynamic parameters for the different geometries are collected in Figure 12.

It can be seen that convergence is reached at a resolution of about  $1000 \times 330$  flat panels. Furthermore, at the level of modelling detail used in this study, there the simplified geomtry gives results (in terms of hydrodynamic parameters) very close to those of the Oyster800.

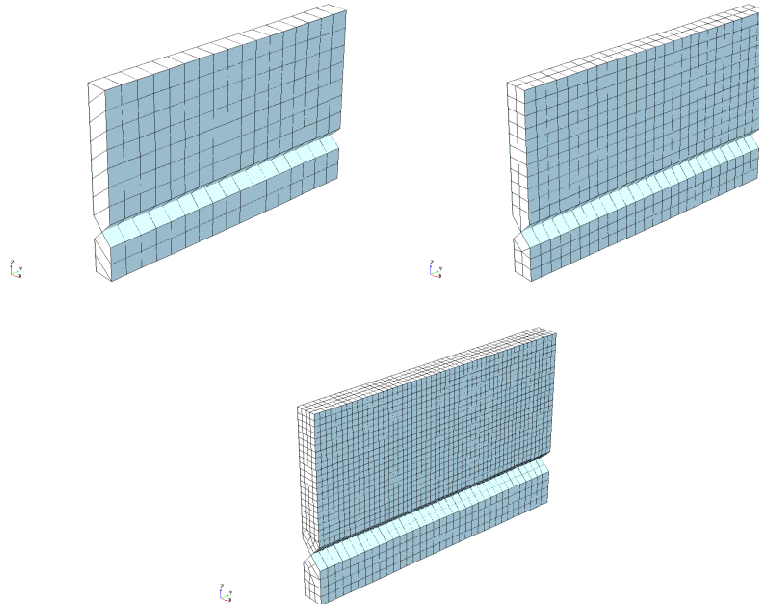


Figure 7: Meshes used for the the hydrodynamic calculations on the geometry used in this study. The coarsest meshing in the upper left is composed of 253 and 108 flat panels for the flap and the barrier, respectively. The medium mesh in the upper right has 501 + 221 flat panels, while the finest mesh in the lower graph has 2114 + 448 flat panels.

### 2.5.2 Hydrodynamic parameters transferred to pivot axis

Figures 13 and 14 show the excitation torque and the impedance for oscillation about the pivot axis as they occur in equation (17).

### 2.5.3 Estimation of viscous damping coefficients

Assuming that the amplitude of motion of the top of the flap will be of the order the of wave amplitude, Keulegan Carpenter number  $KC = \frac{2\pi A}{B}$  is found to be very low in case of the B-OF, typically smaller than 1. According to [8],  $C_v = 7.8 KC^{-1/3}$  at low  $KC$  numbers for a plate in oscillatory flow. Therefore, we retain  $C_v = 8.0$  in the calculations. According to the previous formula, it is a low estimate, so it should not be too penalising for derivation of power absorption.

Table 3 shows the parameters which were used in equation (3).

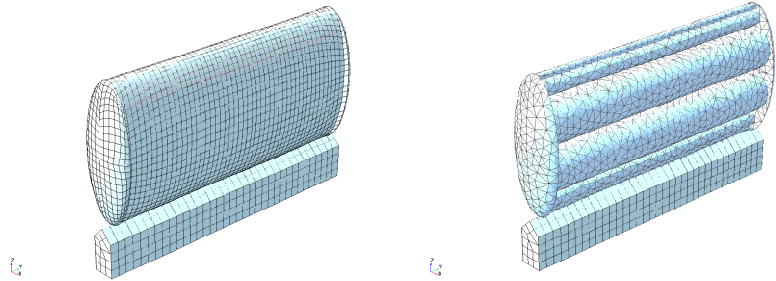


Figure 8: Meshes used for the hydrodynamic calculations of the detailed approximation (left) and simplified approximation (right) of Oyster800 geometry. The first one is composed of 2350 flat panels for the flap and 448 panels for the barrier, while the second one consists of 3271 + 448 panels.

$i$	$z(M_i) - z_P$ (m)	$A_i$ ( $\text{m}^2$ )
1	0.5	26.0
2	1.5	26.0
3	2.5	26.0
4	3.5	26.0
5	4.5	26.0
6	5.5	26.0
7	6.5	26.0
8	7.5	26.0
9	8.5	26.0

Table 3: Parameters used for the calculation of the viscous forces.

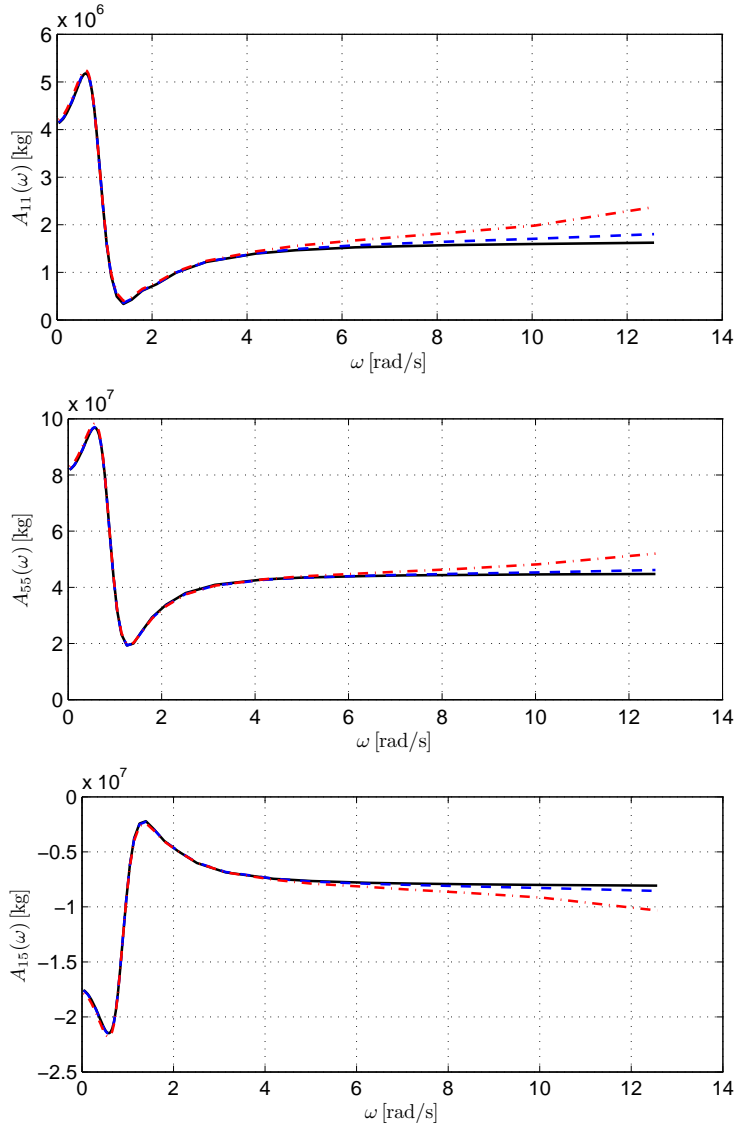


Figure 9: Hydrodynamic added mass coefficients for the radiation force in the frequency domain. Index  $ij$  means the force measured on axis  $i$  of the flap due to a motion along axis  $j$ . The solid black lines are results of computation with the fine mesh, blue dashed lines are computed with the medium mesh and the red dash-dotted line are due to the coarse mesh.

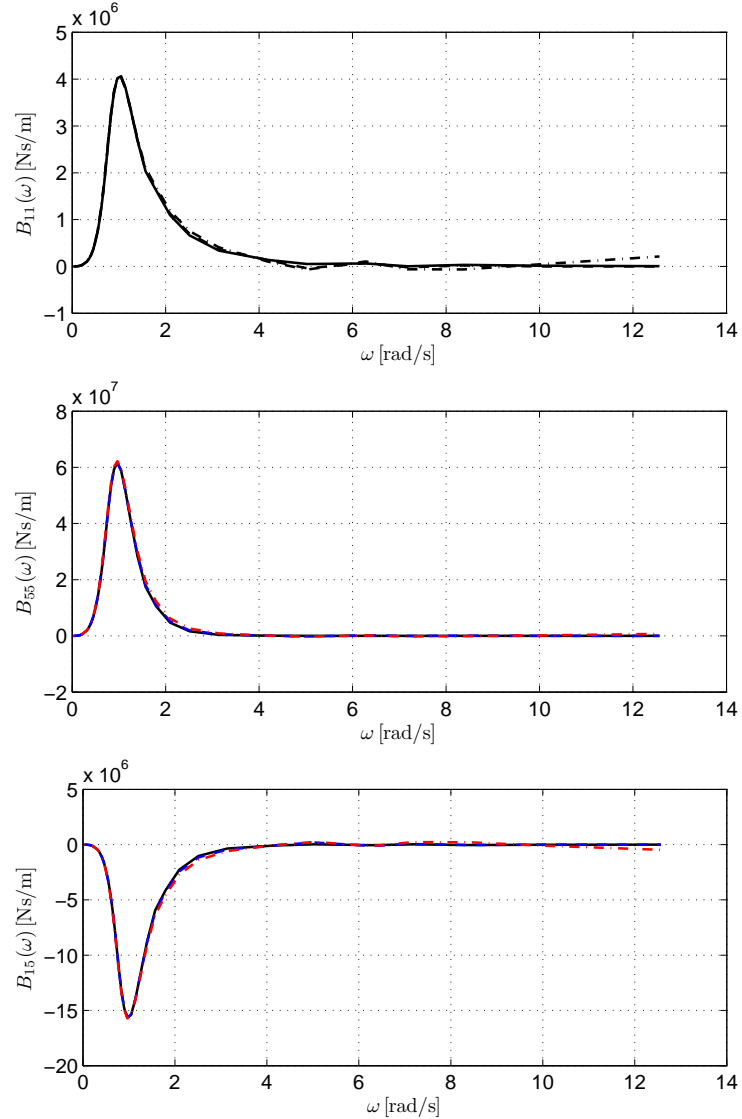


Figure 10: Hydrodynamic resistance coefficients for the radiation force in the frequency domain, computed with Wadam. Different line patterns refer to different mesh size and are the same as for Figure 9.

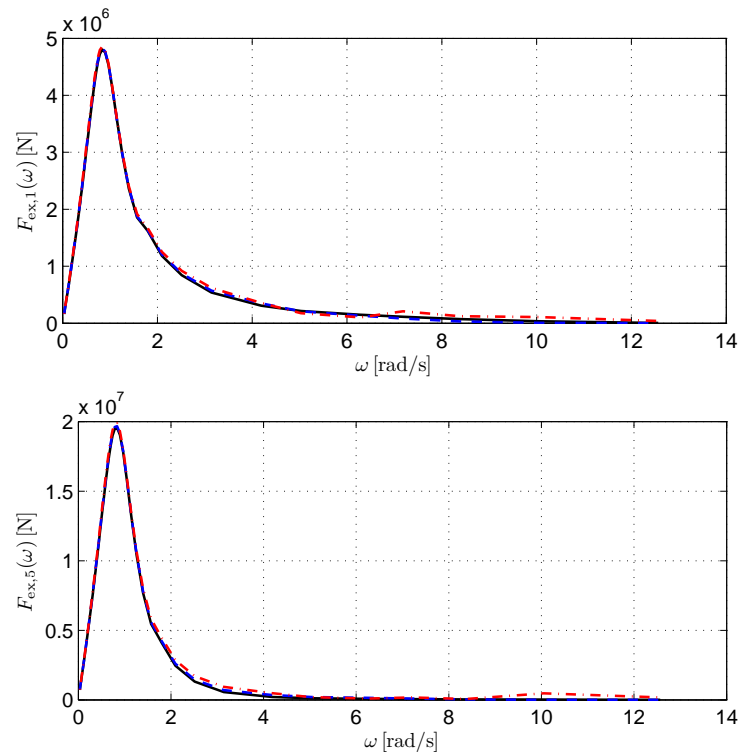


Figure 11: Wave excitation force coefficients for index 1 (surge) and index 5 (pitch) in the frequency domain computed with Wadam. Different line patterns refer to different mesh size and are the same as for Figure 9.

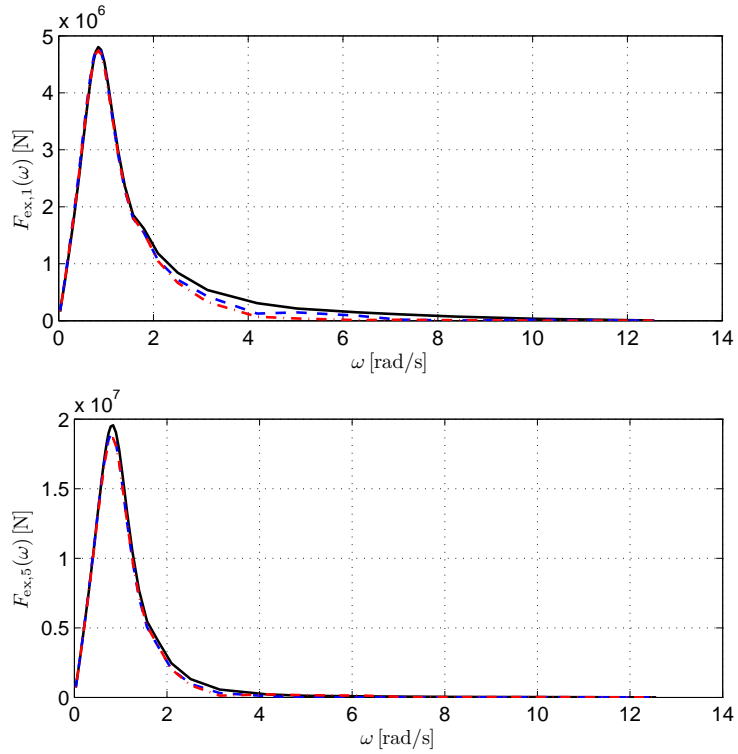


Figure 12: Comparison of wave excitation force coefficients for different flap geometries. The solid black lines correspond to the simple flat-wall case. Further, the blue dashed lines correspond to the simplified Oyster800 geometry, while the red dash-dotted lines correspond to a detailed estimation of the Oyster800 geometry. For the two last geometries, cf. Figure 8.

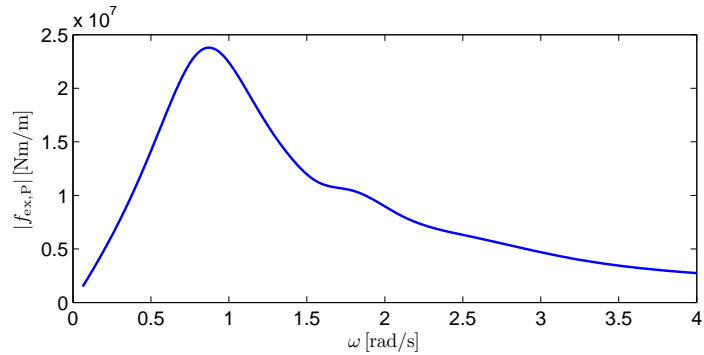


Figure 13: Excitation torque about axis P.

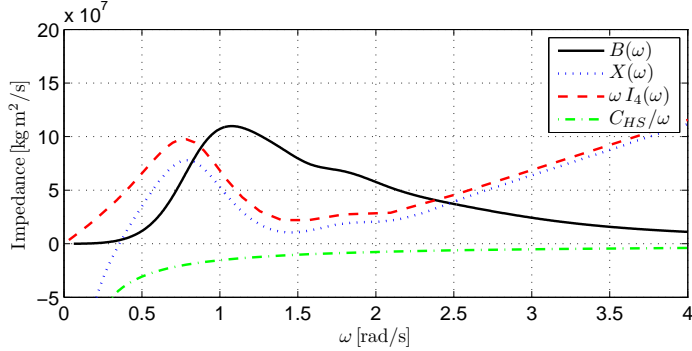


Figure 14: Impedances for motion about axis P.

#### 2.5.4 W2W models

Based on equations (19) and (20), two numerical models were derived: one in the frequency domain and the other one in the time domain. They were implemented for solution in Fortran90.

### 3 Simulation results and energy assessment

When they are not explicitly specified, the parameters which were used in all the simulations presented here are the ones given in Table 2.

#### 3.1 Verification and initial analysis

##### 3.1.1 Decay tests and responses in regular waves

The natural period of the body is given by:

$$\omega_0 = \sqrt{\frac{C_{55} + g(\rho V - M - M_{PTO})d + K_{PTO}}{I_y + (M + M_{PTO})d^2 + A(\omega)(\omega_0)}} \quad (21)$$

By setting  $M_{PTO}$  and  $K_{PTO}$  to 0, one gets  $\omega_0 = 0.32$  rad/s. Figure 15 shows the corresponding response amplitude operator (RAO). As expected, one can see that there exists a resonance peak at frequency 0.32 rad/s.

Figure 16 shows the comparison of the RAO of the B-OF WEC calculated with the frequency domain model and the time domain model. In time domain, all non linear terms were discarded.  $M_{PTO}$  and  $K_{PTO}$  are equal to 0. The machinery resistance  $B_{PTO} = 10^7$  N m s. A perfect coincidence is observed between the results from the two models, giving confidence that the implementation has been done correctly.

Figure 17 shows decay tests computed with the time domain model, with and without viscous damping. The initial angle was 10 degrees. The PTO parameters are the same as in the previous case. As expected the excursions are smaller when viscous damping is introduced. In this case the difference between results with and without inclusion of viscous losses is not so large, which can be explained by low velocities (due to the high natural period of

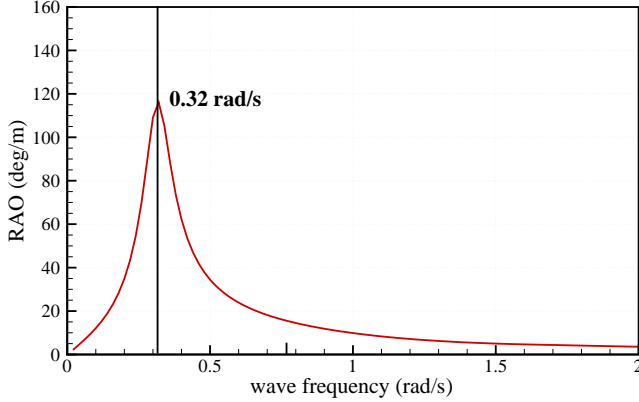


Figure 15: RAO of the B-OF WEC computed with the frequency domain model.  $M_{PTO}$  and  $K_{PTO}$  equal to 0.  $B_{PTO} = 10^7 \text{ N m s}$ .

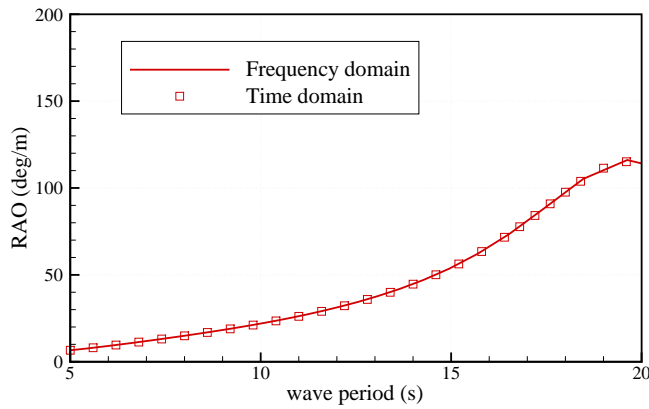


Figure 16: Comparison of Oyster WEC's RAO calculated with the frequency and the time domain model.  $M_{PTO}$  and  $K_{PTO}$  are equal to 0.  $B_{PTO} = 10^7 \text{ N m s}$ . The RAO in time domain was calculated without viscous damping.

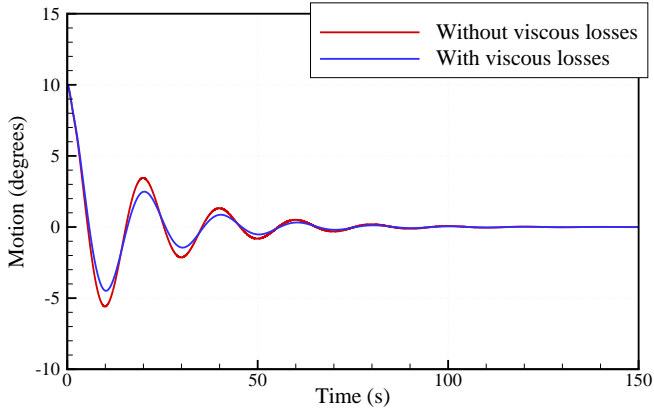


Figure 17: Decay tests with and without viscous damping. The initial angle is 10 degrees. The PTO parameters are the same as in the previous case.

about 20 s), and by the large PTO damping force that has been included and which dominates the viscous force.

### 3.1.2 Influence of PTO parameter variations

Table 4 summarises the set of PTO coefficients which were used. In Figures 18 and 19 we plotted the associated RAOs and power functions.

Set number	$B_{PTO}$ (MN.m.s)	$K_{PTO}$ (MN.m)
1	10	0
2	50	0
3	10	0
4	200	0
5	400	0
6	50	50
7	50	100

Table 4: Settings for the PTO parameters; the machinery resistance  $B_{PTO}$  and the machinery stiffness  $K_{PTO}$ .

We see for purely resistive loading ( $K_{PTO} = 0$ , sets 1-5), increasing the resistance reduces the amplitude response and shifts the peak of the power response to lower wave periods. As expected each wave period has a different value for the optimal machinery resistance.

The introduction of a stiffness term in the machinery force as seen in Figure 19 also leads to a downwards shift of the wave period where the peak power is found. This is combined with an increased power output for lower wave periods. The bandwidth is, however, reduced if the resistance is at the same time kept constant, as in Figure 19.

The influence of the parameter  $M_{PTO}$  was not investigated because it would lead to an even longer resonance period, which is already very long. It is,

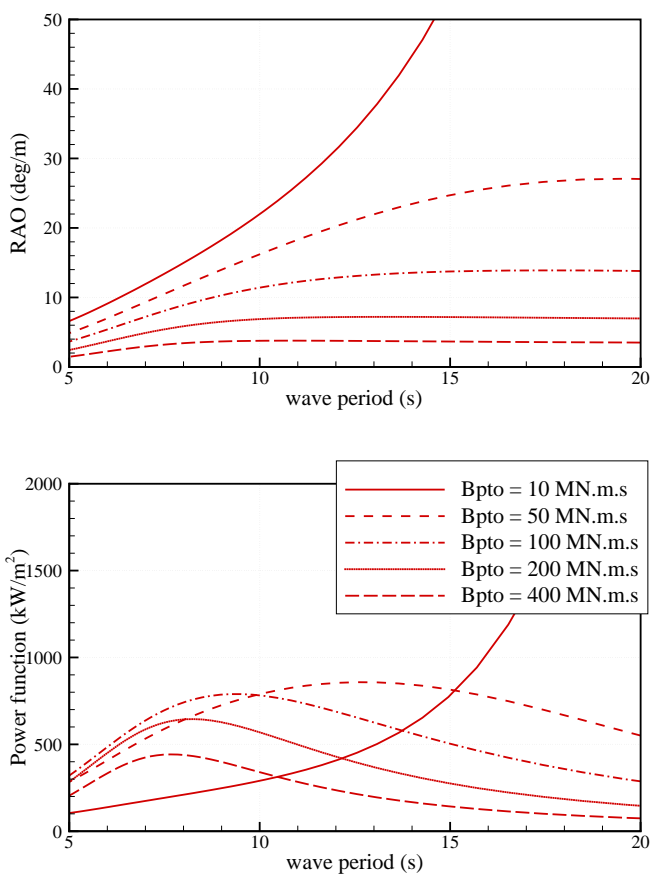


Figure 18: RAOs and power function for the B-OF with PTO settings 1 to 5.

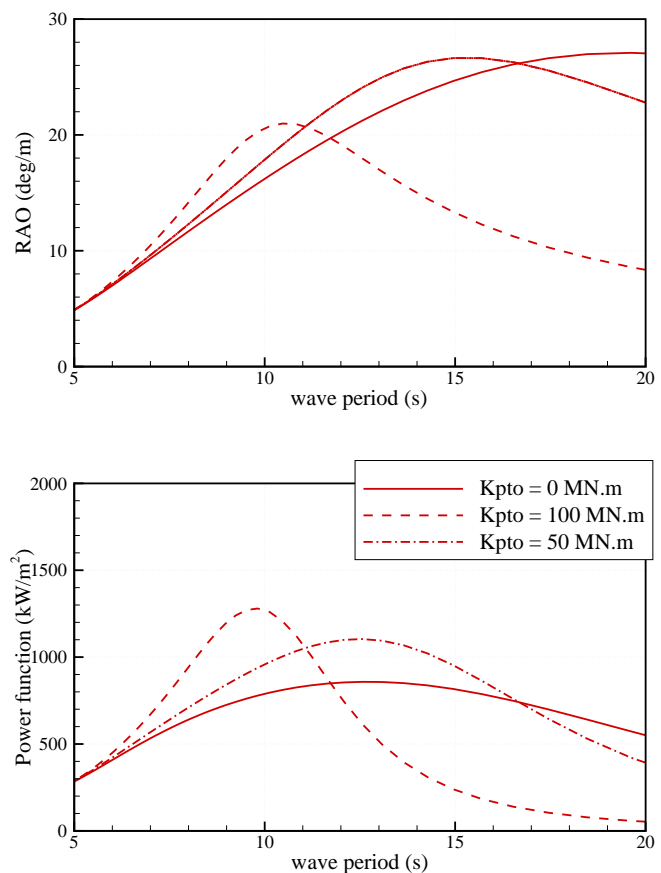


Figure 19: RAOs and power function for the B-OF with PTO settings 5, 6 and 7.

however, possible that redistribution of mass within the flap could lower the moment of inertia, and hence both the natural period and the amount of reactive power flow. This would make it easier to control the device, as the phase relation would be inherently improved.

### 3.1.3 Effect of quadratic damping

In order to get an idea of the importance of non-linear effects on the response of the B-OF WEC, RAO and power function of the system were calculated for wave amplitudes of 0.5, 1.0 and 2 meters. The PTO was set to linear, with PTO parameter setting number 2.

From Figure 20 we may see that the viscous loss has considerable influence on the response and power output of the system. Linear approximations as with the frequency domain model should therefore be avoided or used with special care. In the main range of interest for wave energy harvesting, 5-12 s wave period, the output power is found in the range between 300 and 750 kW per squared incident wave height. The reduction in power as compared to the non-viscous case is typically in the order of 25 % for 4 m wave height, and smaller for low wave periods or smaller wave heights.

### 3.1.4 Conclusions from verification tests

The results from regular waves tests lead us to the following conclusions:

- The implementation of frequency domain and time-domains were shown to be consistent.
- With the current configuration, the B-OF has a natural period higher than the period of predominant waves. A positive spring effect exerted by the machinery therefore improves the performance for typical wave periods.
- The order of magnitude of absorbed power from the B-OF is several hundreds of kW per squared wave amplitude (in regular waves)
- The PTO parameters ( $B_{PTO}$  and  $K_{PTO}$ ) have a large influence on the transfer functions of the B-OF. Hence, the estimation of the power absorption should be done with optimisation of the PTO parameters.
- Viscous damping reduces the amplitude and power responses substantially. Linearised models should therefore be used with great care, and the variation due to uncertainty in the viscous drag coefficients should be assessed.

## 3.2 Power matrix and criteria

In this section, all time domain simulations were performed in irregular waves using the JONSWAP spectrum. All quantities are derived from 1200 s duration simulations, with a time step of 0.05 s. To remove the transient effects, the first  $15 \times T_p$  seconds of the simulations are not taken into account.

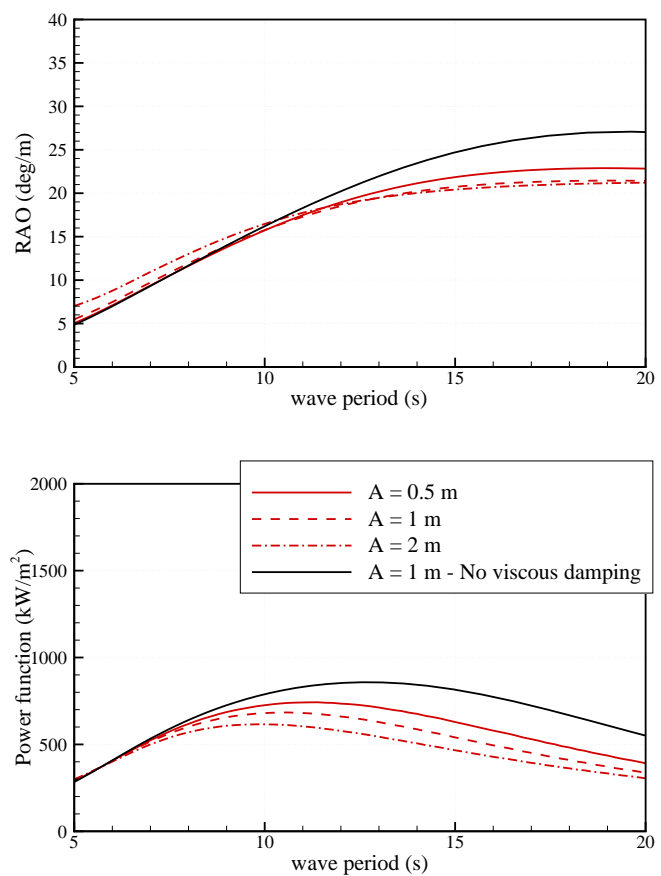


Figure 20: Effect of viscous damping on the RAO and power function of the B-OF WEC. The PTO is linear with setting number 2.

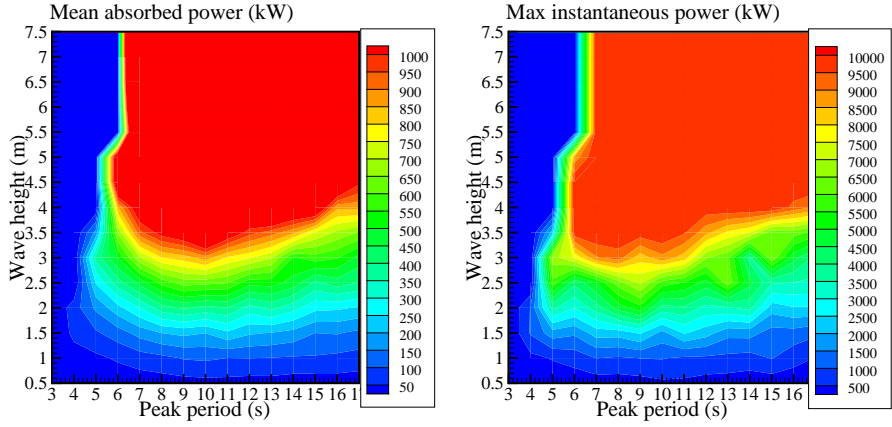


Figure 21: Power matrix of the B-OF with optimised PTO coefficients. The left-hand figure is the mean absorbed power and the right-hand figure is the maximum instantaneous power recorded during each simulation.

### 3.2.1 Power matrix of the B-OF

Figure (21) shows the power matrix of the B-OF, for a water depth of 13 m. The left-hand figure is the mean absorbed power and the right-hand figure is the maximum recorded over the duration of the simulation for each sea state.

For each sea state, the set of PTO parameters ( $B_{PTO}, K_{PTO}$ ) were optimised. The range of values for optimisation of the PTO parameters is given in Table 5.

$B_{PTO}$ (MN.m.s/rad)	$K_{PTO}$ (kN.m/rad)
Minimum	0
Maximum	200

Table 5: Range of values for optimisation of the PTO parameters

For a typical sea state of 9 s wave peak period and 2.5 m significant wave height, the mean absorbed power is as large as 600 kW. A mean power absorption higher than 1 megawatt is quickly reached as the significant height increase. The system exhibits an efficiency rather insensitive to the wave period.

The maximum instantaneous machinery power is typically about 10 times the mean power. It is very large. This might be a drawback of the system from the power electronics point of view. The effect of limiting the instantaneous power is investigated later.

Figure (22) shows the matrices of the optimised values of the PTO coefficients. One can see that they vary mostly with the wave period. For a fixed wave height, the optimal damping coefficient reaches a maximum for 5-7 seconds. It decreases slowly as the wave peak period increases. As an average, one can say that the nominal value of  $B_{PTO}$  should be about 100 MN m.s/rad.

The optimal stiffness coefficient reaches a maximum for wave periods of about 6-8 seconds. As an average,  $K_{PTO}$  should be about 50 MN m/rad.

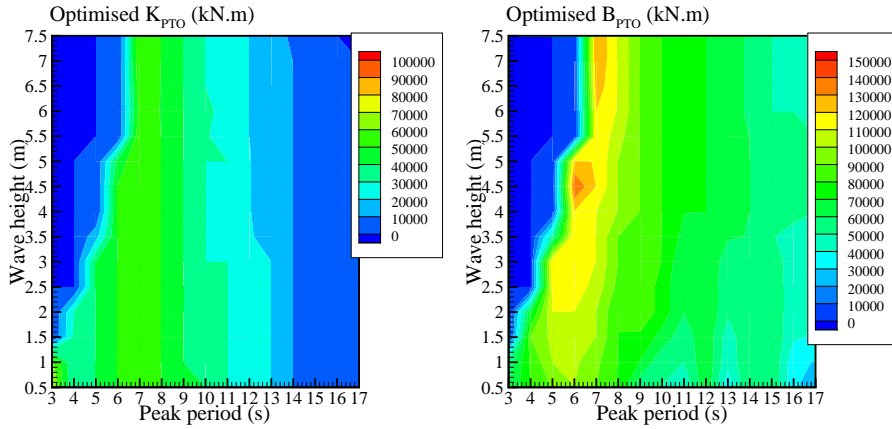


Figure 22: Optimised value of the PTO coefficients.

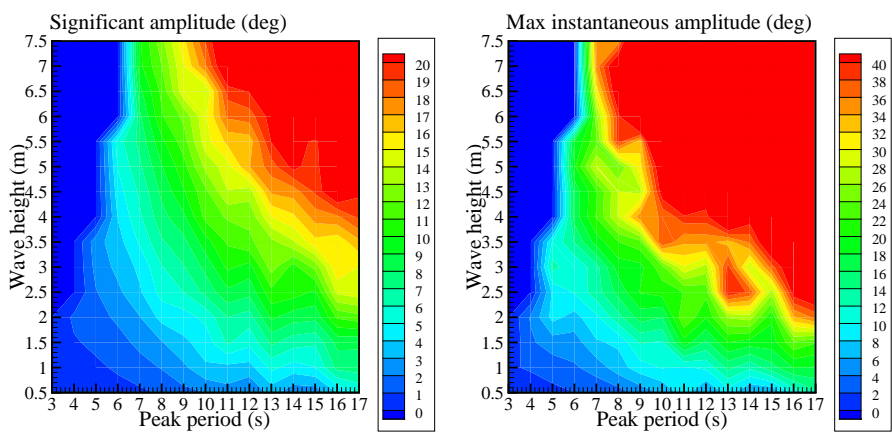


Figure 23: Matrices of the RMS values (left) and maximum excursion (right) for the angular motion with PTO coefficients optimised for each sea state.

Figure 23 shows the matrices of the RMS value and maximum recorded value during the simulation for the motion. We observe that the typical amplitude for normal wave conditions is within the range of 10 degrees, with maxima reaching up to 25 degrees, whereas in more energetic sea states the amplitudes are predicted to reach up to 40 degrees and above. Care should be taken, though, in interpreting results with such large amplitudes, as the assumptions of small amplitudes used to establish the mathematical model is violated.

By multiplying the power matrix with wave data statistics, one can calculate the annual energy absorption for each considered wave site. The values are reported in Table 6 together with the assessment criteria. As mentioned before, in order to simulate the wave resource at 13 m water depth, the wave energy resource at each site has been scaled to incorporate an assumed power loss of 10 % as compared to the offshore level. Linear refraction was also accounted for.

Parameter	Unit	SEM-REV	EMEC	Yeu	Lisboa	Bel-mullet	Danish study
$\gamma$		1	1	3.3	3.3	3.3	1
$J$	[kW/m]	13.3	19.6	23.5	33.7	72.5	12.0
Mean power	[kW]	211	348	440	513	981	243
Capture width	[m]	15.8	17.8	18.7	15.2	13.5	20.0
$E_y / \text{mass}$	[kWh/kg]	0.49	0.80	1.0	1.2	2.3	0.56
$E_y / A_{\text{wet}}$	[MWh/m <sup>2</sup> ]	0.92	1.5	1.9	2.2	4.2	2.0
$E_y / F_{\text{PTO}}^{\text{RMS}}$	[kWh/N]	N/A	1.1	1.4	1.6	2.1	0.97
$E_y / F_{\text{wave}}^{\text{RMS}}$	[kWh/N]	N/A	3.4	4.1	4.8	6.6	2.8

Table 6: Evaluation criteria for the B-OF WEC for chosen sites having mean annual wave energy transport  $J$ , and where sea states are synthesised with a spectrum peakedness factor  $\gamma$ . The parameters are calculated based on the yearly energy delivery  $E_y$ . The mass is taken as the total mass of the ballasted installed structure and its concrete gravity base, and  $A_{\text{wet}}$  is the total wetted surface area of the structure (flap, barrier and base). Significant PTO force  $F_{\text{PTO}}^{\text{RMS}}$  and significant wave force  $F_{\text{wave}}^{\text{RMS}}$  are taken as the yearly RMS values. The uncertainty of the numbers is estimated to [-4, 30] %.

One can see that the mean annual power delivery that one can expect from the B-OF ranges from 211 kW for the SEM-REV site up to 981 kW for the highly energetic Belmullet site. For a typical wave resource of about 25 kW/m, the typical absorbed wave power by the B-OF is about 400 kW. The typical mean capture width is about 20 meters, depending on the site. That result corresponds to a capture width ratio of about 70 % which agrees perfectly with capture width ratio for the Oyster device reported by Henry *et al.* in [6], Figure 7. Note that they are experimental results.

Figure 24 shows the distribution of the absorbed power in function of the power level. The left-hand figure shows the probability for the power production to be between two levels and right-hand figure shows the probability for the power to be greater than a given power level. It has been calculated with the wave statistics of the Yeu site. One can see that the absorbed wave power is greater than the mean power about 40 % of the year.

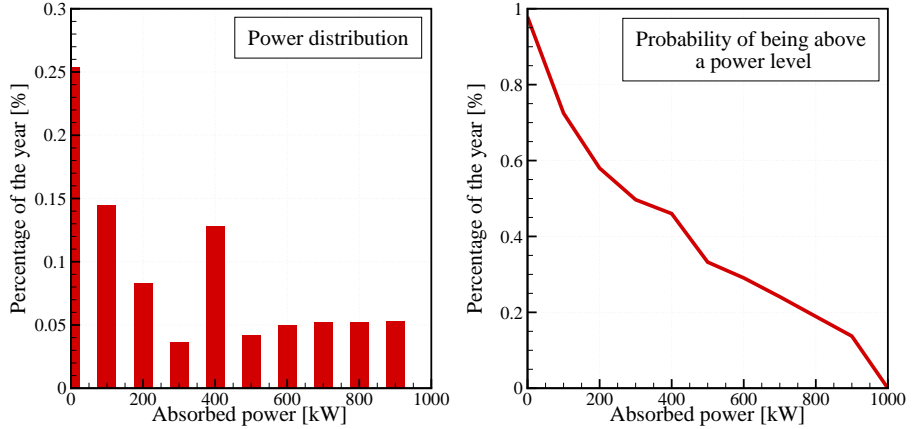


Figure 24: Distribution of the power delivery for the B-OF placed at Yeu off the French coast.

### 3.2.2 Assessment of the uncertainties

From the regular wave tests, the main uncertainty source was identified as the choice of the viscous damping coefficient.

In order to assess the uncertainty of yearly energy output associated with the modelling of the viscous losses, the mean annual absorbed power at the Danish site was calculated with different values for the viscous damping coefficients. The PTO coefficients were optimised for each sea state. Figure 25 shows the results in function of the percentage of viscous damping coefficients with respect to the nominal values.

One can see that the modelling of the viscous damping has considerable influence on the results for the mean power output. If viscous damping is set to zero, the mean absorbed power is about 30 % greater than the one with nominal values. One can see that increasing the viscous damping coefficient only possibly give a slight reduction of power, at most 4 % reduction.

Therefore, the retained uncertainty is  $[-4\%, +30\%]$ .

## 3.3 Parametric studies

### 3.3.1 Threshold on the instantaneous absorbed power

Table 7 shows the mean absorbed power at the Danish site in function of a threshold on the instantaneous power. It means that the maximum of instantaneous power is limited to this threshold. The difference between the available instantaneous power and the maximum would then be lost.

One can see that the instantaneous power can be limited to a maximum of 4 MW with only negligible losses in the mean annual absorbed power. Further limiting the instantaneous output to 2 MW would have a significant effect on the mean absorbed power.

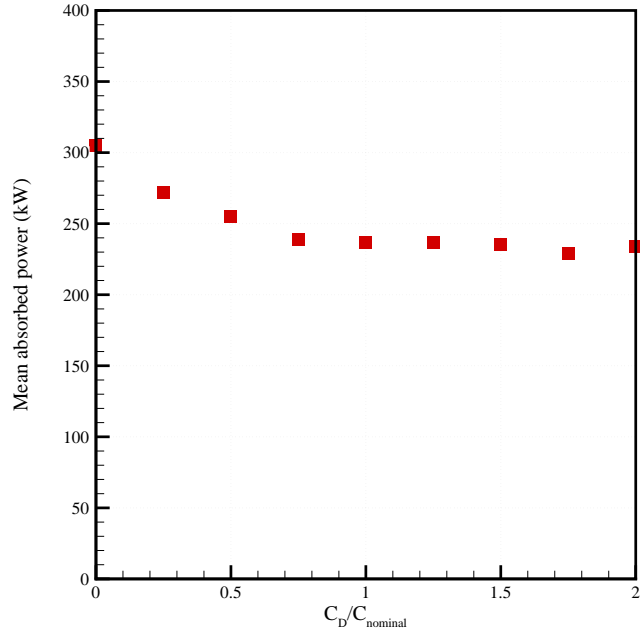


Figure 25: Mean absorbed power at the Danish site in function of the percentage of viscous damping with respect to the nominal value.

Max. instantaneous absorbed power (kW)	Mean annual absorbed power (kW)
2000	196
4000	234
No limitation	235

Table 7: Mean annual absorbed power at the Danish site in function of the threshold of maximum instantaneous absorbed power. The PTO coefficients were optimised for each sea state.

### 3.3.2 Threshold on the mean absorbed power

A calculation of the mean annual power at Yeu site was performed with limiting the mean output power for each sea state to 1 and 2 MW. The resulting reduction in the mean annual power was found to be 7% and 1%, respectively. It can therefore be concluded that the B-OF WEC could be rated at 1 MW with only a small loss of energy output.

### 3.3.3 Effect of scale

Figure 26 shows the effect of geometric scaling on the mean power absorption of the B-OF, at the Yeu site. This figure has been calculated using the frequency domain model. For every sea state the PTO parameters are kept fixed and equal to the setting at scale 1, but scaled according to Froude scaling.

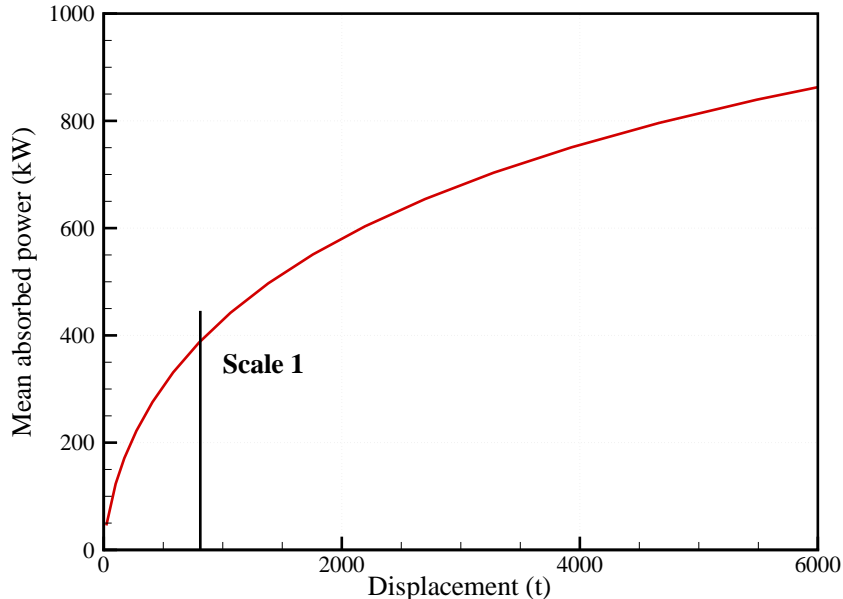


Figure 26: Influence of the scale on the mean power absorption of the B-OF placed at Yeu. The computations have been done with the frequency domain model (disregarding viscous losses) and are thus only indicative.

One can see that the mean absorbed power grows very fast with the displacement for small devices. As the displacement increases, the slope decreases. For a displacement twice the nominal displacement of the B-OF, one can see that the increase in power absorption is 41 %. In the same time, the increase in the wetted surface is 58 %. Therefore, it seems unlikely that scaling up the platform would improve its economics.

## 4 Conclusions and recommendations

From these results and the study, the main conclusions are :

- The mean power level that one can expect from the B-OF WEC is about 440 kW on a shallow-water site whose off-shore wave resource is about 30 kW/m. The uncertainty is about [-4 %, +30 %], and comes mainly from the modelling of the viscous losses.
- The yearly energy delivery per mass is about 1 kWh/kg, and the yearly energy delivery per wetted surface area is about 2 kWh/m<sup>2</sup> for the Yeu site which may be taken to represent typical European wave conditions.
- The rated power output power (i.e. the maximum average delivered power during each sea state) of the B-OF could be limited to 2 MW with only a small decrease in energy delivery. Limitation of the instantaneous absorbed power to 10 times the mean output power (4 MW) would not significantly reduce the mean absorbed power.
- Viscous losses may be important for the dynamics of this type of device, and should thus be thoroughly considered in mathematical modelling of such systems.

## References

- [1] Matt Folley, Trevor Whittaker, and Alan Henry. The performance of a wave energy converter in shallow water. In *6th European Wave and Tidal Energy Conference*, Glasgow, UK, August 29 - September 2 2005.
- [2] Trevor Whittaker, David Collier, Matt Folley, Max Osterried, Alan Henry, and Michael Crowley. The development of oyster – a shallow water surging wave energy converter. In *7th Annual European Wave & Tidal Energy Conference*, Porto, Portugal, September 2007.
- [3] M. Folley, T.W.T. Whittaker, and J. van't Hoff. The design of small seabed-mounted bottom-hinged wave energy converters. In *Proceedings of the 7th European Wave and Tidal Energy Conference*, Porto, Portugal, 2007.
- [4] Trevor Whittaker, David Collier, Matt Folley, Max Osterried, Alan Henry, and Michael Crowley. The construction of oyster – a nearshore surging wave energy converter. In *2nd International Conference on Ocean Energy*, Brest, France., October 2008.
- [5] L. Cameron, R. Doherty, A. Henry, K. Doherty, J. Van't Hoff, D. Kaye, and T. Whittaker. Naylor, D. S. Bourdier. Design of the next generation of the oyster wave energy converter. In *3rd International Conference on Ocean Energy*, Bilbao, 6 October 2010.
- [6] A. Henry, K. Doherty, L. Cameron, T. Whittaker, and R. Doherty. Advances in the design of the oyster wave energy converter. In *Proc. Of the Royal Institution of Naval Architects Marine and Offshore Renewable Energy Conference*, London, UK, April 2010.
- [7] Jørgen Hals and Aurélien Babarit. Note on the transfer of ocean wave sea states from deep to shallow water. Internal memo writtten as part of the project "Numerical estimation of energy delivery from a selection of Wave Energy Converters" at Centre for Ships and Ocean Structures, 2011.
- [8] P. W. Bearman, M. J. Downie, J. M. R. Graham, and E. D. Obasaju. Forces on cylinders in viscous oscillatory flow at low Keulegan-Carpenter numbers. *Journal of Fluid Mechanics*, 154:337–356, 1985.

## Chapter 7

# A bottom-fixed heave-buoy array (B-HBA) inspired by the Wavestar WEC

# Numerical estimation of energy delivery from a selection of Wave Energy Converters – B-HBA study

Aurélien Babarit<sup>1</sup>, Jørgen Hals<sup>2</sup>

<sup>1</sup>Laboratoire de Mécanique des Fluides - CNRS UMR6598

Ecole Centrale de Nantes, 1 rue de la Noe, 44300 Nantes, France

<sup>2</sup>Centre for Ships and Ocean Structures

Norges teknisk-naturvitenskapelige universitet, Otto Nielsens V. 10, 7491 Trondheim, Norway

24 May 2011

## Summary

This document reports the study of a bottom-fixed heave-buoy array (B-HBA) wave wave energy converter in the frame of the project “Numerical estimation of energy production from a selection of Wave Energy Converters”. Its geometry and working principle has been strongly inspired by the Wavestar wave energy converter currently under development in Denmark.

The results of the study are given in terms of the following measures:

- The annual mean power.
- The yearly energy output / mass.
- The yearly energy output / wetted surface.
- The power per unit of significant PTO force.
- The power per unit of excitation force
- The duration curves.

These performance measures were estimated for the B-HBA using the mathematical model described in this report. Results are given in the following table and in Figure 1.

From these results and the study, main conclusions are :

- The mean power level that one can expect from the B-HBA WEC is about 300 kW on a site whose wave resource is about 25 kW/m. The uncertainty is about [-20%, +20%]. It comes from the estimation of the interaction factor between the floats.
- The influence of the PTO modelling – linear or hydraulic – has only a small influence (few percents) on the mean power absorption.

Parameter	Unit	SEM-REV	EMEC	Yeu	Lisboa	Bel-mullet	Danish study
$\gamma$		1	1	3.3	3.3	3.3	1
$J$	[kW/m]	13.3	19.6	23.5	33.7	72.5	12.0
Mean power	[kW]	127	225	280	303	612	201
Capture width	[m]	9.5	11.4	11.9	9.0	8.4	16.7
$E_y / \text{Mass}$	[kWh/kg]	0.69	1.23	1.53	1.66	3.36	1.10
$E_y / A_{\text{wet}}$	[MWh/m <sup>2</sup> ]	0.25	0.45	0.56	0.61	1.23	0.40
$E_y / F_{\text{PTO}}^{\text{RMS}}$	[kWh/N]	0.93	1.16	1.20	1.15	1.62	1.24
$E_y / F_{\text{wave}}^{\text{RMS}}$	[kWh/N]	2.03	3.01	3.34	3.10	4.24	3.30

Table 1: Evaluation criteria for the B-HBA WEC for chosen sites having mean annual wave energy transport  $J$ , and where sea states are synthesised with a spectrum peakedness factor  $\gamma$ . The parameters are calculated based on the yearly energy delivery  $E_y$ . The mass is taken as the total mass of the installed bottom-fixed structure, and  $A_{\text{wet}}$  is the wetted surface area of the structure. Significant PTO force  $F_{\text{PTO}}^{\text{RMS}}$  and significant wave force  $F_{\text{wave}}^{\text{RMS}}$  are taken as the yearly RMS values. The uncertainty is estimated to  $[-20, 20]\%$ .

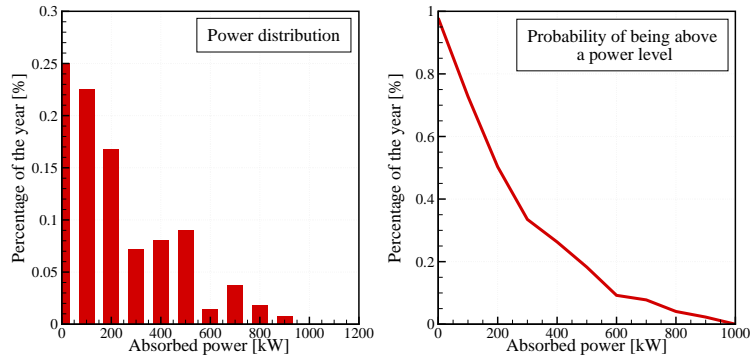


Figure 1: Distribution of the power production on a typical 23 kW/m wave site.

- The B-HBA could be rated at 1200 kW without losing a significant amount of energy production. Likewise, limitation of the instantaneous absorbed power to 4 MW would not reduce significantly the mean absorbed power.

# Contents

<b>1 System description - The B-HBA Wave Energy Converter</b>	<b>5</b>
1.1 Dimensions and mechanical parameters . . . . .	7
1.2 PTO and control . . . . .	7
1.3 Site and wave resource . . . . .	8
1.4 Cost related criteria . . . . .	9
1.5 Comment from the Wavestar developer . . . . .	9
<b>2 Equation of motion</b>	<b>9</b>
2.1 Assumptions and notations . . . . .	9
2.2 Kinematics . . . . .	10
2.3 Forces . . . . .	10
2.3.1 Hydrostatic forces . . . . .	10
2.3.2 Wave excitation and radiation forces . . . . .	12
2.3.3 Viscous damping forces . . . . .	12
2.3.4 PTO forces . . . . .	12
2.4 Final equations of motion . . . . .	14
2.4.1 Frequency domain . . . . .	14
2.4.2 Time domain . . . . .	14
2.5 Implementation . . . . .	14
2.5.1 Calculation of the hydrodynamic coefficients and functions . . . . .	14
2.5.2 Estimation of viscous damping coefficients . . . . .	17
2.5.3 W2W models . . . . .	17
<b>3 Simulation results and energy assessment</b>	<b>17</b>
3.1 Verification tests . . . . .	17
3.2 RAOs . . . . .	21
3.2.1 Linear damper . . . . .	21
3.2.2 Coulomb damping . . . . .	23
3.2.3 Effect of quadratic damping . . . . .	27
3.2.4 Conclusions . . . . .	28
3.3 Power matrix and criteria . . . . .	28
3.3.1 Power matrix of the B-HBA . . . . .	28
3.3.2 Assessment of the uncertainties . . . . .	32
3.4 Parametric studies . . . . .	35
3.4.1 Threshold on the instantaneous absorbed power . . . . .	35
3.4.2 Threshold on the mean output power . . . . .	35
3.4.3 Effect of scale . . . . .	35
<b>4 Conclusions and recommendations</b>	<b>37</b>

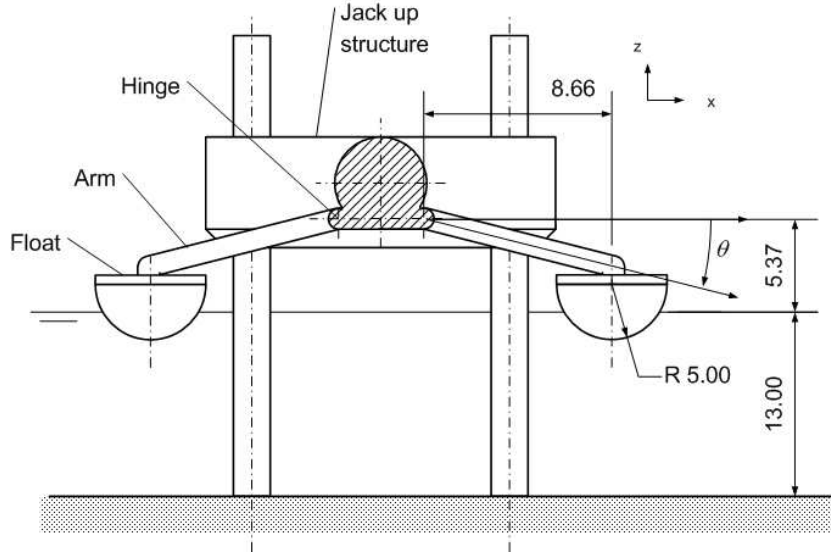


Figure 2: Sketch of the Wavestar WEC.

## 1 System description - The B-HBA Wave Energy Converter

The wave energy converter studied here is a bottom-fixed heave-buoy array (B-HBA) which has been defined according to available information about the Wavestar wave energy converter. The Wavestar is composed by two arrays of floats connected to a single jack-up structure. The jack-up structure stands on the seabed and provides a fixed reference to the floats. The floats are semi-submerged hemispheres. Each one is rigidly connected to an arm that is attached to the main structure via a hinge. With the action of the waves, each float moves up and down. The relative motion between floats and the structure is converted into useful energy via hydraulic rams. A simplified sketch of the system is shown in Figure 2.

Figure 3 shows a picture of the Wavestar test section which was installed at Hanstholm in Denmark in 2009. In comparison with a full-scale machine, it has only two floats and the length is shortened. The diameter of the float is 5 m.

Figure 4 shows an artistic view of a full scale Wavestar WEC. According to the Wavestar company website, a commercial 500 kW machine would have 20 floats with same diameter as in the test section (5 m). Its length would be 70 meters. In a later stage, it is proposed to double the dimensions of the system, in order to increase the rated power up to 6MW.

In order to get a smooth power output, the Wavestar WEC is aligned with the dominant wave direction, i.e. it is an attenuator. Hence, when the wave travels along the machine, each float is worked one after the other. Then, the total primary power production is smoother than with single point absorbers or terminator type wave energy converters.



Figure 3: Picture of the test section of the Wavestar Wave Energy Converter.



Figure 4: Artistic view of a full scale Wavestar Wave Energy Converter.

Property	Value	Unit
<b>Float+arm</b>		
Diameter	5	m
Diameter at WL	4.946	m
Height	5	m
Displacement	25.5	$\text{m}^3$
Mass	35	Mg
Surface	60	$\text{m}^2$
Length of arm $l$	10	m
Angle $\theta$ at rest	30	$^\circ$
Height $d$	0.366	m
Moment of inertia at hinge	$4.5 \cdot 10^6$	$\text{kg m}^2$
<b>Jack-up structure</b>		
Length	70	m
Width	17	m
Height	15	m
Draft	10	m
Diameter of columns	2	m
Mass	900	Mg
Surface	2000	$\text{m}^2$

Table 2: System parameters

### 1.1 Dimensions and mechanical parameters

Dimensions of the system were provided by Wavestar [8] or derived from pictures. The diameter of the floats is 5 m. The length of the arm is 10 meters and it is attached at to main frame through a hinge 5.37 m above the mean water level.

Estimation of the surface of the float is straightforward. For the arm, an estimate was obtained by assuming that it is a triangle of height 10 m and hinge side 5 m. For the platform, it was assumed that it is composed of a 10 m long 5 m diameter tube, on which the floats are connected, two barges of length 17 m and width 5 m and four 25 m tall 2 m diameter piles. It leads to a total surface of 4200 square meters. It is in agreement with data provided by the company [8]. It says that the surface of the system is 4 350 square meters.

Mass of an arm + float is 35 tonnes. The test section weighs 1000 tonnes. Extrapolating from that, one can estimate the weight of the full scale device to 1750 tonnes. It is in agreement with data provided by the company [8], stating that the mass of the complete platform plus 20 floats is about 1600 tonnes.

Parameters used in the calculations are summarised in Table 2.

### 1.2 PTO and control

In the Wavestar WEC, the mechanical power of the motion of each float is converted into hydraulic power by means of a hydraulic cylinder which is connected at one side to the arm and at the other side to the supporting structure, see Figure 5.

A hydraulic PTO can be modelled as a Coulomb damping force acting in the opposite direction of the cylinder velocity. For small amplitudes of motion, it

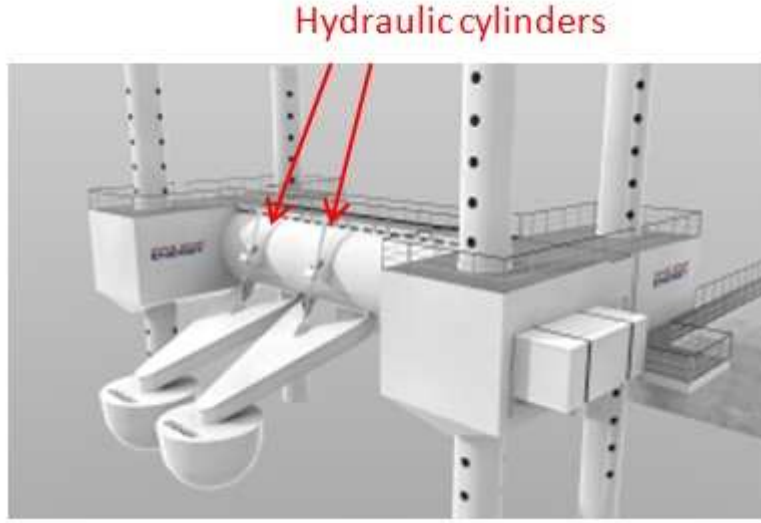


Figure 5: Power Take Off of the Wavestar Wave Energy Converter.

can be shown easily that the cylinder velocity has the same sign as the rotational velocity  $\dot{\theta}$ . Therefore, one can show that the PTO torque at the hinge  $F_{PTO}$  can be written:  $F_{PTO} = -H_{PTO}\text{sign}(\dot{\theta})$ , with  $H_{PTO}$  being a Coulomb damping coefficient.

As an alternative version, we also considered the case of a linear PTO system, with forces proportional to the angle  $\theta$  and its time derivative. Let  $B_{PTO}$  and  $K_{PTO}$  be the damping and restoring coefficients. As in the other studies, only cases with positive  $K_{PTO}$  were considered, because it can be achieved technically by adding a physical spring to the PTO system. This is not the case with negative  $K_{PTO}$ , which is the reason why it was not considered.

The possibility of non-neutral buoyancy was also considered. If the buoyancy of the float exceeds its own weight, it still can be kept in the half submerged position if one counteracts the excess buoyancy force by applying a static torque at the hinge. Technically, this can easily be achieved using the hydraulic PTO. Of course, the reverse effect (too small buoyancy) can be managed in the same way. The corresponding parameter is the difference between the actual mass of the float and the mass that it would have had if it were neutrally buoyant. It is denoted  $M_{PTO}$ , and Assuming one would use the volume of the float to adapt  $M_{PTO}$  through ballasting or de-ballasting, its range of variation is estimated to be  $[-10, 10]$  tonnes.

### 1.3 Site and wave resource

The Wavestar WEC is designed to be installed at site with small or intermediate water depth. In this study, the water depth was supposed to be the same as with the Oyster WEC study, i.e. 13 m.

The same annual wave statistics as with the Oyster WEC were used. They were obtained from wave data at larger water depths. The principle is that for each wave frequency component in the sea state, 90 % of the energy is

Criterion	Value	Unit
Characteristic wetted surface	4350	m <sup>2</sup>
Characteristic mass	1600	Mg

Table 3: Significant surface and mass of the B-HBA.

transferred from deep to intermediate water depths.

#### 1.4 Cost related criteria

The overall characteristic mass of the 70 m long 500 kW machine is estimated to be about 1600 tonnes and its surface area to be 4 350 m<sup>2</sup> [8]. See Table 3.

The two other cost criteria considered are the significant PTO force and the significant wave force. They both have zero mean values. So, they are defined as their RMS over the whole year.

#### 1.5 Comment from the Wavestar developer

In working with this study we have been in contact with the developer of the Wavestar device. They have been informed about our study, and have received a draft copy of this report. We proposed to the developer to give comment for inclusion into the report, and this is the comment from the Wavestar team:

*At Hanstholm, in the northwest of Denmark where the Wavestar test section of 2 floats is installed, a Wavestar machine of 20 floats would harvest in average approximately 87 kW, producing 0.76 Gae per year if linear damping is used as a control strategy to harvest energy. It is assumed a nominal installed electrical power of 600 kW, a PTO efficiency of 80 % and a maximum control torque of 10<sup>6</sup> Nm. However, under the same conditions, if reactive control is allowed, where the negative spring effect is achieved by means of control, the performance of the machine is doubled, harvesting in average approx. 175 kW, producing 1.51 GWh per year.*

## 2 Equation of motion

### 2.1 Assumptions and notations

In this study, only one single float is considered. The energy absorption is obtained by multiplying the result of energy absorption of this single float by the number of float in the whole machine. It means that the effect of wave interactions between the floats on the energy absorption are not modelled.

To take this effect into account, we use results from a study recently published [9]. It shows that the energy absorption is reduced by 20 % in a closely spaced array of heaving buoys WECs (FO3 platform), even with independent optimisation of the PTO of each buoy. This value will be retained in the computations of overall power.

The incident waves are assumed to be mono-directional. In agreement with the working principle of the B-HBA WEC, let us assume that they propagate

in the  $y$  direction. Let  $\theta$  be the angle between the arm of the float and the  $x$  axis, see Figure 6. Let  $\theta_0$  be this angle at rest. Let  $A$  be the axis of rotation for the arm and  $B$  be the point where it is connected to the float. Let  $I$  be the intersection point between the water plane at rest and the vertical axis of the float. Let  $l$  be the length  $|AB|$  and  $d$  be the height  $|BI|$ .

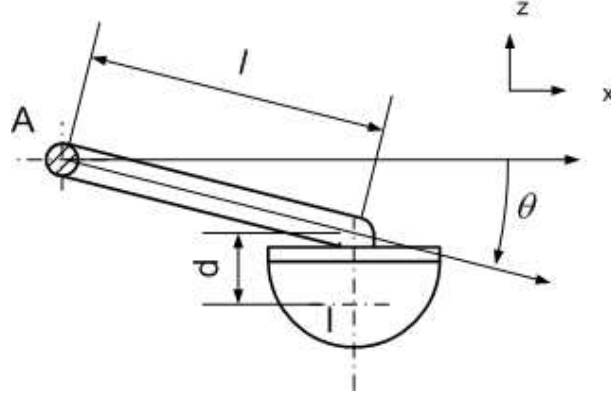


Figure 6: Notations used

It is assumed that all motions are of small amplitude. All hydrodynamical second-order effects are neglected.

Let  $M$  be the mass of the float+arm. Let  $G$  be its gravity centre. Let  $I_y$  be the respective moment of inertia of the float at the rotational axis  $A$ .

## 2.2 Kinematics

Seen from the hinge  $A$ , the position of  $I$  is given in function of  $\theta$  by:

$$\vec{AI} = (l \cos \theta - d \sin(\theta - \theta_0)) \vec{x} + (-l \sin \theta - d \cos(\theta - \theta_0)) \vec{z} \quad (1)$$

or, alternatively:

$$\vec{AI} = (l \cos(\theta - \theta_0) \cos \theta_0 - (d + l \sin \theta_0) \sin(\theta - \theta_0)) \vec{x} \quad (2)$$

$$+ (-d + l \sin \theta_0) \cos(\theta - \theta_0) - l \cos \theta_0 \sin(\theta - \theta_0) \vec{z} \quad (3)$$

At the hinge, the dynamic moment of the float is:

$$\vec{\delta}(A) = (I_y + M_{PTO} l^2) \ddot{\theta} \vec{y} \quad (4)$$

in which  $M_{PTO}$  is a parameter for describing additional ballast which could be added to the float at point  $B$  (see Section 1.2 for details).

## 2.3 Forces

### 2.3.1 Hydrostatic forces

In the frame of linear theory, one can show that the effect of the Archimedes force at  $I$  reads:

$$\vec{F}_B(I) = \rho g V \vec{z} - K_{H33}(-l(\sin \theta - \sin \theta_0) + d(1 - \cos(\theta - \theta_0))) \vec{z} \quad (5)$$

or, alternatively:

$$\vec{F}_B(I) = \rho g V \vec{z} - 2K_{H33} \sin \frac{\theta - \theta_0}{2} (-l \cos \frac{\theta + \theta_0}{2} + d \sin \frac{\theta - \theta_0}{2}) \vec{z} \quad (6)$$

Therefore, the moment force in  $A$  reads:

$$\begin{aligned} M_B(A) &= -K_{H55}(\theta - \theta_0) - \rho g V (l \cos \theta - d \sin(\theta - \theta_0)) \\ &+ 2K_{H33} (l \cos \theta - d \sin(\theta - \theta_0)) \\ &\times \sin \frac{\theta - \theta_0}{2} (-l \cos \frac{\theta + \theta_0}{2} + d \sin \frac{\theta - \theta_0}{2}) \end{aligned} \quad (7)$$

Linearised, it reads:

$$\begin{aligned} M_B(A) &= -(K_{H55} + K_{H33} l^2 \cos^2 \theta_0 - \rho g d V \\ &- \rho g V l \sin \theta_0)(\theta - \theta_0) - \rho g l V \cos \theta_0 \end{aligned} \quad (8)$$

At  $A$ , the effect of the gravity forces is:

$$M_g(A) = g(M|\vec{AG}| + M_{PTO}l) \cos \theta - g M_{PTO} d \sin(\theta - \theta_0) \quad (9)$$

Linearised, it reads:

$$\begin{aligned} M_g(A) &= g(M|\vec{AG}| + M_{PTO}l) \cos \theta_0 \\ &- g \left( (M|\vec{AG}| + M_{PTO}l) \sin \theta_0 + M_{PTO}d \right) (\theta - \theta_0) \end{aligned} \quad (10)$$

One can see that the effect of  $M_{PTO}$  would be to increase the hydrostatic stiffness if it is positive.

Summing the effect of gravity and buoyancy forces, one gets the hydrostatic force:

$$\begin{aligned} M_H(A) &= -K_{H55}(\theta - \theta_0) + g \left( M|\vec{AG}| + M_{PTO}l - \rho V l \right) \cos \theta \\ &+ gd(\rho V - M_{PTO}) \sin(\theta - \theta_0) + 2K_{H33} (l \cos \theta - d \sin(\theta - \theta_0)) \\ &\times \sin \frac{\theta - \theta_0}{2} \left( -l \cos \frac{\theta + \theta_0}{2} + d \sin \frac{\theta - \theta_0}{2} \right) \end{aligned} \quad (11)$$

Linearised, it reads:

$$M_B(A) = -K(\theta - \theta_0) + g(M|\vec{AG}| + M_{PTO}l - \rho l V) \cos \theta_0 \quad (12)$$

with

$$\begin{aligned} K &= K_{H55} + K_{H33} l^2 \cos^2 \theta_0 \\ &+ g \left( (M|\vec{AG}| + M_{PTO}l - \rho V l) \sin \theta_0 - (\rho V - M_{PTO})d \right). \end{aligned} \quad (13)$$

Note that by design  $-\rho l V + M|\vec{AG}| = 0$ .

### 2.3.2 Wave excitation and radiation forces

In the frame of linear theory, the hydrodynamic forces reads in the frequency domain:

$$M_D(A) = M_{ex}(A) - C_M \ddot{\theta} - C_A \dot{\theta} \quad (14)$$

in which:

- $M_{ex}(A)$  is the excitation force at the hinge.
- $C_M$  and  $C_A$  are the added mass and radiation damping coefficients.

### 2.3.3 Viscous damping forces

The viscous damping forces are modelled under the form of a drag force applying at  $I$ :

$$\vec{F}_V(I) = -\frac{1}{2}\rho \mathbf{C}_D \mathbf{A}_D \left\| \vec{V}(I) - \vec{V}_0(I) \right\| (\vec{V}(I) - \vec{V}_0(I)) \quad (15)$$

where:

- $\vec{V}_0(I)$  is the undisturbed flow velocity at point I.
- $C_D = \begin{pmatrix} C_x & 0 & 0 \\ 0 & C_y & 0 \\ 0 & 0 & C_z \end{pmatrix}$  is the drag coefficient matrix
- $A_D = \begin{pmatrix} A_x & 0 & 0 \\ 0 & A_y & 0 \\ 0 & 0 & A_z \end{pmatrix}$  is the characteristic surface matrix.
- $\vec{V}(I) = \begin{pmatrix} -l \sin \theta - d \cos(\theta - \theta_0) \\ -l \cos \theta + d \sin(\theta - \theta_0) \end{pmatrix} \dot{\theta}$  is the velocity of the float at point I.

The corresponding torque at point A is obtained by:

$$\vec{M}_V(A) = \vec{AI} \times \vec{F}_V(I) \quad (16)$$

### 2.3.4 PTO forces

As stated in Section 1.2, two alternative models are used. One is Coulomb damping and the other one is linear PTO:

$$\begin{aligned} M_{PTO,C}(A) &= -M_{PTO} g l \cos \theta_0 \\ &+ \begin{cases} -H_{PTO} \operatorname{sign}(\dot{\theta}) & \text{for Coulomb damping} \\ -B_{PTO} \dot{\theta} - K_{PTO} \theta & \text{for linear PTO} \end{cases} \end{aligned} \quad (17)$$

In this last equation, the static term is required to cancel the static term in the hydrostatic force.

The numerical implementation of the Coulomb damping is difficult because it adds a very stiff term in the equations. This can lead to unphysical oscillations for velocities around zero, which may cause erroneous values for the power

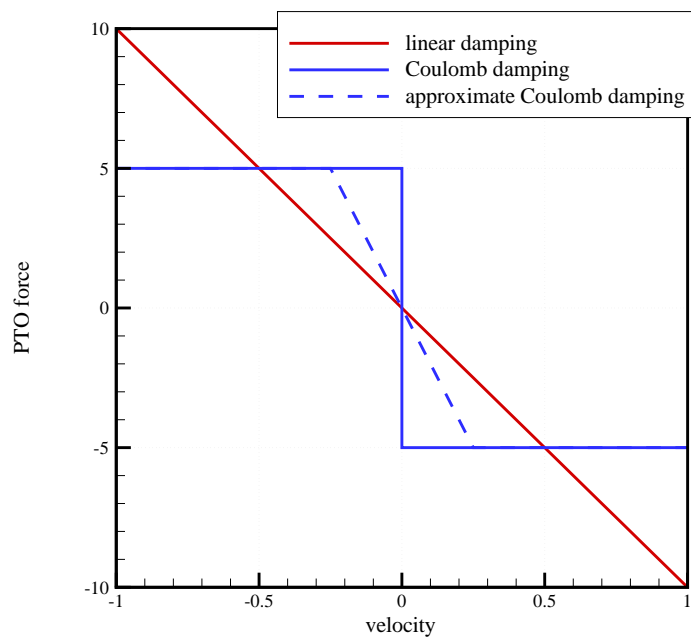


Figure 7: PTO force vs velocity for linear PTO forces, Coulomb damping and approximate Coulomb damping.

absorption. Hence, in practise, perfect Coulomb damping has been replaced by approximate Coulomb damping, in which the PTO force is supposed to be linear with the velocity for small velocities; and constant when the velocity is large enough. The principle is illustrated in Figure 7.

$$M_{PTO,C}(A) = -M_{PTO}gl \cos \theta_0 - \min(G_{PTO}|\dot{\theta}|, H_{PTO}) \operatorname{sign}(\dot{\theta}) \quad (18)$$

(approximate Coulomb damping)

In this study, the large  $G_{PTO}$  coefficient was set to 100 times the inertia + added mass coefficient.

## 2.4 Final equations of motion

### 2.4.1 Frequency domain

In the frequency domain, only the linear PTO is considered. The viscous forces are not taken into account. By expressing Newton's law to balance inertia forces with other forces, one find that the equation of motion of the float in the frequency domain is:

$$(I_y + M_{PTO}l^2 + C_M(\omega)) \ddot{\theta} + (B_{PTO} + C_A(\omega)) \dot{\theta} + (K + K_{PTO})(\theta - \theta_0) = F_{ex}(\omega) \quad (19)$$

### 2.4.2 Time domain

In time domain, viscous forces may be included as well as approximate Coulomb damping for the PTO. The equation of motion is:

$$(I_y + M_{PTO}l^2 + \mu_\infty) \ddot{\theta} = M_{ex} - M_{PTO} - M_V - M_H - \int_0^t K_{rad}(t - \tau) \dot{\theta}(\tau) d\tau \quad (20)$$

with:

$$\mu_\infty = \lim_{\omega \rightarrow +\infty} C_M(\omega) \quad (21)$$

$$K_{rad}(t) = \frac{2}{\pi} \int_0^{+\infty} C_A(\omega) \cos \omega t d\omega \quad (22)$$

where  $M_{PTO}$ ,  $M_V$ ,  $M_H$  given in the previous equations.

## 2.5 Implementation

### 2.5.1 Calculation of the hydrodynamic coefficients and functions

The BEM code Aquaplus [4] was used to calculate the hydrodynamic coefficients in the frequency domain. Figure 8 shows the meshes which were used. The first one is composed of 140 flat panels. A finer mesh, composed of 300 flat panels, was also considered in order to verify convergence.

Results of computation of added mass, radiation damping coefficients and excitation force coefficient at hinge point A are plotted in Figure 9. The solid lines are results of calculation with Aquaplus with the 300 panels mesh and the square are results of the calculation with Aquaplus with the 140 panels mesh.

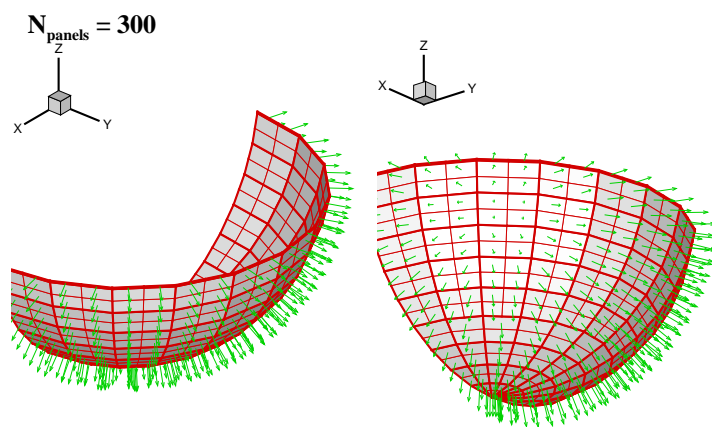
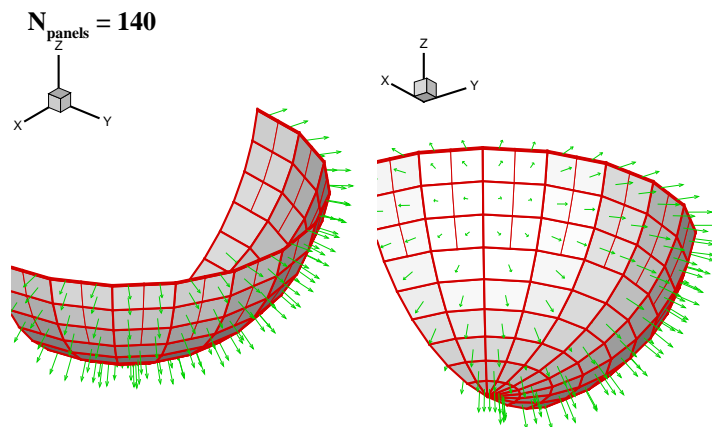


Figure 8: Meshes used for the hydrodynamic calculations. The top one is composed of 140 flat panels. The bottom one is composed of 300 panels.

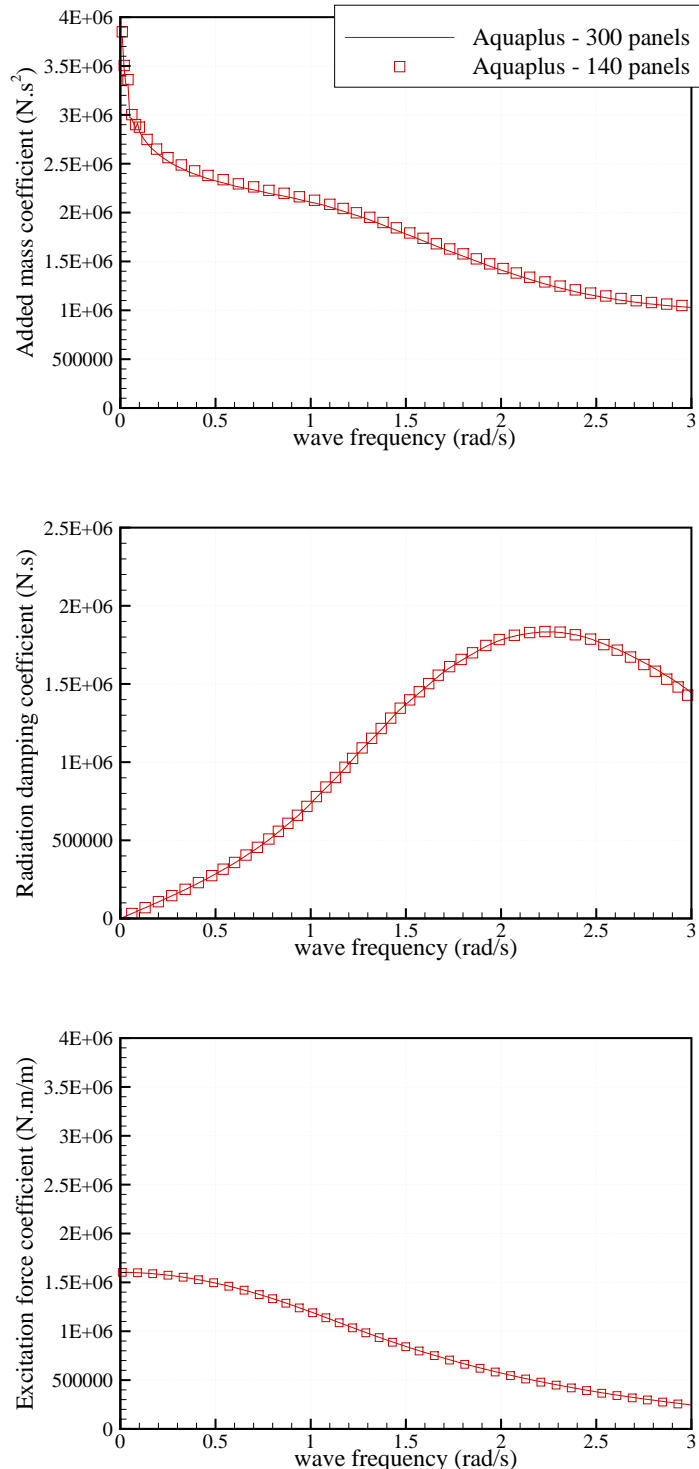


Figure 9: Hydrodynamic coefficients of the radiation force and excitation force in frequency domain, computed with Aquaplus. The top figure shows the added mass coefficient, the middle figure shows the radiation damping coefficient and the bottom figure shows the modulus of the excitation force coefficient. It was calculated with a wave direction parallel to the axis of the hinge.

For the calculation of the excitation force coefficients, the wave direction was set parallel to the axis of the hinge.

The agreement between the two meshes is very good. Therefore, calculations for the hydrodynamic coefficients are considered as converged.

Aquaplus was also used for calculating the hydrostatic coefficients  $K_{H33}$  and  $K_{H55}$ . They were found to be:

- $K_{H33} = 193 \text{ kN/m}$
- $K_{H55} = 33 \text{ kN m/rad}$

### 2.5.2 Estimation of viscous damping coefficients

The order of magnitude of the motion of the float is likely to be of the same order of the diameter of the buoy, i.e. 5m. Hence, the Keulegan Carpenter number  $KC = \frac{2\pi A}{D}$  of the float is expected to be in the range [0, 6]. Hence, according to [2], the drag coefficients should be something between 0.5 and 1. In this study, we chose to set  $C_x = C_y = 0.5$  and  $C_z = 1$ . They are thought to be minimal values for these viscous losses. So they should not be exaggeratedly penalising for assessing the energy absorption of the device.

The corresponding representative areas were calculated. Their values are  $A_x = A_y = 7.0 \text{ m}^2$  and  $A_z = 14.0 \text{ m}^2$ .

### 2.5.3 W2W models

Based on equations (19) and (20), two numerical models were derived: one in the frequency domain and the other one in the time domain. They were both implemented in Fortran90.

## 3 Simulation results and energy assessment

When they are not otherwise specified, the parameters which were used in all the simulations presented here are those given in Table 2.

### 3.1 Verification tests

The natural period of the float is given by:

$$\omega_0 = \sqrt{\frac{K}{I_y + C_M(\omega_0)}} \quad (23)$$

with  $K$  and  $I_y$  as in equation (19).

After a few iterations, one gets  $\omega_0 = 1.50 \text{ rad/s}$ . In comparison with the usual range of wave frequencies, the natural frequency of the B-HBA WEC is quite high. Then, its working principle is probably not based on resonance. The characteristics of its response is expected to be close the Bref-HB (inspired by the Seabased WEC), placed in a close array.

Figure 10 shows the RAO (Response Amplitude Operator) of the hinge motion with no PTO damping nor PTO stiffness. As expected, one can see that there exists a resonance peak at frequency 1.49 rad/s. For small frequencies,

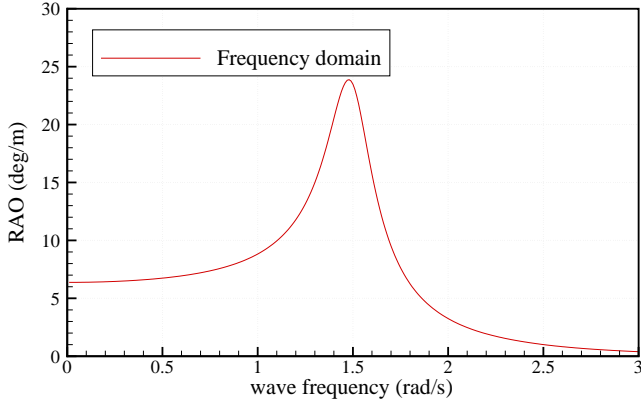


Figure 10: RAO of the B-HBA WEC computed with the frequency domain model. All PTO parameters are set equal to 0.

one can see that the amplitude of the motion is about 6.4 degrees. We shall show that it is according to what should be expected.

For long waves, the float motion in heave will match the wave amplitude. From this, one can calculate the asymptotic response of the motion of the hinge  $\theta_a$  per meter of wave amplitude by:

$$\theta_a = \lim_{\omega \rightarrow 0} (\theta - \theta_0) = \frac{1}{A} (\arcsin(\frac{h - A}{l_0}) - \theta_0) \quad (24)$$

Using  $A = 0.1$  m,  $h = 5.37$  m,  $l_0 = 10.18$  m, one gets  $\theta_a = 6.6$  degrees, which agrees well with the numerical result.

Figure 11 shows the comparison of the RAO of the B-HBA WEC calculated with the frequency domain model and the time domain model. In the time domain model, the viscous damping is set equal to 0 and a small wave amplitude was used ( $A = 0.1$  meters). The agreement is excellent. It shows that both implementations of the equations are correct, at least to first order.

Figure 12 shows decay tests of the motion buoy computed with the time domain model, with and without viscous damping. The initial angle is set equal to 10 degrees. The PTO parameters are set to 0.

As expected, the motion is more damped with viscous damping than without. It indicates that the implementation of the viscous damping is correct.

Finally, results of the frequency domain model were compared with experiments. Datas of measured mechanical power from 1/40 scale experiments at Aalborg University and scale 1/10 at Nissum Bredning where found in a presentation by P. Frigaard [13]. They are shown in Figure 13.

Results at 1/40 scale are given for significant wave height of 1,2,3,4 and 5 meters. The corresponding wave peak periods are not given. However, they are likely to correspond with the sea states which are considered in [10] and [14]. Therefore, these sea states were considered for calculation of the power absorption with the numerical model.

One can see that experimental results at 1/10 scale are very much scattered.

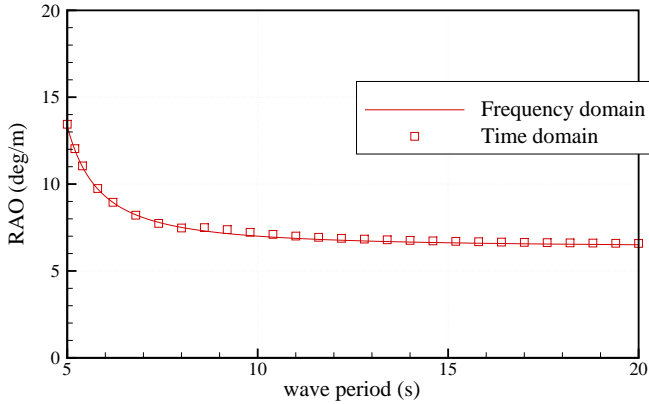


Figure 11: Comparison of B-HBA WEC’s RAO calculated with the frequency and the time domain model. All PTO parameters are set equal to 0. In the time domain model, a wave amplitude of 0.1 meters was used. The agreement is excellent which gives confidence that both models are implemented correctly.

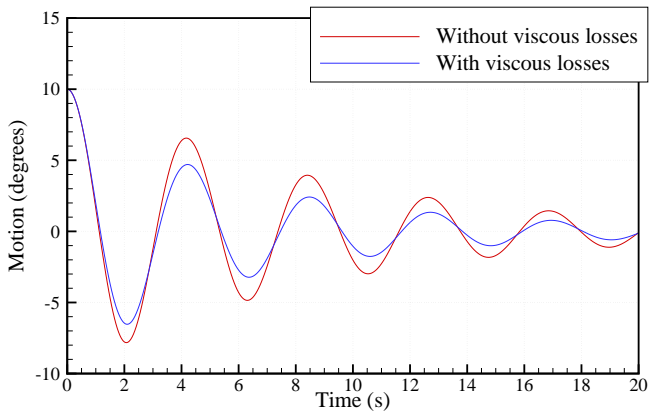


Figure 12: Decay test of the motion of the buoy, with and without viscous damping. The initial angle is 10 degrees. The PTO parameters were set equal to 0.

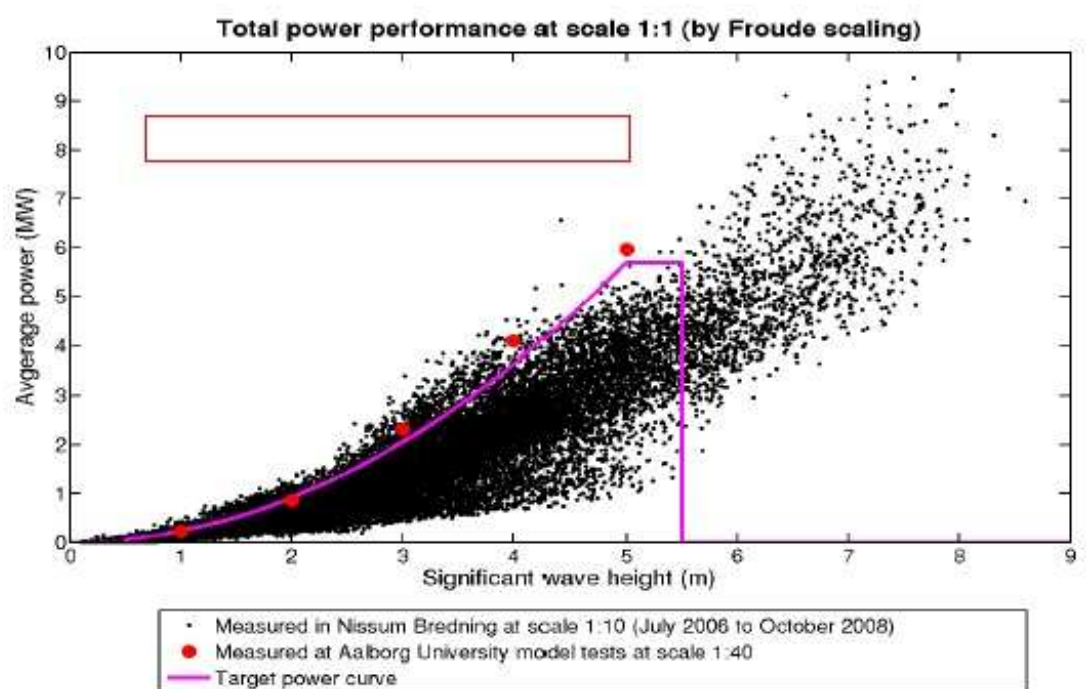


Figure 13: Power absorption of the B-HBA WEC at scale 1 extrapolated from results at 1/40 and 1/10 scale experiments. This figure is taken from [13].

However, one could say that, as an average, the power absorption is reduced to half in comparison with the results of the experiments at 1/40 scale.

Table 4 shows the comparison of the power absorption measured in the experiments and calculated with the frequency domain model. For this last model, the power corresponds with 20 times the absorbed power of one single float. No park interaction factor was taken into account.

Table 4: Comparison of power absorption calculated with the frequency domain model and measured in experiments at scale 1/40 and scale 1/10. Experimental results are taken from [13].

sea state $H_s$ (m)	1/40 scale	power absorption (kW)	
		1/10 scale	FD model
1	250	[0-300]	160 with $T_p = 5.6$ s
2	800	[100-1 200]	910 with $T_p = 7$ s
3	2 200	[300-2 800]	2 100 with $T_p = 8.4$ s
4	4 100	[700-4 000]	3 700 with $T_p = 9.8$ s
5	6 000	[1 000-5 500]	5 400 with $T_p = 11.2$ s

There is a good agreement between the numerical model and the experimental results at scale 1/40, except for the smaller sea state for which the numerical model under-predicts the energy absorption. This gives us confidence in the ability of the numerical model to give good estimates of the energy absorption of this device.

### 3.2 RAOs

The PTO coefficients have an influence on the RAO and power function of the B-HBA WEC. To understand this influence, RAOs and power functions with several sets of PTO coefficients were computed. They were calculated with the frequency domain model when the PTO is linear, and with the time domain model when it is Coulomb damping. With the time domain model, RAOs are actually the maximum of the motion during a 1200 s duration simulation in which the transients were removed. Viscous effects were neglected.

#### 3.2.1 Linear damper

First, a linear damper is considered. Table 5 summarises the set of PTO coefficients which were used. For the  $M_{PTO}$  parameter, a range from 0 to one time the displacement of the buoy (10 Mg) was considered as reasonable. We plotted in Figures 14, 15 and 16 the associated RAOs and power functions.

In Figure 14, we have plotted the RAOs and power function for PTO settings from 1 to 5. For these settings, both  $K_{PTO}$  and  $M_{PTO}$  are equal to 0. One can see that:

- The order of magnitude of power absorption of one buoy of the B-HBA WEC is about 20-30 kW per squared amplitude of incident wave.
- The amplitude of motion is reduced as the  $B_{PTO}$  coefficient increases.

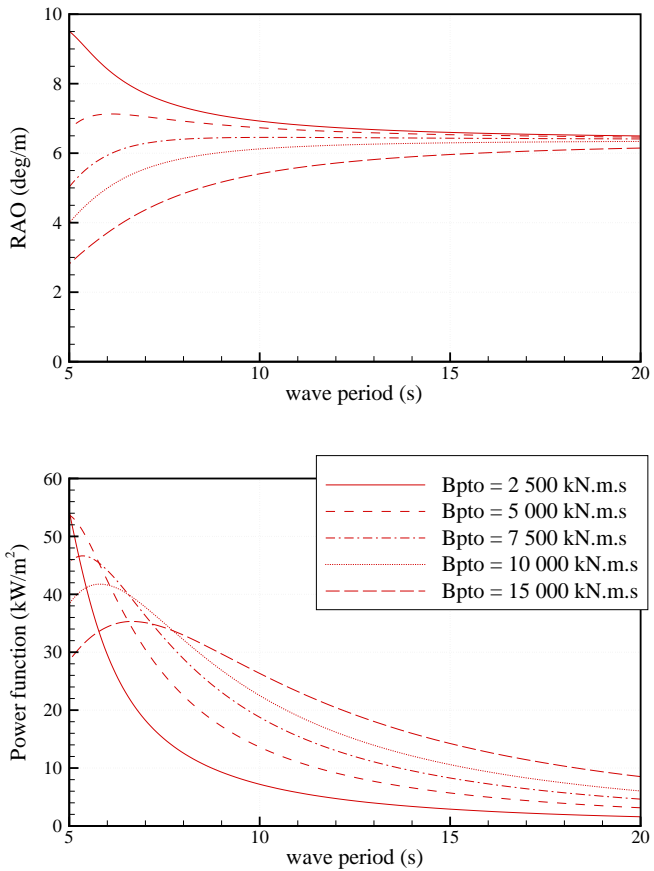


Figure 14: RAO and power function of the motion of the B-HBA with PTO settings 1 to 5. In these settings, the PTO model is linear, with both  $K_{PTO}$  and  $M_{PTO}$  equal to 0. Results have been computed with the frequency domain model.

Set number	$B_{PTO}$ (kN m s)	$K_{PTO}$ (kN m)	$M_{PTO}$ (Mg)	$H_{PTO}$ (kN m)
1	2 500	0	0	—
2	5 000	0	0	—
3	7 500	0	0	—
4	10 000	0	0	—
5	15 000	0	0	—
6	5 000	0	-10	—
7	5 000	0	10	—
8	5 000	1 000	0	—
9	5 000	5 000	0	—
10	5 000	10 000	0	—
11	—	—	—	500
12	—	—	—	1000
13	—	—	—	2000

Table 5: PTO settings for different test cases.

- The power function depends strongly on the damping coefficient. As  $B_{PTO}$  increases, the maximum of power absorption shifts to the longer period, and decreases. At the same time, the bandwidth gets broadened.
- The WEC behaves like a damped harmonic oscillator that within the range of typical wave frequencies works within its stiffness-dominated region.

From the annual energy absorption point of view, some of these effects are good (period shifting, broadening of bandwidth), and some are bad (decrease in the maximum of power absorption). Therefore one has to look for a compromise. It is likely that it will be beneficial to optimise this coefficient for every sea state.

Since the device behaves like a damped harmonic oscillator but is far into the stiffness-dominated region, it should be expected that increasing the mass and reducing the stiffness would improve its power absorption performance.

In Figure 15, we have plotted the RAOs and power function for PTO settings 3, 6 and 7. One can see that an increase of the  $M_{PTO}$  leads to an increase in the the maximum of power absorption. The effect on the natural period is small. Decreasing  $M_{PTO}$  decreases the natural period. It might be beneficial for the shortest wave periods. Therefore, this parameter was included as an optimisation parameter in the calculations of energy absorption.

In Figure 16, we have plotted the RAOs and power function for PTO settings 3 and 8 to 10. In these settings,  $M_{PTO}$  is equal to 0 and  $B_{PTO}$  equal to 7500 kN m/s (case 3) or 5000 kN m s (cases 6 and 7). One can see that the only effect of increasing the  $K_{PTO}$  coefficient is to decrease the power absorption. This was to be expected as the system already works in the stiffness-dominated region. Since we have assumed that the PTO spring coefficient cannot be negative, one should select  $K_{PTO}$  equal to 0 kN m.

### 3.2.2 Coulomb damping

Then, an approximate Coulomb damping is considered. As it is a non linear component, the time domain model was used to calculate the pseudo-RAO of the B-HBA WEC with three settings for the PTO force coefficient  $H_{PTO} =$

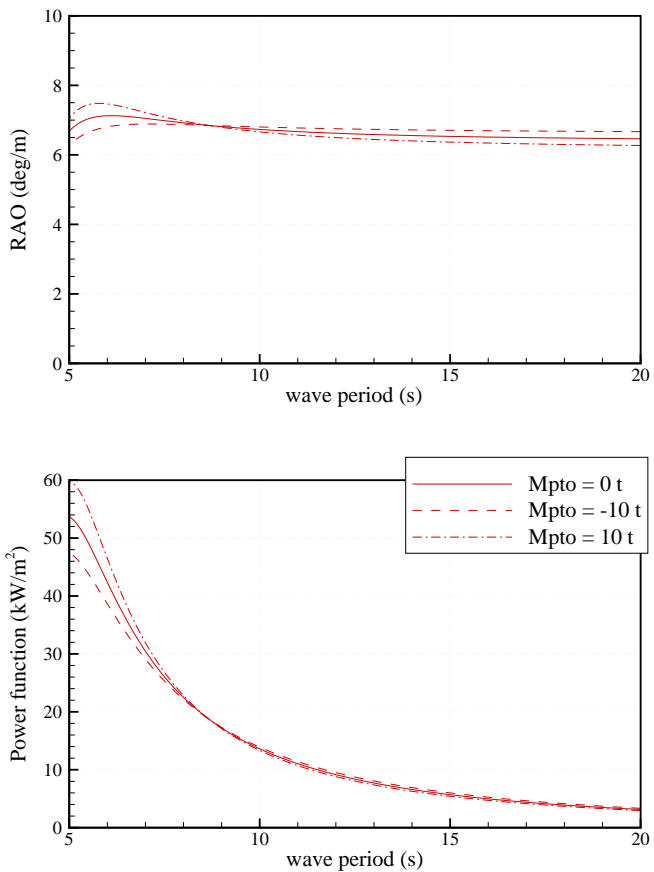


Figure 15: RAO and power function of the motion of the B-HBA with PTO settings 2, 6 and 7. In these settings, the PTO model is linear, with  $K_{PTO}$  equal to 0 and  $B_{PTO}$  equal to 7500 kN m/s (case 3) or 5000 kN m s (cases 6 and 7). Results have been computed with the frequency domain model.

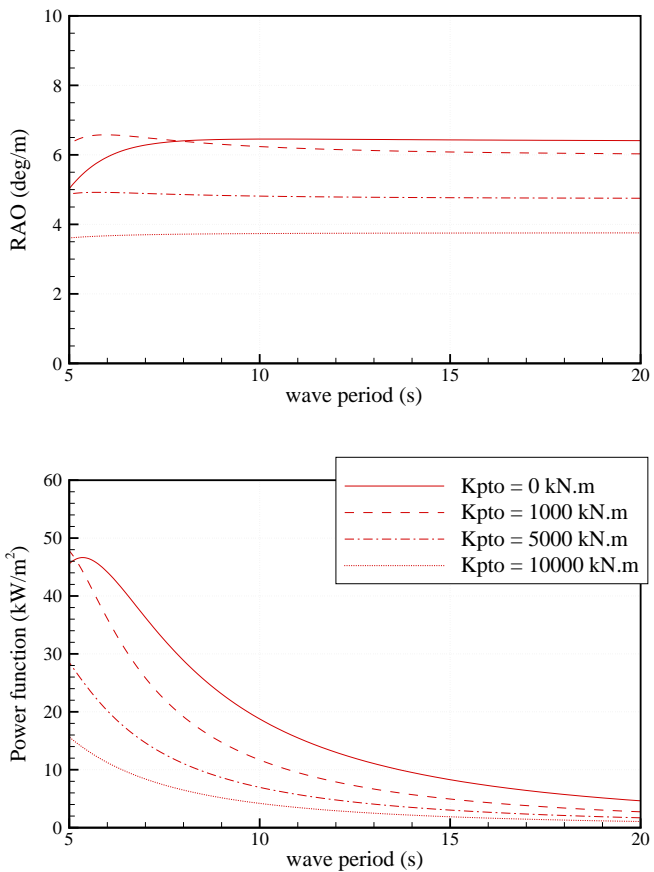


Figure 16: RAO and power function of the motion of the B-HBA with PTO settings 3 and 8 to 10. In these settings, the PTO model is linear, with  $M_{PTO}$  equal to 0 and and  $B_{PTO}$  equal to 7500 kN m/s (case 3) or 5000 kN m s (cases 8 to 10). Results have been computed with the frequency domain model.

500, 1000 and 2000 kN.m. The wave amplitude was set equal to 1m. The viscous damping coefficients were set equal to 0.

Results are shown in Figure 17 together with the case of linear damping with  $B_{PTO} = 5000$  kN.m.s.

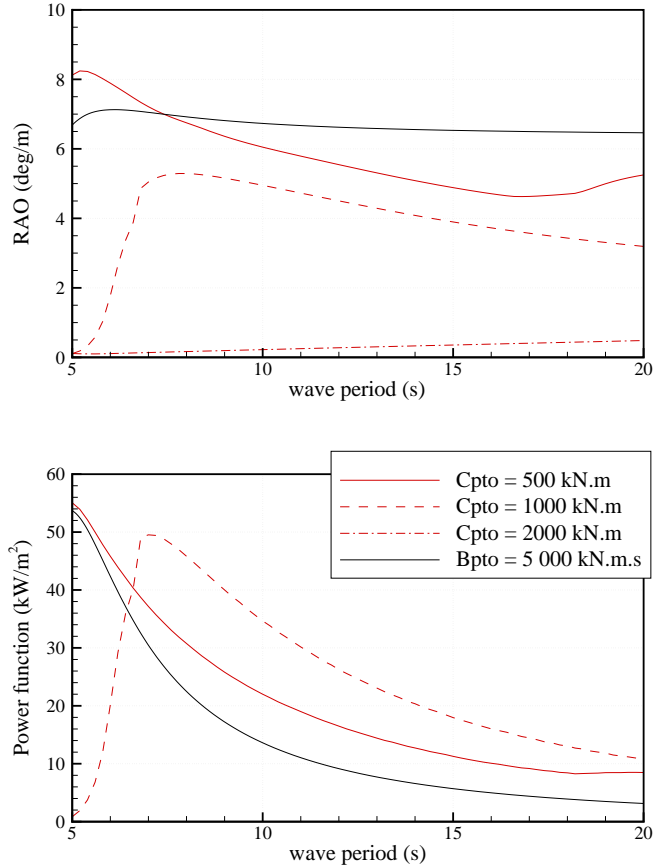


Figure 17: RAO and power function of the motion of the B-HBA with PTO settings 2 and 11 to 13. In case 2, the PTO model is linear as before, with  $M_{PTO}$  equal to 0 and  $B_{PTO}$  equal to 5000 kN.m/s. In cases 11 to 13 the PTO uses approximate Coulomb damping. Those results have been computed with the time-domain model.

In comparison with the case of linear damping, one can see that at least the same levels of power absorption can be achieved with the hydraulic PTO. Similar result was reported in [11] in case of the SEAREV WEC. Moreover, one can see that the hydraulic PTO has the ability to significantly increase the power absorption of the B-HBA WEC in comparison with a linear PTO. It can be explained by the fact that Coulomb damping gives a small effect of phase control, as it was shown by Falcao in [12].

As expected, a too large value of the PTO coefficient (case  $C_{PTO} = 2000$  kN.m) would prevent the system to move, virtually latching it in a fixed position.

It would lead to zero power absorption, so one has to be careful in setting the value of the PTO coefficient, i.e the high-pressure level in the hydraulic circuit.

### 3.2.3 Effect of quadratic damping

In order to get an idea of the importance of viscous effect on the response of the B-HBA WEC, the power function of the system was calculated with nominal viscous coefficients for wave amplitude of 0.5, 1 and 2 meters. The PTO was set to linear, with PTO setting number 2.

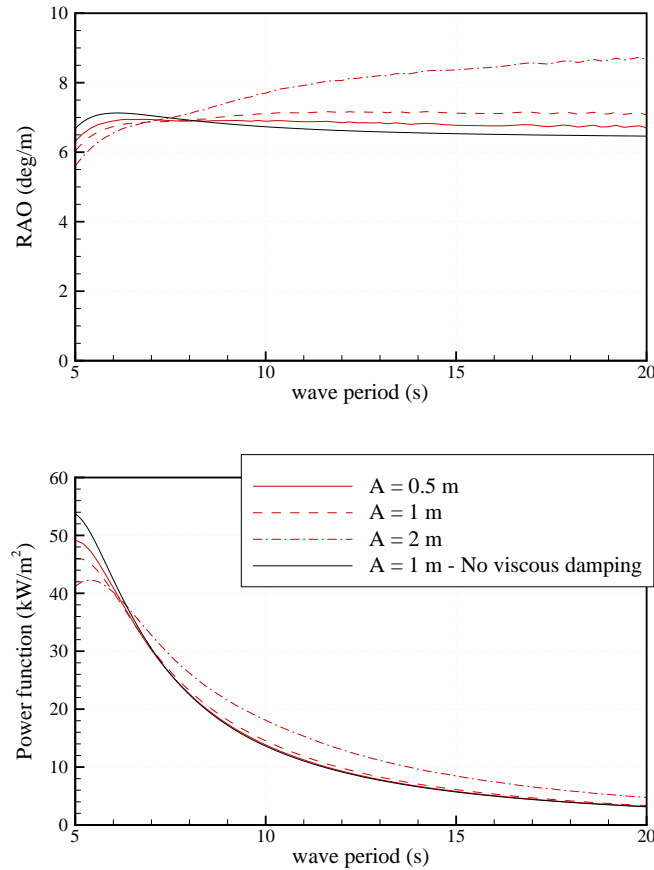


Figure 18: Effect of quadratic damping on pseudo RAO and the power function of the B-HBA WEC. PTO is linear with settings 2.

Results are shown in Figure 18. One can see that quadratic damping has two main effects on the response of the system. For periods close to the resonance, the amplitude of the motion is reduced and also the energy absorption. For long periods, the amplitude of the motion is increased, in function of the wave amplitude. This effect was also observed in the Bref-HB (inspired by Seabased) study.

Overall, one can see that quadratic damping has a considerable effect, so it has to be taken into account in order to improve the accuracy of estimation of the energy absorption.

### 3.2.4 Conclusions

From these results in regular waves, it appears that:

- The order of magnitude of absorbed power from the B-HBA WEC is several tens of kilowatts per squared wave amplitude in regular waves.
- With linear PTO, both the PTO damping and the PTO mass parameters have a large influence on the RAO and power function of the B-HBA WEC. The PTO mass parameter  $M_{PTO}$  should be optimised for each sea state in the calculation of annual energy absorption. As the device is working in its stiffness-dominated region, and we assume that the PTO stiffness coefficient  $K_{PTO}$  can only take positive values, its value should be set to zero.
- Same or even better levels of energy absorption can be achieved with hydraulic PTO in comparison with linear PTO.
- Viscous damping has a negative influence on the power absorption for short waves, and a positive influence for long waves. This effect is rather small for normal wave heights.

## 3.3 Power matrix and criteria

In this section, results are reported from time domain simulations performed with irregular waves synthesised using the JONSWAP spectrum. All quantities are derived from 1200s duration simulations, with a time step of 0.05s. To remove the transient effects, the first  $15 \times T_p$  seconds of the simulations are not taken into account.

### 3.3.1 Power matrix of the B-HBA

Figure 19 shows the power matrix of one of the float of the B-HBA WEC. The left-hand figure is the mean absorbed power and the right-hand figure is the maximum recorded over the duration of the simulation for each sea state.

The PTO model was set to linear damping. For each sea state, the PTO parameters  $B_{PTO}$  and  $M_{PTO}$  were optimised. The range of optimisation of the PTO parameters is given in Table 6.

	$H_{PTO}$ (kN.m)	$B_{PTO}$ (kN.m/rad)	$M_{PTO}$ (t)
Minimum	200	2 000	-10
Maximum	3 000	30 000	10

Table 6: Range of optimisation of the PTO parameters

For a typical sea state of 9s wave peak period and 2.5m significant wave height, the mean absorbed power for one float is 24kW. Power absorption higher than 100 kW is reached for the strongest sea states. As expected from a system

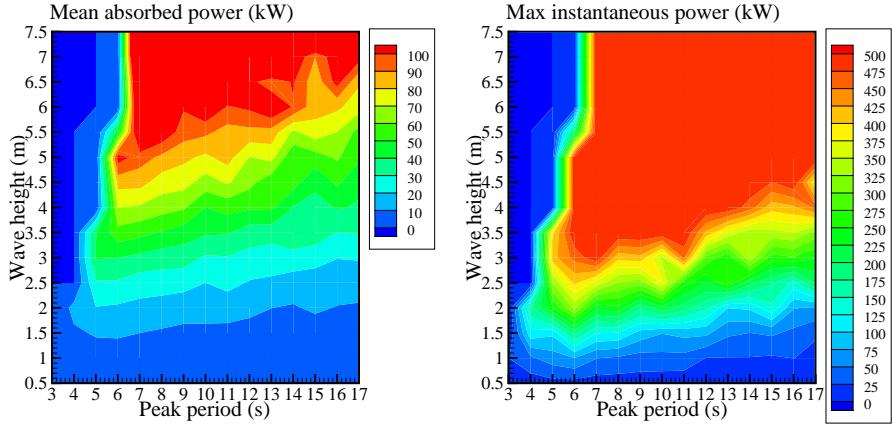


Figure 19: Power matrix of one float of the B-HBA with linear PTO. The PTO coefficients  $B_{PTO}$  and  $M_{PTO}$  were optimised for each sea state. The left-hand figure is the mean absorbed power and the right-hand figure is the maximum instantaneous power recorded during each simulation run.

with such a low resonance period and restrictions on the phase control efforts as assumed here, the absorbed power is highest for relatively low wave periods in the range 5 to 7s. However, the decrease in absorbed power with increased wave period is quite small.

The maximum absorbed power is typically about 10 times the mean power. It is large. It means that the PTO system has to deal with large peaks of instantaneous power. This is a drawback that most of the proposed WECs have to face. However, in the case of the Wavestar WEC, one should notice that it is possible to smooth the delivered power by having all buoys pumping into the same high-pressure storage. This was not investigated here. However, it was shown in [15] that the RMS of the instantaneous power can be divided by a factor 3 with 10 devices using this approach. Such reduction in the variability of the output power can probably be expected in the case of the Wavestar WEC.

Figure 20 shows the matrix of the optimised value of the PTO coefficients. One can see that they vary strongly with the wave period. For peak periods in range [5 – 9] seconds, the mass coefficient takes its maximum allowed value. For periods outside of this range (and small to moderate wave heights), it takes its minimum. It corresponds with a tuning of the natural period of the system to the spectrum of the waves. For the damping coefficient, one can see that its optimal value increases with the wave peak period. As an average, one can say that the nominal value of  $B_{PTO}$  should be about 10 MN m.

Figure 21 shows matrices of the RMS and maximum values for the excursion recorded during each sea-state simulation. One can see that the RMS of the motion is almost independent of the wave period. It increases linearly with the wave height. For a typical sea state of 9 seconds wave peak period 2.5 meters significant wave height, the RMS of the motion is 3 degrees. It corresponds with an amplitude of motion of the buoy of about 0.5 m, i.e. 20% or the float radius. It is not very small, but it is not very large either. Therefore, it is believed that

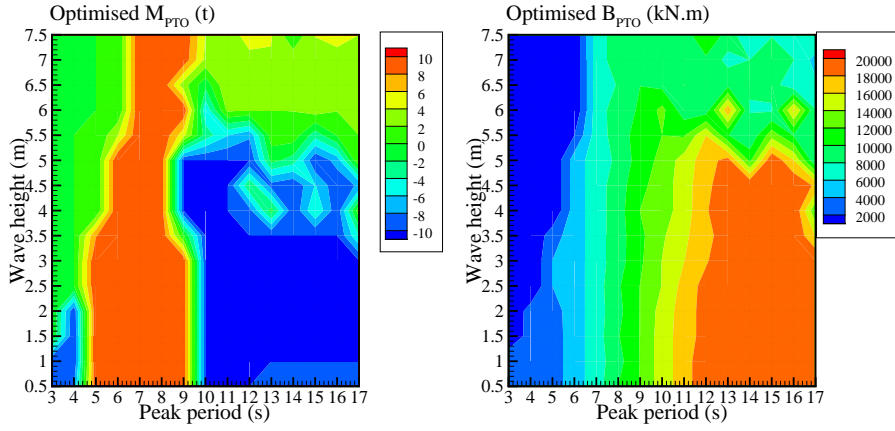


Figure 20: Optimised values of the PTO coefficients.

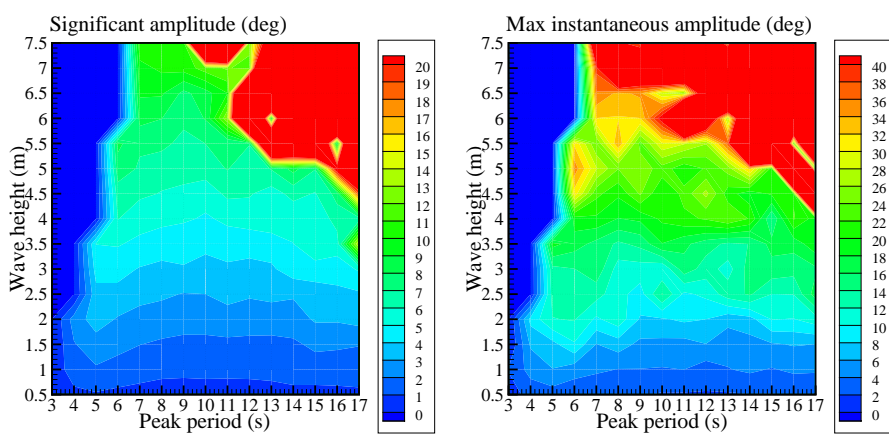


Figure 21: Matrices of the RMS of the motion of the B-HBA WEC.

linear theory is a sufficient frame work.

For the same sea state, the maximum recorded amplitude of motion was 9 degrees. It corresponds with a buoy motion of about 1 radius. In that case, it is likely that non linear effects will play an important role. However, it is not seen as a problem since the main focus of this study is on averaged values (mean absorbed wave power).

By multiplying the power matrix with wave data statistics, one can calculate the annual energy absorption of this float for each considered wave site. Wave statistics were obtained by transferring the energy from deep water to shallow water, according to Section 1.3. From that number, the energy absorption of the whole system (20 floats) was estimated by multiplying the energy absorption of a single float by 20 times 80%; the 80% being for taking into account the uncertainty due to the wave interactions effect. It is based on the work of De Backer *et al.* [9]. It is the best wave interaction factor she achieved for the FO3 platform as an annual average. It was obtained by optimising separately the PTO coefficients for each float of the platform. However, it is recognised as a very rough approach, and this should be reflected in the uncertainty assessment.

From another perspective, one could say that for each float, the wave resource is the ambient wave resource, minus the resource which has been absorbed by the floats in front of the device. Using this assumption, one can estimate an interaction factor of 63%. On the other side, if one neglects the interactions, the factor is 100%. Therefore, one can see that choosing a interaction factor of 80% seems reasonable, with an uncertainty range of [-20,20%].

Based on this interaction factor, the mean annual power absorption is reported in Table 7 together with the performance measures, estimated for all of the six considered sites.

Parameter	Unit	SEM-REV	EMEC	Yeu	Lisboa	Bel-mullet	Danish study
$\gamma$		1	1	3.3	3.3	3.3	1
$J$	[kW/m]	13.3	19.6	23.5	33.7	72.5	12.0
Mean power	[kW]	127	225	280	303	612	201.
Capture width	[m]	9.5	11.4	11.9	9.0	8.4	16.7
$E_y / \text{Mass}$	[kWh/kg]	0.69	1.23	1.53	1.66	3.36	1.10
$E_y / A_{\text{wet}}$	[MWh/m <sup>2</sup> ]	0.25	0.45	0.56	0.61	1.23	0.40
$E_y / F_{\text{PTO}}^{\text{RMS}}$	[kWh/N]	0.93	1.16	1.20	1.15	1.62	1.24
$E_y / F_{\text{wave}}^{\text{RMS}}$	[kWh/N]	2.03	3.01	3.34	3.10	4.24	3.30

Table 7: Evaluation criteria for the B-HBA WEC for chosen sites having mean annual wave energy transport  $J$ , and where sea states are synthesised with a spectrum peakedness factor  $\gamma$ . The parameters are calculated based on the yearly energy delivery  $E_y$ . The mass is taken as the total mass of the installed bottom-fixed structure, and  $A_{\text{wet}}$  is the wetted surface area of the structure. Significant PTO force  $F_{\text{PTO}}^{\text{RMS}}$  and significant wave force  $F_{\text{wave}}^{\text{RMS}}$  are taken as the yearly RMS values. The uncertainty is estimated to [-20,20] %.

One can see that the mean annual power output that one can expect from the B-HBA WEC is in order of a few hundred of kilowatts. It goes from 127 kW for the SEM-REV site up to 612 kW for the highly energetic Belmullet site. For a typical wave resource of about 25 kW/m, the typical absorbed wave power by

the B-HBA is about 300 kW. The typical mean capture width is about 12 m, depending on the site. It is up to 16.7 m for the Danish site.

Table 8 shows a comparison of the performance measures for the B-HBA with the F-3OF (inspired by Langlee), the F-2HB (inspired by Wavebob), the Bref-HB (inspired by Seabased) and the F-OWC (inspired by OE buoy), for the Yeu site.

	B-HBA	F-3OF	F-2HB	Bref-HB	F-OWC*	Pelamis P1**
Mean power (kW)	280	219	191	3.3	337.5*	230.3**
Capture width (m)	11.9	8.17	7.12	5.30	12.7*	8.6**
Hydrodynamic efficiency $\eta_1$	17 %	33%	36%	6%	53%*	6%**
$E_y / \text{Mass}$ (kWh/kg)	1.53	1.36	0.338	0.92	1.62*	2.88**
$E_y / A_{\text{wet}}$ (MWh/m <sup>2</sup> )	0.56	0.89	0.79	0.68	0.77*	1.2**
$E_y / F_{\text{PTO}}^{\text{RMS}}$ (kWh/N)	1.20	3.29	2.03	2.3	N/A	N/A
$E_y / F_{\text{wave}}^{\text{RMS}}$ (kWh/N)	3.34	2.67	3.03	1.27	N/A	N/A

Table 8: Comparison of B-HBA’s criteria with the F-3OF (inspired by Langlee), the F-2HB (inspired by Wavebob), the Bref-HB (inspired by Seabased) and the F-OWC (inspired by OE buoy) at the Yeu site. The parameters are calculated based on the yearly energy delivery  $E_y$ . The mass is taken as the total mass of the ballasted installed structure, not including the moorings, and  $A_{\text{wet}}$  is the wetted surface area of the structure. Significant PTO force  $F_{\text{PTO}}^{\text{RMS}}$  and significant wave force  $F_{\text{wave}}^{\text{RMS}}$  are taken as the yearly RMS values. \* and \*\* means that the numbers were obtained respectively with a frequency domain model and using the power matrix provided by the developer. They need to be confirmed.

One can see that the B-HBA’s relative capture width is between the one of resonator devices and attenuators. It has a very good Energy to mass ratio, almost as good as for the floating OWC. However, one can see that the ratio of Energy and Wetted surface area is smaller than for the other devices. The same goes for the Energy per PTO force. The ratio of Energy and Wave force is rather high.

Figure 22 shows the distribution of the absorbed power in function of the power level. The left-hand figure shows the probability for the power production to be between two levels and the right-hand figure shows the probability for the power to be greater than a given power level. It has been calculated with the wave statistics of the Yeu site. One can see the absorbed wave power is greater than the mean power 35% of the year.

### 3.3.2 Assessment of the uncertainties

#### Viscous losses

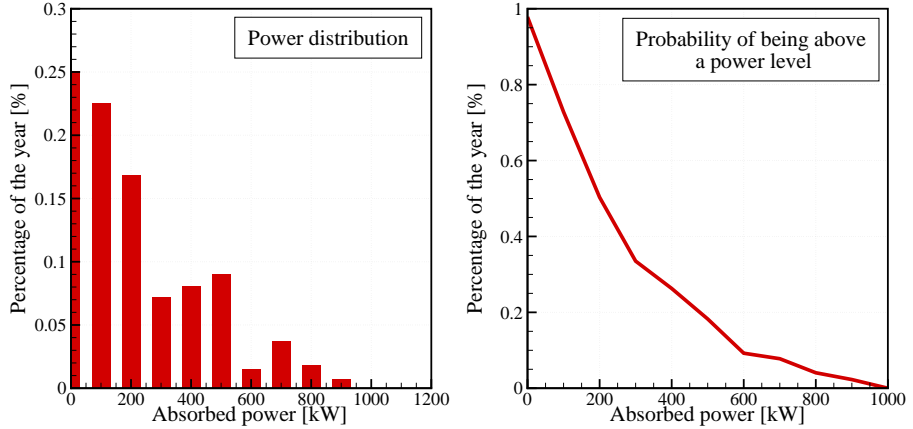


Figure 22: Distribution of the power production.

To assess the uncertainty associated with the modelling of viscous losses, the mean annual absorbed power at the Yeu site was calculated with different values of the viscous coefficients. Calculations were made with the linear PTO model, with optimisation of the damping parameter. Figure 23 shows the results. One can see that the modelling of the viscous damping has quite limited influence on the results of mean power. If viscous damping is set to zero, the mean absorbed power is 9% larger than the one found with nominal values. If viscous damping is underestimated by a factor 2, then the absorbed power is over-predicted by 2.5%.

Based on this, the uncertainty associated with the modelling of viscous damping was considered as negligible compared to other sources of uncertainty.

#### PTO modelling and optimisation

Calculation of the mean annual absorbed power at the Yeu site was performed with the hydraulic PTO model, with optimisation of the PTO parameter, in order to evaluate the effect of the PTO modelling on energy output. In this case the absorbed power was found to be equal to 272 kW, i.e 2% less than with the linear PTO model. It shows that the PTO model has only a small influence on the level of mean annual absorbed power. The same result was found in the case of the Bref-HB (inspired by Seabased). Then the difference of mean annual power calculated with a linear PTO model and with a full machinery model was less than 10%. In the case of the B-HBA, it is even smaller. Therefore, the uncertainty associated with the modelling of PTO was considered as negligible compared to other sources of uncertainty.

To assess the benefit of optimising the PTO coefficients for each sea state, calculation of the mean annual power absorption was performed with fixed PTO settings, in case of linear PTO. Results are shown in Table 9.

One can see that optimising the PTO parameter increases the mean annual power absorption by 6 to 38%. This type of slow control is simple and easy to apply, and should certainly be considered in practise.

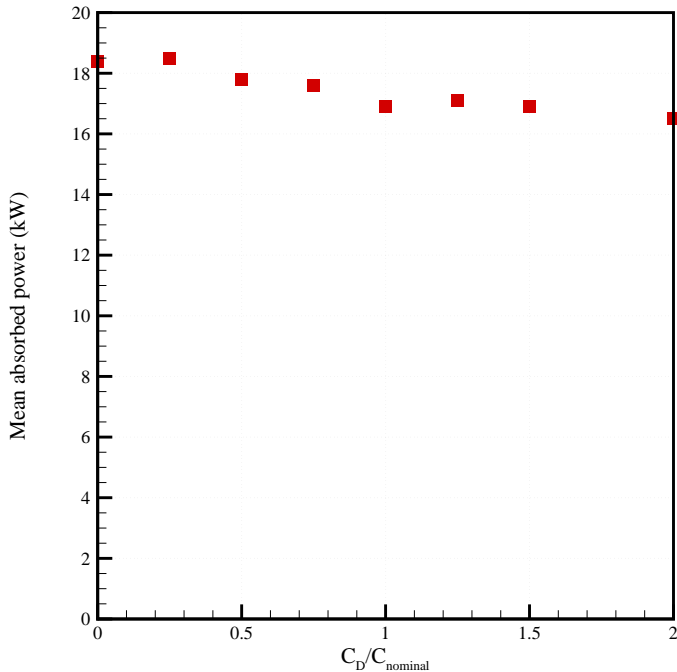


Figure 23: Mean absorbed power at Yeu in function of the drag coefficient relative to its nominal value. PTO setting number 5 was used.

Site	SEM-REV	EMEC	Yeu	Lisboa	Bel-mullet	Danish study
$B_{PTO} = 5000 \text{ kN m s}$	91	196	213	219	464	187
$B_{PTO}$ optimised	127	225	280	303	612	201
Difference (%)	28	13	24	38	24	6
$H_{PTO}$ optimised	121	219	272	298	604	202
$B_{PTO}$ optimised	127	225	280	303	612	201
Difference (%)	5	3	2	1	1	-1

Table 9: Mean annual power with and without optimisation of the PTO parameter for each sea state.

### Comparison with Wavestar WEC power matrix

Table 10 shows the comparison of the power matrix that was calculated in this study and a power matrix which was provided by the developer. One should note that it is the power matrix of delivered electricity and not absorbed energy. Hence, it includes the losses associated with the PTO, the power converters, etc.

At first look, one can see that the order of magnitudes agrees between the two power matrices. However, one can see that they agree well only in the limited range of cases of wave periods smaller than 4 seconds. In other cases, the power matrix provided by the developer predicts roughly 50% more energy production. One possible reason for this discrepancy is that the power matrix provided by the developer includes active control, whereas the power matrix calculated in this study includes only passive control.

Since storm protection is enabled when the significant wave height is higher than 3m, the power matrix provided by the developer is valid for sites with low resource, such as in Danish waters. Therefore, calculation of the mean annual power production at the Danish site was done using the power matrix provided by the developer. Result shows a mean power production of 220 kW. It is only 10 % more than the value calculated in the present study (201 kW). Therefore, although we realise that there are probably features in the actual Wavestar WEC that were not taken into account in our B-HBA model, we are confident in the fact that the figures given here give a good indication of the performances of this class of devices.

## 3.4 Parametric studies

### 3.4.1 Threshold on the instantaneous absorbed power

Table 11 shows the mean absorbed power at Yeu in function of a rating on the instantaneous power. It means than the maximum of instantaneous power is limited to this threshold. The difference between the available instantaneous power and the maximum is considered as lost. The calculation was performed with the linear PTO model.

One can see that the instantaneous power can be rated to a maximum of 4 MW with negligible losses in the mean annual absorbed power.

### 3.4.2 Threshold on the mean output power

Calculations of the mean annual power at Yeu site were performed with power rating of the platform of 600 kW and 1200 kW. It means that if the calculated value of mean absorbed power for a sea state is larger than the power rating, then the surplus power is considered as lost.

Differences on the mean annual power were found to be smaller than 14% and 4%, respectively. It means than the B-HBA WEC could be rated at 1.2 MW without losing much energy.

### 3.4.3 Effect of scale

Figure 24 shows the effect of scaling on the mean power absorption of the B-HBA, at the Yeu site. This figure has been calculated using the frequency domain model. The PTO model is set to linear, with fixed PTO parameter set

Wave height (m)		Wave period Tz (s)												
		2 - 3	3 - 4	4 - 5	5 - 6	6 - 7	7 - 8	8 - 9	9 - 10	10 - 11	11 - 12	12 - 13		
0.0 - 0.5	Wavestar	0	0	0	0	0	0	0	0	0	0	0		
	B-HBA	0 14	0 22	0 21	0 17	0 14	0 13	0 13	0 11	0 11	0 10	0 9		
0.5 - 1.0	Wavestar	0	49	73	85	86	83	78	72	67	63	59		
	B-HBA	0 53	14 291	22 79	21 65	17 60	14 58	13 50	13 47	11 47	11 43	10 37		
1. - 1.5	Wavestar	54	136	193	205	196	182	167	153	142	132	123		
	B-HBA	0 97	53 175	91 171	79 146	65 124	60 118	58 109	50 93	47 80	47 92	43 79		
1.5 - 2.0	Wavestar	106	265	347	347	322	294	265	244	224	207	193		
	B-HBA	0 150	97 311	175 286	171 256	146 223	124 229	118 216	109 175	93 150	80 175	92 152		
2.0 - 2.5	Wavestar	175	429	522	499	457	412	372	337	312	286	267		
	B-HBA	X	150 463	311 430	286 394	256 377	223 331	229 342	216 297	175 246	150 234	175 227		
2.5 - 3.0	Wavestar	262	600	600	600	600	540	484	442	399	367	340		
	B-HBA	X	0 600	463 600	430 567	394 553	377 463	331 454	342 342	297 424	246 393	234 322		
3.0 -	Wavestar	Storm protection												
	B-HBA	X	0 600	463	600	567	553	463	454	342	424	393		

Table 10: Comparison of the calculated power matrix and the power matrix provided by the Wavestar company.

Max. instantaneous absorbed power (kW)	Mean annual absorbed power (kW)
2 000	246
4 000	275
20 000	280

Table 11: Mean annual absorbed power at Yeu in function of the rating of maximum instantaneous absorbed power. The PTO model is linear. The PTO coefficient was optimised for each sea state.

to  $B_{PTO} = 5000 \text{ kN m s}$  and  $M_{PTO} = 10 \text{ tonnes}$  at scale 1. The PTO parameters were scaled accordingly to the Froude law for other scales.

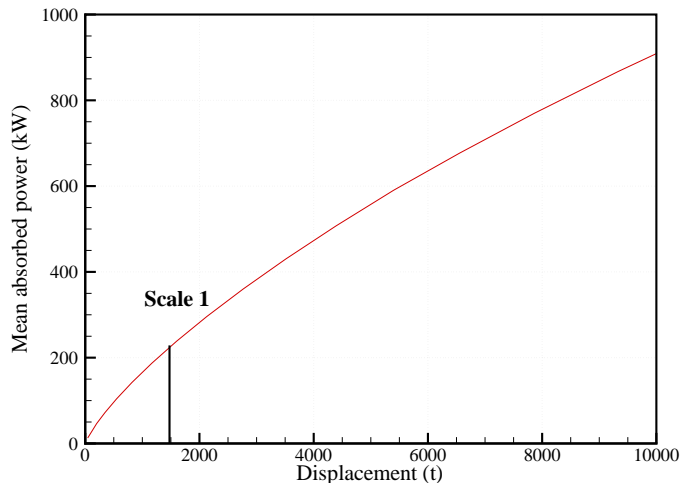


Figure 24: Influence of the scale on the mean power absorption of the B-HBA at Yeu.

One can see that the mean absorbed power grows linearly with the displacement for small devices. As the displacement increases, the slope decreases.

For a displacement twice the nominal displacement of the B-HBA, one can see that the increase in power absorption is 64%. In the same time, the increase in the wetted surface is 58%. Hence, if the structural mass (which often governs costs) depends mostly on the wetted surface, one can see that scaling up the B-HBA would slightly improve its economics. But if it depends mostly on the displacement, there is no point in scaling up, since the ratio power per mass decreases with the size.

## 4 Conclusions and recommendations

From these results and the study, the main conclusions are:

- The mean power level that one can expect from the B-HBA WEC is

about 300 kW on a site whose shallow-water wave power level is about 23.5 kW/m. The uncertainty of the reported numbers is estimated to about  $[-20\%, +20\%]$ . It comes from the estimation of the interaction factor between the floats.

- The influence of the PTO modelling – linear or hydraulic – has only a small influence (a few percents) on the mean power absorption.
- The mean output power of the B-HBA could be rated to 1200 kW without losing a significant amount of energy production. Limitation of the instantaneous absorbed power to 4MW would not significantly reduce the mean absorbed power.

## References

- [1] J. Falnes, 2002. Ocean waves and oscillating systems. Linear interactions including wave energy extraction. Cambridge university press.
- [2] B. Molin, 2002. Hydrodynamique des structures offshore, Guides Pratiques sur Les Ouvrages En Mer, TECHNIP Eds.
- [3] A. Babarit, Achil3D v2.0 : User Manual, Laboratoire de Mécanique des Fluides, CNRS UMR6598, Ecole Centrale de Nantes, October, 2008.
- [4] G. Delhommeau, 1997. Seakeeping Code Aquaplus
- [5] J. Falnes, 1999. Wave-energy conversion through relative motion between two single-mode oscillating bodies. Journal of Offshore Mechanics and Arctic Engineeringm Vol. 121, 32–38.
- [6] [www.wavestarenergy.com](http://www.wavestarenergy.com) Accessed February, 14th, 2011.
- [7] [www.danwec.com](http://www.danwec.com) Accessed February, 14th, 2011.
- [8] M. Kramer 2011. Info for Babarit - Wave Star C5.pdf. Technical note.
- [9] G. De Backer, M. Vantorre, C. Beels, J. De Rouck, P. Frigaard 2010. Power absorption by closely spaced point absorbers in constrained conditions. In IET Renewable Power Generation Vol. 4(6), pp 579-591.
- [10] Bølgekraftprogram, Afslutningsrapport 2002. Bølgekraftudvalgets Sekretariat, RAMBØLL, Teknikerbyen 31, 2830 Virum.
- [11] C. Josset, A. Babarit, A.H. Clement 2007. A wave-to-Wire model for the SEAREV Wave Energy Converter. Proc. of the Institution of Mechanical Engineers, Part M-Journal of Engineering for the Maritime Environment, Vol. 221(2), pp 81-93.
- [12] A.F.O. de Falcao 2008. Phase control through load control of oscillating-body wave energy converters with hydraulic PTO system. Ocean Engineering Vol. 35, pp 358-366.
- [13] P. Frigaard 2010. SDWED: Wave to wire modelling. Presentation downloaded February, 23rd 2010 from [www.sdwed.civil.aau.dk/digitalAssets/9/9203\\_wp4-wave-to-wire.pdf](http://www.sdwed.civil.aau.dk/digitalAssets/9/9203_wp4-wave-to-wire.pdf).
- [14] A. Pecher, J.P. Kofoed, J. Espedal, S. Hagberg 2010. Results of an Experimental study of the Langlee Wave Energy Converter. In Proc. of the 20<sup>th</sup> International Offshore and Polar Engineering Conference, Beijing, China, June 20-25.
- [15] J. Tissandier, A. Babarit, A.H. Clément. Study of the smoothing effect on the power production in an array of SEAREV wave energy converters. In Proc. of the 18<sup>th</sup> International Offshore and Polar Engineering Conference, Vancouver, Canada.

## Chapter 8

A bottom-referenced  
submerged heave-buoy  
(Bref-SHB) inspired by the  
Ceto device

# Numerical estimation of energy delivery from a selection of Wave Energy Converters

## – Bottom-reference submerged heave buoy report

Aurélien Babarit<sup>1</sup>, Jørgen Hals<sup>2</sup>

<sup>1</sup>Laboratoire de Mécanique des Fluides - CNRS UMR6598  
Ecole Centrale de Nantes, 1 rue de la Noe, 44300 Nantes, France  
<sup>2</sup>CeSOS, NTNU

29 June 2011

## Summary

This document reports the pilot study of the project “Numerical estimation of energy production from a selection of Wave Energy Converters”. It contains a mathematical model and simulation results for the study of a bottom-referenced submerged heaving buoy (Bref-SHB). Its geometry and working principle has been inspired by the Ceto wave energy converter currently under development by the company Carnegie Wave Energy Limited in Australia.

Results of the study are the following performance measures:

- The annual mean output power.
- The yearly energy output / displacement.
- The yearly energy output / wetted surface.
- The average power per unit of significant PTO force.
- The average power per unit of excitation force
- The duration curves.

These criteria were estimated for the Bref-SHB device using the mathematical model described in this report. Results are given in the following table and in Figure 1.

From these results and the study, main conclusions are :

Parameter	Unit	SEM-REV	EMEC	Yeu	Lisboa	Bel-mullet	Danish study
$\gamma$		1	1	3.3	3.3	3.3	1
$J$	[kW/m]	13.3	19.6	23.5	33.7	72.5	12.0
Mean power	[kW]	8.8	18.5	22.0	19.0	31.3	19.1
Capture width	[m]	0.66	0.94	0.94	0.57	0.43	1.64
$E_y / \text{Mass}$	[kWh/kg]	0.39	0.81	0.97	0.83	1.37	0.84
$E_y / A_{\text{wet}}$	[MWh/m <sup>2</sup> ]	0.35	0.74	0.88	0.76	1.24	0.76
$E_y / F_{\text{PTO}}^{\text{RMS}}$	[kWh/N]	1.53	2.08	2.37	2.29	2.95	2.06
$E_y / F_{\text{wave}}^{\text{RMS}}$	[kWh/N]	2.57	3.60	4.05	3.84	4.73	3.57

Table 1: Evaluation criteria for the Bref-SHB WEC for chosen sites having mean annual wave energy transport  $J$ , and where sea states are synthesized with a spectrum peakedness factor  $\gamma$ . The parameters are calculated based on the yearly energy delivery  $E_y$ . The mass is taken as the total mass of the ballasted installed structure, not including the moorings, and  $A_{\text{wet}}$  is the wetted surface area of the structure. Significant PTO force  $F_{\text{PTO}}^{\text{RMS}}$  and significant wave force  $F_{\text{wave}}^{\text{RMS}}$  are taken as the yearly RMS values. The uncertainty of  $E_y$  is estimated to  $[-40, 20]\%$ .

- The mean power level that one can expect from the Bref-SHB WEC is about 20 kW on a site whose wave resource is about 25 kW/m. The uncertainty is about  $[-40\%, +20\%]$ . It comes from the estimation of the viscous losses and the PTO modelling.
- The PTO modelling -linear or hydraulic- has a rather large influence on the mean power absorption. Annual mean power is 20 % less with hydraulic PTO than with linear PTO.
- The Bref-SHB could be rated to 100 kW without losing a significant amount of energy production. Limitation of the instantaneous absorbed power to 10 times the mean output power (200MW) would not reduce significantly the mean absorbed power either.
- The stroke length could be set to 4 meters with negligible losses in the annual energy absorption.

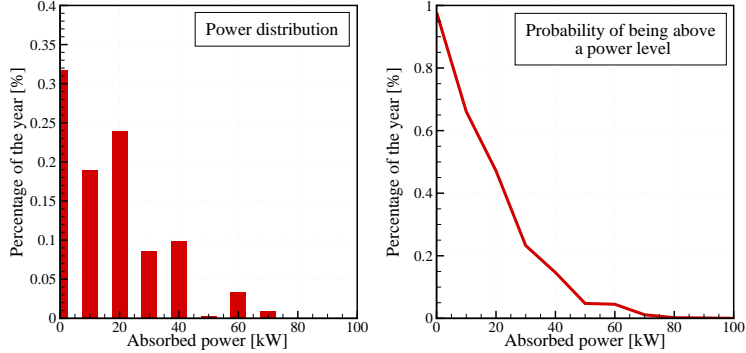


Figure 1: Distribution of the power production on a typical 30 kW/m wave site.

## Contents

<b>1 System description - The Bref-SHB Wave Energy Converter</b>	<b>5</b>
1.1 Mechanical parameters . . . . .	5
1.1.1 Buoy . . . . .	5
1.1.2 PTO and control . . . . .	7
1.2 Site and wave resource . . . . .	8
1.3 Cost criteria . . . . .	8
<b>2 Equation of motion</b>	<b>9</b>
2.1 Assumptions and notations . . . . .	9
2.2 Kinematics . . . . .	9
2.3 Forces . . . . .	11
2.3.1 Hydrostatic forces . . . . .	11
2.3.2 Wave excitation and radiation forces . . . . .	12
2.3.3 Viscous damping forces . . . . .	12
2.3.4 Wire tension . . . . .	13
2.3.5 PTO forces . . . . .	13
2.3.6 End stop forces . . . . .	15
2.4 Equation of motion . . . . .	15
2.4.1 Frequency domain . . . . .	15
2.4.2 Time domain . . . . .	16
2.5 Implementation . . . . .	16
2.5.1 Calculation of the hydrodynamic coefficients and functions	16
2.5.2 Estimation of viscous damping coefficients . . . . .	16
2.5.3 W2W models . . . . .	18
<b>3 Simulation results and energy assessment</b>	<b>18</b>
3.1 Verification tests . . . . .	18

<b>3.2</b>	<b>RAOs . . . . .</b>	<b>20</b>
3.2.1	Linear damper . . . . .	23
3.2.2	Coulomb damping . . . . .	24
3.2.3	Effect of quadratic damping . . . . .	25
3.2.4	Conclusions . . . . .	27
<b>3.3</b>	<b>Power matrix and criteria . . . . .</b>	<b>27</b>
3.3.1	Power matrix . . . . .	27
3.3.2	Assessment of the uncertainties . . . . .	31
<b>3.4</b>	<b>Parametric studies . . . . .</b>	<b>34</b>
3.4.1	Threshold on the instantaneous absorbed power . . . . .	34
3.4.2	Threshold on the mean absorbed power . . . . .	35
3.4.3	Effect of stroke length . . . . .	35
3.4.4	Effect of buoy size . . . . .	35
<b>4</b>	<b>Conclusions and recommendations</b>	<b>35</b>

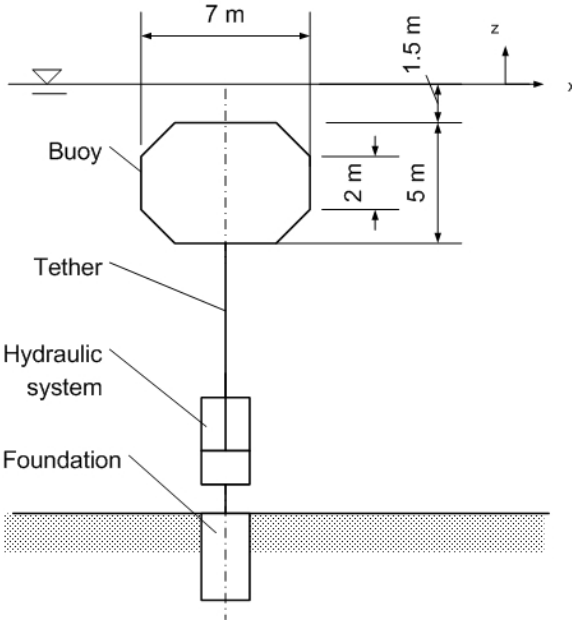


Figure 2: Sketch of the system.

## 1 System description - The Bref-SHB Wave Energy Converter

The Ceto wave energy converter consists of a cylindrical buoy immersed 1 to 2 meters below the free surface. It has a positive buoyancy. Through a wire it is connected to a machinery unit standing at the sea bottom. The machinery consists of a hydraulic system, pumping sea water and sending it to the shore. At shore, it is converted into fresh water via reverse osmosis units and/or into electricity using a Pelton wheel. A simplified sketch of the system is shown in Figure 2, and a picture including the different components is found in Figure 3. Based on this the bottom-referenced submerged heaving buoy (Bref-SHB) studied in this report is defined as follows.

### 1.1 Mechanical parameters

The system parameters used in the present study has is based on information gathered from web pages on the internet website of the Ceto company [4].

#### 1.1.1 Buoy

In the original design, the Ceto buoy shape was a sphere. In the commercial version of the buoy, which was released in 2010, the shape is still axi-symmetric, but with some kind of sharp ellipsoidal cross-section, see Figure 4. Its parameters are given in Table 2.

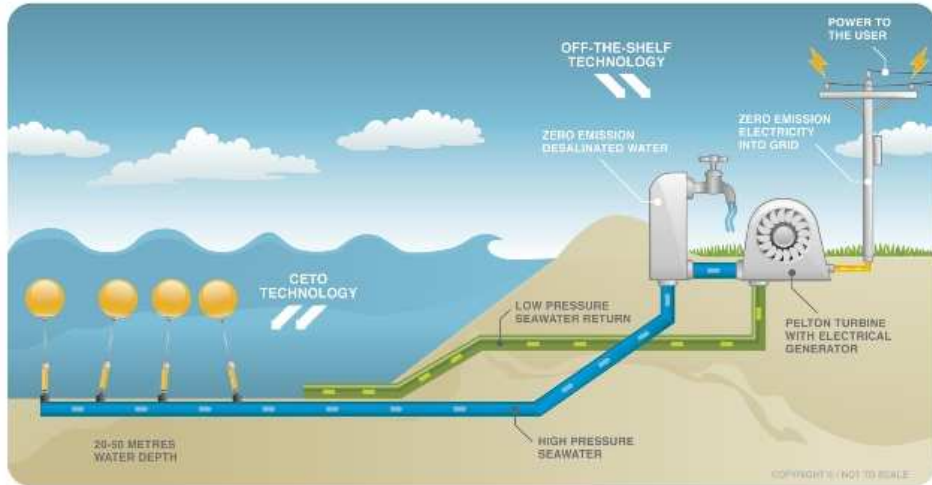


Figure 3: Components of the Ceto wave energy converter.

Table 2: System parameters

Property	Value	Unit
long axis of the buoy	7	m
short axis of the buoy	5	m
submersion (top of the buoy)	1.5	m
height	56	m
displacement	148	$\text{m}^3$
mass of the buoy	35	t
centre of mass	-3.5	m (i.e. below the free surface)
Moment of inertia $I_y$	172	$\text{t} \cdot \text{m}^2$
Stroke length	6	m
Stiffness upper end stop spring	243000	kg/m
Stiffness lower end stop spring	215000	kg/m
Water depth	20	m



Figure 4: Picture of the unveiling of the buoy.

### 1.1.2 PTO and control

In the Ceto WEC, the mechanical power of the motion of each float is converted into hydraulic power by means of a hydraulic cylinder which is connected at one side to the tether and at the other side to the foundation, see Figure 3. A hydraulic PTO can be modelled as a Coulomb damping term acting in the opposite direction of the cylinder velocity. The PTO damping force  $F_{PTO}$  is then written:  $F_{PTO} = -H_{PTO} \operatorname{sign}(l)$ , with  $H_{PTO}$  a Coulomb damping coefficient and  $l(t)$  the instantaneous length of the tether.

As an alternative version, we also considered the case of a linear PTO system, with machinery force proportional to  $l$ , such that  $F_{PTO}(t) = -B_{PTO} \dot{l}(t)$ . In addition we have then assumed that the PTO system may exert a spring force on the buoy. Then  $B_{PTO}$  is the damping coefficient and  $K_{PTO}$  is the damping and restoring coefficients. As in the other studies, only cases with positive  $K_{PTO}$  were considered, because it can be achieved technically by adding a physical spring to the PTO system. This is not the case with negative  $K_{PTO}$ .

In both cases, an additional constant term  $C_{PTO}$  was introduced in order to counteract the initial pretension of the tether.

As the PTO is of the linear kind, it has end stops. The total stroke length is estimated to be about 6 m.

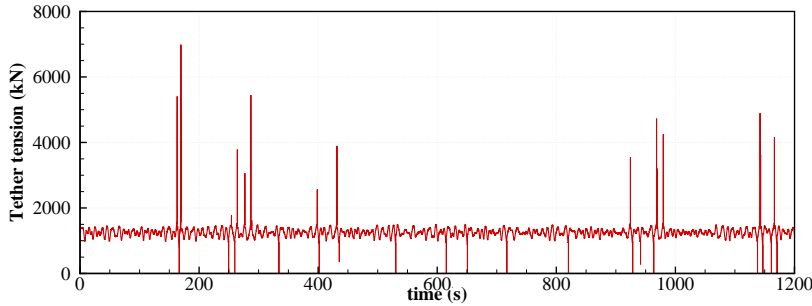


Figure 5: Time serie of recorded tension in the tether

## 1.2 Site and wave resource

According to the developers, the Ceto WEC has been designed to be installed at site with small to intermediate water depth. In this study, the water depth was assumed to be 20 meters.

Annual wave statistics were obtained from wave data at larger water depths. As for the B-OF study, it is assumed that for each wave frequency, 90 % of the energy contained in each frequency component is transferred from deep to intermediate water depths.

## 1.3 Cost criteria

According to [4], the overall significant mass of the buoy is about 25 tonnes. It means that the buoy is largely buoyant. This buoyancy has to be counteracted by the anchoring system. It means that it is an essential part to the system. Therefore, as in the Bref-HB study (inspired by the Seabased device), one should include the weight of the anchoring system in the overall significant mass of the device.

Figure 5 shows a time series of the tension in the wire connecting the device to the sea bottom. It was obtained through numerical simulation, using the time domain model which is explained in more detail later in this report. The sea state parameters are  $T_p = 12\text{ s}$ ,  $H_s = 5\text{ m}$ , and  $\gamma = 3.3$ . It is a strong sea state, but likely to happen several times a year.

One can see that most of the time, the tension oscillates around a mean value of 1 200 kN, which corresponds to the net buoyancy of the buoy. However, there exist high peaks of tension, up to 7 000 kN, which correspond to time when the PTO reaches the high end stop. If nothing is made to avoid them, these snap loads will cause large fatigue in the tether, which could result in breaking. However, these high peaks are related with the dynamic modelling of the tether. One can see that they are of very short duration. So in this study they will not be considered in the dimensioning of the anchoring

Criteria		unit
Significant wetted surface	220	$\text{m}^2$
Significant mass	200	tons

Table 3: Significant surface and mass of the Bref-SHB.

system.

Therefore, the anchoring system will have to counteract only the part of the tether tension associated with buoyancy and the wave force. According to Figure 5, a gravity based structure weighting 1.5 times the buoyancy force should be sufficient. Eventually, the overall significant mass of the buoy plus mooring is estimated to be about 200 tons.

According to calculation, the surface area of the buoy is about  $140 \text{ m}^2$ . According to pictures found on the internet, the mooring structure looks like a flat cylinder of radius similar to the one of the buoy. Therefore, the surface of the mooring structure is estimated to be about  $80 \text{ m}^2$ . The overall significant wetted surface is then  $220 \text{ m}^2$ .

The two other considered cost criteria are the significant PTO force and the significant wave force. They both have zero mean values. So, they are defined as their RMS over the whole year.

## 2 Equation of motion

### 2.1 Assumptions and notations

Here, the waves are assumed to be monodirectional. Let us assume that they propagate in the positive  $x$  direction. It is further assumed that all motions are of small amplitude. All second order hydrodynamic effects are neglected.

Let  $G$  be the gravity centre of the buoy,  $A$  be the attachment point of the tether to the buoy, and  $C$  be the attachment point of the PTO system to the sea bottom. Further, let  $x_G$  and  $z_G$  denote the surge and heave motion of the gravity centre of the buoy. The angle  $\alpha$  gives the excursion of the tether relative to the z-axis, while the angle  $\theta$  gives the buoys pitch motion relative to the tether axis. Moreover, let  $l$  be the instantaneous length of the tether and  $l_0$  its length at rest. The length  $d = \overline{AG}$  denotes the distance between the attachment point and the gravity centre of the buoy.

Finally, let  $M$  be the mass of the buoy and  $I_y$  its moment of inertia.

### 2.2 Kinematics

From the hinge  $C$ , the position of  $G$  can be written:

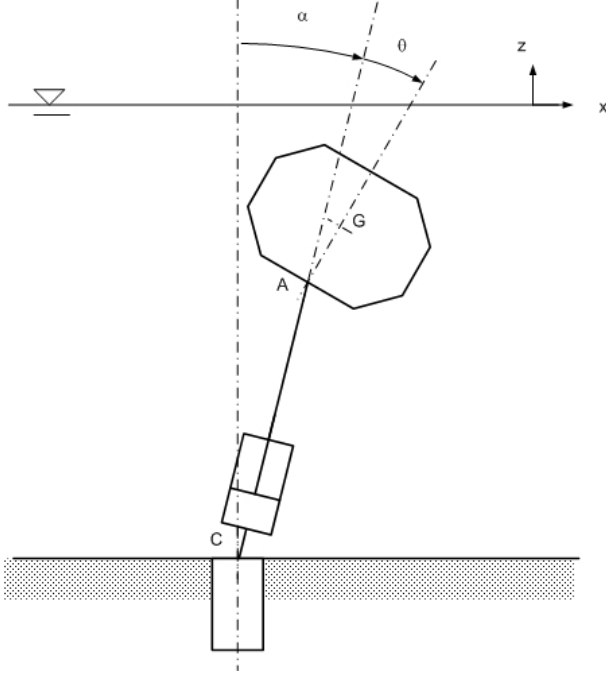


Figure 6: Notations used

$$\overrightarrow{CG} = x_G \vec{x} + (l_0 + z_G) \vec{z} \quad (1)$$

$$= (l \sin \alpha + d \sin(\theta + \alpha)) \vec{x} + (l \cos \theta + d \cos(\theta + \alpha)) \vec{z} \quad (2)$$

By time differentiation, one gets the velocity.

$$u = \dot{l} \sin \alpha + l \dot{\alpha} \cos \alpha + d(\dot{\alpha} + \dot{\theta}) \cos(\alpha + \theta) \quad (3)$$

$$w = \dot{l} \cos \alpha - l \dot{\alpha} \sin \alpha - d(\dot{\alpha} + \dot{\theta}) \sin(\alpha + \theta) \quad (4)$$

where  $u$  and  $w$  are the horizontal and vertical velocities of the gravity centre  $G$ . Let  $\mathbf{X}_G = (x_G \ z_G \ \theta + \alpha)^T$ , and let us define the position vector  $\mathbf{X} = (\Delta l \ \alpha \ \theta)^T$ . Using these two last equations, one can show:

$$\dot{\mathbf{X}}_G = \bar{\bar{\mathbf{T}}}(\mathbf{X}, \dot{\mathbf{X}})\dot{\mathbf{X}} \quad (5)$$

with

$$\bar{\bar{\mathbf{T}}}(\mathbf{X}, \dot{\mathbf{X}}) = \begin{pmatrix} \sin \alpha & l \cos \alpha + d \cos(\alpha + \theta) & d \cos(\alpha + \theta) \\ \cos \alpha & -l \sin \alpha - d \sin(\alpha + \theta) & -d \sin(\alpha + \theta) \\ 0 & 1 & 1 \end{pmatrix} \quad (6)$$

The acceleration is obtained by time differentiating once again:

$$\begin{aligned}\dot{u} &= \ddot{l} \sin \alpha + 2\dot{l}\dot{\alpha} \cos \alpha + l\ddot{\alpha} \cos \alpha - l\dot{\alpha}^2 \sin \alpha \\ &\quad + d(\ddot{\alpha} + \ddot{\theta}) \cos(\alpha + \theta) - d(\dot{\alpha} + \dot{\theta})^2 \sin(\alpha + \theta)\end{aligned}\quad (7)$$

$$\begin{aligned}\dot{w} &= \ddot{l} \cos \alpha - 2\dot{l}\dot{\alpha} \sin \alpha - l\ddot{\alpha} \sin \alpha - l\dot{\alpha}^2 \cos \alpha \\ &\quad - d(\ddot{\alpha} + \ddot{\theta}) \sin(\alpha + \theta) - d(\dot{\alpha} + \dot{\theta})^2 \cos(\alpha + \theta)\end{aligned}\quad (8)$$

which can be rewritten:

$$\ddot{\mathbf{X}}_G = \bar{\bar{\mathbf{T}}}(\mathbf{X}, \dot{\mathbf{X}})\ddot{\mathbf{X}} + \mathbf{Q}(\mathbf{X}, \dot{\mathbf{X}}) \quad (9)$$

with

$$\mathbf{Q}(\mathbf{X}, \dot{\mathbf{X}}) = \begin{pmatrix} 2\dot{l}\dot{\alpha} \cos \alpha - l\dot{\alpha}^2 \sin \alpha - d(\dot{\alpha} + \dot{\theta})^2 \sin(\alpha + \theta) \\ -2\dot{l}\dot{\alpha} \sin \alpha - l\dot{\alpha}^2 \cos \alpha - d(\dot{\alpha} + \dot{\theta})^2 \cos(\alpha + \theta) \\ 0 \end{pmatrix} \quad (10)$$

## 2.3 Forces

The generalised force  $\mathbf{F}$  is defined as a column vector whose two first components are the horizontal and vertical forces. The third component is the moment of force. Therefore it depends on the application point.

Let define the operator  $\bar{\bar{\mathbf{G}}}\bar{\mathbf{A}}$  which transports any generalised force applying at the gravity centre of the buoy to the attachment point of the tether  $A$ . One can show that it is given by:

$$\bar{\bar{\mathbf{G}}}\bar{\mathbf{A}} = \begin{pmatrix} 1 & 0 & 0 \\ 0 & 1 & 0 \\ d \cos(\theta + \alpha) & -d \sin(\theta + \alpha) & 1 \end{pmatrix} \quad (11)$$

### 2.3.1 Hydrostatic forces

As the buoy is submerged, the sum of the gravity force and the buoyancy force is independent of its position.

$$\vec{F}_B = (\rho V - M)g \vec{z} \quad (12)$$

At  $A$ , the moment reads:

$$M_B(A) = -(\rho V - M)gd \sin(\alpha + \theta) \quad (13)$$

Therefore, the generalised hydrostatic force at  $A$  reads:

$$\mathbf{F}_B(A) = \begin{pmatrix} 0 \\ (\rho V - M)g \\ -(\rho V - M)gd \sin(\alpha + \theta) \end{pmatrix} \quad (14)$$

### 2.3.2 Wave excitation and radiation forces

Within the frame of linear theory, the hydrodynamic forces reads in the frequency domain:

$$\mathbf{F}_D(G) = \mathbf{F}_{ex}(G) - \mathbf{C}_M \ddot{\mathbf{X}}(G) - \mathbf{C}_A \dot{\mathbf{X}}(G) \quad (15)$$

in which:

- $\mathbf{F}_{ex}(G)$  is the generalised excitation force at  $G$ .
- $\mathbf{C}_M$  and  $\mathbf{C}_A$  are the added mass and radiation damping coefficients.

At  $A$ , it reads:

$$\mathbf{F}_D(A) = \overline{\mathbf{GA}} \mathbf{F}_{ex}(G) - \overline{\mathbf{GA}} \mathbf{C}_M \mathbf{T} \ddot{\mathbf{X}} - \overline{\mathbf{GA}} \mathbf{C}_M \mathbf{Q} - \overline{\mathbf{GA}} \mathbf{C}_A \mathbf{T} \dot{\mathbf{X}} \quad (16)$$

### 2.3.3 Viscous damping forces

The viscous damping forces are modelled under the form of a drag force applying at  $G$ :

$$\vec{F}_V^B(G) = -\frac{1}{2}\rho \mathbf{C}_D \mathbf{A}_D \left\| \vec{V}(G) - \vec{V}_0(G) \right\| \left( \vec{V}(G) - \vec{V}_0(G) \right) \quad (17)$$

$$M_V(G) = -\frac{1}{2}B_Q |\dot{\alpha} + \dot{\theta}| (\dot{\alpha} + \dot{\theta}) \quad (18)$$

where:

- $\vec{V}_0(G)$  is the undisturbed flow velocity at point  $G$  in the body fixed coordinate system.
- $\mathbf{C}_D = \begin{pmatrix} C_x & 0 \\ 0 & C_z \end{pmatrix}$  is the drag coefficient matrix and  $\mathbf{A}_D = \begin{pmatrix} A_x & 0 \\ 0 & A_z \end{pmatrix}$  the corresponding characteristic surface area matrix.
- $\vec{V}(G)$  is the velocity of the buoy at point  $G$  in the body fixed coordinate system.
- $B_Q$  is the quadratic roll damping coefficient.

The corresponding generalised force at point  $A$  is obtained by:

$$\mathbf{F}_V(A) = \overline{\mathbf{GA}} \begin{pmatrix} \vec{F}_V^0(G) \\ M_V(G) \end{pmatrix} \quad (19)$$

in which the superscript  $0$  means that the force is expressed in the earth fixed coordinate system.

### 2.3.4 Wire tension

The buoy is connected to the PTO and end stop system via a wire. In practice, this wire may become slack. In simulation, this happens when the wire tension becomes negative. In order for the modelled wire not to behave as a rod, the wire tension will be set to 0 in this case. Otherwise (in normal operation), it will be equal to the sum of the PTO force plus the end stop force. Formally, it reads:

$$\mathbf{T} = \min(\mathbf{0}, \mathbf{F}_{\text{PTO}} + \mathbf{F}_{\text{es}}) \quad (20)$$

in which  $\mathbf{F}_{\text{PTO}}$  and  $\mathbf{F}_{\text{es}}$  are the PTO and end stops forces, defined in the following.

### 2.3.5 PTO forces

According to Section 1.1.2, two alternative models are used. One is Coulomb damping and the other one is linear PTO force.

With linear PTO, the generalised PTO force is:

$$\mathbf{F}_{\text{PTO}}(A) = (C_{\text{PTO}} - B_{\text{PTO}}\dot{\Delta}l - K_{\text{PTO}}\Delta l) \begin{pmatrix} \sin\alpha \\ \cos\alpha \\ 0 \end{pmatrix} \quad (21)$$

The constant  $C_{\text{PTO}}$  exists for counteracting the buoyancy force at rest. Therefore, it is equal to:

$$C_{\text{PTO}} = -(\rho V - M)g \quad (22)$$

In case of hydraulic PTO, the numerical implementation of the Coulomb damping is difficult because it adds a very stiff term in the equations. This can lead to unphysical oscillations of the velocity around 0 which can lead to erroneous values for power absorption. Hence, in practice, perfect Coulomb damping has been replaced by approximate Coulomb damping, in which the PTO force is supposed to be linear with a large proportionality coefficient around the point of zero velocity; and constant when the velocity is large enough, see Figure 7.

Mathematically, the generalised force in the case of hydraulic PTO reads:

$$\mathbf{F}_{\text{PTO}}(A) = (C_{\text{PTO}} - \min(G_{\text{PTO}}|\dot{\Delta}l|, H_{\text{PTO}})\text{sign}(\dot{\Delta}l)) \begin{pmatrix} \sin\alpha \\ \cos\alpha \\ 0 \end{pmatrix} \quad (23)$$

In this study, the large  $G_{\text{PTO}}$  coefficient was set to 100 times the dry mass plus added mass coefficient of the buoy.

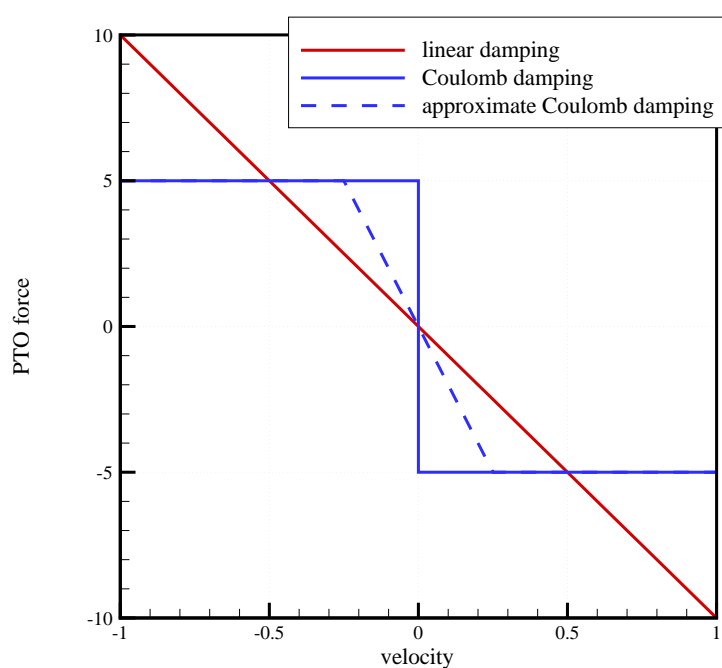


Figure 7: PTO force versus velocity when PTO forces of different kinds: Linear damping, Coulomb damping and approximate Coulomb damping.

### 2.3.6 End stop forces

The endstops are modelled by a repulsive energy potential. It results in the following generalised force equation, at  $A$ :

$$\begin{aligned} \mathbf{F}_{es}(A) = & (-K_{es}(\Delta l - \Delta l_{es}) u(\Delta l_{es} - \Delta l) \\ & - K_{es}(\Delta l - Z_{es}) u(\Delta l - \Delta l_{es})) \begin{pmatrix} -\sin \alpha \\ -\cos \alpha \\ 0 \end{pmatrix} \end{aligned} \quad (24)$$

in which  $K_{es}$  is the spring coefficients of the end stop; and  $2\Delta l_{es}$  is the maximum stroke.

## 2.4 Equation of motion

The total equation of motion is obtained by assembling the previous equations and expressing Newton's law.

### 2.4.1 Frequency domain

In the frequency domain, only the linear PTO is considered. The viscous forces and end stops forces are not taken into account. The kinematic is linearised. Therefore, the equation of motion can be written in the frequency domain:

$$\begin{aligned} \overline{\mathbf{GA}} (\mathbf{M} + \mathbf{C}_M(\omega)) \mathbf{T} \ddot{\mathbf{X}} + (\mathbf{B}_{PTO} + \overline{\mathbf{GA}} \mathbf{C}_A(\omega) \mathbf{T}) \dot{\mathbf{X}} \\ + (\mathbf{K}_{PTO} + \mathbf{K}) \mathbf{X} = \overline{\mathbf{GA}} F_{ex}(\omega) \end{aligned} \quad (25)$$

with:

- $\mathbf{M} = \begin{pmatrix} M & 0 & 0 \\ 0 & M & 0 \\ 0 & 0 & I_y \end{pmatrix}$
- $\mathbf{C}_M = \begin{pmatrix} C_{M,11} & 0 & C_{M,15} \\ 0 & C_{M,33} & 0 \\ C_{M,51} & 0 & C_{M,55} \end{pmatrix}$
- $\mathbf{B}_{PTO} = \begin{pmatrix} 0 & 0 & 0 \\ B_{PTO} & 0 & 0 \\ 0 & 0 & 0 \end{pmatrix}$
- $\mathbf{C}_A = \begin{pmatrix} C_{A,11} & 0 & C_{A,15} \\ 0 & C_{A,33} & 0 \\ C_{A,51} & 0 & C_{A,55} \end{pmatrix}$

$$\bullet \mathbf{K}_{\text{PTO}} = \begin{pmatrix} 0 & 0 & 0 \\ K_{PTO} & 0 & 0 \\ 0 & 0 & 0 \end{pmatrix}$$

$$\bullet \mathbf{K} = \begin{pmatrix} 0 & (\rho V - M)g & 0 \\ 0 & 0 & 0 \\ 0 & (\rho V - M)gd & (\rho V - M)gd \end{pmatrix}$$

### 2.4.2 Time domain

In time domain, viscous forces may be included as well as Coulomb damping for the PTO. The equation of motion is now:

$$\overline{\overline{\mathbf{GA}}} (\mathbf{M} + \mu_\infty) \mathbf{T} \ddot{\mathbf{X}} = \overline{\overline{\mathbf{GA}}} F_{ex} - \int_0^t \overline{\overline{\mathbf{GA}}} \mathbf{K}(t - \tau) \mathbf{T} \dot{\mathbf{X}}(\tau) d\tau + \mathbf{F}_B + \mathbf{F}_V + \mathbf{F}_{\text{PTO}} + \mathbf{F}_{\text{es}} \quad (26)$$

with:

$$\mu_\infty = \lim_{\omega \rightarrow +\infty} C_M(\omega) \quad (27)$$

$$\mathbf{K}_{\text{rad}}(t) = \frac{2}{\pi} \int_0^{+\infty} C_A(\omega) \cos \omega t d\omega \quad (28)$$

The rest of the forces are the same as given in the previous equations.

## 2.5 Implementation

### 2.5.1 Calculation of the hydrodynamic coefficients and functions

The BEM code Aquaplus [1] was used to calculate the hydrodynamic coefficients in the frequency domain. Figure 8 shows the mesh which was used. It is composed of 600 flat panels. Results of computation of added masses, radiation damping coefficients and excitation force coefficients at the gravity centre are plotted in Figures 9 and 10.

### 2.5.2 Estimation of viscous damping coefficients

The order of magnitude of the motion of the float is likely to be similar to the radius of the buoy, so the Keulegan Carpenter number  $KC = \frac{2\pi A}{D}$  is expected to be in the range [0, 3]. Hence, according to [3], setting the drag coefficients to  $C_x = 1$  and  $C_z = 1$  should not be exaggeratedly penalising for assessing the energy absorption of the device.

According to the same author, the quadratic roll damping coefficient was set to  $B_Q = \frac{1}{2}\rho b_Q B^4 L$  with  $b_Q = 0.1$ ,  $B = 7$  m and  $L = 7$  m.

The corresponding representative area were calculated. Their values are  $A_x = 30.5 \text{ m}^2$  and  $A_z = 38.0 \text{ m}^2$ .

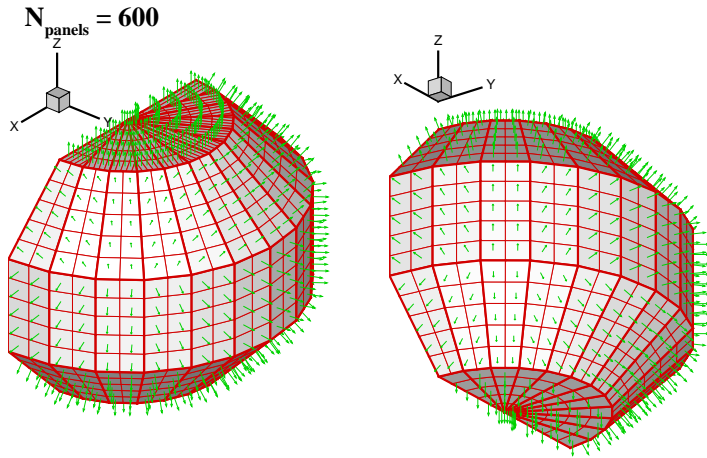


Figure 8: Mesh used for the calculation of the hydrodynamic coefficients.

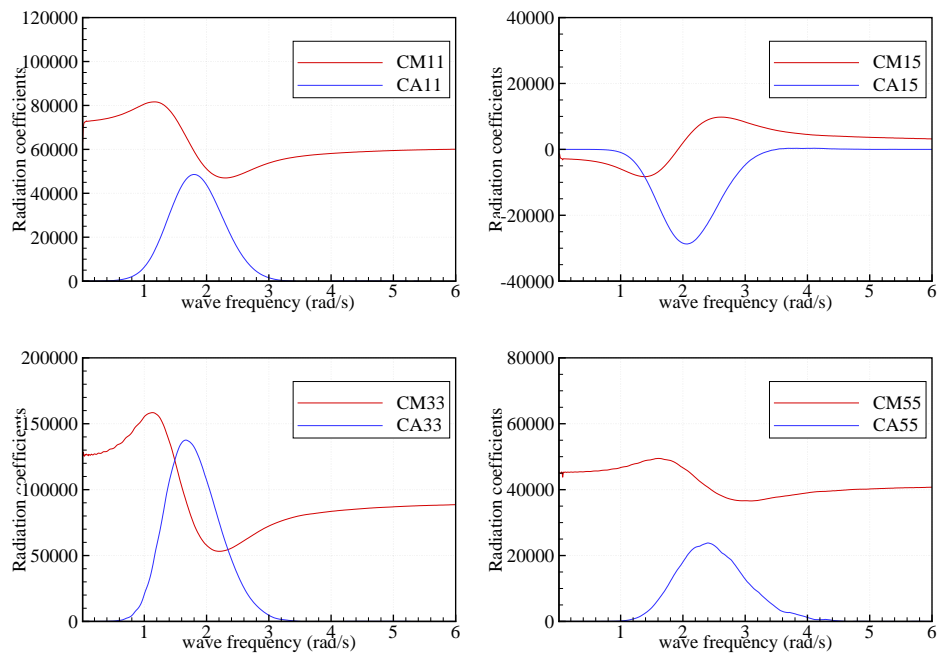


Figure 9: Frequency domain radiation coefficients, computed with Aquaplus.

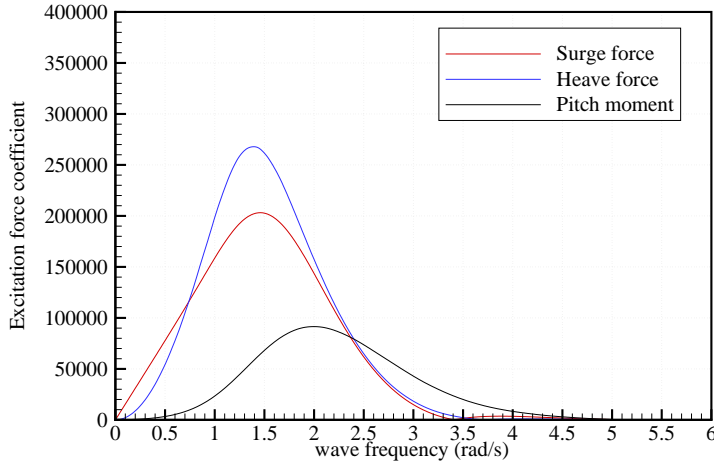


Figure 10: Excitation force coefficients in the frequency domain, computed with Aquaplus. Units on the vertical axis are N/m for the forces and N for the moment of force.

### 2.5.3 W2W models

Based on equations (25) and (26), two numerical models were derived: one in the frequency domain and the other one in the time domain. They were both solved by implementation in Fortran90.

## 3 Simulation results and energy assessment

When they are not otherwise specified, the parameters which were used in all the simulations presented here are the ones given in Table 2.

### 3.1 Verification tests

The natural period of the buoy in heave is given by:

$$\omega_0 = \sqrt{\frac{K_{PTO}}{M + C_{M33}(\omega_0)}} \quad (29)$$

By setting  $K_{PTO}$  to 60 kN/m, one gets  $\omega_0 = 0.60$  rad/s. Figure 11 shows the corresponding RAO (Response Amplitude Operator). As expected, one can see that there exists a resonance peak at frequency 0.61 rad/s for the heave motion.

One can see that there exists also a resonance frequency for the pitch motions of the buoy. It corresponds to the natural frequency of the inverse

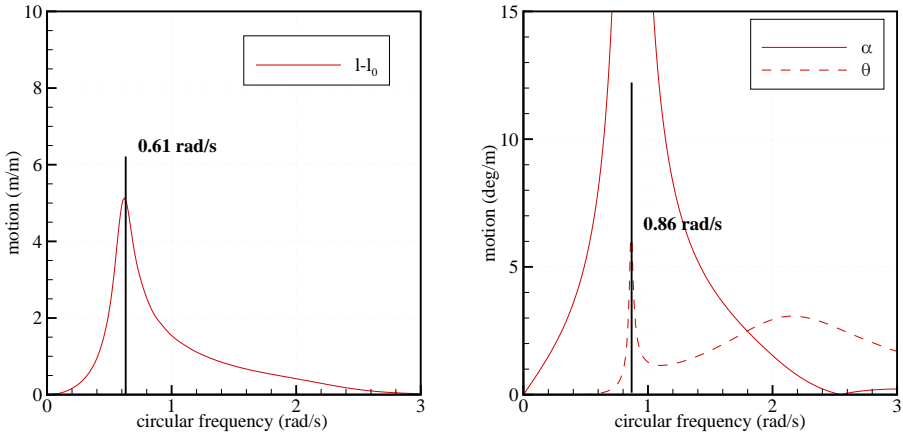


Figure 11: RAO of the Bref-SHB WEC computed with the frequency domain model.  $K_{PTO}$  is set to 60 kN/m and  $B_{PTO}$  is set to 25 kN/m.s.

pendulum motion of the buoy. One can see that for the chosen water depth (20 meters), this oscillation will be excited by the waves as it is found in the frequency range of occurring waves. In deeper water, this natural frequency will be lower, leading to even stronger excitation by the waves. In the linear theory approximation, this motion is not coupled with the productive motion, so it does not affect the energy absorption. However, non linear terms in the equation of motion will create coupling. Its effect on the energy absorption will be investigated later.

Figure 12 shows a comparison of the RAO of the Bref-SHB WEC calculated with the frequency domain model and the time domain model. In time domain, the RAO was calculated with a very small wave amplitude (0.01 m), in order to have negligible influence from the non linear terms. One can see that the agreement is excellent, except at short periods for the pitch motion  $\theta$  in blue. This was investigated and it was found that it actually comes from a beating effect due to low damping of the transient motion. Longer simulations would then give perfect agreement. Therefore, we trust that both implementations of the equations are correct in the two models, at least at first order.

Figure 13 shows decay tests of the buoy motion computed with the time domain model, with and without viscous damping. Left figures are for an initial stretching of the line of 1 meter, middle figures are for an initial angle of  $\alpha = 10$  degrees, and right figures are for an initial angle  $\theta = 10$  degrees. The PTO parameters are the same as in the previous case.

As it was expected, the heave and pitch motion  $\alpha$  are more damped with viscous damping than without. It indicates that the implementation of the viscous damping is correct. However the viscous contribution to damping

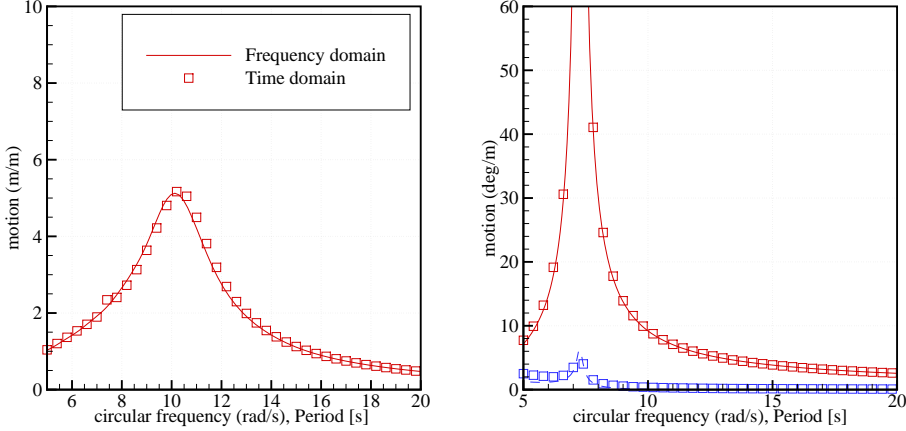


Figure 12: Comparison of Bref-SHB WEC’s RAO calculated with the frequency and the time domain model.  $K_{PTO}$  is set 60 kN/m and  $B_{PTO}$  is set 25 kN/m.s. RAO in time domain was calculated with wave amplitude 0.01 meters. Left figure is the heave motion of the buoy. In the right figure, red curve is the pitch motion  $\alpha$  and blue curve is the pitch motion  $\theta$ . One can see that the agreement is excellent which shows that both models are implemented correctly.

appears to be much smaller for the heave motion than for the pitch motion. It is probably due to the fact that in heave, PTO damping is already the dominant damping part.

An interesting phenomenon appears on the  $\theta$  pitch decay test, without viscous damping. One can see that the  $\theta$  motion induces an offset in the heave motion. This offset vanishes as the amplitude of the  $\theta$  motion decreases. The origin of this phenomenon comes from the fact that the contribution to the restoring moment from the buoyancy is proportional to  $(\alpha + \theta)$ , whereas the contribution from the constant part of the PTO force is only proportional to  $\alpha$ . However, one can see that this effect disappears as soon as viscous damping is applied.

Finally, a verification of the implementation of the end stops was performed by calculating the motion response of the buoy in a 12 seconds 4 m height regular wave, with a buoy stroke limited to 4 meters. Results are shown in Figure 14. The behaviour is as expected.

### 3.2 RAOs

The PTO coefficients have a strong influence on the RAO and power function of the Bref-SHB WEC. To understand this influence, RAOs and power functions with several sets of PTO coefficients were computed. They were

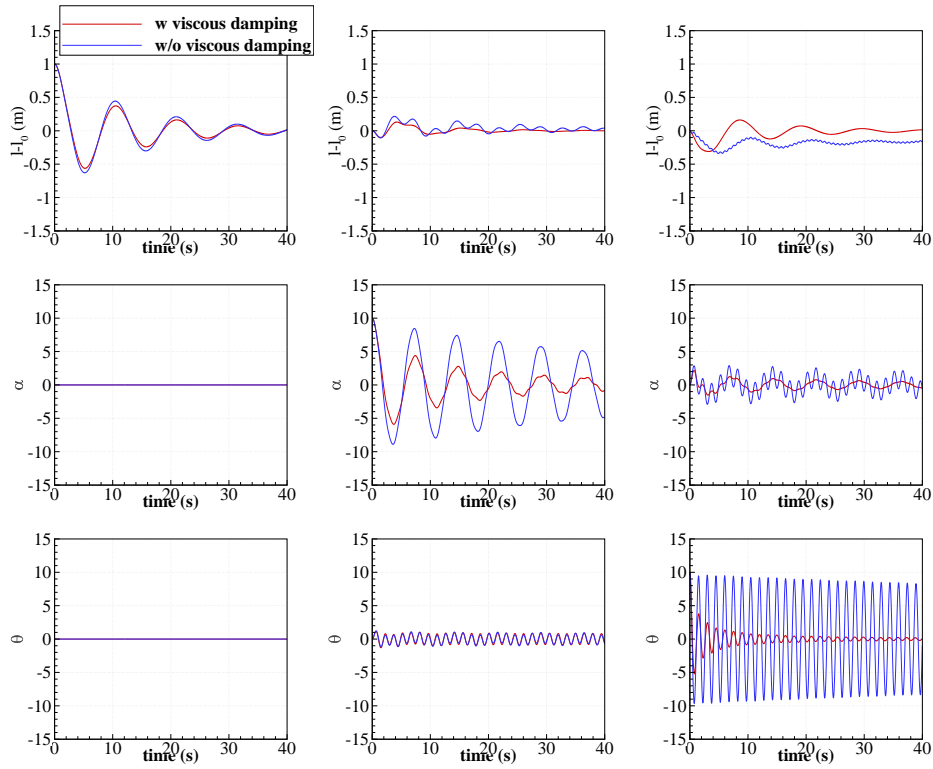


Figure 13: Decay test of the motion of the buoy, with and without viscous damping. Left figures are for an initial stretching of the line of 1 meter, middle figures are for an initial angle of  $\alpha = 10$  degrees, and right figures are for an intial angle  $\theta = 10$  degrees. The PTO parameters are the same as in the previous case. Top figures are the heave motion, middle figure are the pitch motion  $\alpha$  and bottom figures are the pitch motion  $\theta$ .

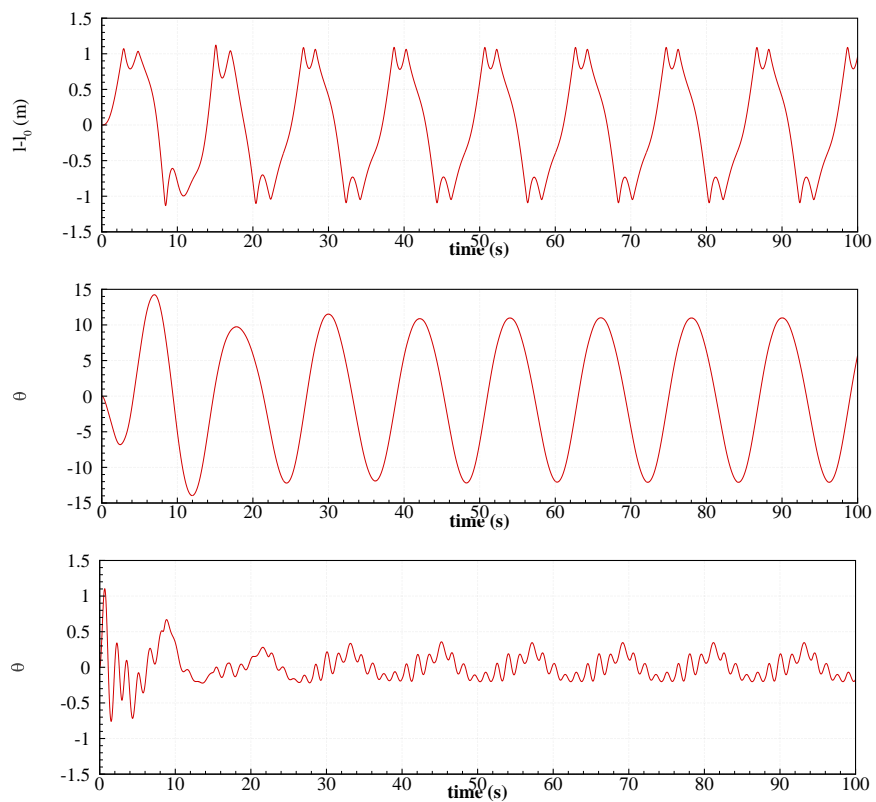


Figure 14: Motion response of the buoy in a 12 seconds 4 m height regular wave, with a buoy stroke limited to 4 meters

calculated with the frequency domain model when the PTO is linear, and with the time domain model when it is Coulomb damping. With the time domain model, the RAOs are estimated by finding the maximum of the motion during a 1200 s duration simulation in which the transients were removed. Viscous effects and end stops were included in the time domain model.

### 3.2.1 Linear damper

First, a linear damper is considered. Table 4 summarises the set of PTO coefficients which were used. In Figures 15 and 16 we have plotted the associated RAOs and power functions.

Set number	$B_{PTO}$ (kN/m.s)	$K_{PTO}$ (kN/m)
1	25	100
2	50	100
3	75	100
4	100	100
5	150	100
6	25	50
7	25	150

Table 4: PTO settings for the linear damper

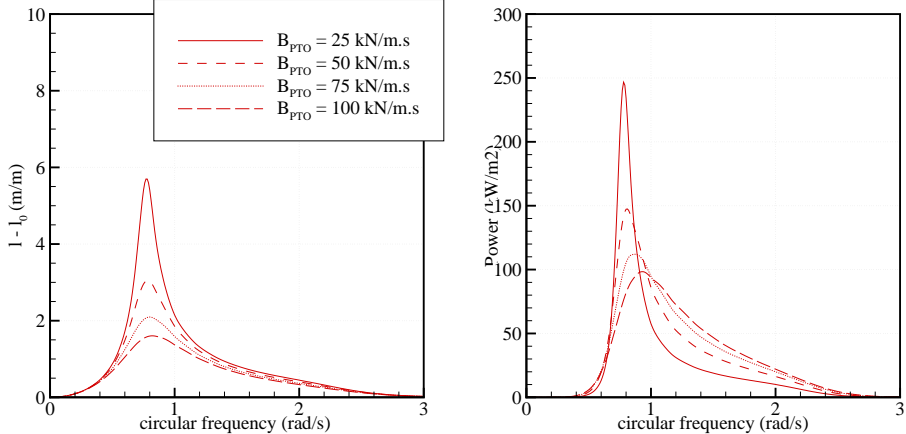


Figure 15: RAO and power function for the Bref-SHB with PTO settings 1 to 4. In these settings, the PTO model is linear, with  $K_{PTO}$  equal to 100 kN/m. The results have been computed with the frequency domain model.

In Figure 15 PTO settings 1 to 4 are used. For these settings,  $K_{PTO}$  is equal to 100 kN/m. One can see that:

- The power absorption of the Bref-SHB WEC can be as high as 200 kW per square meter of incident wave at resonance. However, it comes with a large amplitude of motion (amplification factor of almost 6). It is thus likely to be damped by additional viscous effects. In practice, one could expect the maximum amplification factor to be about 2 or 3.
- The amplitude of motion is reduced as the  $B_{PTO}$  coefficient increases. The power function depends strongly on this coefficient. As the  $B_{PTO}$  coefficient increases, the peak of power absorption shifts to longer wave periods, and the maximum power decreases. However, at the same time the bandwidth gets broadened.

From the annual energy absorption point of view, some of these effects are good (period shifting, broadening of bandwidth), and some are bad (decrease in the maximum of power absorption). Therefore one has to look for a compromise.

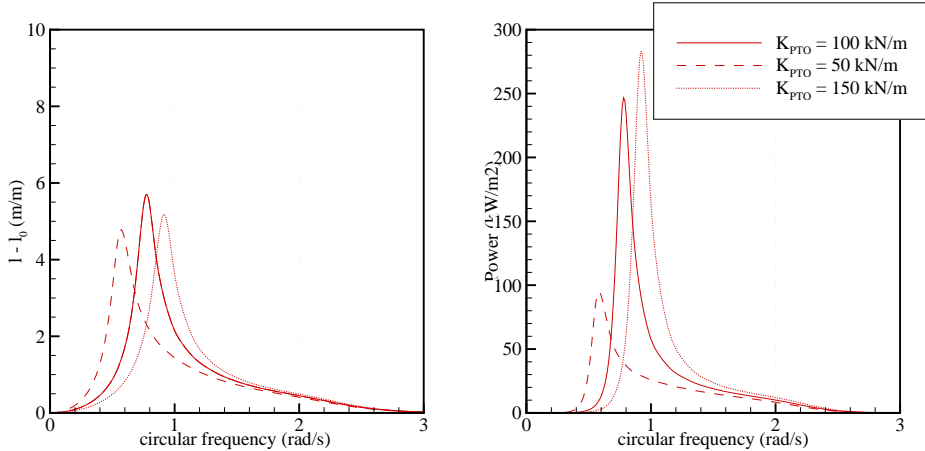


Figure 16: RAO and power function for the Bref-SHB with PTO settings 1, 6 and 7. In these settings, the PTO model is linear, with  $B_{PTO}$  equal to 25 kN/m.s. Results have been computed with the frequency domain model.

In Figure 16, we have plotted the RAOs and power function for PTO settings 1, 6 and 7. In these settings,  $B_{PTO}$  is equal to 25 kN/m.s. As expected, changing the PTO stiffness gives the possibility to tune the natural period of the system.

### 3.2.2 Coulomb damping

Then, an approximate Coulomb damping is considered. As it is a non-linear component, the time domain model was used to calculate the pseudo-RAO

of the Bref-SHB WEC with three settings for the PTO force coefficient  $H_{PTO} = 25, 50$  and  $100\text{ kN}$ . The  $K_{PTO}$  coefficient was set to  $100\text{ kN/m}$ . The wave amplitude was set equal to  $1\text{ m}$ . Viscous damping and end stop effects were included.

The results are shown in Figure 17 together with the case of linear damping with  $B_{PTO} = 100\text{ kN/m.s}$ . We chose to compare with this setting for the linear damping because in the other cases the RAO is larger than the allowed stroke (4 meters in this case).

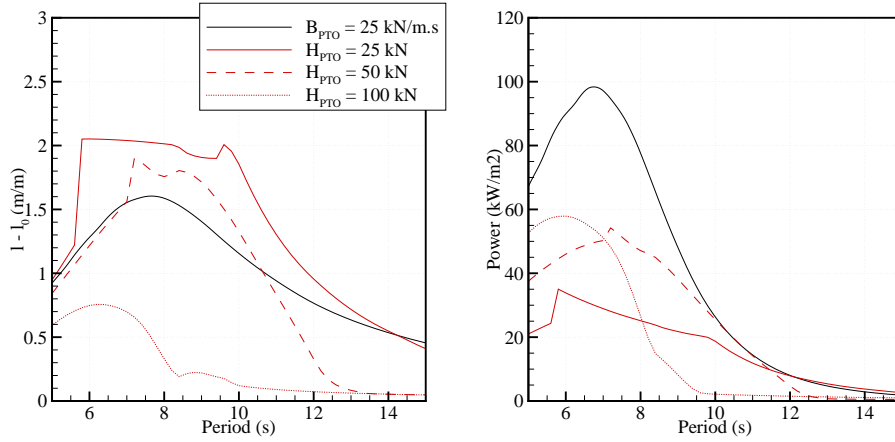


Figure 17: RAO and power function for the Bref-SHB with Coulomb damping. The results have been computed with the time domain model.

Compared to the case of linear damping, one can see that the power absorption is reduced with Coulomb damping. The reduction factor is large, in the range from 2 to 3. One can see that if the damping coefficient is too small ( $H_{PTO} = 25\text{ kN}$ ), the motion reaches the end stop limit for a large range of frequencies. This limiting effect can be observed on the energy absorption as well. It results in a net waste of energy, in comparison with cases with larger PTO coefficients. On the other hand, if the damping coefficient is too large, the system cannot move, which leads to zero energy absorption. It is what happens in case of  $H_{PTO} = 100\text{ kN}$ , for wave periods longer than 10 seconds. Therefore, one has to be careful in setting the value of the PTO coefficient, i.e the high-pressure level in the hydraulic circuit.

As a nominal value, one can conclude from these graphs that one should choose  $H_{PTO}$  around  $50\text{ kN}$ .

### 3.2.3 Effect of quadratic damping

In order to get an idea of the importance of non-linear effects on the response of the Bref-SHB WEC, RAO and power function of the system were

calculated for wave amplitudes of 0.25, 0.5 and 1 meters. The PTO was set to linear, with PTO settings number 4.

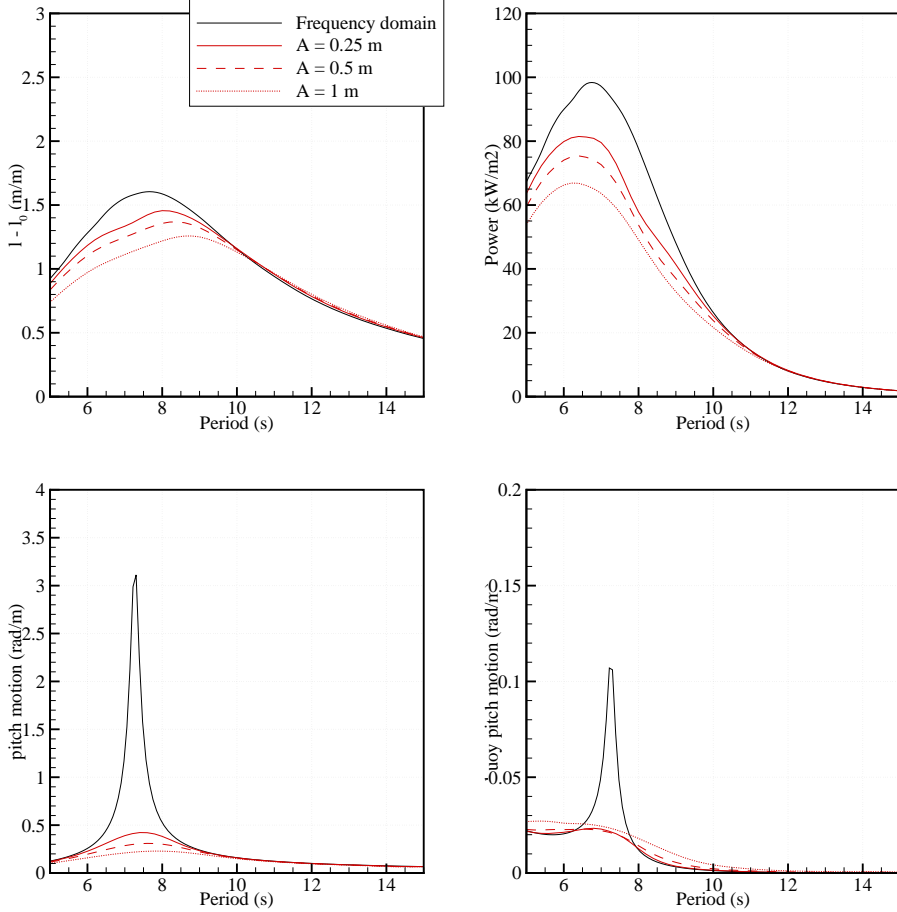


Figure 18: Effect of non linearities (mechanical, viscous damping and end stops) on the pseudo RAO and power function of the Bref-SHB WEC. PTO is linear with settings 4.

Results are shown in Figure 18. One can see that the effect of non linearities on the response of the system is important, even for the smaller waves. As expected, these non-linearities reduce the level for resonance peak for all the three degrees of freedom. The power absorption is reduced by 30 % at resonance for a wave of 1 m amplitude. Therefore, it is important to take these non-linearities into account in the derivation of the mean annual power absorption.

### 3.2.4 Conclusions

From these results in regular waves, it appears that:

- The order of magnitude of absorbed power from the Bref-SHB WEC is 50 to 100 kW per square meters of wave amplitude in regular waves.
- With linear PTO, both PTO damping and stiffness parameters have an influence on the RAO and power function of the Bref-SHB WEC. They should be optimised for each sea state in the calculation of annual energy absorption.
- With hydraulic PTO, it was not possible to achieve the same levels of energy absorption as with the linear PTO in regular waves. The reason is probably the limited stroke. Therefore, the derivation of the power matrix of the Bref-SHB will be done using the linear PTO model.
- Non-linear effects have a large influence on the power absorption, even in the case of small waves.

## 3.3 Power matrix and criteria

In this section, all time domain simulations were performed in irregular waves using the JONSWAP spectrum. All quantities are derived from 1200 s duration simulations, with a time step of 0.05 s. To remove the transient effects, the first  $15 \times T_p$  seconds of the simulations are not taken into account. When it is not otherwise specified, the maximum stroke length is taken to be equal to 6 meters.

### 3.3.1 Power matrix

Figure 19 shows the power matrix of the Bref-SHB WEC. The left-hand figure is the mean absorbed power and the right-hand figure is the maximum recorded over the duration of the simulation for each sea state.

The PTO model was set to linear. For each sea state, the PTO damping and stiffness parameters were optimised. The range of optimisation of the PTO parameters is given in Table 5.

	$K_{PTO}$ (kN/m)	$B_{PTO}$ (kN/m.s)
Minimum	20	10
Maximum	200	200

Table 5: Range of optimisation of the PTO parameters.

For a typical sea state of 9 seconds wave peak period and 2.5 meters significant wave height, the mean absorbed power of one Bref-SHB buoy is 30 kW. Power absorption higher than 100 kW is reached for the strongest sea

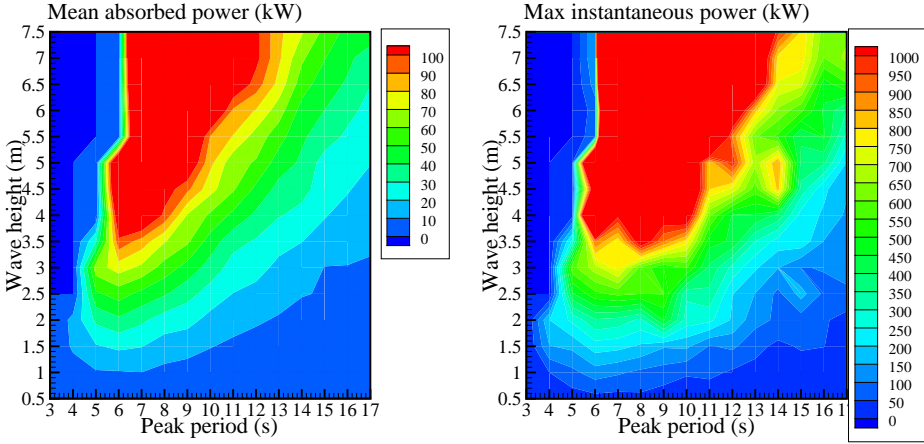


Figure 19: Power matrix of the Bref-SHB WEC with linear PTO. The PTO coefficients are optimised for each sea state. Left figure is the mean absorbed power and right figure is the maximum instantaneous power recorded during each simulation.

states. As expected from the results in regular waves, the system exhibits the best efficiency for the shorter wave periods. The efficiency decreases rapidly with increasing wave peak period.

The maximum absorbed power is typically 15 times the mean power. It is very large. It means that the PTO system has to deal with large amounts of instantaneous power, much larger than the average power absorption. This is a drawback indeed, but one should note that most of proposed WECs have to face this issue.

Figure 20 shows the matrices containing optimised values of the PTO coefficients. One can see that for the stiffness coefficient, it varies essentially with the wave period, in a somehow linear manner. This was expected, since the aim of varying the stiffness coefficient is to tune the natural period of the system. About the damping coefficient, one can see that it does not vary much with the wave height nor with the wave period. As an average value, one could choose  $B_{PTO}$  equal to 100 kN/m.s for all sea states.

Figure 21 shows matrices of the RMS and instantaneous maxima of the line motion recorded during the simulations. As expected, the RMS value for the line motion is typically about one fourth of the significant wave height. It seems that it does not vary much with the wave period. On the right-hand figure, one can see that events during which end stops are reached occur as soon as the wave height is larger than 3 meters. It means that it would happen quite often. Therefore, special attention should be paid in the design of the end stop mechanisms.

Significant pitch motion is typically in the order of 5 degrees. It increases

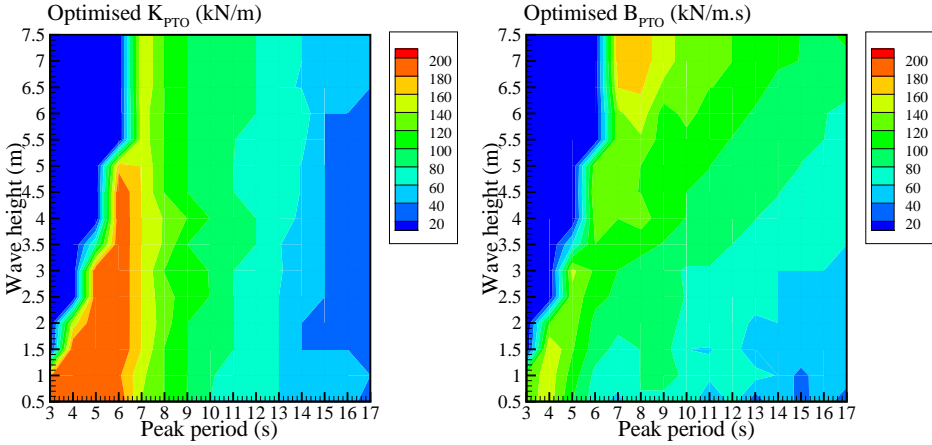


Figure 20: Optimised value of the PTO coefficients.

linearly with the wave period and the wave height. The buoy's pitch motion appears to be very small, so it could probably be neglected.

By multiplying the power matrix with wave data statistics, one can calculate the annual energy absorption of the Bref-SHB WEC for each considered wave site. Deep water wave statistics were obtained by transferring the energy from deep water to shallow water, according to Section 1.2. Results of mean annual power absorption are reported in Table 6 as well as the assessment criteria for the six considered sites.

One can see that the mean annual absorbed power that one can expect from the Bref-SHB WEC is a few tens of kilowatts. It goes from 8.8 kW for the SEM-REV site up to 31.1 kW for the highly energetic Belmullet site. For a typical wave resource of about 25 kW/m, the typical absorbed wave power by the Bref-SHB is about 20 kW. The typical mean capture width is about 1 m, depending on the site. It is up to 1.6 m for the Danish site.

Table 7 shows the comparison of the criteria of the Bref-SHB device to the B-HBA, F-3OF, F-2HB, Bref-HB and F-OWC devices, for the Yeu site.

One can see that the Bref-SHB's relative capture width is in the lower range. It has an average Energy to mass ratio and a good Energy to Wetted surface ratio. The ratio Energy per PTO force is good also. The ratio Energy per Wave force is rather high in comparison with the other considered technologies.

Figure 22 shows the distribution of the absorbed power in function of the power level. The left-hand figure shows the probability for the power production to be between two levels and right-hand figure shows the probability for the power to be greater than a given power level. It has been calculated with the wave statistics of the Yeu site. One can see the absorbed wave power is greater than the mean power about 45% of the year.

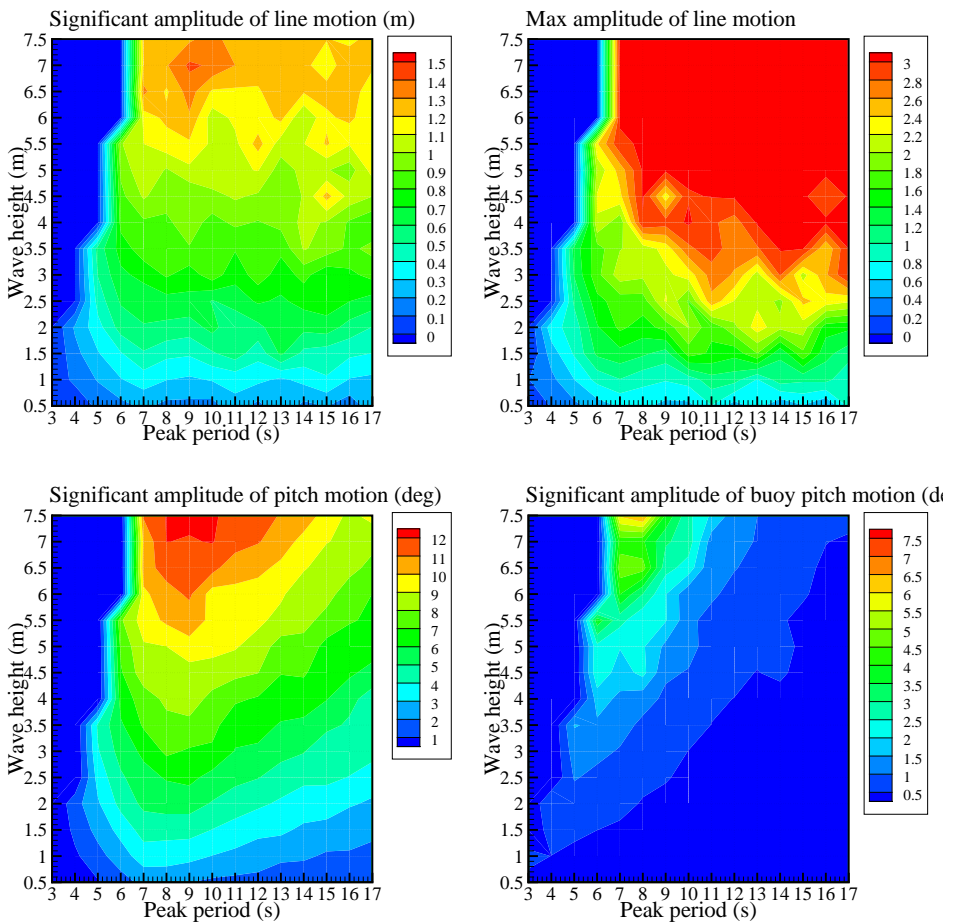


Figure 21: Matrices of the RMS of the motion of the Bref-SHB WEC.

Parameter	Unit	SEM-REV	EMEC	Yeu	Lisboa	Bel-mullet	Danish study
$\gamma$		1	1	3.3	3.3	3.3	1
$J$	[kW/m]	13.3	19.6	23.5	33.7	72.5	12.0
Mean power	[kW]	8.8	18.5	22.0	19.0	31.3	19.1
Capture width	[m]	0.66	0.94	0.94	0.57	0.43	1.64
$E_y / \text{Mass}$	[kWh/kg]	0.39	0.81	0.97	0.83	1.37	0.84
$E_y / A_{\text{wet}}$	[MWh/m <sup>2</sup> ]	0.35	0.74	0.88	0.76	1.24	0.76
$E_y / F_{\text{PTO}}^{\text{RMS}}$	[kWh/N]	1.53	2.08	2.37	2.29	2.95	2.06
$E_y / F_{\text{wave}}^{\text{RMS}}$	[kWh/N]	2.57	3.60	4.05	3.84	4.73	3.57

Table 6: Evaluation criteria for the Bref-SHB WEC for chosen sites having mean annual wave energy transport  $J$ , and where sea states are synthesized with a spectrum peakedness factor  $\gamma$ . The parameters are calculated based on the yearly energy delivery  $E_y$ . The mass is taken as the total mass of the ballasted installed structure, not including the moorings, and  $A_{\text{wet}}$  is the wetted surface area of the structure. Significant PTO force  $F_{\text{PTO}}^{\text{RMS}}$  and significant wave force  $F_{\text{wave}}^{\text{RMS}}$  are taken as the yearly RMS values. The uncertainty of  $E_y$  is estimated to  $[-40, 20]\%$ .

### 3.3.2 Assessment of the uncertainties

#### Viscous losses

To assess the uncertainty associated with the modelling of the viscous losses, the mean annual absorbed power at the Yeu site was calculated with different values of the viscous coefficients. Calculations were made with the linear PTO model, with optimisation of the parameters. Figure 23 shows the results in function of the percentage of viscous damping coefficients with respect to the nominal values.

One can see that the modelling of the viscous damping has a large influence on the results of mean power. If the viscous damping coefficient is doubled, the mean absorbed power is 19 % smaller than the one with nominal values. If the viscous damping coefficient is divided by a factor 2, then the absorbed power is increased 20 %.

Therefore, the retained uncertainty associated with the modelling of viscous damping is roughly  $[-20, 20]\%$ .

#### PTO modelling and optimisation

Calculation of the mean annual absorbed power at the Yeu site was performed with the hydraulic PTO model, with optimisation of the PTO parameters, in order to evaluate the effect of the PTO modelling on the system energy absorption's ability. The absorbed power was found to be equal to 17.9 kW, i.e 19 % less than with the linear PTO model. It shows that in this case the PTO model has influence on the level of mean annual absorbed power. We recall that in the case of the Seabased the difference

	Bref-SHB	B-HBA	F-3OF	F-2HB	Bref-HB	F-OWC*	Pelamis P1**
Mean power (kW)	22.0	190	219	191	3.3	337.5*	230.3**
Capture width (m)	0.94	8.08	8.17	7.12	5.30	12.7*	8.6**
Hydrodynamic efficiency $\eta_1$	13 %	11 %	33%	36%	6%	53%*	6%**
$E_y / \text{Mass}$ (MWh/m <sup>3</sup> )	0.94	1.04	1.36	0.338	0.92	1.62*	2.88**
$E_y / A_{\text{wet}}$ (MWh/m <sup>2</sup> )	0.88	0.383	0.89	0.79	0.68	0.77*	1.2**
$E_y / F_{\text{PTO}}^{\text{RMS}}$ (kWh/N)	2.37	0.79	3.29	2.03	2.3	N/A	N/A
$E_y / F_{\text{wave}}^{\text{RMS}}$ (kWh/N)	4.05	2.29	2.67	3.03	1.27	N/A	N/A

Table 7: Comparison of Bref-SHB’s criteria with the B-HBA (Wavestar-inspired), the F-3OF (Langley-inspired), the F-2HB (Wavebob-inspired), the Bref-HB (Seabased-inspired), the F-OWC (OEbuoy-inspired) and the Pelamis at the Yeu site. The parameters are calculated based on the yearly energy delivery  $E_y$ . The mass is taken as the total mass of the ballasted installed structure, not including the moorings, and  $A_{\text{wet}}$  is the wetted surface area of the structure. Significant PTO force  $F_{\text{PTO}}^{\text{RMS}}$  and significant wave force  $F_{\text{wave}}^{\text{RMS}}$  are taken as the yearly RMS values. \* and \*\* means that the numbers were obtained respectively with a frequency domain model and using the power matrix provided by the developer. They need to be confirmed.

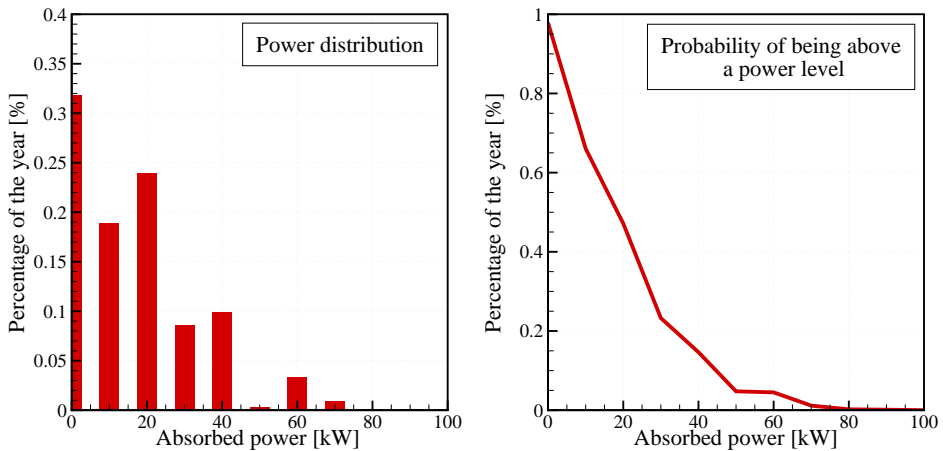


Figure 22: Distribution of the power production.

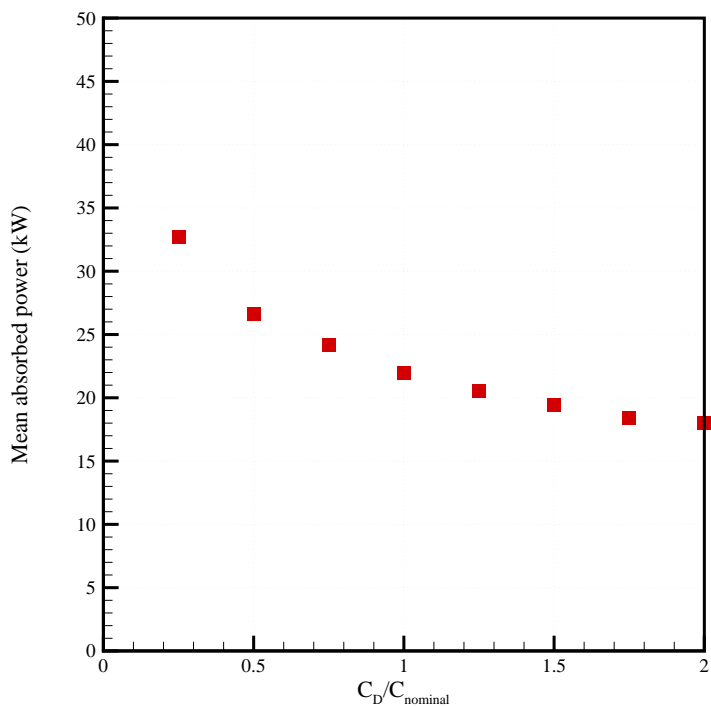


Figure 23: Mean absorbed power at Yeu in function of the percentage of viscous damping with respect to the nominal value.

of mean annual power calculated with a linear PTO model and with a full machinery model was less than 10 %. In the case of the Wavestar, it was less than 2 %. Therefore, the retained uncertainty associated with the modelling of PTO is  $[-20, 0]$  %. If we add that to the uncertainty from the viscous loss modelling in a summed squares manner, we find that the total uncertainty due to these two factors is  $[-28, 20]$  %.

To assess the benefit of optimising the PTO coefficients for each sea state, calculation of the mean annual power absorption was performed with a linear PTO with fixed PTO settings. Results are shown in Table 8.

Table 8: Mean annual power with and without optimisation of the PTO parameters for each sea state.

PTO	SEM-REV	EMEC	Yeu	Lisboa	Bel-mullet	Danish study
Setting 4	5.4	11.5	13.7	12.1	21.9	11.8
Optimised parameters	8.8	18.5	22.0	19.0	31.3	19.7
Difference (%)	39	38	38	36	30	40

One can see that optimising the PTO parameter increases the mean annual power absorption by 30 to 40%. This slow control is simple and easy to apply, so it should definitely be considered in practice.

### 3.4 Parametric studies

#### 3.4.1 Threshold on the instantaneous absorbed power

Table 9 shows the mean absorbed power at Yeu in function of a rating on the instantaneous power. It means that the instantaneous power is limited to this threshold. The difference between the available instantaneous power and the maximum is lost. The calculation was performed with the linear PTO model.

Table 9: Mean annual absorbed power at Yeu in function of the rating of maximum instantaneous absorbed power. The PTO model is linear and the PTO coefficient was optimised for each sea state.

Max. instantaneous absorbed power (kW)	Mean annual absorbed power (kW)
200	21.7
400	21.7
None	22.0

One can see that the instantaneous power could be rated at 200 kW with negligible losses in the mean annual absorbed power.

### 3.4.2 Threshold on the mean absorbed power

Calculations of the mean annual power at Yeu site were performed with power rating of the platform of 100 kW and 200 kW. It means that if the calculated value of mean absorbed power for a sea state is larger than the power rating, then the surplus power is considered as lost.

Differences on the mean annual power were found to be smaller than 1% in both cases. It means that the Bref-SHB WEC could be rated at 100 kW without losing significant amounts of energy output over the year.

### 3.4.3 Effect of stroke length

Calculations of the mean annual power at the Yeu site were performed with stroke length of 4 m and 8 m instead of the normal value of 6 m. Differences on the mean annual power were found to be smaller than 2% in both cases. It means that the stroke length could be set to 4 meters with negligible losses in annual energy absorption.

### 3.4.4 Effect of buoy size

Figure 24 shows the effect of scaling the size of the converter on the mean power absorption of the Bref-SHB placed at the Yeu site. This figure has been calculated using the frequency domain model. The PTO model is set to linear, with fixed PTO parameters set to  $B_{PTO} = 100 \text{ kN/m s}$  and  $K_{PTO} = 100 \text{ kN m s}$  at scale 1. They are scaled according to the Froude scaling law at other scales.

One can see that the mean absorbed power grows linearly with the displacement for small devices. As the displacement increases, the slope decreases.

For a displacement twice the nominal displacement, one can see that the increase in power absorption is 34%. At the same time, the increase in the wetted surface is 58%. Hence, it seems that scaling up the Bref-SHB is likely to increase its economics.

## 4 Conclusions and recommendations

From the results and the study presented above, main conclusions are:

- The mean power level that one can expect from the Bref-SHB WEC is about 20 kW on a site whose wave resource is about 25 kW/m. The uncertainty is about  $[-28\%, +20\%]$ . It comes from the estimation of the viscous losses and the PTO modelling.

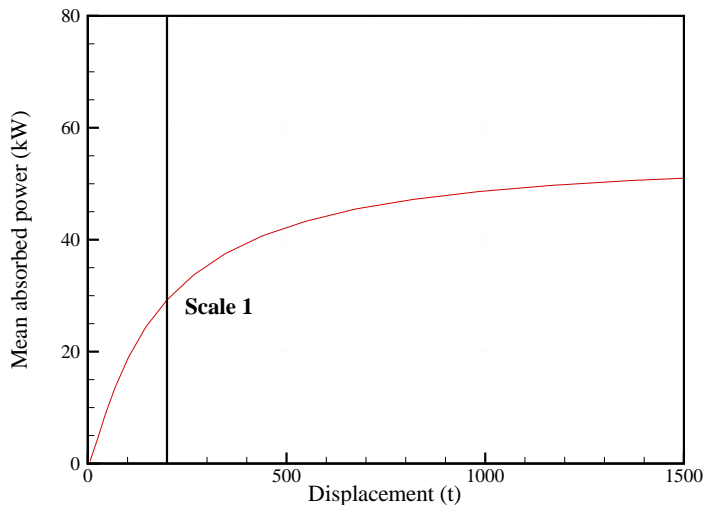


Figure 24: Influence of the scale on the mean power absorption of the Bref-SHB at Yeu.

- The PTO modelling – linear or hydraulic – has a rather large influence on the mean power absorption. The annual mean power is 20 % less with hydraulic PTO than with linear PTO.
- The Bref-SHB could be rated to 100 kW without losing a significant amount of energy production. Limitation of the instantaneous absorbed power to 10 times the mean output power (200 kW) would not significantly reduce the mean absorbed power either.
- The stroke length could be set to 4 meters with negligible reduction in the annual energy absorption.

## References

- [1] G. Delhommeau, 1997. Seakeeping Code Aquaplus
- [2] J. Falnes, 2002. Ocean waves and oscillating systems. Linear interactions including wave energy extraction. Cambridge university press.
- [3] B. Molin, 2002. Hydrodynamique des structures offshore, Guides Practiques sur Les Ouvrages En Mer, TECHNIP Eds.
- [4] [www.carnegiecorp.com.au](http://www.carnegiecorp.com.au) Accessed April, 7th, 2011.